Free-span Analyses

of an

Offshore Pipeline

400 ton

MADE IN MATLAB/ABAQUS

Kristian Ruby
Peres A. Hartvig
Master Project 2007-2008
Department sof Civil Engineering, Aalborg University

SYNOPSIS

Title: Free-span Analyses of an Offshore Pipeline

Theme: Design and Analysis of Advanced/Unusual Structures

Period: 5 September 2007 – 11 June 2008

Students: Synopsis:

_____
Peres Akrawi Hartvig

_____
Kristian Ruby

Supervisors:

Thomas Lykke Andersen

Lars Andersen

Pages: 303

Attachment: DVD

Finished: 11 June 2008

This project is focused on numerical modelling of dynamic problems with basis in a free-spanning offshore pipeline located at the Danish area of the North Sea.

Hydrodynamic force models are evaluated considering time variation of force coefficients and wake effects. A force model due to vortex lock-in is also considered. Hydrodynamic damping is implemented by a force feedback model.

Analytical and numerical models of soil springs have been compared. Transmitting boundary elements for the pipeline and soil springs have been developed and implemented in a numerical Winkler model. Liquefaction problems of the soil have also been evaluated.

Free-span analyses are made in a non-linear Winkler model with main focus on fatigue damage due to dynamic excitation from waves and current. Parametric study is performed to detect the governing parameters for the damage of a pipeline free-span.

Finally, the project contains multi-span analyses that treat the interaction of two neighbouring free-spans.

RESUMÉ

Dette projekt omhandler numerisk modellering af dynamiske problemstillinger med udgangspunkt i fritspændsanalyser af en offshore rørledning i det danske område af Nordsøen. Fritspændsanalyserne er tværfaglige og projektet indeholder tre fagområder: konstruktion, hydrodynamik og geoteknik.

Hydrodynamiske lastmodeller, der inkluderer tidsvarierende kraftkoefficienter og wake-effekt er undersøgt og sammenlignet med den konventionelle Morison Model. Implementering af hydrodynamisk dæmpning er inddraget i lastmodellerne som en feedback lastmodel. Empirisk lastmodellering af hvirvel lock-in er også inddraget i projektet.

Jorden omkring rørledningen er i den numeriske modellering beskrevet som fjedre efter princippet for en Winkler-model. De analytiske fjedre er blevet vurderet i forhold til stivheden beregnet i en numerisk 2D kontinuummodel. Transmitterende randbetingelser for rør og jord er blevet udviklet og implementeret i Winkler-modellen. Udmattelse i jorden som konsekvens af cyklisk belastning af jorden omkring rørledningen er blevet vurderet kvalitativt.

De konstruktionsmæssige problemstillinger har primært fokus på udmattelse af rørledningen som konsekvens af den dynamiske påvirkning af fritspændet. Søjleinstabilitet er også inddraget i projektet for at vurdere denne problemstilling i forhold til udmattelse.

Et parameterstudie er blevet foretaget for et enkeltspænd for at få overblik over de styrende parametre for det dynamiske respons og udmattelse af rørledningen. Herunder er forskellen i udmattelseskonsekvensen ved at benytte laster fra regelmæssige og uregelmæssige bølger blevet analyseret. Analyse af flerspænd er inddraget med fokus på de dynamiske konsekvenser der opstår når to nærliggende fritspænd interagerer.

TABLE OF CONTENTS

PREFACE

This master project is made by two students attending the 3-4 semester of the master program in civil engineering at Aalborg University, Denmark. The project is written in the period from 5 September 2007 until 11 June 2008. The main theme for the master project is "Design and analysis of advanced/unusual structures".

The project is composed of two parts:

- A report containing design conditions, results, conclusions and chosen calculations.
- A DVD with the students' programs, numerical models, simulations and a digital version of the report.

The reader is suggested to read the appendices that are available for the individual chapters before reading the next chapter in order to get the full perspective of the analyses. Formulas are repeated in the appendices if they are considered to improve the context between report and appendix.

The following notation and sign-convention has generally been used in this project:

- In the chapters on soil mechanics and buckling, compressive stresses and strains are defined as positive, but everywhere else compression is defined as negative.

- Differentiation of a variable with respect to time t is denoted with prime, e.g. $\frac{dy}{dt} \equiv \dot{y}$, whereas differentiation of a variable with respect to other variables are shown in full conventional notation, e.g. $\frac{dy}{dx}$.

- Vectors and matrices are shown in bold typography.

- When using index notation, Greek indices denote 1..2 and Latin indices denote 1..3.

- Values or formulas that have been changed in the report in comparison with the original sources are denoted with *.

INTRODUCTION

In this chapter, a broad perspective at offshore pipelines is taken. First, the background and involved fields of engineering are described. Then, the life cycle of an offshore pipeline is elaborated. Then follows an overview of typical loads and limit states. The chapter closes with a brief description of modelling challenges for an offshore pipeline.

BACKGROUND

Offshore pipelines are an effective way to transport oil and gas between offshore platforms or to transport oil and gas directly from offshore to land. In Denmark, offshore pipelines are used in the North Sea where most of the Danish oil reserves are located. The Danish shipping company Maersk daily handles more than 600.000 barrels of oil and 27.000.000 m^3 gas [Maersk 2008], which has made the use of offshore pipelines a necessity.

The use of offshore pipelines is a more recent development of the latter part of the twentieth century. The design of an offshore pipeline is multidisciplinary and typically involves three fields of engineering: Structural mechanics, hydrodynamics and soil mechanics which is illustrated in Figure 1.
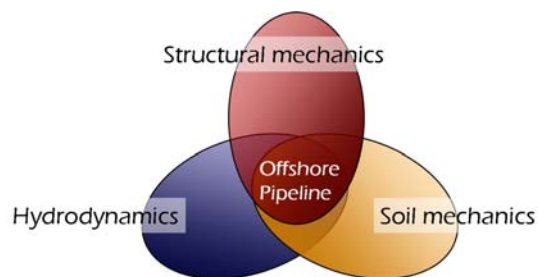
Figure 1: The involved fields of engineering for an offshore pipeline.

The design procedures for offshore pipelines are still under development which has lead to a substantial field of research that deals with a proper physical determination of the many aspects of a pipeline life cycle.

LIFE CYCLE

Many different aspects before and during the life cycle of a pipeline must be considered. Planning of the route demands a great deal of considerations. During the life cycle from fabrication to abandoning the installed pipeline after years of operation, the pipeline must provide safe transportation. In case of failure, severe environmental pollution and great economic loss may occur. The main aspects of pipeline life cycle have been evaluated in this section. Figure 2 shows the main aspects of a life cycle for a typical offshore pipeline.
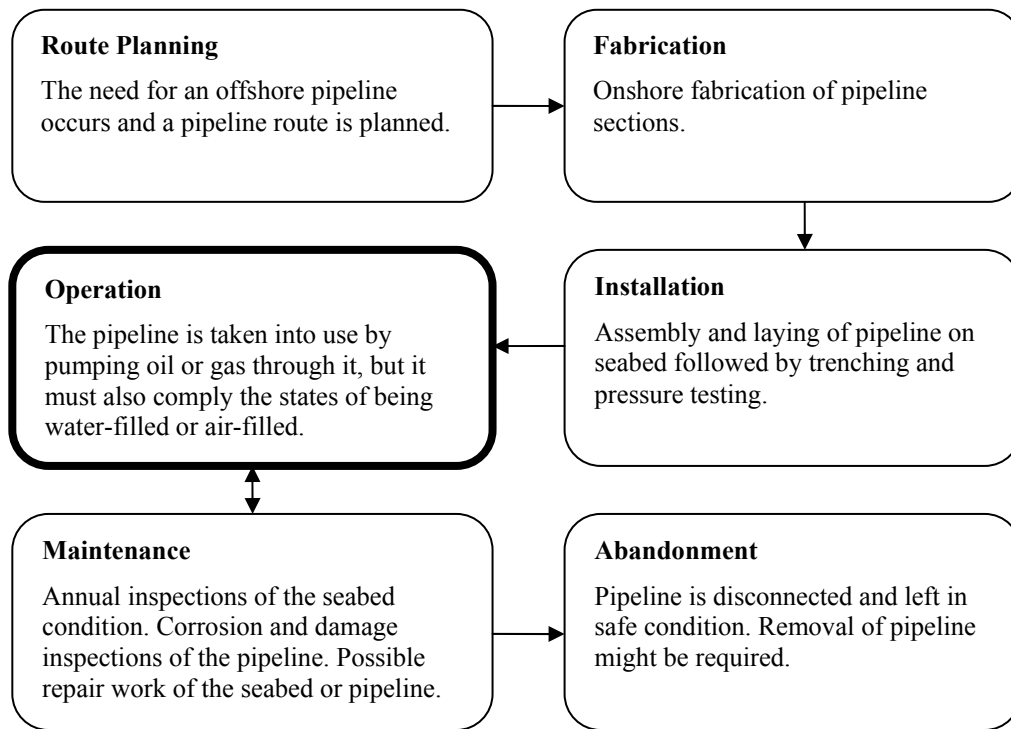
Figure 2: Life cycle of an offshore pipeline.

The enhanced box in Figure 2 shows the state of the pipeline life cycle that is in focus in this project. Most of the other states of the life cycle have to be considered in some way when the design conditions for the pipeline are determined.

During route planning, it is important to consider the seabed conditions and the wave and current action on the pipeline. The pipeline sections must comply the transportation demand and at the same time have a bearing capacity and a proper protection to resist the rather rough environment of the sea during installation and operation.

At installation, it is necessary to know the following: How is the pipe welded together, what laying technique is used (S-laying or J-laying) and is the pipeline trenched or not? Assembly and laying of the offshore pipeline is done by customised vessels. Pressure testing must be performed before the pipeline is taken into use.

During the operational state, free-spans of the pipeline may appear due to an uneven seabed or erosion. The latter has been illustrated in Figure 3. The above-mentioned states in the life cycle have great influence on how to analyse the consequences of a free-span. Failure due to fatigue damage and buckling must be considered.
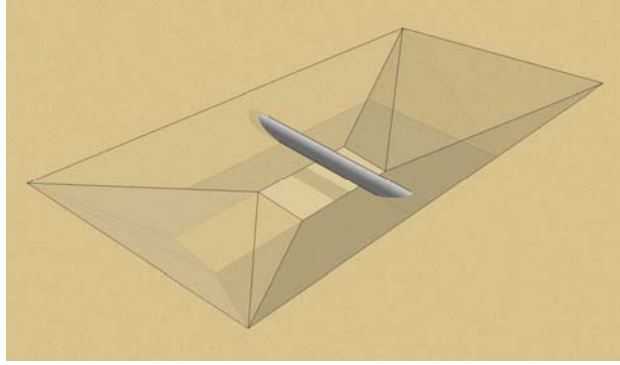
Figure 3: Illustration of a pipeline free-span due to erosion.

The maintenance is another important aspect of a pipeline life cycle. Annual inspections are made by video whereas the repair work of the seabed can be done by local rock-dumping at the free-span to prevent erosion in the future. If a pipeline section has suffered severe damage or buckling, it may be necessary to repair or replace the section. As mentioned before, this could have severe environmental and economical consequences. The combination of annual inspections and immediate repair work of a free-span will limit the design duration of a erosion-induced free-span to maximum one year which decrease the excitation from wave and current.

When the pipeline has outlived its lifetime of typical 25 years or for some reason has lost its usability, the pipeline is emptied and disconnected. If no request for removal is made from the local authorities, the pipeline is typically left in a safe condition on the seabed.

TYPICAL LOADS AND LIMIT STATES

An offshore pipeline experiences loads from a variety of sources. In this section, a brief overview is given of the loads and limit states that are typical for an offshore pipeline. The loads that affect the side-span and free-span of an offshore pipeline are illustrated in Figure 4.
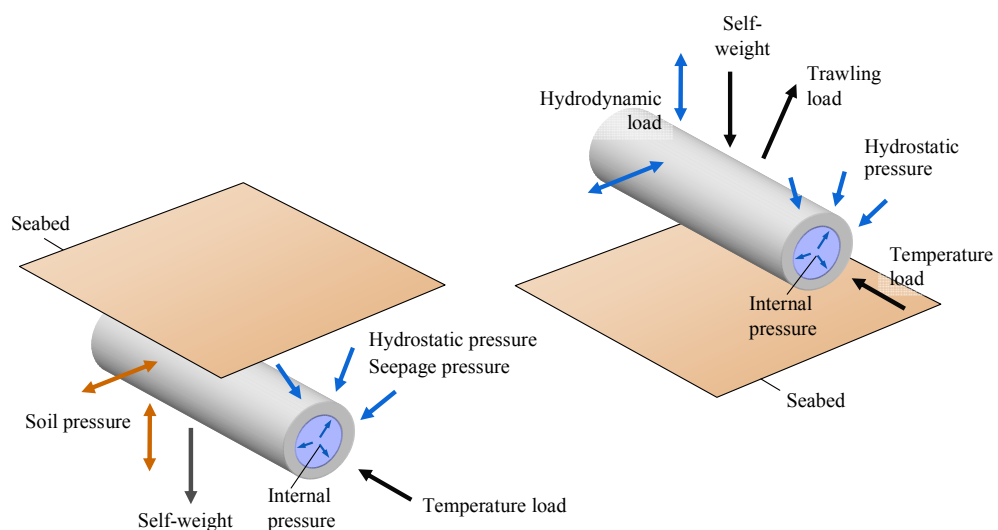
Figure 4: Typical loads that affect the side-span (left) and free-span (right) of an offshore pipeline.

The typical loads are briefly explained in the following:

- **Self-weight:** This static vertical load arises due to gravity and the mass of the pipeline with coating, internal fluid and possible marine growth for the free-span. The self-weight is typically largest during a water-filled state since the density of water is larger than air or oil.

- **Trawling load**: This load arises from accidental trawling and may affect the free-span. The trawling load has not been considered further in this project.

- **Temperature load:** This static axial load arises during an operational state due to the combination of the differences in temperature between the contents of the pipeline and the surrounding water and the prevention of expansion due to the relatively large length of the pipeline. The axial load from temperature is of considerable magnitude.

- **Internal pressure:** This static pressure affects the inner surface of the pipe-wall and arises during the operational state of the pipeline. The internal pressure may be more than 20 times larger than the hydrostatic pressure at the seabed for an offshore pipeline in the North Sea.

- **Hydrostatic pressure:** This static pressure affects the external surface of the pipeline and arises from the water pressure above the seabed.

- **Seepage pressure:** This dynamic pressure arises in the pores of the soil that cover the pipeline side-span if the soil is sufficiently permeable. In this case, the pore pressure of the soil will be governed by the ambient pressure field which in turn is governed by the waves. When the waves attack the pipeline at a skew angle, the pressure gradient will also vary along the side-span and may cause different forces upon the side-spans. The sea page pressure has not been considered further in this project.

- **Hydrodynamic load:** This dynamic load arises from the flow field around the pipeline free-span that is induced by current and waves. The hydrodynamic forces may be both lateral and vertical where the latter is a known principle from aerodynamics to make airplanes airborne.

- **Soil pressure:** When the pipeline is displaced, active or passive soil pressure may occur along the side-span in the same or opposite direction of the pipe displacement.

The pipeline is typically evaluated in the following three limit states:

- **Ultimate Limit State Failure (ULS):** In this limit state, the bearing capacity of the pipeline and the supporting soil is evaluated during extreme conditions. For the pipeline, the effects of global and local buckling may be considered. The pipeline is a dynamic system where considerable dynamic amplification may occur. Thus, analyses that consider the dynamic loads as static should include the possible effect of dynamic amplification. The combination

of vertical static self-weight and a considerable compressive axial load makes the pipeline susceptible for global buckling. Therefore, this limit state is typically governing for an offshore pipeline.

- **Fatigue Limit State (FLS):** This limit state considers the pipeline and the soil during dynamic excitation which may induce fatigue in the pipeline and liquefaction in the soil. The latter may occur in saturated, cohesionless soil when locally undrained conditions arise due to cyclic loading which causes an increase in the pore pressure and a loss in soil strength. This is typically not investigated for offshore pipelines but could have devastating effects since it may increase the length of the free-span.

- **Accidental Limit State (ALS):** This limit state considers the pipeline during accidental impact from a trawling load. This limit state is optional and has not been considered further in this project.

MODELLING CHALLENGES

An offshore pipeline is a complex structural system that poses several modelling challenges. In order to illustrate this, the challenges that lie in modelling the composite nature of the pipeline, the hydrodynamic loads and soil pressure are briefly described. In this context, one may bear in mind the following thoughtful words from an author in turbulence modelling:

> *…an ideal model should introduce the minimum amount of complexity*
> *while capturing the essence of the relevant physics. [Wilcox 2000, p1]*

Composite Pipeline

The pipeline is composed of several materials. For simplicity and without loss of accuracy for the global system, the pipeline may be regarded as homogenous. This requires that the effects of the internal and external pressure that act upon the pipe-wall are introduced as an additional compressive axial load. This is an important aspect when considering the ULS and FLS. The considerable stiffness of the concrete coating of the pipeline may also be included as additional stiffness.

Hydrodynamic Loads

The challenges of modelling hydrodynamic loads arise from the complexity of hydrodynamics. A myriad of analytical or numerical approaches are available. A relatively simple approach is to determine the hydrodynamic loads upon the oscillatory undisturbed plane flow according to appropriate wave theories such as 1st order Stoke's waves. The hydrodynamic load is typically based upon the classical Morison Model (1950) and the determination of the corresponding force coefficients has been the objective of research for the last century.

A relatively complex approach is to determine the hydrodynamic forces upon the disturbed three-dimensional oscillatory flow by the method of Computational Fluid Dynamics (CFD). At the time of writing, such results depend greatly upon the choice of turbulence model and mesh size and require validation against experiments. Wave flume experiments of a model-scale pipeline are usually not possible for the severe sea states, but U-tube model-scale experiments may be performed. A further step with increased complexity is a numerical model that couples the hydrodynamics and the structural system which may capture the effects of hydrodynamic damping and vortex lock-in.

Soil Pressure

Another modelling challenge is the interaction between the pipeline and the soil at the side-spans of the pipeline. Since soil is a highly non-linear material, the structural system is inherently more computationally expensive than a linear system and further complexity is unappealing. The conventional approach is relatively simple and models the soil as a series of springs as illustrated in Figure 5. This is typically referred to as a Winkler foundation or a Winkler model. The springs may act in multiple directions and interact only through the pipeline.
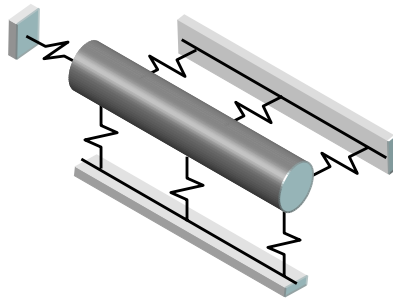
Figure 5: A Winkler foundation which is constituted by springs.

A relatively complex approach is to model soil by anisotropic, three-dimensional continuum elements with plastic behaviour. Several plastic constitutive numerical models may be used such as the Mohr-Coulomb Model, Critical State Models or Hardening Soil Model. The numerical model that is in best accordance with experiments may be chosen which in practice limits the usability of plastic models with many empirical parameters. An accurate determination of the soil characteristics is rarely performed due to the great variation along the pipe route and the many resources that are involved in extracting offshore specimens and conducting triaxial tests.

The modelling challenges that have been explored in this project are described in the following chapter on Project Thesis.

PROJECT THESIS

This master project is about free-span analysis of an offshore pipeline placed in Danish waters. The topics of free-span analysis that have been treated in this project are explained below.

Part 1: Design Conditions

The design conditions for the free-span analyses are determined. This includes the location, environmental conditions, structural data, soil parameters, damping parameters and safety factors.

Part 2: Structural Mechanics

The main objective of a free-span analysis is to determine the maximum allowable free-span in the Fatigue Limit State (FLS) considering fatigue damage and the Ultimate Limit State (ULS) considering instability problems. A part of the objective of this project has been to present the current design procedures for these two limit states with regard to free-span analysis.

Part 3: Hydrodynamics

Flow conditions around a near-wall cylinder are examined by studying theory and experimental results in the literature. This should give basic knowledge about the origin of the hydrodynamic forces affecting the pipeline free-span.

Different hydrodynamic force models have been studied primarily to challenge the conventional Morison Model by comparing this with more recently developed Wake Models. The force models are evaluated on their capability to describe the time variation in forces from regular and irregular waves including current. Also the calibration of the models is discussed.

Part 4: Soil Mechanics

The theory behind analytical modelling of soil springs has been studied. Analytical and numerical load-displacement curves have been compared. The latter has been made in Plaxis 8.2 which is a commercial geotechnical FEM-program.

The concept of transmitting boundary conditions has been discussed considering the modelling of a finite soil domain. Transmitting boundary elements (TBE) are developed for a plane, straight Bernoulli-Euler beam with constant axial force upon a Winkler foundation. An analytical formulation of TBE is derived and cast into an element formulation to be used in the finite element models of the pipeline.

The dynamic response of the soil has been studied with respect to liquefaction. An overview of the theory of liquefaction is given and the liquefaction problem is evaluated considering a pipeline free-span.

Part 5: Single-span Analyses

The pipeline free-span is modelled as a three-dimensional beam model with non-linear soil springs using Abaqus 6.7 which is a commercial general-purpose FEM-program. A force feedback model that accounts for fluid damping of the free-span is implemented in the Abaqus Model by the use of user-defined FORTRAN subroutines. A two-dimensional beam model with linear soil springs has been made in the commercial programming environment Matlab for benchmark testing of the Abaqus Model.

The Abaqus Model is used for free-span analyses in FLS and ULS. An extensive parametric study has been made to determine the parameters of greatest influence to the dynamic response and fatigue of the pipeline free-span. Maximum spanning lengths of the pipeline free-span have been determined when considering FLS and ULS.

Part 6: Multi-span Analyses

Multi-span analyses have been made to examine the effect of potential interaction between two neighbouring free-spans. A parametric study of the governing parameters has been made considering the dynamic behaviour and fatigue of the neighbouring free-spans. Multi-span analysis when detecting neighbouring free-spans is a relatively new requirement. The objective for this part of the project is therefore also to outline some guidance for the verification of a multi-span pipeline.

CONCLUSION

The main conclusions from chosen chapters of the project are given below.

Near-wall Cylinder

Studying literature and experiments made for a near-wall cylinder in simple and more complex ambient flows has given a good understanding of the origin of the hydrodynamic forces that affect a pipeline free-span. As the gap ratio decreases, the in-line force that affects the near-wall cylinder increases and the time variation of the in-line force is relatively consistent with the ambient flow. The time variation of the cross-flow force is more complex to describe because it originates from two phenomena. For decreasing gap ratios, the cross-flow force originates partly from the wall proximity and partly from vortex-shedding and vortex lock-in.

Hydrodynamic Force Models

The hydrodynamic force models that have been considered in this project generally estimate in-line forces that are in overall accordance with measurements. The main difference between the models lies in the estimation of the cross-flow force which is strongly dependent upon the patterns of vortex shedding and the correlation length. For a pipeline above the seabed, vortex shedding is usually limited to small cells along the pipeline so the resulting cross-flow force is practically zero. If lock-in occurs, a Morison Model with a cross-flow force that oscillates at the lowest vertical eigenfrequency is used. For a pipeline upon the seabed, the Morison Model and the Wake Models are considered. The latter incorporate time-varying force coefficients and adjust the flow velocity based upon prior wakes. This offers a better description of the time history of the cross-flow at the expense of additional parameters to calibrate.

Soil Springs

Comparison of analytically modelled soil springs and a two-dimensional numerical model made in Plaxis has shown overall good agreement with respect to the maximum bearing capacity of the soil around the pipeline. However, the stiffness of the analytical soil springs is sensible to the choice of displacement that correspond to the maximum bearing capacity which must be estimated since the analytical solutions assume the soil is rigid-plastic. In the numerical model, the choice of Young's modulus is governing for the stiffness of the soil. The choice of a single value of Young's modulus in the numerical model does not agree with the analytical determined stiffness in various directions. The analytical springs are considered to give a good overall approximation of the soil stiffness and bearing capacity and are implemented in the Winkler model for the pipeline.

Transmitting Boundary

The properties of the pipeline, soil and load in this project provide evanescent waves that reside relatively near the load source and vanish before they reach the pipe-ends when the side-spans are wide enough. Thus, the implementation of a transmitting boundary is hardly necessary. In case transmitting boundary elements are taken into use to obtain a reduced model, they are expected to perform satisfactorily for a range of load frequencies once they have been calibrated to a single load frequency. In practice, the efforts in deriving, verifying and implementing a transmitting boundary element may greatly exceed its computational gains and the method of using a boundary zone of highly damped material may be considered as a practical alternative.

Liquefaction

The liquefaction hazard for the pipeline free-span is evaluated in the context that the soil at the free-span shoulders are exposed to cyclic excitation due to hydrodynamic loads at the free-span. Numerical modelling of liquefaction has been attempted but has been unsuccesful due to limitations in the pre-defined material models that are available in the used version of Abaqus. A qualitative evaluation based on the knowledge of the liquefaction mechanisms and susceptibility has led to the conclusion that flow liquefaction of the soil is highly unlikely to cause problems for the pipeline free-span. Cyclic mobility is considered to be a more likely liquefaction mechanism to affect the pipeline free-span but is not considered to be critical because of the relatively small pipe diameters and trenching depth. Vortex lock-in will increase the risk of liquefaction.

Winkler Model

The Winkler Model has been created in two FEM-models – the relatively simple linear Matlab Model and the relatively complex non-linear Abaqus Model. The latter is a three-dimensional pipeline with initial stresses, large deformations, Rayleigh damping, user-defined force feedback and non-linear springs at the side-spans. The models show identical static and dynamic response in the case of a linear system. Thus, the results of the non-linear Abaqus Model are considered to be reliable. The non-linear Pipe Soil Elements that constitute the Winkler foundation in the Abaqus Model introduce irreversible plastic deformation and evolve the elastic range of the backbone load-displacements curves. This deviates from the traditional understanding of a spring but is in better agreement with the plastic constitutive behaviour of soil.

Fatigue of Single-span Pipeline for Regular or Irregular Waves

A study of the parameters that are important for the dynamic response and fatigue damage of the pipeline free-span has been conducted. The axial load during the operational state was found to have great influence on the dynamic response and the estimated damage in this state was the most critical. Since the project pipeline is out of the range of vortex lock-in, the damage caused by in-line excitation is governing. This is also why a gap ratio of zero has been used conservatively in the

reference model which increases the damage considerable. A pipeline free-span that is sensible to vortex lock-in may show some diversity when comparing results from the parametric study in this project.

The conventional approach of using regular waves with the significant wave height for fatigue analysis has been conservative since it provides relatively much damage due to the large amount of large-amplitude stress cycles in the pipeline. In contrast, impact from irregular waves provides few extreme stress cycles in the pipeline that correspond to the maximum wave height. In the latter case, the extreme loads introduce plastic deformation of the soil and considerable changes in the physical configuration of the pipeline but the total fatigue damage is negligible, nevertheless.

Buckling of Single-span Pipeline

Buckling analysis of the single-span has shown that global buckling is much more critical than fatigue damage of the pipeline free-span. The large axial force in the pipeline due to internal pressure and temperature expansion is critical when considering global buckling and does not allow the pipeline free-span to experience much bending from transversal load before the maximum bearing capacity in ULS is exceeded. Local buckling has been examined by empirical formulas according to DNV which has shown that this is not a problem for the project pipeline.

Fatigue and Buckling of Multi-span Pipeline

The analysis on a multi-span pipeline has shown that frequency analysis is efficient to detect interaction between neighbouring free-spans since the lowest eigenfrequency of the multi-span pipeline differs from the eigenfrequency of an equivalent single-span pipeline. The consequence of interaction increases with increasing spanning length and decreasing length of the mid-support. The multi-span analysis for the project pipeline does not indicate that interaction between neighbouring free-spans causes the fatigue damage to become more critical than global buckling. Failure analysis of the mid-support has shown that the mid-support fails in ULS before the interaction between two neighbouring free-span will cause severe damage in FLS.

Part 1

Design Conditions

The design conditions for the free-span analyses are determined. This includes the location, environmental conditions, structural data, soil parameters, damping parameters and safety factors.

1.1 DESIGN CONDITIONS

This chapter describes the design conditions. Additional properties may be applied in some analyses although they may not appear in this chapter mainly in order to perform parametric studies. It will however be made clear in the analyses, when the conditions differ from those that appear in this chapter.

1.1.1 ENVIRONMENTAL CONDITIONS

The environmental conditions are determined with general reference to the pipeline design basis in [LICengineering 2005]. This is done in order to model realistic environmental conditions for pipelines that are located in the Danish part of the North Sea.

1.1.1.1. Field Location

The field location is the Danish sector of the North Sea. Figure 6 shows Maersk's licence area where Danish oil platforms are located. The pipeline is assumed to have environmental conditions that are identical to those measured from the oil platforms in this area.

Figure 6: Location of Danish licence area for extraction of oil. [Maersk 2008]

DNV divides the free-spans into four different categories depending on the ratio between the length and the outer diameter of the pipeline [DNV-RP-F105 2006, p9]. Figure 7 shows the first three cases

of free-spans. The fourth case of free-span is an extreme version of case 3 with a ratio $\frac{L}{D} > 200$ and
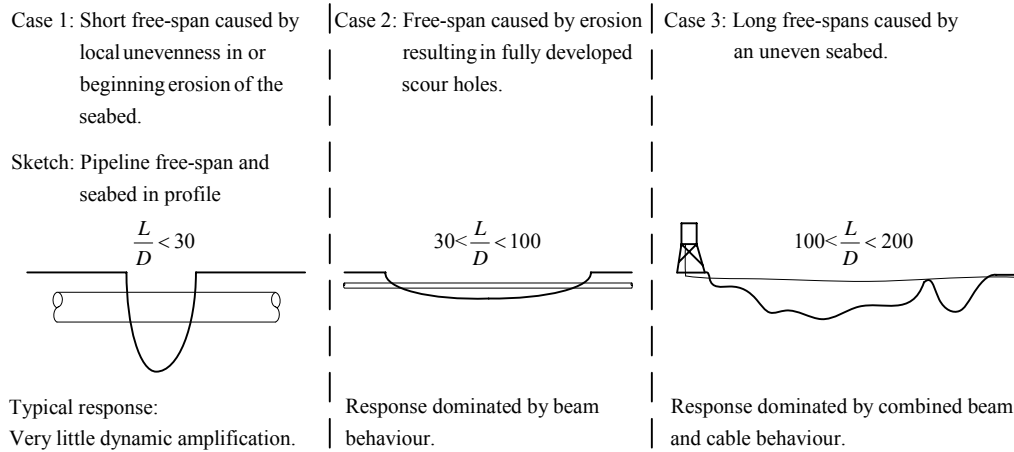
a response dominated by cable behaviour.

Case 1: Short free-span caused by local unevenness in or beginning erosion of the seabed.

Case 2: Free-span caused by erosion resulting in fully developed scour holes.

Case 3: Long free-spans caused by an uneven seabed.

Sketch: Pipeline free-span and seabed in profile

$\frac{L}{D} < 30$

$30 < \frac{L}{D} < 100$

$100 < \frac{L}{D} < 200$

Typical response:
Very little dynamic amplification.

Response dominated by beam behaviour.

Response dominated by combined beam and cable behaviour.

Figure 7: Cases of free-spans and their typical response behaviour. L is the length of the free-span and D is the outer pipe diameter.

At the field location, inspections have shown that free-spans of pipelines are primarily caused by erosion which leads to relatively small spanning lengths. This observation entails that this project deals primarily with free-spans in Case 2. For this case, the response is dominated by beam behaviour which is in good agreement with the assumption made for the calculation models in Chapter 5.1 (Winkler Model).

1.1.1.2. Water Depth

It is assumed that the pipeline is located at relatively deep water corresponding to a pipeline near an offshore platform. The design water depth is taken as the Lowest Astronomic Tide which gives the highest particle velocities at the seabed. A design water depth of $h = 42.9\,\text{m}$ is taken at the DAN FG field as in [Design Basis 2005, p5].

1.1.1.3. Wave Data

The wave data is taken from the IGOR-1 field which has the worst sea state as in [LIC-engineering 2005, p 12].

Wave Data for Fatigue Limit State

The wave data for FLS is determined based on the assumption that the free-span is a temporary condition. Annual seabed inspections followed by instant repair work limits the exposure from waves and current to a duration of 1 year for a free-span. The waves are divided into five characteristic sea states. Sea states 1-4 represent the distribution of waves within one year. Sea state 5 corresponds to the significant wave height associated with a storm that has a return period of 10

years and a duration of 24 hours per year. The wave data for the fatigue limit state is shown in Table 1.

Table 1: Wave data for fatigue limit state [LICengineering 2005, p12].

FLS sea states	H_{m0} [m]	T_z [s]	H_{max} [m]	T_p [s]	Duration [hours/year]
Sea state 5	9.6	10.2	17.9	12.8	24
Sea state 4	7.0	8.6	13.0	11.6	41
Sea state 3	5.0	7.5	9.4	9.8	350
Sea state 2	3.0	6.0	5.6	7.6	2662
Sea state 1	1.0	4.0	1.9	4.4	5707

The relation between the significant wave height H_{m0} and the maximum wave height H_{max} is determined under the assumption that the wave heights are Rayleigh distributed. This assumption is normally a good assumption for waves at deep water and implies that H_{max} can be calculated as

$$H_{max} = 1.86 H_{m0} \tag{1.1.1}$$

where

$\quad H_{max}$ is the maximum wave height [m]

$\quad H_{m0}$ is the significant wave height [m]

[Frigaard og Hald 2004, p57]

The mean period T_z has been determined from a scatter diagram but the peak period T_p is determined as a function of H_{m0}. The empirical relation between T_p and H_{m0} is assumed to be

$$T_p = \sqrt{190 \frac{H_{m0}}{g}} \tag{1.1.2}$$

where

$\quad T_p$ is the peak period [s]

$\quad g$ is gravity $\left[\frac{m}{s^2} \right]$

[LICengineering 2005, p12]

It is noticed that the wave period in (1.1.2) corresponds to a wave steepness equal to 3-4% where the steepness is calculated as

$$S_{0P} = \frac{H_{m0}}{L_0} = \frac{H_{m0} \cdot 2\pi}{g \cdot T_p^2} \tag{1.1.3}$$

where

$\quad S_{0p}$ is the wave steepness [-]

$\quad L_0$ is the wave length assuming deep water [m]

[Frigaard & Hald 2004, pp28-29]

This shows that the waves described by the significant wave height are not assumed to be near the breaking state which is assumed to occur at wave steepnesses of 6-8%.

The particle velocities from the waves are evaluated at half an outer pipe diameter above the seabed, i.e. $z = -h + \dfrac{D}{2}$, where z is the vertical coordinate with origin at the water surface and that is defined positive in upward direction. This corresponds to the state where the pipeline lies upon the seabed and the velocity is assumed constant over the diameter of the pipe. The velocity profile from the waves is almost constant near the seabed if boundary layer effects from the seabed are neglected.

Time Series

Time series of regular and irregular waves are created in WaveLab2 which is a program for data acquisition and analysis in wave laboratories and has been developed at the department of civil engineering at Aalborg University. WaveLab2 is also used to determine the particle velocities for the waves where the wave kinematics for the regular waves are determined by Stoke's 5th order theory. This theory has been evaluated in comparison with stream function theory and has been found to be sufficiently accurate for all the sea states since the water depth is relatively deep.

The time series for the irregular waves are determined by a parameterized JONSWAP spectrum with white noise filtering. The filter is implemented to simulate the stochastic behaviour of waves which also implies that the generated time series will be non-deterministic. A peak enhancement factor of $\gamma = 3.3$ is chosen which is known to be an average value for the North Sea [Liu & Frigaard 2001, pp35-36]. Figure 8 shows an example of a JONSWAP spectrum that is generated for sea state 5.

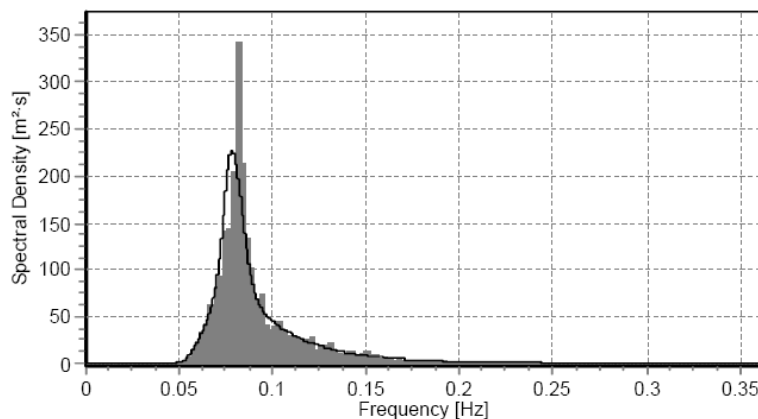*Figure 8: Standard JONSWAP spectrum (solid line) and a generated JONSWAP spectrum with white noise filtering (grey blocs).*

Figure 8 shows that the spectrum generated with white noise filter deviates from the target JONSWAP spectrum. This is due to the finite length of the time series and will thus also be the case for real measured waves. Data sheets for irregular sea states 1-5 can be found in Appendix E (Irregular Sea States).

Wave Data for Ultimate Limit State

The wave data for the ultimate limit state is determined only for one sea state which represents a wave with a return period of 100 years. Table 2 show the wave data for the ultimate limit state

Table 2: Wave data for ultimate limit state [LICengineering 2005, p11]

ULS sea states	H_{m0} [m]	T_z [s]	H_{max} [m]	T_p [s]
Sea state 100	10.8	10.9	21.0	13.6

The design current that has to be combined with the waves is given in the following section.

1.1.1.4. Current

The current that affects the pipeline is determined by assuming that the velocity profile is polynomial and can be formulated as

$$u(z) = \frac{8}{7} u_c \cdot \left(\frac{z}{h}\right)^{\frac{1}{7}}$$ (1.1.4)

Where

    u is the current velocity affecting the pipe [m/s]

    z is the vertical coordinate with origin at the water surface [m]

    h is the water depth [m]

    u_c is the basic current parameter [m/s]

[LICengineering 2005, p12]

The velocity profile (1.1.4) which uses a $1/7^{th}$-power profile is generally in good agreement with a logarithmic formulation of the velocity profile. However, it is however that the logarithmic velocity profile tends to be more accurate because the seabed roughness is included as an additional parameter in this formulation. In case of an even seabed without significant roughness, the $1/7^{th}$-power profile will underestimate the flow velocity near the seabed. [Braestrup et al. 2005, p99]

The basic current parameter varies according to the return period of the design wave. The basic current parameters have been reduced due to boundary layer interaction according to [DNV-RP-E305 1988, pp 30-34]. The current that affects the pipe is taken at an elevation 1 m above the seabed, i.e. $z = -h + 1\text{m}$. Table 3 shows the steady current that affects the pipe.

Table 3: Steady current affecting the pipe.

	Basic current parameter u_c [m/s]	Current affecting pipe $u_{(z=-h+1m)}$ [m/s]
Extreme current associated with 1-year design wave	0.25	0.17
Extreme current associated with 10-year design wave	0.45	0.30
Extreme current associated with 100-year design wave	0.60	0.40

1.1.1.5. Marine Growth

The effect of marine growth should be taken into account when it is unfavourable for the pipeline. The marine growth is only present at the pipeline free-span.

Due to the annual inspections, marine growth with a thickness of 20 mm and a density of 1400 kg/m^3 is applied to the free-span of the pipe as suggested in [Design Basis 2005, p10] and [LICengineering 2005, p13].

The main effect of marine growth on a pipeline free-span is the change in outer diameter, roughness and mass which lead to increased hydrodynamic forces, increased self-weight and decreased eigenfrequencies of the pipeline.

For the project pipeline, the effect of marine growth has generally been considered unfavourable and been taken into account in all calculation where nothing else is mentioned.

1.1.2 STRUCTURAL AND FUNCTIONAL DATA

The structural data is determined for a 20" Multiphase Pipeline. Figure 9 shows the composition of such a pipeline where also the marine growth is illustrated.
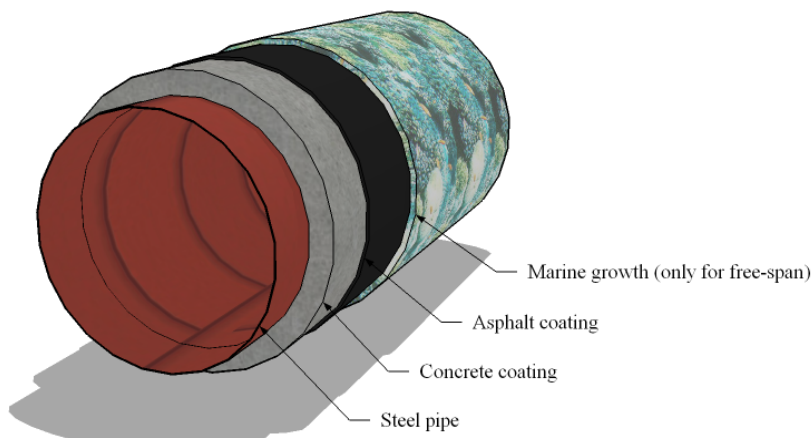

Marine growth (only for free-span)

Asphalt coating

Concrete coating

Steel pipe

Figure 9: Structural composition of 20" Multiphase Pipeline including illustration of marine growth.

1.1.2.1. Pipeline Data

The pipeline data is shown in Table 4 and is taken from [LICengineering 2005, p13].

Table 4: Structural data for a 20" Multiphase Pipeline.

Parameter	Symbol	Magnitude	Unit
Outer pipe diameter	D_{steel}	0.508	[m]
Wall thickness	t_{steel}	0.016	[m]
Steel density	ρ_{steel}	7850	[kg/m^3]
Yield stress	f_{yd}	415	[MPa]
Young's modulus - Steel	E_{steel}	$0.21 \cdot 10^6$	[MPa]
Poisson's ratio - Steel	v_{steel}	0.3	-
Expansion coefficient - Steel	α_{steel}	$12 \cdot 10^{-6}$	[1/C^o]
Concrete coating	$t_{concrete}$	0.050	[m]
Concrete density	$\rho_{concrete}$	3300	[kg/m^3]
Young's modulus - Concrete	$E_{concrete}$	$29.1 \cdot 10^3$	[MPa]
Asphalt coating	$t_{asphalt}$	0.006	[m]
Asphalt density	$\rho_{asphalt}$	1300	[kg/m^3]

Young's modulus for concrete has been estimated for a concrete with the strength $f_{ck} = 35\,\text{MPa}$ as

$$\begin{aligned}
E_{concrete} &= 10000 f_{ck}^{0.3} \\
&= 29.1 \cdot 10^3 \text{ MPa}
\end{aligned}$$

(1.1.5)

[DNV-RP-F105 2006, p31]

1.1.2.2. Functional Data

The functional data for the pipeline is determined for three functional states: water-filled, air-filled and operational state. It is noticed that if the state is either air-filled or operational, the effects of temperature and pressure difference must be included in the eigenfrequency analyses because these effects have influence on the dynamic properties of the pipeline. The functional data for the 20" Multiphase pipeline are shown in Table 5.

Table 5: Functional fluid data for the 20" Multiphase pipeline. p_i and p_e is the internal and external pressure, respectively.

Functional state	Density ρ [kg/m³]	Temperature difference ΔT [°C]	Pressure difference $p = p_i - p_e$ [MPa]
Water-filled	1025	0	0
Air-filled	1.28	0	-0.43
Operational	113	56	9.8

1.1.3 SOIL DATA

The soil data in this project are not determined by geotechnical investigations, but estimated upon the basic knowledge of typical marine soil. The soil is assumed to be homogeneous and isotropic and where nothing else is mentioned the shear strength of the soil is determined by Couloumb's theory

$$\tau_f = c' + \sigma' \tan \varphi' \qquad (1.1.6)$$

where

τ_f is the shear strength [kPa]

c' is the cohesion [kPa]

σ' is the effective normal stress [kPa]

φ' is the effective angle of friction [deg]

[Ovesen et al. 2007, p158]

The soil is assumed to be cohesionless which is a fairly good assumption for a typical marine soil. The basic soil data is shown in Table 6.

Table 6: Basic soil data.

Parameter	Symbol	Sand	Unit
Saturated soil weight	γ_{sat}	20	kN/m³
Cohesion	c	0	kPa
Angle of friction	φ'	30	°

Additional soil data will be applied in some of the following analyses where this is found necessary. These additional soil parameters will be discussed in the analyses where they have been applied.

1.1.4 DAMPING

Damping is an important aspect when determining the dynamic behaviour of a structural system. Damping of a pipeline free-span arises from the following sources where some typical numbers for the damping ratios are also given:

- Structural damping: ($\zeta_{str} = 0.005$)

- Soil damping ($\zeta_{soil} = 0.010$)

- Fluid damping (ζ_{fluid} – implicit in force models)

The structural material damping arises due to internal friction forces of the pipe material. Since the pipe is welded together, the steel in the pipeline does not contribute with much damping. However, the coating contributes with some damping – partly because of the friction between the grains in the concrete and partly because of the friction between the steel and the coating.

The soil at the boundaries of the pipeline has a damping effect in the form of geometrical damping due to wave propagation through the soil and material damping due to friction between the grains. The main parameters for estimating soil damping are to consider the type of soil: Is it a cohesion soil or a friction soil and is it a hard or soft soil.

The fluid around the pipeline free-span also introduces damping due to interaction between the pipeline motion and the ambient flow. The fluid damping depends greatly upon the ratio between the pipeline velocity and the velocity of the ambient flow. For slender structures, this ratio is high and the fluid damping will be significant.

The structural damping and the soil damping are sampled to an estimated global damping ratio of $\zeta_{global} = 0.010$. The significance of this estimation has been evaluated in a parametric study in Chapter 5.2 (Parametric Study for Regular Waves).

The global damping ratio is implemented as Rayleigh damping as explained in Appendix B (Rayleigh Damping).

Fluid damping is implemented in the force models that are applied in the dynamic analyses, see Chapter 3.2 (Hydrodynamic Force Models).

1.1.5 SAFETY ZONES AND SAFETY FACTORS

The primary functional state that is investigated in this project is the operational state of the pipeline. The safety factors that have been used in this project correspond to "high" safety class and are taken from [DNV OS-F101 2000]. For comparisons between the buckling procedures of DNV and Danish Standards (DS), the safety factors from [DS412 1998] are also relevant. Table 7 shows the safety factors that are used in this project.

Table 7: Safety factors corresponding to "high" safety class.

Description of factor	Symbol	ULS		FLS
		DNV	DS	DNV
Material resistance factor	γ_m	1.15	1.17	1.00
Safety class resistance factor	γ_{SC}	1.26	1.10	1.26
Condition load effect factor	γ_C	1.00	-	1.00
Functional load factor	γ_F	1.10	-	1.00
Environmental load factor	γ_E	1.30	-	1.00
Accidental load factor	γ_A	-	-	-
Pressure load factor	γ_P	1.05	-	1.00

Part 2

Structural Mechanics

The main objective of a free-span analysis is to determine the maximum allowable free-span in the Fatigue Limit State considering fatigue damage and the Ultimate Limit State considering instability problems. A part of the objective of this project has been to present the current design procedures for these two limit states with regard to free-span analysis.

2.1 FATIGUE

Dynamic loads from wave action, vortex shedding etc. may give rise to cyclic stresses which may cause fatigue damage to the pipe-wall and ultimately lead to failure [Braestrup et al. 2005, p117].

This chapter is introduced by a small section that briefly explains what causes fatigue damage. The rest of this chapter describes how to document the fatigue damage of the pipeline free-span according to the design criteria given in [DNV-RP-C203 2005]

2.1.1 THE FATIGUE PHENOMENON

In the steel wall and especially around the weldings of the pipeline, imperfection may be points of local crack initiation within the material. When applying load to the structure, the material will experience stress concentrations at the crack points which results in local yielding zones. Figure 10 illustrates a yielding zone for a crack when the pipe-wall is assumed to be thin.
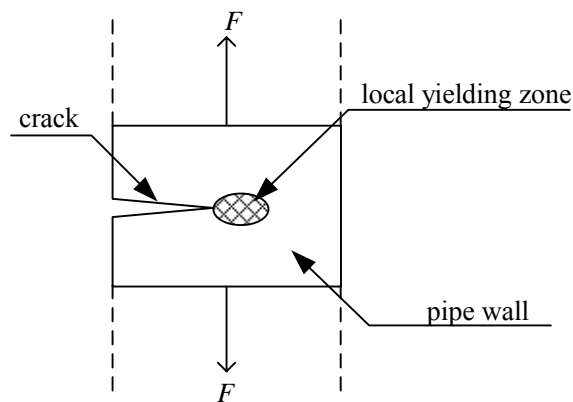

Figure 10: Local yielding zone at crack point.

Dynamic load causes cyclic stresses which induce local hardening followed by fracture near the crack point leading to development of the crack length. This phenomenon is what causes fatigue damage to the structure.

2.1.2 VERIFICATION OF FATIGUE DAMAGE

This section describes how to determine the fatigue damage of the pipeline free-span according to the design criteria given in [DNV-RP-C203 2005]. The overall method for determining fatigue damage for a pipeline free-span is described with reference to [Braestrup et al. 2005, p117-120]. The procedure of a fatigue damage check for the pipeline free-span is:

1. Calculate the stress ranges and verify that the magnitude of the maximum stress is below the yield stress of the steel pipe.
2. Calculate the number of stress cycles.
3. Determine the allowable number of stress cycles to failure from S-N curves.
4. Calculate the damage by Palmgren-Miners rule.
5. Verify that the damage criterion is satisfied.

Each step is described in the following sections.

2.1.2.1. Stress Ranges

Two different methods can be used to determine the stress ranges for the fatigue analysis [Braestrup et al. 2005, p117]:

1. **Load model:** The stress ranges are found by a time-domain dynamic analysis where the external load is applied to the free-span.

2. **Response model:** The stress ranges are determined using the normalised response amplitudes for a given flow situation appropriately scaled to the real free-span.

In this project, the stress ranges are determined from a numerical dynamic model which is described in Chapter 5.1 (Winkler Model). The numerical model includes the dynamic effects when determining stress ranges and is applicable for impact from both regular and irregular waves. Thus, a load model is used.

Response models can be found in [DNV-RP-C203 2005 pp23-26]. These are empirical models that are based upon available experimental laboratory test data and a limited amount of full scale tests. The response models account for vortex induced vibrations. However, the response model is not considered further in this project.

Dominating Principal Stress

The damage of the pipeline is determined for the principal stress with the largest variation, i.e. difference between maximum and minimum stresses. For the pipeline, this will be the normal stresses since the bending moment will cause the largest stress variation. It is noticed that Von Mises stresses defined in (2.1.2) will not be conservative as these will give larger maximum stresses but smaller stress ranges.

Yield stress

To ensure that the maximum stress range does not exceed the yield stress of the steel pipe, the Mises criterion for yielding is applied

$$\sigma_{mises} \leq f_{yd} \qquad\qquad (2.1.1)$$

where

σ_{mises} is the Von Mises stress [Pa]

f_{yd} is the yield stress [Pa]

The definition of Von Mises stresses for isotropic and linear elastic materials is described by the following relation where index notation is used

$$\sigma_{mises} = \sqrt{\tfrac{3}{2} s_{ij} s_{ij}}, \qquad s_{ij} = \sigma_{ij} - \tfrac{1}{3}\sigma_{kk}\delta_{ij}, \qquad i = 1,2,3, \qquad j = 1,2,3 \tag{2.1.2}$$

where

σ_{mises} is the Von Mises stress [Pa]

σ_{ij} is the stress in the ith cutting plane and the jth direction, positive in tension [Pa]

s_{ij} is the stress deviator in the ith cutting plane and the jth direction [Pa]

δ_{ij} is Kronecker's delta, defined as $\delta_{ij} = \begin{cases} 1, & i = j \\ 0, & i \neq j \end{cases}$ [-]

[Byskov 2002, pp107-108]

Determination of the Von Mises stress (2.1.2) is a standard feature in Abaqus. The yield criterion (2.1.1) is important to consider if the static loads on the pipeline have a large impact on the stresses. The potential misinterpretation of the damage of a steel pipe when the stress ranges are not determined from the state of static equilibrium is illustrated in Figure 11 and described below.
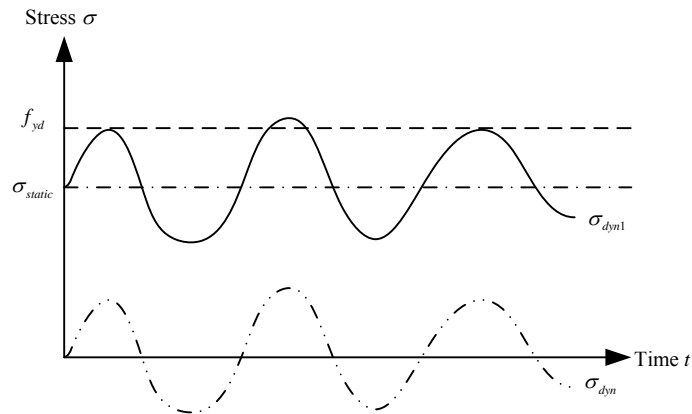

Figure 11: Stress variation.

Figure 11 shows that when the dynamic stress variation σ_{dyn1} exceeds the yield stress limit, the pipeline might fail even though the fatigue damage criterion has not been exceeded. It is noticed that the dynamic stress variations σ_{dyn} and σ_{dyn1} that are shown in Figure 11 will mistakenly cause identical damage according to Palmgreen Miners rule shown in (2.1.4) because fatigue is determined only from the stress ranges which are identical for σ_{dyn} and σ_{dyn1}. This would have been correct if the stress contribution from the static load had been smaller so that σ_{dyn1} did not exceed the yield stress.

2.1.2.2. Stress Cycles

Since each stress cycle causes a certain amount of damage to the structure, it is necessary to determine the number of stress cycles. For harmonic loading, this is relatively simple, but for irregular stress cycles, the counting of stress cycles is usually ambiguous. The two counting methods which are discussed in this section are

- Half-cycle Counting
- Rain Flow Counting

Both counting methods are popular methods. In this project, only the Rain Flow counting method is used for the free-span analyses for irregular waves as this is considered to be the most accurate counting method. This is elaborated in the following.

Half-cycle Counting

As the name of the method implies, the number of cycles that are determined by this method is found by counting half-cycles. Figure 12 shows how this calculation is done by counting local minimum or maximum values of the stresses.
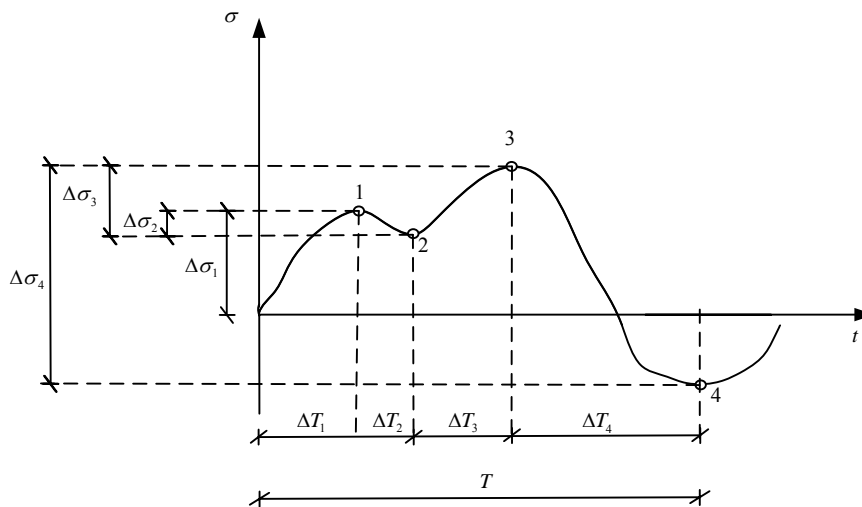

Figure 12: Principle of counting half cycles.

In order to achieve the correct number of stress cycles, the number of stress ranges found by counting half cycles must be divided by two. The disadvantage of this counting method is the fact that it does not detect large stress ranges that occur over a longer period of time when smaller stress fluctuations are included in the response. This is an unfortunate feature since the large stress ranges are known to cause significantly more damage than the smaller stress ranges. An example of an undetected stress cycle and corresponding stress range is illustrated in Figure 13.
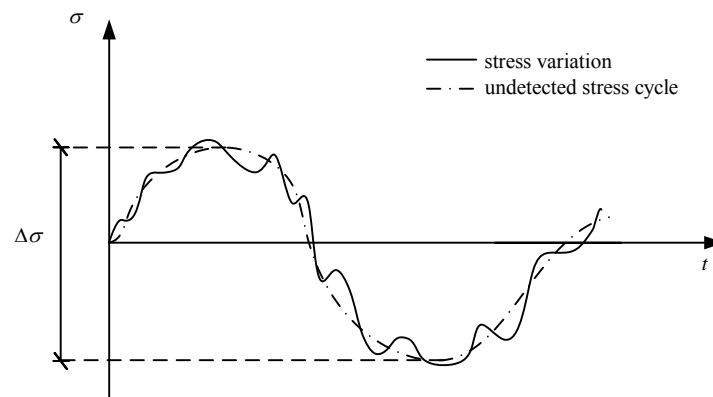
Figure 13: Undetected stress cycle and corresponding stress range.

Rain Flow Counting

The principle of the Rain Flow Counting method is described with reference to [Almar-Næss et al. 1985, pp204-206]. This is the most popular counting method for damage of irregular cycles. The counting procedure is designed to count reversals in the material's stress-strain response. This means that the counting method calculates loops of hysteresis which is illustrated in Figure 14.
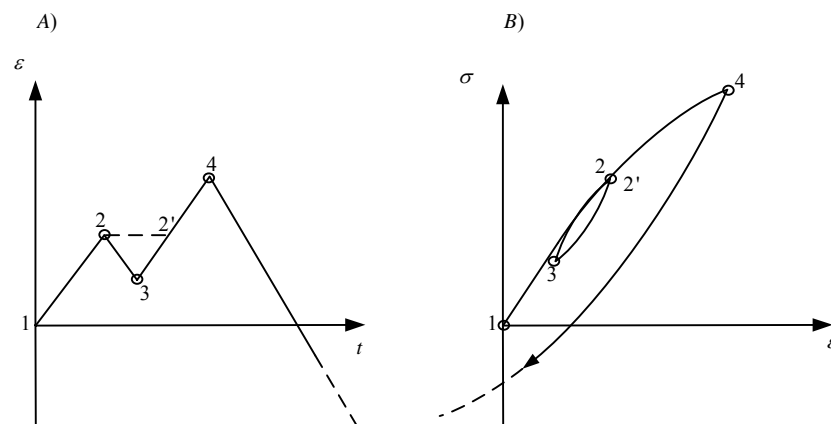

Figure 14: Part of a strain history (A) and the stress strain response (B). Adopted from [Almar-Næss et al. 1985, p204].

Figure 14 shows that the small stress cycle 2-3-2' forms a closed hysteresis loop within the larger stress range 1-4, leaving the count of the latter undisturbed by the interruption. So the rain flow counting method counts both small and large stress range in contrast to the method of counting half-cycles. The Rain Flow Counting method is described in steps to give a rough overview of how the method works. The steps of the method are described as:

1. Reduce the time history to a sequence of tensile and compression peaks.
2. Imagine that the time history is a rigid sheet.
3. Turn the sheet 90° clock wise (earliest time to the top).
4. Each tensile peak is imagined as a source of water that "drips" down the sheet.

5. Count the number of half-cycles by looking for termination of the flow occurring when either:
    a. It reaches the end of the time history.
    b. It merges a flow that started at an earlier tensile peak.
    c. It flows opposite a tensile peak of greater magnitude than the tensile peak for which the flow originates.
6. Repeat step 5 for compression peaks.
7. Assign a stress magnitude to each half-cycle equal to the stress difference between the start and termination of the flow.
8. Pair up half-cycles for tensile and compression with identical magnitude to count the number of complete cycles. Typically, there will be residual half cycles.

A simple example is shown in order to illustrate the method. Figure 15 shows a stress sheet upon completion of steps 1-4 and illustrates the three criteria for counting the stress cycles in step 5.
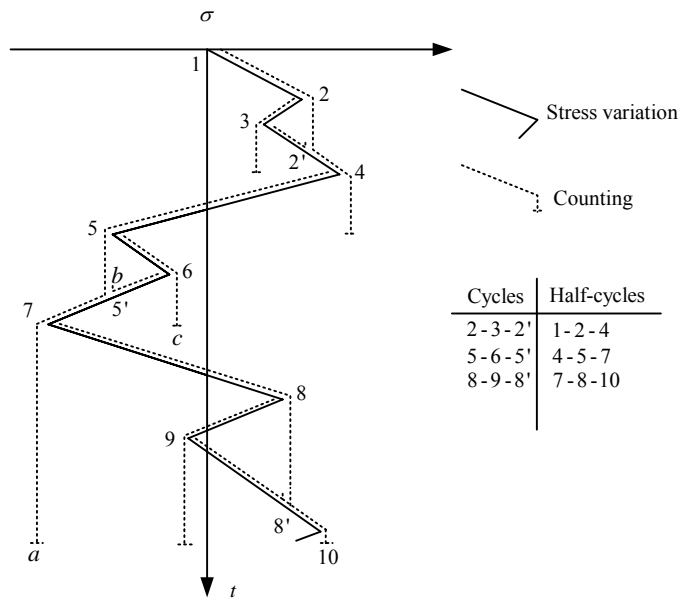

Cycles	Half-cycles
2 - 3 - 2'	1 - 2 - 4
5 - 6 - 5'	4 - 5 - 7
8 - 9 - 8'	7 - 8 - 10

Figure 15: Illustration of Rain Flow Counting. Adopted from [Almar-Næss et al. 1985, p206].

Completing step 7 and 8 will in this example result in the count of 3 cycles and 3 half-cycles which is also illustrated in the table shown in Figure 15. Each count has a corresponding stress range and period. The algorithm for Rain Flow Counting is taken from [Nieslony 2003] and can be found in [DVD/Fatigue/rainflow.m].

2.1.2.3. S-N Curves

S-N curves determine the fatigue resistance of a local part of the structure as a function of the amount of cyclic loading. The S-N curves are based upon the following relationship

$$N_i = \bar{a} \cdot \left(\Delta \sigma_i \right)^{-m} \tag{2.1.3}$$

where

N_i 　　　is the maximum allowable number of cycles at the ith stress range [-]

$\Delta\sigma_i$ 　　is the ith stress range [MPa]

$\bar{a}$ 　　　is the intersect parameter of the S-N curve with the log N axis [-]

m 　　　is the negative slope parameter of the S-N curve

The S-N curves depend upon the detail category. This considers the type of constructional detail, welding type, the site conditions during the welding as and the loading type of the structure. The S-N curves for a steel structure in seawater with cathodic protection and in different detail categories are shown in Figure 16.
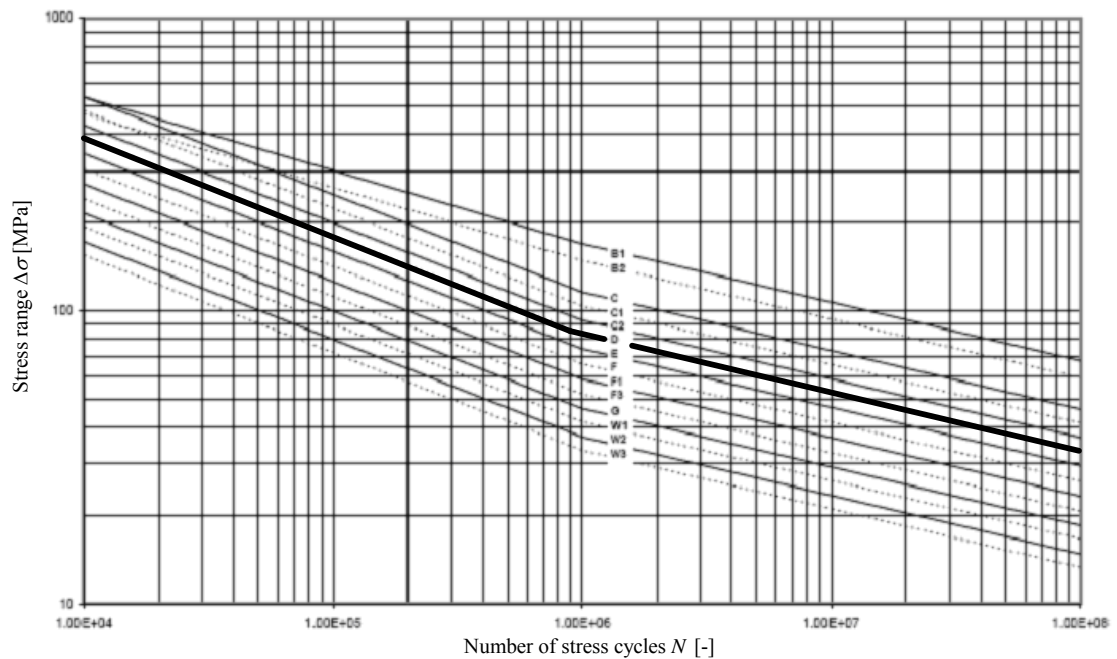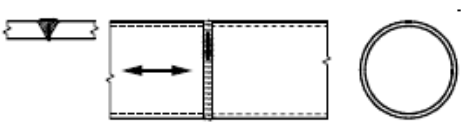

Figure 16: S-N curves in seawater with cathodic protection [DNV-RP-C203 2005, p14].

Table 1 shows the definition of detail categories for the pipeline according to [DNV-RP-C203 2005]. In this project, the detail category D is chosen which is marked by the bold line in Figure 16.

Table 8: Detail categories for hollow sections [DNV-RP-C203 2005, p63]

Detail category	Constructional detail	Description	Requirement
C1		Circumferential but weld made from both sides dressed flush	The applied stress must include the stress concentration factor to allow for any thickness change and for fabrication tolerances, [DNV-RP-C203 2005, section 3.3.7]\n\nThe requirements to the corresponding detail category in [DNV-RP-C203 2005, Table A-5]
D		Circumferential but weld made from both sides.	
E		Circumferential but weld made from both sides at site	
F		Circumferential but weld made from one side at a backing	

The parameters for the S-N curve in category D are given in Table 9.

Table 9: Parameters for S-N curve for category D, adopted from [DNV-RP-C203 2005, p13].

Number of cycles	Stress range	m	$\log_{10}\bar{a}$
$N \leq 10^6$ cycles	$\Delta\sigma \geq 83.4\,\text{MPa}$	3.0	11.764
$N > 10^6$ cycles	$\Delta\sigma < 83.4\,\text{MPa}$	5.0	15.606

2.1.2.4. Fatigue Damage

The damage caused by cyclic loading is determined by Palmgren-Miners accumulation rule. This way of determining damage assumes that the order of stress cycles does not have influence on the damage of the material. The stress range distribution is replaced by a histogram with a chosen number of blocks with constant stress ranges. The fatigue damage is then determined by

$$D_{fat} = \sum_{i=1}^{k} \frac{n_i}{N_i} \leq \alpha_{fat} \tag{2.1.4}$$

where

D_{fat} is the accumulated fatigue damage [-]

α_{fat} is the allowable damage ratio [-]

n_i is the actual number of stress cycles of the ith stress range [-]

k is the total number of stress ranges [-]

[DNV-RP-C203 2005, p10]

Failure due to fatigue damage is assumed to occur when D_{fat} =1. It is however common industry practice to allow no more damage than 10 % during the temporary phase in order to ensure a

reasonable fatigue life in the operational state [Braestrup 2005, p120]. The allowable damage ratio according to DNV is shown in Table 10.

Table 10: Allowable damage ratio for fatigue [DNV-OS-F101 2000, p40]

Safety class	α_{fat}
Low	1/3
Normal	1/5
High	1/10

The pipeline free-span is considered to be in a temporary phase and the safety class is considered to be high. In this project the allowable damage ratio for fatigue is taken as $\alpha_{fat} = 0.1$ which is a conservative value. The damage ratio can be calculated by combining the S-N curves (2.1.3) and Palmgren-Miners rule (2.1.4) which provides

$$D_{fat} = \frac{1}{\bar{a}} \sum_{i=1}^{k} n_i \cdot \left(\Delta \sigma_i \right)^m \leq 0.1 \qquad (2.1.5)$$

[DNV-RP-C203 2005, p10]

2.2 BUCKLING

In this chapter, the pipeline free-span is analysed for global and local buckling. Global buckling features the concept of instability of a beam exposed to axial pressure combined with bending moment around two axes. The global buckling analysis has been made according to two different structural codes: [DS412 1998] and [DNV No. 30.1 2004]. Comparison has been performed of the procedure of buckling analysis in the two codes. The local buckling analysis contains an instability analysis of the section wall of the pipeline. This analysis is made according to the specification of [DNV No. 30.1 2004].

2.2.1 GLOBAL BUCKLING

The pipeline is exposed to axial compression when oil or gas is pumped through the pipeline during its operational state. The pipeline free-span is also exposed to in-line and cross-flow load from wave and current. The forces are illustrated in Figure 17. In this chapter, the axial load is defined as positive in compression.
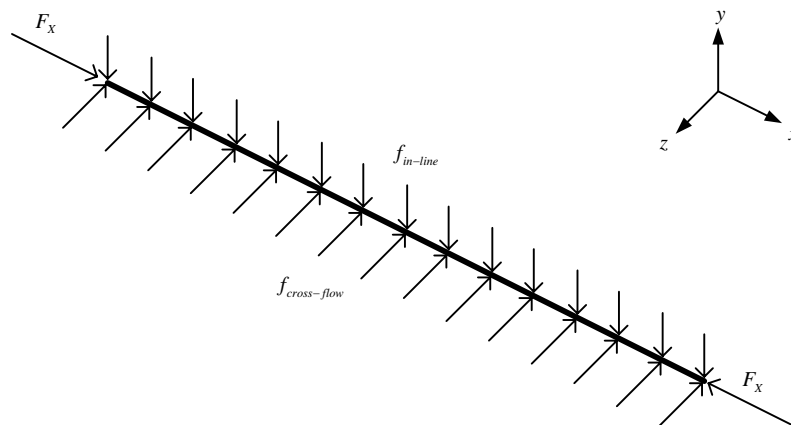

Figure 17: Forces affecting a part of the pipeline free-span.

The procedure for analysing global buckling is to analyse the pipeline as a beam exposed to axial compression and bending moment around two axes. The crux of the matter is to include the moment enhancement that arises from large deformation and the presence of the axial force. This is illustrated for the in-line direction in Figure 18. The same principle must be applied in the cross-flow direction. Since the pipe is a closed section, torsional instability in not considered.
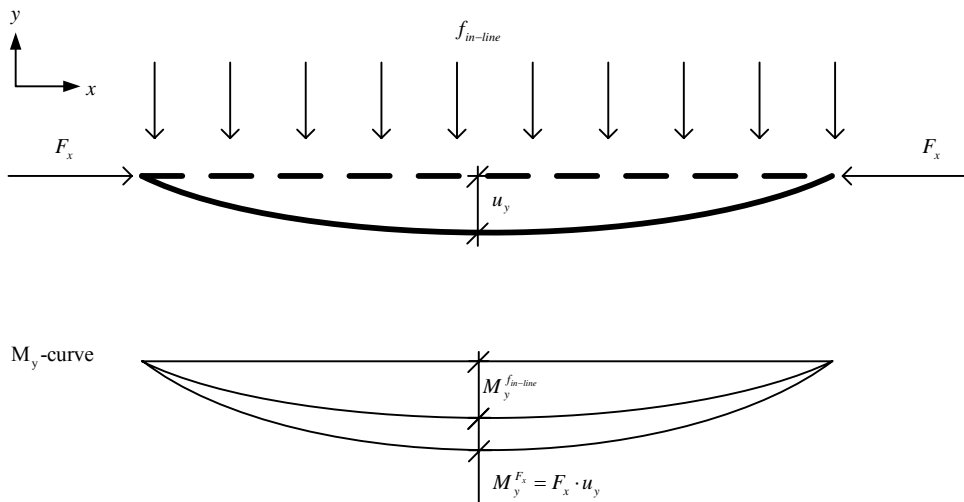
Figure 18: Moment enhancement due to axial load.

Besides moment enhancement, other practical factors have to be considered when analysing buckling failure. Examples of such practical factors are pre-curvature of the pipe, residual stresses, slenderness, imperfections, plastic versus elastic stress distribution etc. [DS412 1998] and [DNV No. 30.1 2004] provide procedures that include the necessary safety to prevent buckling failure and all the mentioned effects. Since the procedures are not identical, the main principles of the procedures of both structural codes have been evaluated and compared. The procedure for global buckling analysis in this section has the following structure:

- Global buckling according to DS412
- Global buckling according to DNV
- Comparison

2.2.1.1. Global Buckling According to DS412

According to DS412, the interaction formula for a bar subjected to compression and biaxial bending is presented as

$$\frac{F_{sd}}{A_s f_{yd} \chi} + k_y \frac{M_{sdy}}{W_y f_{yd}} + k_z \frac{M_{sdz}}{W_z f_{yd}} \leq 1.0 \qquad (2.2.1)$$

where

$\quad F_{sd}$ is the design axial compressive force, defined as positive in compression [N]

$\quad A_s$ is the cross section area [m^2]

$\quad f_{yd}$ is the yield stress [Pa]

$\quad \chi$ is the reduction factor for buckling [-]

$\quad M_{sdy}$ is the design bending moment about the strong axis (y-axis) [N/m]

$\quad M_{sdz}$ is the design bending moment about the weak axis (z-axis) [N/m]

$\quad W_y$ is the section modulus about the strong axis [m^3]

W_z is the section modulus about the weak axis [m^3]

k_y is the bending moment enhancement factor about the strong axis [-]

k_z is the bending moment enhancement factor about the weak axis [-]

The first term in (2.2.1) evaluates the compression resistance of the member including global buckling. The second and third term evaluate the resistance due to bending moment in lateral and vertical directions, respectively, where moment enhancement factors are included.

Axial Compression

To evaluate the buckling resistance due to compression in the member, the reduction factor for buckling that has to be implemented in (2.2.1) can be found as

$$\chi = \frac{1}{\phi + \sqrt{\phi^2 - \lambda^2}}, \quad \chi \leq 1.0 \tag{2.2.2}$$

where
     λ is the factor for slenderness [-]
     ϕ is a factor [-]

The factor ϕ is defined as

$$\phi = 0.5 \cdot \left(1 + \alpha \cdot (\lambda - 0.2) + \lambda^2\right) \tag{2.2.3}$$

where
     α is a factor [-]

The factor α is a table value that is defined according to the classification of the cross section and reduces the compression resistance due to imperfections. When assuming the pipeline section to be hot-rolled, the value $\alpha = 0.21$ is obtained which is identical to the buckling curve a) in [DS412 1998, p51].

The slenderness factor is defined as

$$\lambda = 1.05 \sqrt{\frac{A_s f_{yd}}{F_E}} \tag{2.2.4}$$

where
     F_E is the Euler load [N]
[DS412 1998, p49]

The Euler load in (2.2.4) is commonly known to be defined as

$$F_E = \frac{\pi^2 E_d I}{l_c^2} \tag{2.2.5}$$

where

E_d is the design value for Young's modulus [Pa]

l_c is the column length [m]

[Bonnerup 2005, p126]

Moment Enhancement Factor

The moment enhancement factor that has to be implemented in (2.2.1) can be found as

$$k = 1 - \frac{\mu F_{sd}}{\chi A f_{yd}}, \qquad k \leq 1.5 \qquad (2.2.6)$$

where

μ is a factor [-]

The factor μ is defined as

$$\mu = \lambda \cdot (2\beta_m - 4) + \frac{W_{pl} - W_{el}}{W_{el}}, \qquad \mu \leq 0.9 \qquad (2.2.7)$$

where

W_{pl} is the plastic second moment of area [m^3]

β_m is a factor for equivalent bending moment [-]

The factor β_m is determined according to [DS412 1998, p55] and compensates for curvature of the member due to bending moment.

When evaluating (2.2.6) and (2.2.7) it is seen that the moment enhancement factor depends in a rather complex way upon the ratio of the axial load normalised to the compression resistance, the slenderness, the difference between plastic and elastic second moment of area and the curve shape of the bending moment.

2.2.1.2. Global Buckling According to DNV No. 30.1

This section evaluates the procedure for buckling analysis according to [DNV No. 30.1 2004]. During the evaluation, comparisons are made with the buckling procedure of [DS 412 1998].

As in [DS 412 1998], the buckling resistance according to [DNV No. 30.1 2004] is also determined by a similar interaction formula for a bar that is subjected to compression and biaxial bending

$$\frac{\sigma_a}{\sigma_{acr}} + \frac{\alpha' \sigma_{by}}{\left(1 - \frac{\sigma_a}{\sigma_E}\right) f_{yd}} + \frac{\alpha' \sigma_{bz}}{\left(1 - \frac{\sigma_a}{\sigma_E}\right) f_{yd}} = \eta \qquad (2.2.8)$$

where

η is the usage factor [-]

σ_a is the axial stress due to the compressive force F_{sdx} [Pa]

σ_{acr} is the characteristic buckling stress [Pa]

σ_{by} is the effective axial stress due to bending about the strong axis (y-axis) [Pa]

σ_{bz} is the effective axial stress due to bending about the weak axis (z-axis) [Pa]

σ_E is the Euler stress [Pa]

α' is a factor depending on the type of structure and reduced slenderness [-]

[DNV No. 30.1 2004]

It is seen that [DNV No. 30.1 2004] evaluates stresses when analysing buckling, similar to [DS412 1998] that also evaluates stresses but with these formulated by the section forces. Similar to the interaction formula in (2.2.1), the individual terms in (2.2.8) express the bearing capacity with respect to axial compression and bending about two axes, respectively.

Axial Compression

Similar to the reduction factor χ defined in (2.2.2), a reduction ratio for buckling is defined in [DNV No. 30.1 2004]. The reduction ratio is defined as

$$\frac{\sigma_{acr}}{f_{yd}} = \begin{cases} 1.0, & \lambda \leq \lambda_0 \\ \dfrac{1 + \mu + \lambda^2 - \sqrt{\left(1 + \mu + \lambda^2\right)^2 - 4\lambda^2}}{2\lambda^2}, & \lambda > \lambda_0 \end{cases} \qquad (2.2.9)$$

where

μ is a factor [-]

In [DNV No. 30.1 2004], the factor for slenderness is defined as

$$\lambda = \sqrt{\frac{f_{yd}}{\sigma_E}} = \sqrt{\frac{A_s f_{yd}}{F_E}} \qquad (2.2.10)$$

When comparing (2.2.10) with (2.2.4), it is seen that [DS412 1998] introduces additional safety compared to DNV in the form of increasing the slenderness factor by a factor 1.05. The factor μ is defined as

$$\mu = \alpha \cdot \left(\lambda - \lambda_0\right) \qquad (2.2.11)$$

where

α is a factor [-]

λ_0 is a factor [-]

In (2.2.11), one obtains the imperfection factor $\alpha = 0.20$ and the factor $\lambda_0 = 0.2$ according to [DNV N0. 30.1 2004, p6] .A comparison of the reduction factor χ defined in (2.2.2) and the reduction ratio σ_{cr} / f_{yd} defined in (2.2.9) is shown in Figure 19.
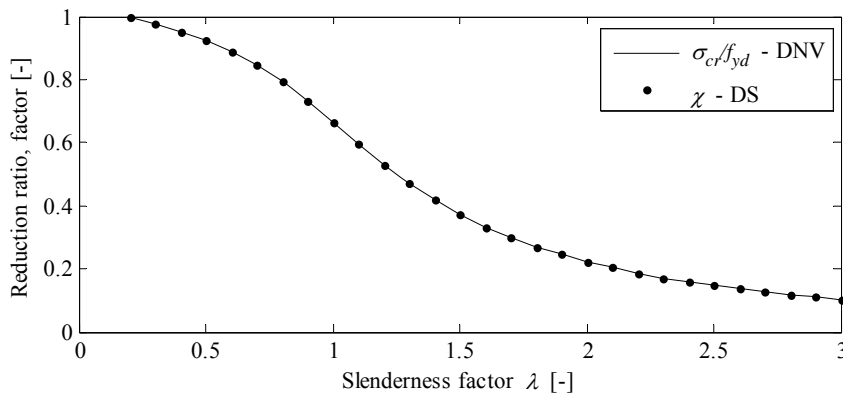
Figure 19: Reduction for buckling due to axial compression according to [DS 412 1998] and [DNV No. 30.1 2004], respectively.

It is seen from Figure 19 that the reduction factors due to buckling are similar in the two codes. However, some difference is found in the compression resistance since the two structural codes have different definitions of the slenderness factor and safety factors applied to the material.

Moment Enhancement Factor

By study of the interaction formula in (2.2.8), it may be seen that the moment enhancement factors can be defined as

$$k = \frac{\alpha'}{\left(1 - \dfrac{\sigma_a}{\sigma_E}\right)} = \frac{1}{\left(1 - \dfrac{F_{sd}}{F_E}\right)} \tag{2.2.12}$$

The moment enhancement factor in (2.2.12) is the theoretical exact value for moment enhancement of a beam subjected to compression and bending moment which is elaborated in [Albertsen et al. 1997, pp238-240]. [DNV No. 30.1 2004] does not compensate for the influence of practical factors on the moment enhancement as in [DS412 1998]. To compensate for this, the usage factor in the interaction formula in (2.2.8) is reduced to a value below 1.0.

2.2.1.3. Comparison

It is seen that the global buckling procedures in [DS412 1998] and [DNV No. 30.1 2004] are generally similar. The consequences of the differences in the analysing procedure are showed in Chapter 5.4 (Buckling Analyses) where the maximum spanning length of the pipeline free-span is evaluated according to both codes.

2.2.2 LOCAL BUCKLING

Local buckling covers the concept of a local collapse of the pipe-wall as the compressive stresses in a local pipeline section exceed the bearing capacity of the pipe-wall. The bearing capacity is

analysed according to [DNV-OS-F101 2000] but the formulas have not been investigated further. Figure 20 illustrates the local buckling problem.
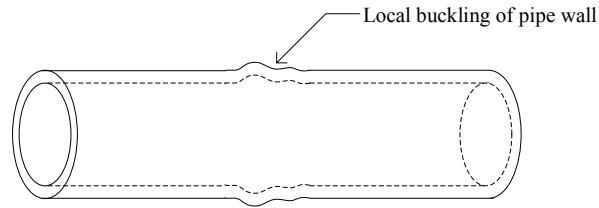

Figure 20: Illustration of the local buckling problem.

Local buckling is prevented if the pipeline section fulfils the following empirical formulation in every section along the free-span

$$\gamma_{SC}\gamma_{M}\left(\frac{S_{d}}{\alpha_{c}S_{p}}\right)^{2} + \gamma_{SC}\gamma_{M}\left(\frac{M_{d}}{\alpha_{c}M_{p}}\sqrt{1-\left(\frac{\Delta p_{d}}{\alpha_{C}p_{b}(t_{2})}\right)^{2}}\right) + \left(\frac{\Delta p_{d}}{\alpha_{C}p_{b}(t_{2})}\right)^{2} \leq 1.0, \quad \text{for } \frac{D}{t} \leq 45 \text{ and } p_{i} \geq p_{e} \quad (2.2.13)$$

where

γ_{SC}　　　is the safety class resistance factor [-]

γ_{M}　　　is the material resistance factor [-]

S_{d}　　　is the design effective axial force [N]

S_{p}　　　is the plastic axial force resistance [N]

M_{d}　　　is the design bending moment [Nm]

M_{p}　　　is the plastic moment resistance [Nm]

α_{c}　　　is the flow stress parameter accounting for strain hardening [-]

Δp_{d}　　　is the design differential overpressure [Pa]

$p_{b}(t_{2})$　　is the burst pressure [Pa]

t_{2}　　　is the wall thickness for fabrication and corrosion allowances [m]

D　　　is the diameter [m]

[DNV-OS-F101 2000, p38]

It is seen that the formulation above evaluates the stresses in the pipe-wall due to axial force, bending moments and differential overpressure. Also the ratio between the diameter and the wall thickness and whether the internal pressure is higher than the external pressure is important parameters when analysing local buckling for pipelines. The latter is solved by introducing ranges of applicability for the empirical formulation. The definition of the parameters included in (2.2.13) can be found in [DNV-OS-F101 2000, pp37-p38].

Part 3

Hydrodynamics

Flow conditions around a near-wall cylinder are examined by studying theory and experimental results in the literature. This should give basic knowledge about the origin of the hydrodynamic forces affecting the pipeline free-span.

Different hydrodynamic force models have been studied primarily to challenge the conventional Morison Model by comparing this with more recently developed Wake Models. The force models are evaluated on their capability to describe the time variation in forces from regular and irregular waves including current. Also the calibration of the models is discussed.

3.1 NEAR-WALL CYLINDER

In this chapter, the flow condition for a cylinder near a wall is discussed. This is an important aspect of determining the hydrodynamic forces because the seabed proximity has a large effect on the hydrodynamic forces that affect the pipeline free-span. Usually, the order of magnitude of the gap for a pipeline free-span caused by erosion is in the range of $O(0.1D)$ to $O(1D)$ [Sumer & Fredsøe 1997, p21] and thus these ranges will be discussed. The hydrodynamic forces that act upon buried or partly buried parts of the pipeline are not considered in this project. Figure 21 serves to illustrate some of the basic terms used in the following.
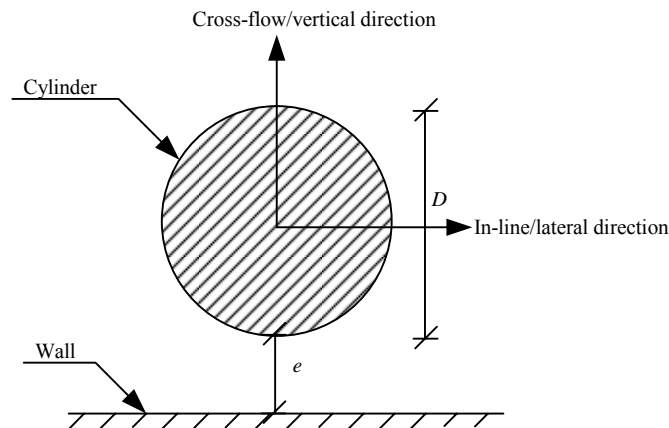

Figure 21: Definition sketch for a near-wall cylinder.

Flow Characteristics

Some basic characteristics for the flow are determined before the flow around the cylinder is explained. The Reynolds number is here defined as

$$Re = \frac{(U_m + U_c) \cdot D}{\upsilon}$$

(3.1.1)

where

   Re is the Reynolds number [-]

   U_c is the in-line flow velocity for current [m/s]

   U_m is the maximum in-line flow velocity for the wave [m/s]

   υ is the kinematic viscosity [m^2 /s]

   D is the outer diameter of the cylinder [m]

In this project, the order of magnitude of Re is in the range $O(10^5) - O(10^6)$ depending on the actual sea state described in Chapter 1.1 (Design Conditions). Re is used to determine the turbulence of the flow around the pipeline and the magnitude of Re in this project implies that the vortex shedding will have turbulence, see [Sumer & Fredsøe 1997, p2].

The Keulegan-Carpenter number is defined as

$$KC = \frac{(U_m + U_c) \cdot T}{D} \tag{3.1.2}$$

where

    KC is the Keulegan-Carpenter number [-]

    T is the wave period [s]

In this project, KC has the magnitude of 0-50, depending on the sea state and the choice of wave height and period, i.e. H_s or H_{max} and T_z or T_p. KC is a value to characterise oscillatory flows.

Temporary Force Model

In most literature, it is common practice to examine the variation of the force coefficients C_D, C_M and C_L instead of comparing the actual load. The Morison Model is applied temporarily in order to define the force terms. The Morison Model for cylindrical structures with infinite stiffness reads

$$f^{in-line} = C_D \frac{1}{2} \rho_w D U |U| + C_M \frac{\pi}{4} \rho_w D^2 \dot{U} \tag{3.1.3}$$

where

    $f^{in-line}$ is the in-line force per unit length of the pipe as function of time $\left[\frac{N}{m} \right]$

    ρ_w is the density of seawater [kg/m^3]

    C_D is the drag force coefficient $[-]$

    C_M is the inertia force coefficient, including the added hydrodynamic mass $[-]$

    U is the in-line flow velocity for wave and current $\left[\frac{m}{s} \right]$

[Burcharth 2002, p33]

Likewise, a temporary expression for the cross-flow force is determined as

$$f^{cross-flow} = C_L \frac{1}{2} \rho_w D U^2 \tag{3.1.4}$$

where

    $f^{cross-flow}$ is the cross-flow force per unit length of the pipe as function of time $[-]$

    C_L is the lift force coefficient $[-]$

[Justesen et al. 1987, p132]

The Morison Model is examined further in Chapter 3.2 (Hydrodynamic Force Models).

3.1.1 CYLINDER IN STEADY CURRENT

The presence of a cylinder in steady current will disturb the flow, especially when the value of $Re > 5$ which induces separation in the flow along the cylinder perimeter. This will create vortices in the flow region behind the cylinder called a wake region. Increasing values of Re induces shedding of the vortices which can create vortex induced vibration (VIV) of the cylinder in both lateral and vertical direction. As the value of Re increases, the vortex shedding and the flow in the wake region becomes more turbulent.

When the cylinder approaches a wall in a steady current, a number of changes occur compared to a free cylinder. These changes can be summarized by the following:

- Vortex shedding is suppressed for gap ratios smaller than $e/D \approx 0.3$.
- The stagnation point moves to a lower angular position as illustrated in Figure 22 (b).
- The angular position of the separation points changes.

[Sumer & Fredsøe 1997, p21]

Figure 22 illustrates the flow around a free cylinder and a near-wall cylinder, respectively.
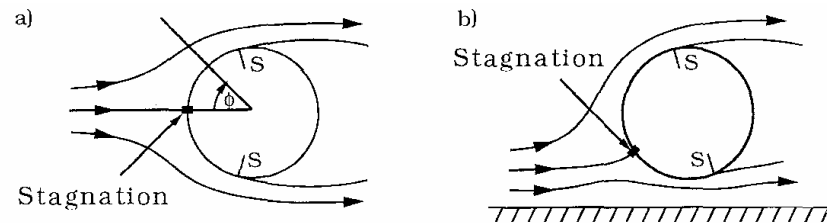

Figure 22: Flow around a free cylinder (a) and a near-wall cylinder (b). S denotes separation points [Sumer & Fredsøe 1997, p21].

3.1.1.1. In-line Force

In steady current, only the drag term has influence on the in-line force. The fluctuation of the drag force caused by VIV has been omitted in this project and only the mean drag from the ambient flow is evaluated. Experimental results from [Sumer & Fredsøe 1997, p59] show that the mean drag decreases as the gap ratio decreases. This is due to the influence of the boundary layer at the wall. The results are shown in Figure 23.
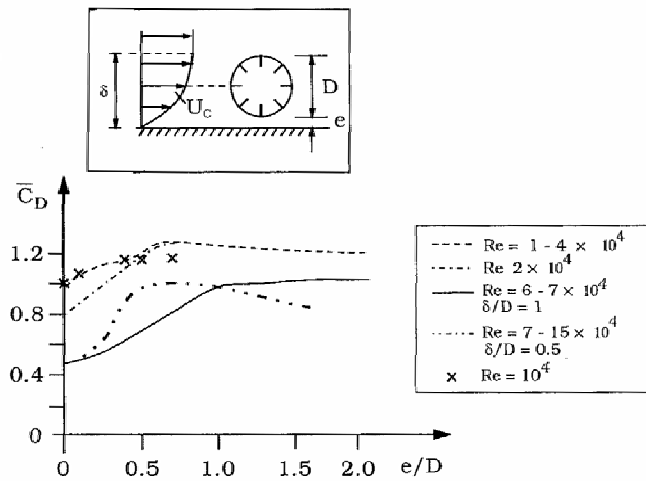
Figure 23: Mean drag force coefficient for a near-wall cylinder in steady current [Sumer & Fredsøe 1997, p59].

3.1.1.2. Cross-flow Force

When the cylinder approaches the wall, the change in pressure along the pipe perimeter causes a resulting cross-flow force that is directed upwards. The change in pressure along the pipe perimeter is illustrated in Figure 24. This cross-flow force is represented by a mean value of the lift force coefficient $\overline{C}_L$.
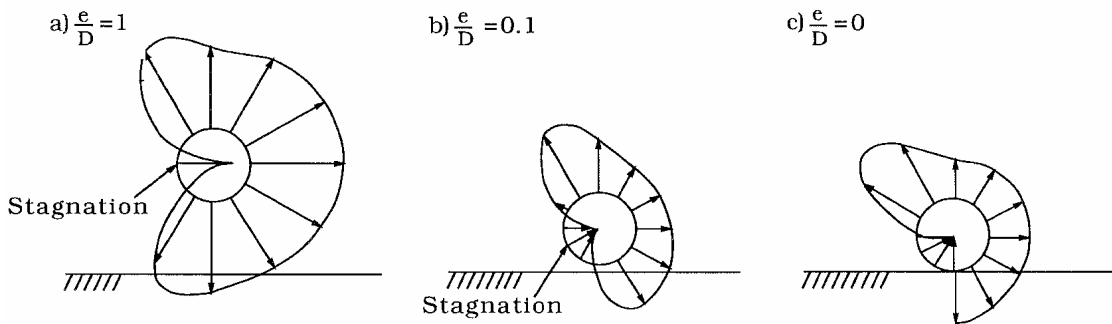

Figure 24: Pressure along the perimeter of a cylinder approaching a wall. [Sumer & Fredsøe 1997, p59].

The cross-flow force contribution from vortex shedding is represented by C_L which is based on the amplitude of the oscillating cross-flow force. Figure 25 shows the tendency of C_L and $\overline{C}_L$ as a function of the gap ratio based on experimental results from [Sumer& Fredsøe 1997, p66].
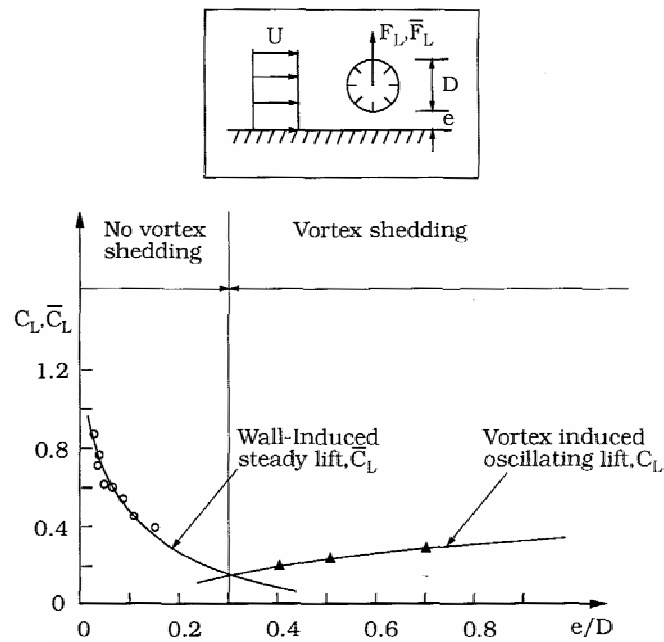
Figure 25: Lift force coefficients for a near-wall cylinder in steady current [Sumer & Fredsøe 1997, p66].

In Figure 25, it is seen that vortex shedding will be suppressed when the gap between the cylinder and the wall becomes small and only the cross-flow force due to the wall proximity will be present. The opposite is the case for a free cylinder where the cross-flow force from vortex shedding will be governing.

The understanding of the changes happening to the flow and forces around a near-wall cylinder in steady current may help the understanding of the changes happening when the ambient flow becomes more complex.

3.1.2   CYLINDER IN REGULAR WAVES

For a near-wall cylinder in regular wave, the effect of the wall proximity depends highly on the flow regime, i.e. the value of KC. In the following, the effect of wall proximity is explained for in-line and cross-flow forces, respectively. Experimental results from [Justesen et al. 1987] have been used to illustrate the change in in-line and cross-flow forces.

3.1.2.1. In-line Force

In [Justesen et al. 1987], experiments have been made for a near-wall cylinder with a large and small gap ratio for a flow regime with high and low values of KC which provides four distinct cases. The in-line force, flow velocity and acceleration in these cases are shown in Figure 26.
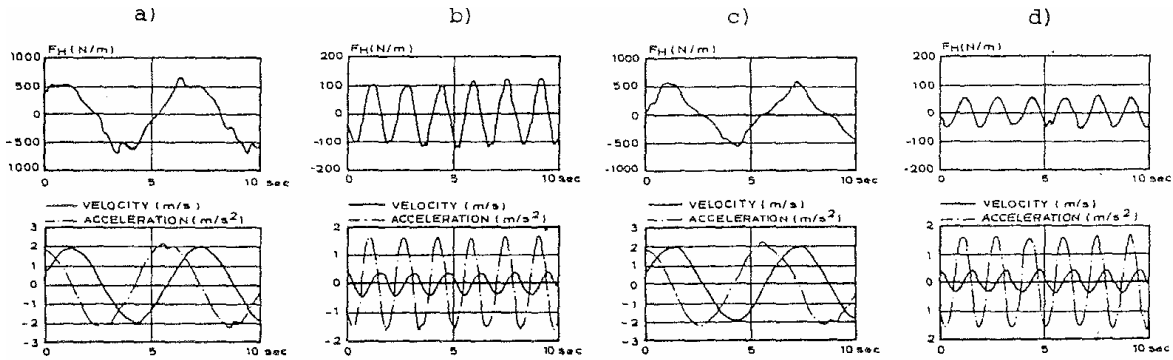
Figure 26: In-line force, flow velocity and acceleration for a near-wall cylinder in regular waves [Justesen et al. 1987, p135].
a) KC = 60, e/D = 0.01   b) KC = 4, e/D = 0.01
c) KC = 60, e/D = 1.0   d) KC = 4, e/D = 1.0

Comparison of Figure 26 a) and c) shows no significant change in the in-line force which means that for high values of KC, the cylinder does not experience any significant increase in the in-line force as the cylinder approaches the wall. This is not the case for low values of KC which are represented by Figure 26 b) and d) which show a significant increase in the in-line force when the pipe approaches the wall.

Another important observation of the experiment is the fact that all four cases show that the in-line load frequency is identical to the wave frequency. For Figure 26 a) and c), the in-line force is in phase with the velocity of the ambient flow due to drag dominance and for Figure 26 b) and d), the in-line force is in phase with the acceleration due to inertia dominance.

Based on additional experiments on this matter, some tendencies for the in-line force coefficients have been illustrated in [Sumer & Fredsøe 1997]. Figure 27 shows C_D and C_M as functions of KC for a cylinder with different gap ratios.
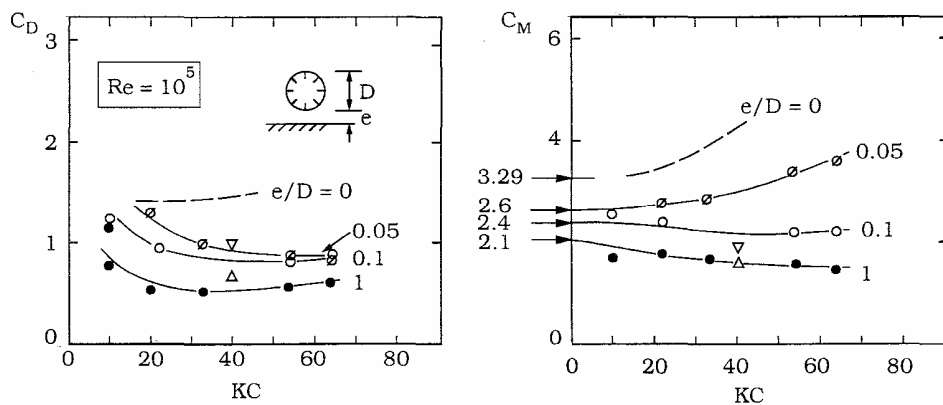

Figure 27: C_D and C_M as functions of KC for different gap ratios in regular waves. The asymptotic values of C_M for $KC \rightarrow 0$ are the potential-flow solution. [Sumer & Fredsøe 1997, p181].

If it is kept in mind that the Morison Model is formulated so the drag term is governing for high values of KC ($KC > 20$) and the inertia term is governing for low values of KC ($KC < 5$), the

tendency of the force coefficients shown in Figure 27 are in relatively good agreement with the experimental results from [Justesen et al. 1987]. The inertia force coefficient C_M which is governing for the experiments in Figure 26 b) and d) is increasing for decreasing gap ratios at $KC = 4$. The drag force coefficient C_D which is governing for the experiments in Figure 26 a) and c) also seems to rise as the gap ratio decreases at $KC = 60$ which contradicts the experimental results in Figure 26. According to Figure 27, the in-line force should increase with approximately 30 % as the gap ratio decreases from 1.0 to 0.05.

3.1.2.2. Cross-flow Force

The cross-flow force is examined upon experimental results from [Justesen et al. 1987] for the same cases of gap ratios and flow regimes as those used for the in-line force. Figure 28 shows the cross-flow force, flow velocity and acceleration for the four cases of gap ratios and flow regimes.
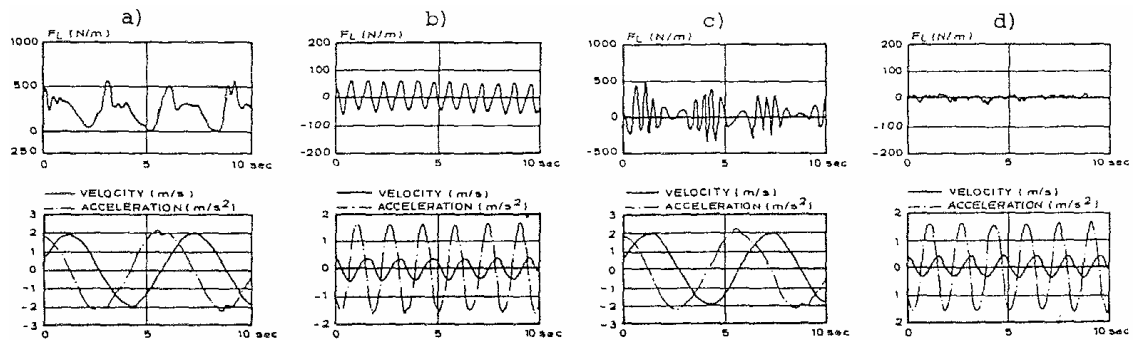

Figure 28: Cross-flow force, flow velocity and acceleration for a near-wall cylinder in a regular wave [Justesen et al. 1987, p135].
a) KC = 60, e/D = 0.01   b) KC = 4, e/D = 0.01
c) KC = 60, e/D = 1.0   d) KC = 4, e/D = 1.0

Comparison of Figure 28 a) and c) shows that for varying gap ratios, the maximum value of the cross-flow force does not change significantly but the variation of the force changes significantly. The cross-flow force in the two experiments arises from two different phenomena. In Figure 28 a), the cross-flow force arises primarily from the asymmetrical pressure field along the cylinder perimeter due to wall proximity. When neglecting the smaller fluctuation of the cross-flow force, the load frequency is nearly twice the wave frequency. In Figure 28 c), the cross-flow force is caused by vortex shedding which acts upon the pipe at a much higher frequency. The frequencies of cross-flow force will be elaborated later in this chapter.

In Figure 28 b) it is seen that for a small value of KC and e/D, the cross-flow force attains negative values of the same magnitude as the positive values. At small values of KC, vortex shedding appears although the gap ratio is small and this causes negative cross-flow forces. The load frequency is equal to twice the wave frequency since the shedding frequency is governed by the fundamental lift frequency which is defined later in this section.

In Figure 28 d), the value of the cross-flow force becomes insignificant as the vortex shedding does not result in any significant cross-flow force when the value of KC is low and the gap ratio is large. Vortex shedding must occur in order to obtain cross-flow forces on a free cylinder. For a free cylinder far from the seabed, the cross-flow force will occur at $KC \geq 4$ [Sumer & Fredsøe 1997, pp149-150].

Based on additional experiments on this matter, some tendencies for the cross-flow force coefficient have been illustrated in [Sumer & Fredsøe 1997]. Figure 29 shows C_L as function of KC for a cylinder with different gap ratios.
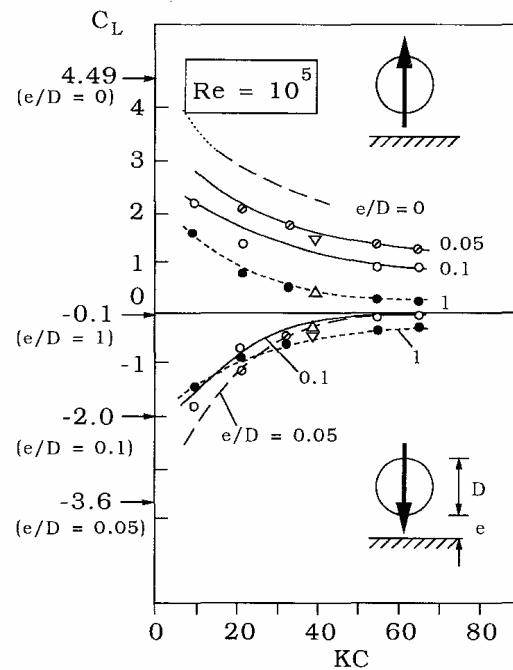

Figure 29: Lift force coefficient for a near-wall cylinder. The asymptotic values of C_L for $KC \to 0$ indicated in the figure are the potential-flow solutions. [Sumer & Fredsøe 1997, p183]

The literature does not distinguish between the values of C_L caused by vortex shedding or wall proximity in oscillatory flow. In this project, it is chosen to use the maximum absolute value of C_L when the gap is small $(e/D < 1)$ and the cross-flow force arises from wall proximity.

For larger gap ratios $(e/D \geq 1)$, the cross-flow force is governed by vortex shedding and the conservative value of $C_L = 0.9$ may be used. This value is taken from [Nedergaard et al. 1994] and is a basic value of C_L due to vortex shedding determined according to full-scale tests.

The basic value of $C_L = 0.9$ is also what is recommended in [LICengineering 2002, p17] assuming that the erosion beneath the pipeline free-span will increase the gap ratio to $e/D \geq 1$ within a short

time from the initial erosion. The cross flow force for small gaps has not been taken into account in [LICengineering 2002].

3.1.2.3. Cross-flow Frequency

The determination of the frequency of the cross-flow force is complex. The frequency of the cross-flow force may be described by tree types of frequencies:

1. Fundamental frequency
2. Vortex shedding frequency (Strouhal frequency)
3. Lock-in frequency

Fundamental Lift Frequency

The cross-flow frequency which is also called the lift frequency can be determined by obtaining the power spectrum of the cross-flow force to identify the dominant frequency. This frequency is called the fundamental lift frequency [Sumer & Fredsøe 1997, p87]. To illustrate this approach, the power spectra of the cross-flow force are shown in Figure 30 for a free cylinder in oscillatory flow.
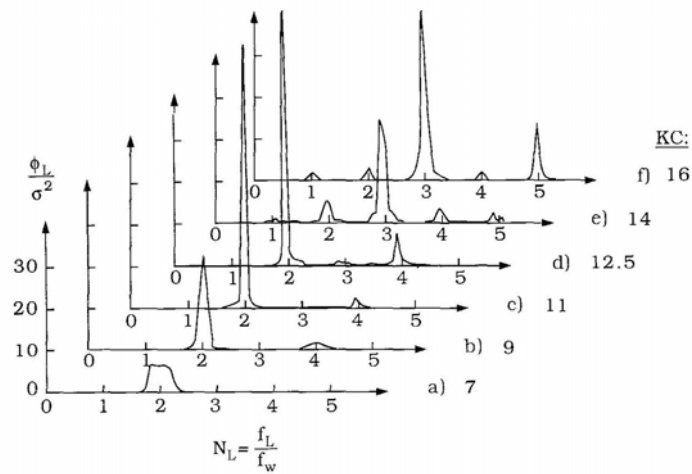

Figure 30: Power spectra of lift for a free cylinder in oscillatory flow. σ^2 is the variance of the lift fluctuations, N_L is the ratio between the lift frequency f_L and the wave frequency f_W. $Re = 5 \cdot 10^5$. [Sumer & Fredsøe 1997, p87]

Following Figure 30, the normalized fundamental lift frequency for a cylinder far from the wall can be approximated as

$$N_L = \frac{f_L}{f_W} = \begin{cases} 2, & \text{for} \quad 4 \le KC \le 13 \quad \text{and} \quad \frac{e}{D} = \infty \\ 3, & \text{for} \quad 13 < KC \le 24 \quad \text{and} \quad \frac{e}{D} = \infty \end{cases} \qquad (3.1.5)$$

where

N_L is the normalized fundamental lift frequency [-]

f_L is the lift frequency [Hz]

f_W is the wave frequency [Hz]

For small gap ratios, the normalized lift frequency will decrease for increasing values of KC according to experimental results in [Sumer & Fredsøe 1997, pp94-102]. The normalized lift frequency for small gap ratios is approximated as

$$N_L = 2, \quad \text{for} \quad 7 \le KC \le 24 \quad \text{and} \quad \frac{e}{D} = 0.1 \tag{3.1.6}$$

In this project, the frequency given by (3.1.6) is used in the force models for pipelines with zero or small gaps when the cross-flow force is governed by wall proximity effects. This is elaborated in Chapter 3.2 (Hydrodynamic Force Models).

Vortex Shedding Frequency

The average vortex shedding frequency can be determined based on the number of short-duration peaks in the cross-flow force over a certain period. To estimate this frequency, the Strouhal number is defined for a cylinder in oscillating flow as

$$St = \frac{f_v D}{U_m} \tag{3.1.7}$$

where

St is the Strouhal number [-]

f_v is the average vortex shedding frequency (Strouhal frequency) [Hz]

U_m is the maximum flow velocity [m/s]

[Sumer & Fredsøe 1997, p104]

Figure 31 shows experimental results for the Strouhal number for different values of KC and gap ratios.
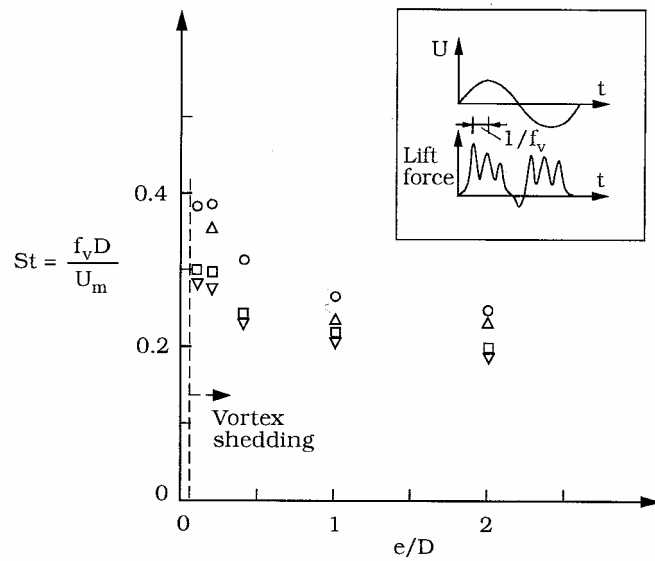
Figure 31: Strouhal number for various gap ratios [Sumer & Fredsøe p105].
o: $KC = 20$; Δ: $KC = 30$; ; $\square$: $KC = 55$; ∇ : $KC = 65$.

It is seen from Figure 31 that St is in the range of 0.2-0.4 and attains the lowest values when the gap ratio increases and KC is large. The Strouhal number also depends on Reynolds number and roughness of the pipe but these effects are not examined further in this project. In this project, a constant value of St is chosen as

$$St = 0.25 \qquad\qquad (3.1.8)$$

The average vortex shedding frequency can now be found by isolating f_v in (3.1.7) as

$$f_v = \frac{St \cdot U_m}{D} \qquad\qquad (3.1.9)$$

The vortex shedding frequency should be implemented in the force models when the gap ratio of the pipe increases and the value of KC increases. It is noticed that the forces that act with the vortex shedding frequency will not have a great affect on the cylinder unless vortex lock-in is present. This is due to the fact that the vortices along the cylinder otherwise work out of phase which is also mentioned in the following section and in Chapter 3.2 (Hydrodynamic Force Models).

Lock-in Frequency

When the vortex shedding frequency approaches the natural frequency of the structure, the frequency of the vortex shedding and response of the structure collapses into one frequency close to the natural frequency of the structure. This phenomenon is called lock-in and is illustrated in Figure 32.
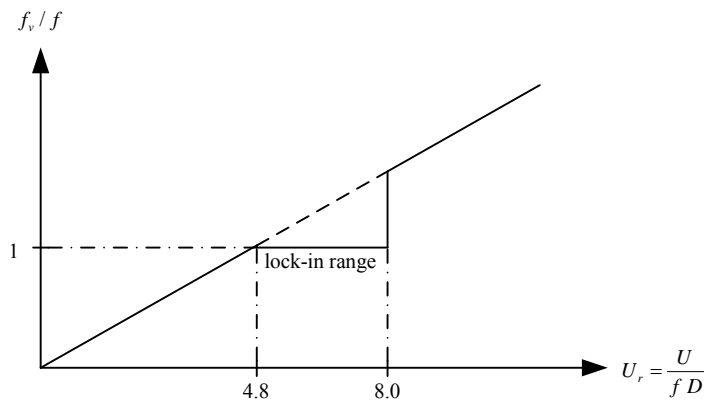
Figure 32: Illustration of lock-in. U_r *is the reduced velocity and f is the natural frequency of the structure.*

The lock-in range is determined according to [Nedergaard et al. 1994] which implies that lock-in happens for

$$4.8 < U_r < 8.0 \qquad\qquad (3.1.10)$$

When applying a force model that includes forces from vortex shedding, the lock-in phenomenon should be considered because lock-in can be crucial to the dynamic response of the structure.

Another important aspect of the cross-flow force from vortex shedding and lock-in is the fact that the vortex shedding along the length of the cylinder can act out of phase in different parts of the structure [Sumer & Fredsøe 1997, pp28-29; pp104-112]. When applying a force model, a correlation length has to be determined which describes the length of a cell where the vortices are in phase.

3.1.3   CYLINDER IN REGULAR WAVES & CURRENT

This section shows the effect of combined waves and current on the force coefficients for in-line and cross-flow forces, respectively. The section is based on experimental results from [Justesen et al. 1987].

3.1.3.1. In-line Force

The in-line force coefficients C_D and C_M and their tendencies are shown in Figure 33.
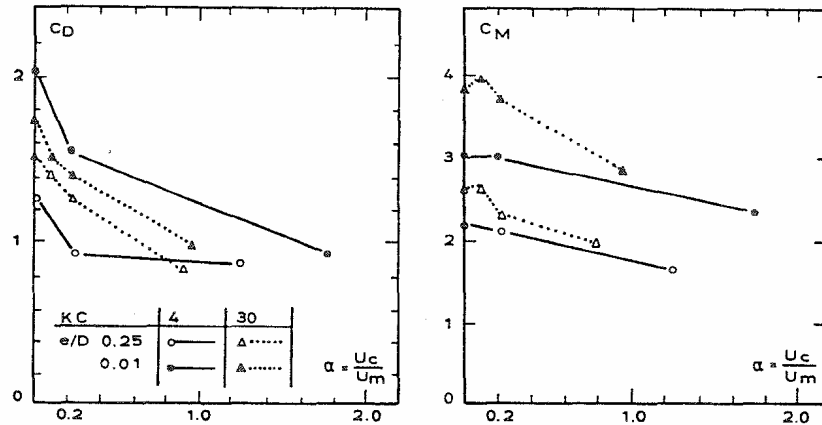
Figure 33: Drag and inertia force coefficient C_D and C_M for a near-wall cylinder in regular wave with co-existing current [Justesen et al. 1987, p136].

It is seen that the drag and inertia force coefficients C_D and C_M generally decrease for increasing ratios of U_c / U_m. The drag force coefficient C_D must be expected to approach an asymptotic value that is equal to C_D for a cylinder in a steady current which is the case for a free cylinder according to [Sumer & Fredsøe 1997, p159].

3.1.3.2. Cross-flow Force

The lift force coefficient C_L is evaluated similarly to the in-line force coefficients. The experimental result is shown in Figure 34.
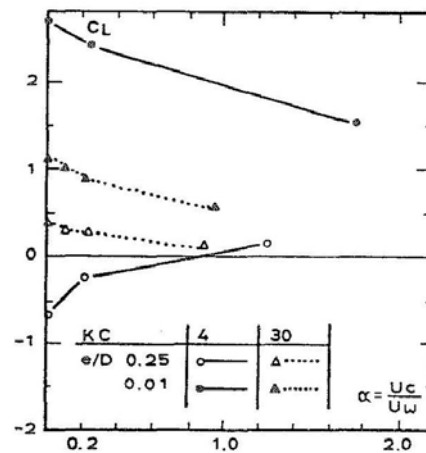

Figure 34: Lift force coefficient C_L for a near-wall cylinder for combined regular wave and current [Justesen et al. 1987, p136].

The lift force coefficient C_L decreases as the ratio of U_c / U_m increases. This coefficient is also expected to reach the asymptotic value of C_L for a cylinder in steady current which is the case for a free cylinder according to [Sumer & Fredsøe 1997, p160].

In this project the effect of co-existing current has been disregarded when C_L is estimated which is concluded to be conservative.

3.1.3.3. Cross-flow Frequency

The cross flow frequency is determined similarly to the method used for regular waves. Assuming combined regular waves and current, the Strouhal number is determined as

$$St = \frac{f_v D}{(U_c + U_m)} \tag{3.1.11}$$

[Sumer & Fredsøe 1997, p158]

Because the Strouhal number is a known value from (3.1.8), the average vortex shedding frequency can be found as

$$f_v = \frac{St \cdot (U_m + U_c)}{D} \tag{3.1.12}$$

Lock-in and correlation length has to be considered as explained in the previous section for a cylinder in regular waves.

3.1.4 EVALUATION

It has been shown that the forces that act upon a near-wall cylinder vary in both magnitude and time depending upon the type of ambient flow. Force coefficients determined for steady current have been shown to be less than those determined for regular waves when assuming the same flow characteristics in the two cases. Determining joint force coefficients for regular waves with co-existing current should therefore be decreased for the presence of current. Conservatively, this has not also been done for the lift force coefficient in this project.

The time variation of the in-line force has been shown to be relatively simple with a load frequency identical to the wave frequency. The time variation of the cross-flow force has been shown to be far more complex. As the gap between the cylinder and the wall increases, the cross-flow force will no longer be affected by the wall proximity and only vortex shedding will create lift upon the cylinder. The difference between the frequency due to wall proximity and the frequency of vortex shedding is significant.

It is an important aspect that the vortices along the cylinder only result in significant forces when vortex lock-in occurs because the vortices otherwise work out of phase.

3.2 HYDRODYNAMIC FORCE MODELS

In this chapter, several models for hydrodynamic forces have been considered. First, the simplest and most popular model which is considered is the classical Morison Model from 1950. This model neglects the pipe's disturbance on the flow and uses constant force coefficients. The force coefficients are determined according to DNV and compared to experimental results.

Another hydrodynamic force model that is considered is an extension of the Morison Model that incorporates the effects of vortex shedding for a pipeline above the seabed.

Finally, three semi-empirical Wake Models are considered, namely the Wake I, Wake II and Wake II Extended Model. These models are intended for pipelines upon the seabed and incorporate the flow disturbance that the pipe creates and time variation of force coefficients. The Wake Models are compared to the Morison Model and their limitations are discussed. One of the Wake Models is chosen for the analyses for irregular waves.

More advanced numerical hydrodynamic models such as those based upon Computational Fluid Dynamics have been considered beyond the scope of this project.

3.2.1 THE MORISON MODEL

The conventional model for determining hydrodynamic forces on cylindrical structures in the offshore industry is the Morison Model. The hydrodynamic forces affecting the pipeline have components in two directions – the in-line force and the cross-flow force. Figure 35 shows the forces affecting the pipeline.
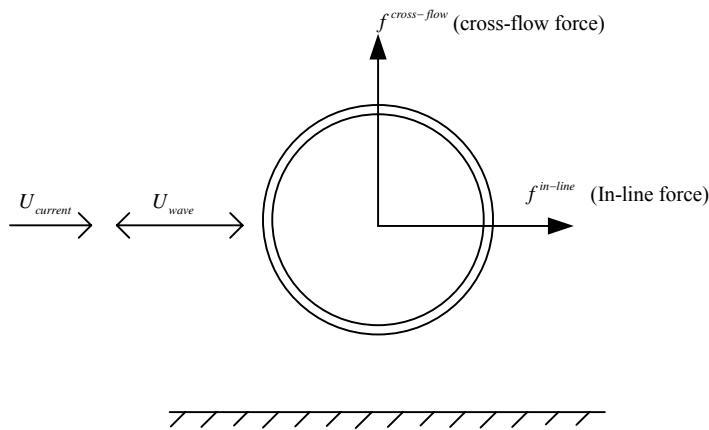
Figure 35: Hydrodynamic forces acting on the pipeline.

3.2.1.1. In-line Force

For a cylindrical structure with infinite stiffness, the Morison Model for determining the in-line force reads

$$f^{in-line} = g_D \cdot U |U| + g_I \dot{U} \qquad (3.2.1)$$

where

$f^{in-line}$ is the in-line force per unit length of the pipe as function of time $\left[\frac{N}{m} \right]$

g_D is the drag force term $\left[\frac{kg}{m^2} \right]$

g_I is the inertia force term $\left[\frac{kg}{m} \right]$

U is the in-line flow velocity for wave and current $\left[\frac{m}{s} \right]$

[Burcharth 2002, p33]

In slender structures, the assumption of infinite stiffness is not applicable since the velocity of the structure is not negligible compared to the water particle velocity. In this case, the Morison Model for determining in-line forces on slender cylindrical structures reads

$$f^{in-line} = g_D \cdot (U - \dot{y}) |U - \dot{y}| + g_I \dot{U} - g_A \ddot{y} \qquad (3.2.2)$$

where

g_A is the added mass term due to movements of the pipe $\left[\frac{kg}{m} \right]$

y is the lateral displacement of the pipe, defined positive in the flow direction $\left[m \right]$

[DNV-RP-F105 2002, p26]

The force terms for drag, inertia and added hydrodynamic mass are defined as

$$g_D = C_D \frac{1}{2} \rho_w D$$

$$g_I = C_M \frac{\pi}{4} \rho_w D^2 \qquad\qquad (3.2.3)$$

$$g_A = C_A \frac{\pi}{4} \rho_w D^2$$

where

$\quad C_D \qquad$ is the drag force coefficient [-]

$\quad C_M \qquad$ is the inertia force coefficient [-]

$\quad C_A \qquad$ is the added mass coefficient [-]

[DNV-RP-F105 2002, p27]

The fluid damping is identified in the drag force term in (3.2.2) since fluid damping may be defined as

$$f_{fluid} = g_D \dot{y} |\dot{y}|, \qquad g_D > 0 \qquad\qquad (3.2.4)$$

where

$\quad f_{fluid} \qquad$ is the damping term for fluid damping $\left[\frac{N}{m}\right]$

[Nielsen 2004, p10]

3.2.1.2. Cross-flow Force

An equivalent formulation can be made for the cross-flow force. The Morison Model for the cross-flow force reads

$$f^{cross-flow} = g_L \cdot (U - \dot{y})^2, \qquad e/D < 1.0 \qquad\qquad (3.2.5)$$

where

$\quad f^{cross-flow}$ is the cross-flow force per unit length of the pipe $\left[\frac{N}{m}\right]$

$\quad g_L \qquad$ is the lift force term $\left[\frac{kg}{m^2}\right]$

The lift force term is determined as

$$g_L = C_L \frac{1}{2} \rho_w D \qquad\qquad (3.2.6)$$

where

$\quad C_L \qquad$ is the lift force coefficient [-]

[Lambrakos et al. 1987, p123]

The formulation made in (3.2.5) describes the variation of the cross-flow force poorly when the gap ratio between the pipeline and seabed increases. The cross-flow force goes from being induced by seabed proximity to being induced by vortex shedding.

For larger gap ratios, an alternative cross-flow force model is implemented according to [Nedergaard et al. 1994]. This model is made so it includes the effect of VIV, lock-in and correlation length

which have been discussed in Chapter 3.1 (Near-Wall Cylinder). The cross-flow force model from VIV reads

$$f_{viv}^{cros-flow} = g_L \cdot U^2 \sin(\omega t), \qquad e/D \geq 1 \tag{3.2.7}$$

where

$f_{VIV}^{cross-flow}$ is the cross-flow force induced by VIV [N/m]

ω is the circular vortex shedding frequency [rad/s]

[Nedergaard et al. 1994]

In this project, (3.2.7) is only considered for pipeline free-spans where the gap ratio is assumed to be equal or larger than 1.0. The lock-in effect is included in (3.2.7) by implementing the following condition for the circular vortex shedding frequency

$$\omega = \begin{cases} \omega_i, & 4.8 < U_{r,i} < 8.0 \\ \omega_{st}, & \text{else} \end{cases}, \qquad U_{r,i} = \frac{U}{f_i D} \tag{3.2.8}$$

where

ω_i is the circular eigenfrequency of the pipeline free-span [rad/s]

ω_{st} is the circular Strouhal frequency [rad/s]

U_r is the reduced velocity [m/s]

f is the eigenfrequency of the pipeline free-span [Hz]

i is the mode number [-]

[Nedergaard et al. 1994]

Because the vortices along the pipeline can work out of phase, a correlation length depending on the amplitude of the structure is estimated as

$$l_c = 3D + 35D \frac{\eta(x,t)}{0.5D - \eta(x,t)} \quad , \quad \eta(x,t) < 0.5D$$
$$l_c = \infty \quad , \qquad\qquad\qquad \eta(x,t) > 0.5D \tag{3.2.9}$$

where

l_c is the correlation length [m]

η is the amplitude of structure [m]

x is the coordinate along the cylinder [m]

[Nedergaard et al. 1994]

The correlation length is short when lock-in does not occur which results in a small total response of the pipeline. The cross-flow force caused by vortex shedding out of the range of lock-in is neglected in this project. The same assumption has been made in [Nedergaard et al. 1994].

3.2.1.3. Force Coefficients

In order to get all contributions from the hydrodynamic load, three different force coefficients need to be determined:

- Drag force coefficient
- Inertia force coefficient
- Lift force coefficient

In reality, the hydrodynamic force coefficients vary with time and depend on multiple parameters, including the Reynolds number, the Keulegan-Carpenter number, the current-flow velocity ratio, seabed proximity and the pipe roughness. This section describes the determination of force coefficients independent of time, which are the estimated values that are typically implemented in the Morison Model.

Drag Force Coefficient

The drag force coefficient C_D is determined according to [DNV-RP-F105 2002, p27], and has been compared to the theory and experimental results from [Sumer & Fredsøe 1997] and [Justesen et al. 1987] which have also been described in Chapter 3.1 (Near-Wall Cylinder).

The drag force coefficient is determined as

$$C_D = C_{D,0} \cdot \psi_k^{CD} \cdot \psi_{proxi}^{CD} \cdot \psi_{trench}^{CD} \cdot \psi_A^{CD} \qquad (3.2.10)$$

where

$\quad C_D$ is the drag force coefficient [-]

$\quad C_{D,0}$ is the basic drag force coefficient [-]

$\quad \psi_k^{CD}$ is a correction factor for the pipe roughness [-]

$\quad \psi_{proxi}^{CD}$ is a correction factor for the seabed proximity [-]

$\quad \psi_{trench}^{CD}$ is a correction factor accounting for a pipe in a trench [-]

$\quad \psi_A^{CD}$ is an amplification factor due to cross-flow vibration [-]

[DNV-RP-F105 2002, p27]

It is noticed that the amplification factor ψ_A^{CD} is equal to 1 in all further calculations because the impact from cross-flow vibration is determined implicitly in the dynamic model.

The basic drag force coefficient for $KC \geq 5$ is taken as

$$C_{D,0} = \begin{cases} 0.9 \cdot (1-\alpha) + 5/KC, & \alpha \leq 0.5 \\ 0.45 + 5/KC, & \alpha > 0.5 \end{cases} \qquad (3.2.11)$$

where

$\quad \alpha$ is the current-flow velocity ratio [-]

[DNV-RP-F105 2002, p27]

For small values of $KC < 5$, the drag force coefficient is of little practical importance as inertia forces are dominating but for completeness $C_{D,0}$ can be determined by interpolation. The basic drag force coefficient is shown in Figure 37 at the end of this section. The current-flow velocity ratio is determined as

$$\alpha = \frac{U_c}{U_c + U_m} \tag{3.2.12}$$

where

$\quad U_c \qquad$ is the velocity of the current [m/s]

$\quad U_m \qquad$ is the maximum velocity of the wave [m/s]

[DNV-RP-F105 2002, p6]

For increasing pipe roughness, the drag force coefficient will increase which is also shown in [Sumer & Fredsøe 1997, p183]. The correction factor for the pipe roughness is taken as

$$\psi_k^{CD} = 1.25 + 0.05 \ln\left(\frac{k}{D}\right) \tag{3.2.13}$$

where

$\quad k \qquad$ is the coefficient for surface roughness [m]

[DNV-RP-F105 2002, p27]

Table 11 shows typical values for the surface roughness. In this project, the value of $k = 1/100$ m is used when assuming marine growth on the pipeline free-span.

Table 11: Surface roughness [DNV-RP-F105 2002, p27].

Pipe surface	k [m]
Steel, painted	10^{-6}
Steel, uncoated (not rusted)	10^{-5}
Concrete	1/300
Marine growth	1/200 – 1/20

For small gap ratios, the seabed will have influence on the flow around the pipe. The drag force generally increases with decreasing gap ratios. The correction factor for the seabed proximity is taken as

$$\psi_{proxi}^{CD} = \begin{cases} 0.9 + \dfrac{0.5}{1 + 5\dfrac{e}{D}}, & \dfrac{e}{D} < 0.8 \\ \\ 1, & \text{else} \end{cases} \tag{3.2.14}$$

where

$\quad e \qquad$ is the gap between the pipe and the seabed [m]

$\quad \dfrac{e}{D} \qquad$ is the gap ratio [-]

[DNV-RP-F105 2002, p27]

The free-span that is examined in this project is caused by erosion. The erosion creates a trench under the pipe which decreases the drag force compared to a plane seabed. The correction factor accounting for a pipe in a trench is taken as

$$\psi_{trench}^{CD} = 1 - \frac{2}{3}\left(\frac{\Delta}{D}\right)$$ (3.2.15)

where

$\frac{\Delta}{D}$ is the relative trenching depth [-]

[DNV-RP-F105 2002, p27]

Figure 36 shows the geometrical parameters to determine the relative trenching depth.
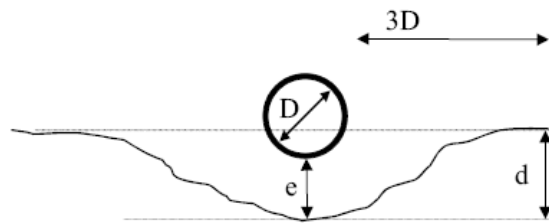
Figure 36: Relative trench depth [DNV-RP-F105 2002, p23].

The relative trenching depth is determined as

$$\frac{\Delta}{D} = \frac{1.25d - e}{D}, \qquad 0 \le \frac{\Delta}{D} \le 1$$ (3.2.16)

[DNV-RP-F105 2002, p23]

In this project, the conservative value of the correction factor $\psi_{trench}^{CD} = 1$ is used.

Figure 37 shows C_D as a function of KC for different values of α before the correction factors are applied which corresponds to the case $C_D = C_{D,0}$. Figure 37 shows that C_D peaks at $KC = 5$ and decreases asymptotically for higher values of KC. Figure 37 also shows that C_D decreases for increasing α. The values of C_D as a function of KC are slightly conservative compared to [Sumer & Fredsøe, p181] and the peak value of C_D has been indicated to appear at $KC = 10$ in [Justesen et al.1987, p132].
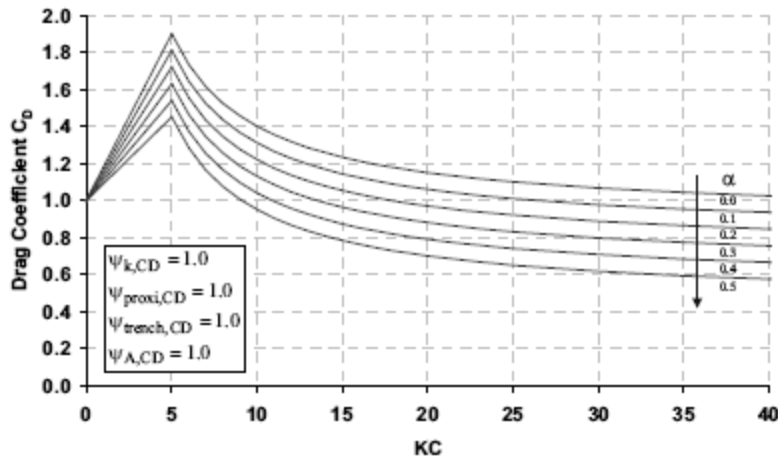
Figure 37: Drag force coefficient in the case $C_D = C_{D,0}$ [DNV-RP-F105 2002, p27].

The correction factors are applied to C_D corresponding to the conditions chosen in the individual analysis. A script has been made to determine C_D and can be found in [DVD/Hydrodynamic Force Models/Force Coefficients/forcecoefficients.m].

Inertia Force Coefficient

The inertia force coefficient is determined according to [DNV-RP-F105 2002, pp27-28] and compared to the same literature as the drag force coefficient. The inertia force coefficient is determined as

$$C_M = C_{M,0} \cdot \psi_k^{CM} \cdot \psi_{proxi}^{CM} \cdot \psi_{trench}^{CM} \tag{3.2.17}$$

where

$\quad C_{M,0} \qquad$ is the basic inertia force coefficient [-]

$\quad \psi_k^{CM} \qquad$ is a correction factor for the pipe roughness [-]

$\quad \psi_{proxi}^{CM} \qquad$ is a correction factor for the seabed proximity [-]

$\quad \psi_{trench}^{CM} \qquad$ is a correction factor accounting for a pipe in a trench [-]

The basic inertia force coefficient is determined as function of the current-flow velocity ratio α defined in (3.2.12) and KC. The basic inertia force coefficient is taken as

$$C_{M,0} = f(\alpha) + \frac{5(2 - f(\alpha))}{KC + 5}, \qquad f(\alpha) = \begin{cases} 1.6 - 2\alpha, & \alpha \le 0.5 \\ 0.6, & \alpha > 0.5 \end{cases} \tag{3.2.18}$$

[DNV-RP-F105 2002, p27]

The basic coefficient is shown in Figure 38 at the end of this section.

For increasing pipe roughness, the inertia force will decrease. This corresponds well to the observation made in [Sumer & Fredsøe 1997, p153]. The correction factor for the pipe roughness is taken as

$$\psi_k^{CM} = 2 - \psi_k^{CD} \tag{3.2.19}$$

[DNV-RP-F105 2002, p28]

Like the drag force, the inertia force will increase for decreasing gap ratios. This tendency is also found in [Sumer & Fredsøe 1997, p181]. The correction factor for the seabed proximity is taken as

$$\psi_{proxi}^{CM} = \begin{cases} 0.84 + \dfrac{0.8}{1 + 5\dfrac{e}{D}}, & \dfrac{e}{D} < 0.8 \\[4mm] 1, & \dfrac{e}{D} \geq 0.8 \end{cases} \tag{3.2.20}$$

[DNV-RP-F105 2002, p28]

The trenching depth caused by erosion also decreases the inertia force. The correction factor accounting for a pipe in a trench is taken as

$$\psi_{trench}^{CM} = 1 - \frac{1}{3}\left(\frac{\Delta}{D}\right) \tag{3.2.21}$$

[DNV-RP-F105 2002, p28]

In this project, the conservative value of the correction factor $\psi_{trench}^{CM} = 1$ is used.

Figure 38 shows the values of C_M as a function of KC for different values of α before the correction factors are applied corresponding to $C_M = C_{M,0}$. The values of C_M are overall in good agreement with [Justesen et al.1987, p135] but for decreasing gap ratios C_M increases rapidly for higher values of KC. This effect is not taken into account in the formulation of C_M in [DNV-RP-F105 2002]. However, it is of minor importance since the in-line force for higher values of KC is drag dominated which has been illustrated in Chapter 3.1 (Near-Wall Cylinder).
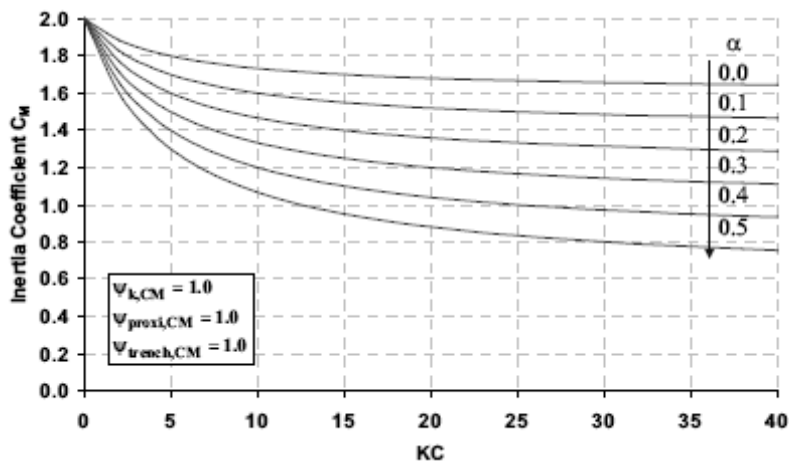
Figure 38: Inertia force coefficient in the case $C_M = C_{m,0}$. [DNV-RP-F105 2002, p28].

The correction factors are applied to C_M corresponding to the conditions chosen in the individual analysis. A script has been made to determine C_M and can be found in [DVD/Hydrodynamic Force Models/Force Coefficients/forcecoefficients.m].

Lift Force Coefficient

[DNV-RP-F105 2002] does not specify values for the lift force coefficient. The lift force coefficient is estimated according to theory and experimental results from [Sumer & Fredsøe 1997] and [Justesen et al. 1987] which have been examined in Chapter 3.1 (Near-Wall Cylinder).

The lift force coefficient for small gaps is estimated from Figure 39 which has been elaborated in Chapter 3.1 (Near-Wall Cylinder). This is the lift force coefficient that is used in (3.2.5) in this project to determine the cross-flow force for pipeline free-spans with small gap ratios $(e/D < 1.0)$.
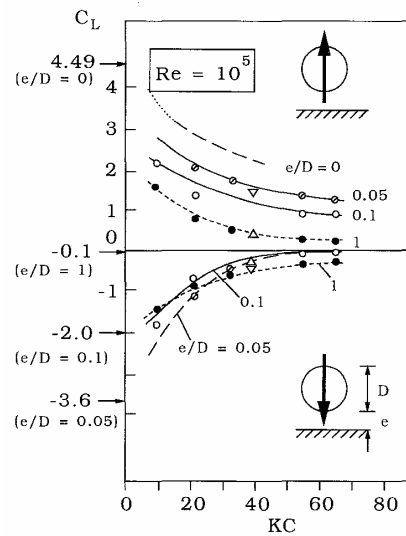
Figure 39: Lift force coefficient for a near-wall cylinder in a regular wave. The asymptotic values of C_L for $KC \rightarrow 0$ indicated in the figure are the potential-flow solutions. [Sumer & Fredsøe 1997, p183].

The current-flow velocity ratio α does also have an effect on the cross-flow force. For increasing α, C_L will tend to decrease to the value determined for steady current. The pipe roughness has a small effect on the cross-flow force. The cross-flow force will increase for increasing pipe roughness which is shown in [Sumer & Fredsøe 1997, p185]. These effects have been disregarded in this project as the values of C_L shown in Figure 39 are considered to be conservative.

For larger gap ratios $(e/D \geq 1)$, the value of $C_L = 0.9$ should be used in the cross-flow force model for vortex shedding shown in (3.2.7). This is also considered to be a conservative value which has been elaborated in Chapter 3.1 (Near-Wall Cylinder).

Lift Frequency

In addition to estimating the value of the lift force coefficient, it is also important to know the lift frequency. For a pipeline free-span with an infinitesimal gap ratio, the lift frequency is about twice the wave frequency as described in Chapter 3.1 (Near-Wall Cylinder). This characteristic of the cross-flow force is inherent in the conventional force model. In the case of no current, (3.2.5) yields a cross-flow force that varies at exactly twice the circular frequency of the wave

$$U = U_m \sin(\omega t) \Rightarrow f^{cross-flow} \propto \sin^2(\omega t) \propto \sin(2\omega t - 90°)$$

where

ω is the circular wave frequency [rad/s]

Figure 40 (left) shows the flow velocity for sea state 5 before any current is applied and Figure 40 (right) shows the corresponding cross-flow force calculated by (3.2.5).
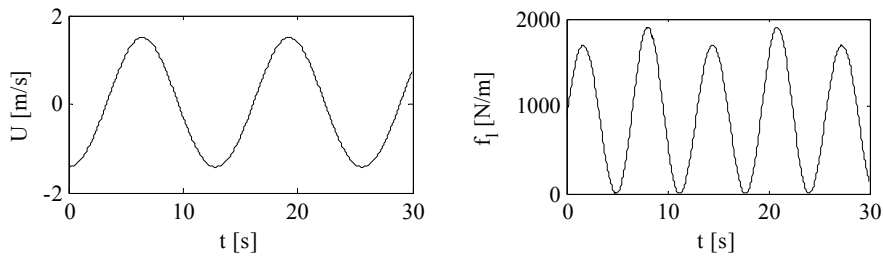
Figure 40: Flow velocity and corresponding cross-flow force by the Morison Model during sea state 5 without current. KC=31, $C_L = 2.5$.

It is seen that if C_L is given a positive constant value, the cross-flow force can only attain non-negative values since the computed force can never have the opposite sign of the lift force coefficient according to (3.2.5), i.e. $C_L > 0 \Rightarrow f^{cross-flow} \geq 0$.

This is not a correct modelling of the cross-flow force when the gap ratio increases because experimental results show that the pipeline free-span will be affected by negative cross-flow forces even for small gaps, also described in Chapter 3.1 (Near-Wall Cylinder).

For larger gaps, the cross-flow force model including vortex shedding is used. Figure 41 (left) shows the flow velocity for sea state 5 before any current is applied and Figure 41 (right) shows the corresponding cross-flow force calculated by (3.2.7). It is noticed that vortex shedding is assumed to be out of the range of lock-in.
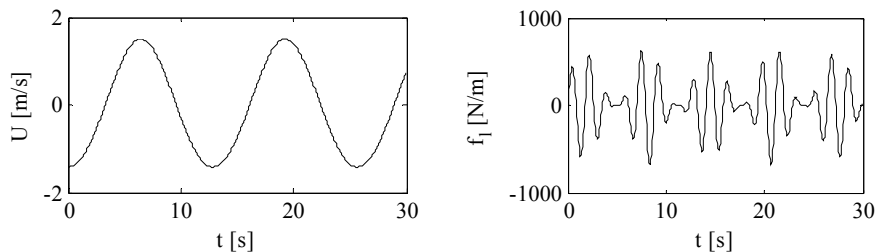

Figure 41: Flow velocity and corresponding cross-flow force by the force model in (3.2.7) during sea state 5 without current. KC=31, $C_L = 0.9$.

The frequency of the vortex shedding according to the cross-flow force model described in (3.2.7) is evaluated according to the experimental result in [Justesen et al. p135] also shown in Chapter 3.1 (Near-Wall Cylinder). It is seen that the cross-flow force is actually modelled quite well compared to the experimental results for high values of KC and a gap ratio $e/D = 1$.

3.2.2 THE WAKE MODELS

Over the past two decades, several models have been proposed to determine the hydrodynamic forces upon pipelines on the seabed. These are the Wake I Model [Lambrakos et al. 1987], the Wake II Model [Soedigdo et al. 1998; Sabag et al. 2000] and the Wake II Extended Model [Aristodemo et al. 2006; Aristodemo et al. 2007]. These three models will be referred to as the Wake Models and are described in this section.

3.2.2.1. Overview

All of the Wake Models extend the Morison Model with the following two features:

- **The start-up effect:** A generic Pipe Impulse Test (PIT) was conducted during the years 1982-1983 where two pipes in longitudinal contact were lifted suddenly through still fluid. The test was conducted on smooth and rough pipes with diameters 0.2 m and 0.3 m. The test showed that the hydrodynamic forces upon pipes which are suddenly moved in still fluid are greatest at the beginning of the impulse movement [Lambrakos et al. 1987, p126]. This effect is called the start-up effect and is incorporated in the Wake Models by the use of time varying force coefficients for the drag and cross-flow force that depend upon the flow and empirical parameters. The Wake Models use identical mathematical formulation of the start-up effect but they differ in the values of the related empirical parameters.

- **The wake effect:** The presence of the pipe is known to disturb the flow and create a wake in the downstream direction of the flow. In oscillatory flow, the pipe will meet this wake upon reversal of the flow direction which will affect the magnitude and phase of the local velocity that the pipe experiences. This effect is called the wake effect, and is incorporated in the Wake Models by use of an effective velocity. The Wake Models differ in the theoretical background, formulation and values of the empirical parameters for the effective velocity.

As mentioned, the Wake Models introduce empirical parameters. These may be limited to the scope of flow and structural conditions which they have been calibrated against. The application scope and calibration bases of the Wake Models are given in Table 12 and described briefly below.

Table 12: Overview of the Wake Models. Compiled upon literature study of [Lambrakos et al. 1987, Soedigdo et al. 1998; Sabag et al. 2000, Aristodemo et al. 2006; Aristodemo et al. 2007].

	Application scope		**Basis for calibration**	
	Regular waves with and without current	Irregular waves with and without current	Experiment	Flow conditions
Wake I Model	Yes	Yes	Full-scale pipe in shallow waters	$\dfrac{e}{D} = 0$ $0 \le KC \le 40$ $0 \le Re \le 8 \cdot 10^5$ Smooth and rough pipe
Wake II Model	Yes	No		
Wake II Extended Model	Yes	Yes	Model-scale pipe in wave flume	$\dfrac{e}{D} = 0$ $4 \le KC \le 12$ (regular) $4 \le \overline{KC} \le 9$ (irregular) Inertia-dominated Smooth pipe

It is seen from Table 12 that the Wake II Model is not valid for irregular waves. It will therefore not enter as a candidate model for the dynamic analysis of the project but it is included in the following descriptions for the sake of completeness and illustration.

The basis of calibration for the Wake I and II Models is results from the Pipeline Field Measurement Program (PFMP) that was conducted during the years 1980-1981 in a bay outside Washington State, U.S. Data were recorded from full-scale smooth and rough pipe-sections with a diameter of 0.61 m on the seabed. The test was performed in shallow waters with a water depth of 18.3 m for a wide range of sea conditions. [Lambrakos et al. 1987, p119-120]

The calibration basis for the Wake II Extended Model is a recent experiment with a model-scale smooth pipe section with a diameter of 0.22 m in a large wave flume which is 132 m long, 1.94 m wide and 2.50 m deep. The test was conducted for inertia-dominated sea states that cover a limited range of characteristic Keulegan-Carpenter numbers. [Aristodemo et al. 2006]

The empirical parameters generally differ for the Wake Models and are shown in Appendix F (Empirical Parameters of Wake Models). In the calibration basis of the Wake I Model, one set of parameters are provided for all flow conditions whereas the Wake II and II Extended Models are provided with different sets of parameters that depend upon the flow condition.

The numerical computations can be found in [DVD/Hydrodynamic Force Models/Force Models/forcemodels.m].

3.2.2.2. Hydrodynamic Forces of the Wake Models

The formulation of the hydrodynamic forces is identical for all the Wake Models and is described in this section. The in-line force for a rigid cylinder in the Wake Models may be written as

$$f^{in-line}(t) = g_D(t) \cdot U_e(t) |U_e(t)| + g_I \cdot \dot{U}(t) - g_A \cdot \dot{U}_w \qquad (3.2.22)$$

where

U_e is the effective flow velocity $\left[\frac{m}{s} \right]$

U_w is the wake flow velocity, defined positive in the ambient flow direction $\left[\frac{m}{s} \right]$

[Lambrakos et al. 1987, p123; Soedigdo et al. 1998, p442; Sabag et al. 2000, p1297; Aristodemo et al. 2006, p2; Aristodemo et al. 2007, p3]

The effective velocity is defined as the superposition of the ambient flow and wake velocity

$$U_e(t) = U(t) + U_w(t) \qquad (3.2.23)$$

where

U is the undisturbed in-line flow velocity for wave and current $\left[\frac{m}{s} \right]$

It may be noted by comparison of (3.2.22) and (3.2.23) that a positive wake velocity correctly provides an increased value of the drag and inertia terms but a decreased value of the added mass term.

The cross-flow force in the Wake Models is given by

$$f^{cross-flow}(t) = g_L(t) \cdot (U_e(t))^2 \qquad (3.2.24)$$

[Lambrakos et al. 1987, p123; Soedigdo et al. 1998, p442; Sabag et al. 2000, p1297; Aristodemo et al. 2006, p2; Aristodemo et al. 2007, p3]

3.2.2.3. Flow Condition Examples

In order to illustrate the start-up and wake effect, some flow conditions are introduced. These flow conditions will be referred to as the flow condition examples. The flow condition is denoted with *R* or *IR* for cases with regular and irregular waves, respectively, and with *NC* or *C* for cases without and with current, respectively.

The regular waves are represented by a sinusoidal function of the following general form

$$U(t) = U_m \sin(\omega t + \theta) + U_c$$

As previously discussed, all of the Wake Models are valid for $KC \approx 10$. In order to compare the models, this value is targeted and may be achieved by the following choice of parameters:

$$T = 9.8\,\mathrm{s}, \qquad U_m = 0.5\,\tfrac{\mathrm{m}}{\mathrm{s}}, \qquad U_c = 0.17\,\tfrac{\mathrm{m}}{\mathrm{s}}, \qquad \theta = 70°, \qquad D = 0.6\,\mathrm{m}$$

By comparison with Chapter 1.1 (Design Conditions), it may be seen that the chosen parameters correspond to the flow condition in the centre-line of the pipe upon the seabed during sea state 3.

For the case of irregular waves with current, a time-series of ambient flow from the PFMP is used because it provides a basis for benchmarking [Lambrakos et al. 1987, p129]. This flow is characterized by the following parameters:

$$T_p = 15\,\mathrm{s}, \qquad U_c = -0.24\,\tfrac{\mathrm{m}}{\mathrm{s}}, \qquad D = 0.61\,\mathrm{m}$$

The irregular flow has a characteristic $\overline{KC} \approx 16$. Since the smoothness of the ambient velocity is important for the computations of flow acceleration, the digitalized discrete signal has been transformed to a Fourier series from which the high-frequent noise has been removed.

The time variation of the flow velocity for the flow condition examples for regular waves with and without current, and regular waves with current is shown in Figure 42.
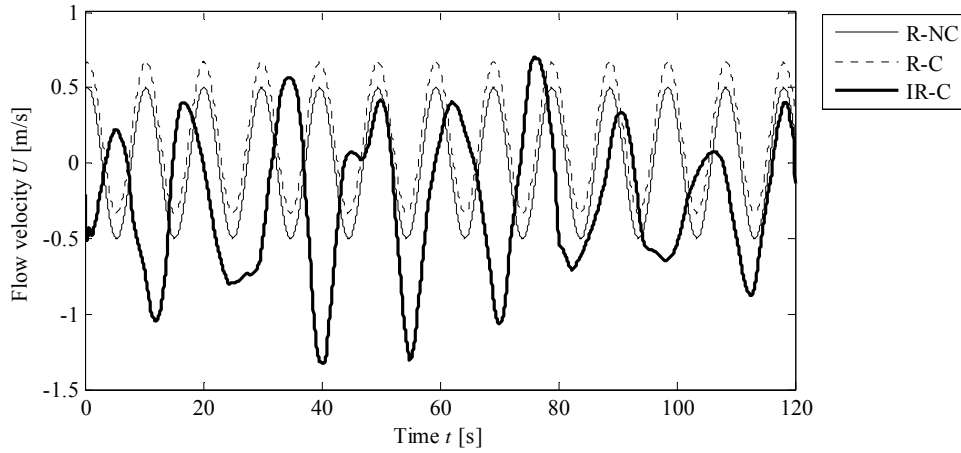
Figure 42: Time variation of flow velocities in flow condition examples.

3.2.2.4. Definition of Intersects and Maxima

Before the start-up and wake effect of the Wake Models are described further, it is appropriate to introduce definitions of some relevant quantities. The instances in time $t_{e,1}{}^{\circ}, t_{e,2}{}^{\circ}, \ldots, t_{e,p}{}^{\circ}$ for intersects with the time axis of the effective velocity are here defined by the relation

$$U_e\left(t_{e,f}{}^{\circ}\right) = 0, \quad f = 1, 2, \ldots, p \tag{3.2.25}$$

where

$t_{e,f}{}^{\circ}$ is the time for the fth intersect of the effective velocity [s]

p is the total number of intersects of the effective velocity [-]

The instances in time $t_1{}^{\circ}, t_2{}^{\circ}, \ldots, t_k{}^{\circ}$ for intersects of ambient velocity are similarly defined by

$$U\left(t_f{}^{\circ}\right) = 0, \quad f = 1, 2, \ldots, k \tag{3.2.26}$$

where

$t_f{}^{\circ}$ is the time for the fth intersect of the ambient velocity [s]

k is the total number of intersects of the ambient velocity [-]

The instances in time $t_1{}', t_2{}', \ldots, t_{k+1}{}'$ for maximum absolute flow velocity within a half-cycle are defined by

$$\max|U(t)| = \begin{cases} \left|U\left(t_1{}'\right)\right| = U_{max,1} & t < t_1{}^{\circ} \\ \left|U\left(t_h{}'\right)\right| = U_{max,h} & t_{h-1}{}^{\circ} < t < t_h{}^{\circ} \quad h = 2,3,\ldots,k \\ \left|U\left(t'_{k+1}\right)\right| = U_{max,k+1} & t_k{}^{\circ} < t \end{cases} \tag{3.2.27}$$

where

t'_j is the time for maximum ambient velocity in the jth half-cycle [s]

$U_{max,j}$ is the maximum absolute flow velocity in the jth half-cycle $\left[\frac{m}{s}\right]$

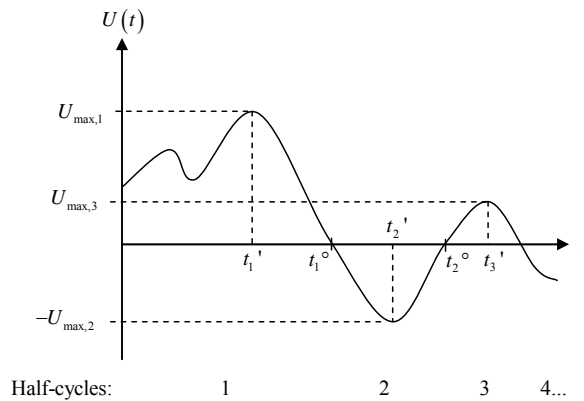The definitions of intersect and maxima of the flow velocity are illustrated on Figure 43.

Figure 43: Definitions of intersect and maxima of flow velocity.

For convenience, the characteristics of the cycles of the flow condition example IR-C are shown in Table 13 where the local half-cycle period is the time difference between two intersects.

Table 13: Characteristics of flow condition example IR-C.

Half-cycle j	Maximum absolute ambient velocity $U_{\max,j}\,[\frac{m}{s}]$	Local half-cycle period $T_{loc,j}\,[s]$
1	0.51	3.50
2	0.22	3.70
3	1.05	7.65
4	0.40	5.15
5	0.80	11.60
6	0.57	5.40
7	1.33	6.85
8	0.42	8.05
9	1.31	7.25
10	0.40	6.70
11	1.06	7.75
12	0.70	5.75
13	0.71	9.05
14	0.34	4.25
15	0.65	11.70
16	0.08	3.45
17	0.88	8.40
18	0.40	3.65
Average	0.66	6.66

3.2.2.5. The Start-up Effect of the Wake Models

The first feature of the Wake Models is the start-up effect. This is formulated in the same general way for all the Wake Models but the values of the empirical parameters differ. The time variation of the drag and lift force coefficients is written as

$$C_k\left(t\right) = C_{kS} + \alpha_k\, r\left(t\right)^{\beta_k} \cdot \exp\!\left(\gamma_k\, r\left(t\right)^{\delta_k}\right), \quad k = D, L \qquad (3.2.28)$$

where

C_k is the time-varying force coefficient for drag or lift [-]

C_{kS} is the steady-flow force coefficient for drag or lift [-]

α_k is the height parameter for drag or lift [-]

β_k is the rise parameter for drag or lift [-]

γ_k is the decay parameter for drag or lift [-]

δ_k is the width parameter for drag or lift [-]

r is a time-varying impulse ratio [-]

[Lambrakos et al. 1987, p127-128]

Thus, the drag and lift force coefficients depend upon the impulse ratio and ten empirical parameters $C_{DS}, C_{LS}, \alpha_D, \beta_D, \gamma_D, \delta_D, \alpha_L, \beta_L, \gamma_L, \delta_L$ when the effective velocity is known. The empirical parameters differ for the Wake Models and are given in Appendix F (Empirical Parameters of Wake Models).

A comparison of the start-up effect follows in a later section but the transient part of the drag and lift force coefficient is illustrated in Figure 44 for the Wake I Model. Generally, the variation of the lift force coefficient is much larger than that of the drag force coefficient.
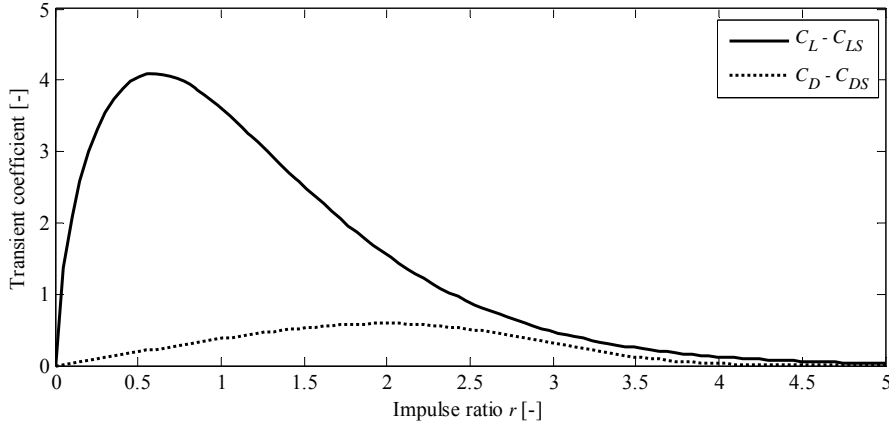

Figure 44: The transient drag and lift force coefficient for the Wake I Model.

The impulse ratio is given by the ratio between the relative distance that the water particles travel after intersects in the effective velocity and the pipe diameter

$$r\left(t\right) = \frac{S\left(t\right)}{D} \qquad (3.2.29)$$

where

S is the relative distance of the water particles after intersects in the effective velocity [m]

By the use of the definition for instances in time for intersects (3.2.25), the relative distance may be determined by numerical integration of the effective velocity

$$S(t) = \left| \int_a^t U_e(\tau) d\tau \right|, \quad a = \begin{cases} 0 & t < t_{e,1}^\circ \\ t_{e,h-1}^\circ & t_{e,h-1}^\circ < t < t_{e,h}^\circ \quad h = 2,3,...,k \\ t_{e,k}^\circ & t_{e,k}^\circ < t \end{cases} \quad (3.2.30)$$

[Lambrakos et al. 1987, p127]

For illustration, the time variation of the relative distance for an effective velocity identical to the flow condition example for regular waves without current is shown in Figure 45.
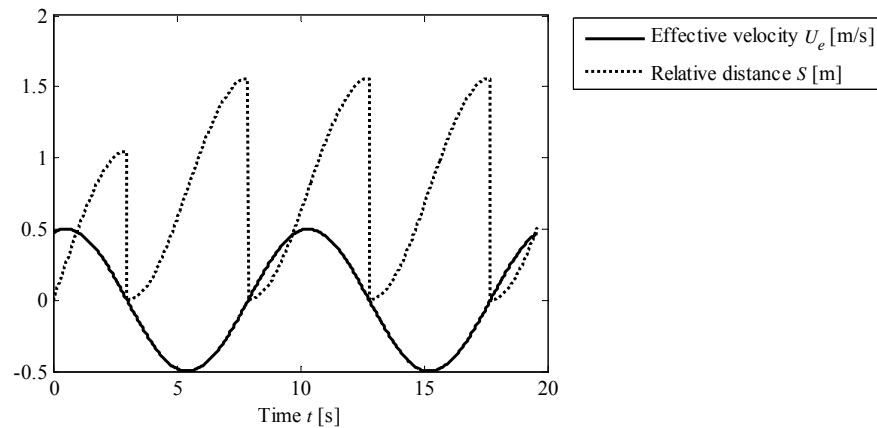

Figure 45: The time variation of the relative distance for the flow condition R-NC.

3.2.2.6. The Wake Effect of the Wake I Model

The second feature of the Wake Models is the wake effect. This is described here for the Wake I Model which is valid for irregular waves with current. The Wake I Model is also known as the EPR (Exxon Production Research) Wake Model.

In the derivation of the wake velocity, one may consider an oscillating pipe in still fluid or a still pipe in oscillatory flow. These two perspectives are illustrated in Figure 46 left and right, respectively.
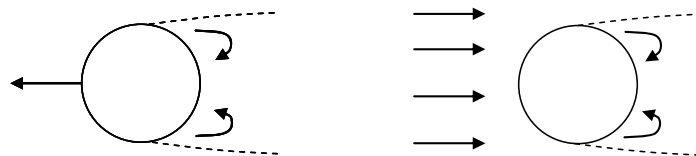
Figure 46: Two perspectives on wake flow around a pipe. Left: An oscillating pipe in still fluid. Right: A still pipe in oscillatory flow.

In the first case, the wake appears behind the pipe with a velocity in the direction of the pipe motion. In the latter case, the wake appears in the downstream direction with a velocity that is directed in the upstream direction. Upon reversal, the wake will either counteract or contribute to the flow in the first and latter case, respectively. Since the first perspective is used in the Wake I Model and the latter perspective is the actual situation of the pipe, the actual wake velocity has the opposite sign of the apparent wake velocity, i.e.

$$U_w = -\tilde{U}_w \qquad (3.2.31)$$

where

$\tilde{U}_w$ is the apparent wake velocity $\left[\frac{m}{s}\right]$

The wake is assumed to be generated at the time of maximum ambient velocity as defined by (3.2.27). Then, the apparent wake velocity may be found upon a simplified solution to the Navier–Stokes equations for the wake flow that is generated by a pipe that moves with constant velocity

$$\tilde{U}_{w,i}(t) = \begin{cases} \tilde{U}_p \cdot K, & |x| \le \dfrac{C_{DS}\, D}{K^2} \\[2ex] \tilde{U}_p \cdot \sqrt{\dfrac{C_{DS}\, D}{|x_i(t)|}}, & elsewise \end{cases} \qquad (3.2.32)$$

where

$\tilde{U}_p$ is the pipe velocity $\left[\frac{m}{s}\right]$

x is the distance along the flow motion between wake particles and pipe perimeter [m]

K is an empirical parameter [-]

[Lambrakos et al. 1987, p124]

The parameters are illustrated on Figure 47.
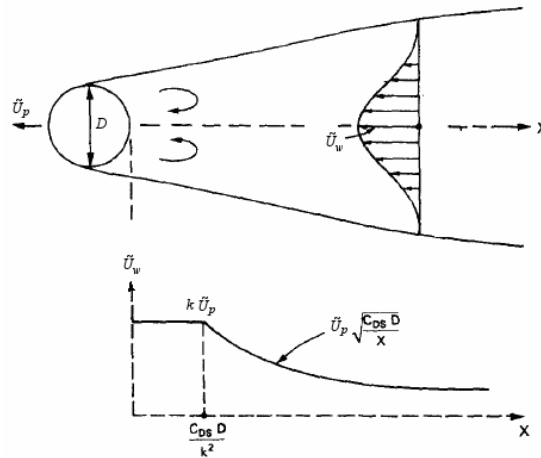
Figure 47: Wake flow for a pipe moving with constant velocity in still fluid. Adopted from [Lambrakos et al. 1987, p124]

All wake particles are assumed to travel with the same velocity as the wake front, i.e. the wake is a rigid segment. The distance travelled by the wake segment after wake generation is

$$x_w(t) = \int_{t'}^{t} J \tilde{U}_w(\tau)\, d\tau \qquad (3.2.33)$$

where

J is an empirical parameter [-]

x_w is the wake distance, defined positive in the flow direction [m]

[Lambrakos et al. 1987, p125]

After wake generation, the pipe travels the distance

$$x_p(t) = \int_{t'}^{t} \tilde{U}_p(\tau) d\tau \tag{3.2.34}$$

where

$\quad x_p \quad$ is the pipe distance, defined positive in the flow direction [m]

[Lambrakos et al. 1987, p125]

The relative distance between the pipe and the wake segment which determines the wake velocity after wake generation is approximated by a Taylor expansion of first order

$$x(t) = x_p(t) - x_w(t) \approx \tilde{U}_p(t') \cdot (t - t') - x_w(t) \tag{3.2.35}$$

[Lambrakos et al. 1987, p125]

Notice that equations (3.2.32), (3.2.33) and (3.2.35) are coupled, so an iterative solving method is needed. Collision is assumed to occur either when the pipe reverses, given by (3.2.26), or when the pipe has decelerated so the pipe and wake have equal distance, given by

$$x_p(t^*) = x_w(t^*) \tag{3.2.36}$$

where

$\quad t_i^* \quad$ is the time for equal distance [s]

[Lambrakos et al. 1987, p125]

It is noticed that in most cases, collision will occur upon reversal of the ambient velocity. The parameters J, K, C_{DS} are determined empirically and can be found in Appendix F (Empirical Parameters of Wake Models).

The effective velocity in a half-cycle is assumed to be affected by the wake velocity of the wake generated in the previous half-cycle. The correction is introduced from the time of collision until the end of the present half-cycle. Unfortunately, it is unclear from the original paper whether the pipe velocity in (3.2.32) is identical to the maximum ambient velocity or the actual value of the ambient velocity at a time shifted from wake generation until collision, i.e.

$$\tilde{U}_p = U_{p,\max}, \qquad\qquad\qquad \text{Interpretation A}$$
$$\tilde{U}_p(t) = U_p(t - \tau), \qquad \tau = t^* - t', \qquad \text{Interpretation B}$$

In this project, both interpretations have been investigated. The wake effect for interpretation A and B of the Wake I Model is illustrated in Figure 48 and Figure 49, respectively, for the flow condition example with regular waves and current. This serves as a basis for understanding the case of irregular waves. In both interpretations, the wake velocity has identical peak values. However, the wake velocities decay at different rates which greatly affect the effective velocity. It is seen from Figure 48 that interpretation A provides blocks of nearly constant wake velocities since the distance x never becomes relatively large. This interpretation is assessed unrealistic and is not considered in

the rest of the project. It may be noticed that none of the mentioned interpretations have been able to fully reproduce the Wake I Model results that appear in [Soedigdo et al. 1998, p449].
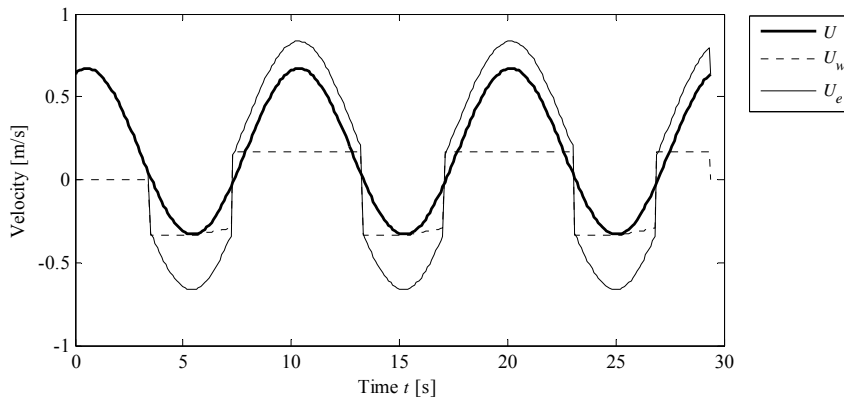

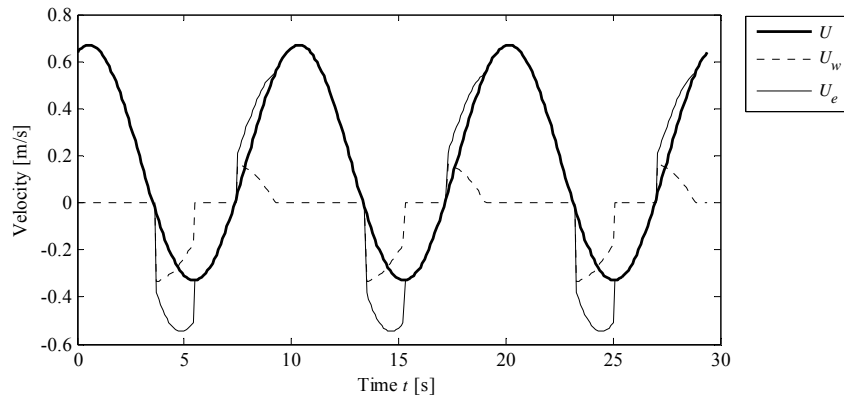*Figure 48: The wake effect in interpretation A of the Wake I Model for flow condition example R-C.*

Figure 49: The wake effect in interpretation B of the Wake I Model for flow condition example R-C.

3.2.2.7. The Wake Effect of the Wake II Model

The Wake II Model is valid for regular waves with and without current and will is briefly described for both cases.

Without Current

For the case of regular waves without current, the flow velocity may be assumed to have the following form

$$U(t) = U_m \sin(\omega t + \theta) \tag{3.2.37}$$

where

θ is an arbitrary phase angle [deg]

The related wake velocity is derived analytically from a closed-form solution to the linearised Navier–Stokes equations for oscillatory flow. The wake velocity, under influence of (3.2.37), is taken as

$$U_w(t) = \frac{U_m C_1 \sqrt{\pi}}{C_2} \text{erf}\left(\frac{1}{2} C_2 \sin^n(\omega t + \theta + \phi + \psi)\right) \tag{3.2.38}$$

where

U_w	is the wake velocity $\left[\frac{\text{m}}{\text{s}}\right]$
C_1	is a parameter that determines the rise of the wake velocity [-]
C_2	is a parameter that determines the decay of the wake velocity [-]
n	is a parameter that determines the sharpness of the wake velocity [-]
ϕ	is the phase shift between the flow velocity and the wake velocity $[\text{deg}]$
ψ	is an additional phase shift $[\text{deg}]$
erf	is the error function [-]

[Soedigdo et al. 1998, p441*]

The empirical parameters C_1, C_2, n, ϕ can be found in Appendix F (Empirical Parameters of Wake Models). The parameter for additional phase shift $\psi \approx -114°$ has been introduced in order to correct an apparently erroneous phase shift in the original formula. The corrected formula has been found to be consistent with the computed wake velocity diagrams in the original paper which may be computed with $D = 0.305\,\text{m}, T = 10\,\text{s}, U_m \in \{0.305\frac{\text{m}}{\text{s}}; 1.220\frac{\text{m}}{\text{s}}\}, \theta = 114°$ [Soedigdo et al. 1998, p442, 449-450].

For the flow condition example for regular waves without current, the following values of the empirical parameters are obtained:

$$C_1 = 0.50, \quad C_2 = 0.95, \quad n = 3, \quad \phi = 173.5°$$
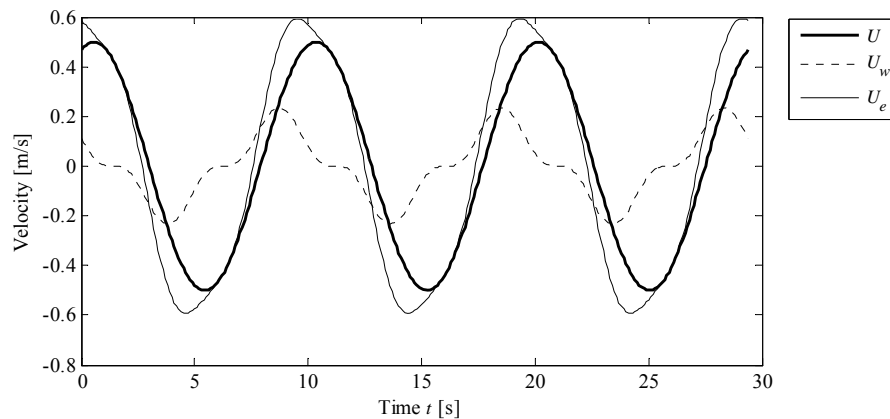
The wake effect is illustrated in Figure 50.

Figure 50: The wake effect in the Wake II Model for flow condition example R-NC.

With Current

For the case of regular waves and current with current-wave ratios less than unity, the flow velocity is assumed to have the following form

$$U(t) = U_m \sin(\omega t + \theta) + U_c, \qquad 0 < U_c \leq U_m \tag{3.2.39}$$

The half-cycles of the flow regime may be characterised by two phases:

- **Phase A:** The flow velocities from current and waves have identical directions which create a large wake with a large period in the downstream direction which is active in phase B.
- **Phase B:** The flow velocities from current and waves have opposite directions where a minor wake with a little period is created in the upstream direction which is active in phase A.

In the Wake II Model with current, the wake effect is based upon a numerical scheme where the wake velocity is similar to (3.2.38). The wake velocities during the two phases are taken as

$$U_{w,k}(t) = -\frac{U_{\max,q} C_{1,k} \sqrt{\pi}}{C_{2,k}} \operatorname{erf}\left(\frac{1}{2} C_{2,k} \sin^n(\omega_k t + \phi_k)\right), \qquad \begin{matrix} k = A, B \\ q = B, A \end{matrix} \tag{3.2.40}$$

where

$U_{w,k}$ is the wake velocity during phase A or B $\left[\frac{m}{s}\right]$

$U_{\max,q}$ is the maximum absolute flow velocity during phase B or A $\left[\frac{m}{s}\right]$

C_{1k} is a parameter that determines the rise of the wake velocity during phase A or B [-]

C_{2k} is a parameter that determines the decay of the wake velocity during phase A or B [-]

ω_k is the circular frequency of the wake velocity during phase A or B $\left[\frac{rad}{s}\right]$

ϕ_k is the phase shift between flow and wake velocity in phase A or B $[\deg]$

[Sabag et al. 2000, p1303*]

It may be noticed that (3.2.40) has been changed compared to the formula in the original paper, which does not have a negative sign and uses $U_{\max,B}, U_{\max,A}$ in phase A and B, respectively. However, the implementation in this project has been found consistent with table values and wake velocity diagrams in the original paper which may be computed with $D = 0.305\,\mathrm{m}$, $T = 10\,\mathrm{s}$, $U_m \in \{0.610\,\frac{m}{s}, 1.220\,\frac{m}{s}\}$, $U_c/U_m = 0.6\,\frac{m}{s}$, $\theta = 114°$ [Sabag et al. 2000, pp1307,1310-1311].

The phase shifts θ and ψ are not implemented directly in (3.2.40), since they are implemented indirectly in the numerical scheme which is described later.

The empirical parameters $C_{1,A}, C_{1,B}, C_{2,A}, C_{2,B}, \phi_A, \phi_B, n$ generally differ from those for (3.2.38) and are given in Appendix F (Empirical Parameters of Wake Models). Some of the other parameters are illustrated in Figure 51.
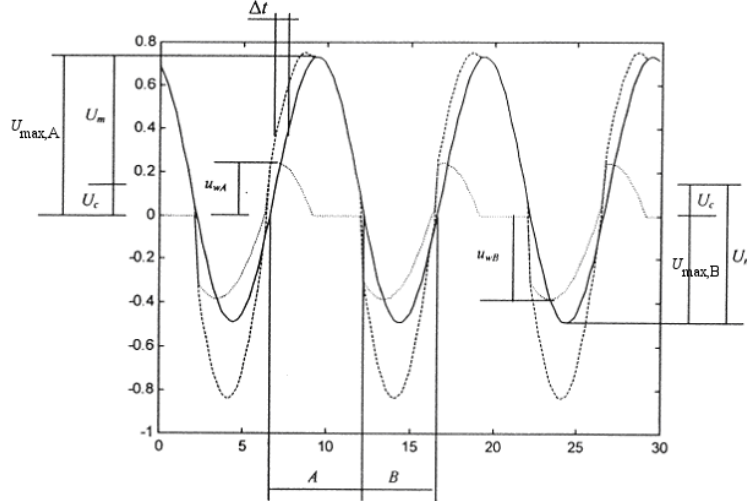

Figure 51: Definition of Wake II parameters. Adopted from [Sabag et al., p1302].

Since $U_m \geq U_c$, the maximum absolute values of the flow velocity (3.2.39) during the phases are

$$U_{\max,A} = U_m + U_c$$
$$U_{\max,B} = U_m - U_c$$

(3.2.41)

[Sabag et al. 2000, p1302]

The circular wake frequencies are taken as

$$\omega_A = \frac{\pi\,\omega}{\pi + 2\,\omega\,\Delta t},$$
$$\omega_B = \frac{\pi\,\omega}{\pi - 2\,\omega\,\Delta t}, \qquad \Delta t < 0$$

(3.2.42)

where

$\quad \Delta t \qquad$ is the time shift [s]

[Sabag et al. 2000, p1302-1303]

Then, the related wake periods are given as

$$T_k = \frac{2\pi}{\omega_k}, \qquad k = A, B, \qquad T_A < T < T_B$$

(3.2.43)

where

$\quad T_k \qquad$ is the period of the wake velocity during phase A or B [s]

$\quad T \qquad$ is the period of the flow velocity [s]

The time shift describes the difference between the period of oscillatory flow with and without current which may be determined from the following relation

$$U_m \sin\left(\omega \Delta t\right) + U_c = 0, \quad \Delta t < 0 \qquad (3.2.44)$$

[Sabag et al. 2000, p1303]

Finally, the local Keulegan-Carpenter number is given by

$$KC_{loc,A} = \frac{U_{m,B} T_A}{D}, \qquad KC_{loc,B} = \frac{U_{m,A} T_B}{D} \qquad (3.2.45)$$

where

$KC_{loc,k}$ is the local Keulegan-Carpenter number during phase A or B [-]

[Sabag et al. 2000, p1304*]

Again, (3.2.45) has been corrected compared to the formula in the original paper since the wake velocity during phase A should be determined by the maximum flow velocity and the local Keulegan-Carpenter number during phase B.

Once the wake velocities during the two phases have been estimated from (3.2.40), a correction needs to be performed. The wake velocities that are used range from $t = 0$ until the first intersection which is indicated with bold curves in Figure 52 for the flow condition example for regular waves with current.
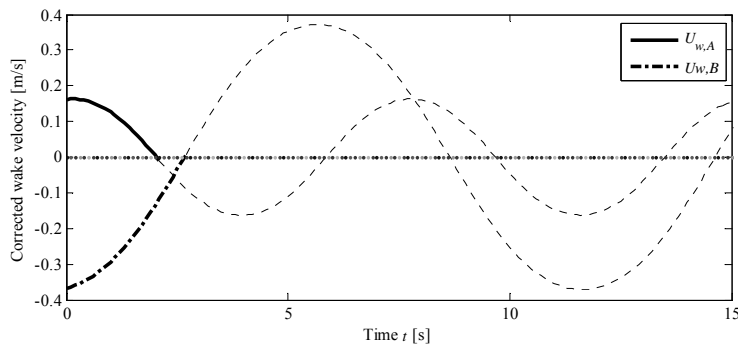

Figure 52: The correction of actual wake velocities for flow condition example R-C.

For the flow condition example for regular waves with current, the following parameters are obtained:

$$U_{\max,A} = 0.67 \tfrac{m}{s}, \ \phi_A = 263.9°, \ \omega_A = 0.82 \tfrac{rad}{s}, \quad KC_A = 4.20, \quad C_{1,A} = 0.53, \quad C_{2,A} = 0.95, \quad n = 1$$

$$U_{\max,B} = 0.33 \tfrac{m}{s}, \ \phi_B = 99.8°, \quad \omega_B = 0.53 \tfrac{rad}{s}, \quad KC_B = 13.36, \quad C_{1,B} = 0.60, \quad C_{2,B} = 0.95$$
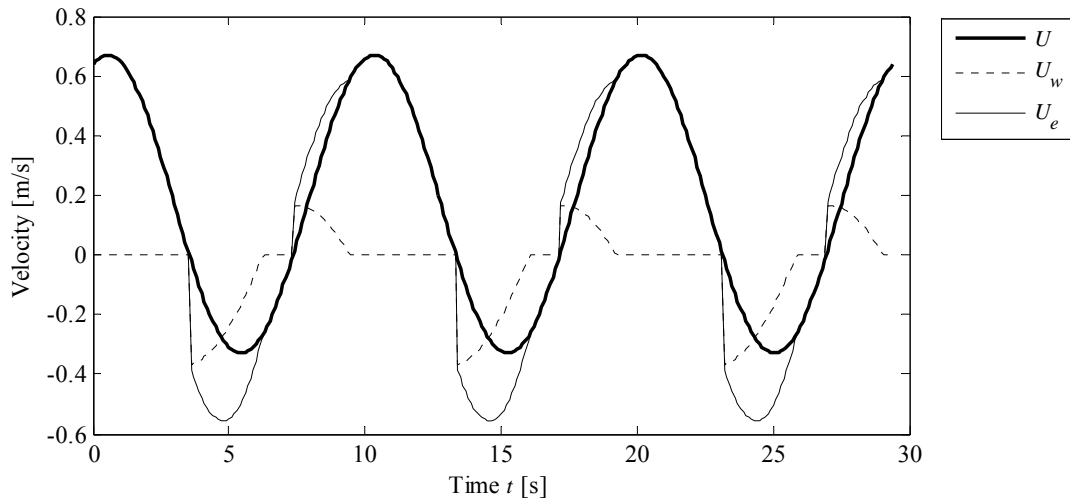
The wake effect is illustrated in Figure 53.

Figure 53: The wake effect in the Wake II Model for flow condition example R-C.

3.2.2.8. The Wake Effect of the Wake II Extended Model

The final Wake Model which is considered is the Wake II Extended Model. This is valid for irregular waves with and without current. The wake velocity for the Wake II Extended Model is for all cases given in the following general form

$$U_w\left(t_j\right) = \frac{1}{2}C_D\,\text{erf}\left(\frac{1}{4}\sqrt{\frac{D}{0.0222\,xC_D}}\right)\cdot U\left(t_j - \tau_j\right), \quad \tau_j \geq 0 \qquad (3.2.46)$$

where

τ_j is the time shift between the ambient and wake flow during the *j*th half-cycle [s]

C_D is an empirical parameter for drag [-]

[Aristodemo et al. 2007, p5*]

It may be noticed that (3.2.46) has been changed compared to the original formula. In the original formula, the actual wake velocity is a function of the ambient flow velocity at a subsequent time, i.e. $U_w\left(t_j\right) \propto U\left(t_j + \tau_j\right)$. This is considered unphysical in the case of irregular waves. Unfortunately, the original formula has been found consistent with wake velocity diagrams in the original paper. For this reason, the implementation according to (3.2.46) which is used in this project cannot be verified against the original paper.

One of the original diagrams is shown in Figure 54 for a case of irregular waves without current that is computed with $D = 0.2191\,\text{m}$, $T_p = 4.65\,\text{s}$, $\bar{U}_m = 0.4\,\frac{\text{m}}{\text{s}}$, $\overline{KC} = 8.53$. It may be seen from Figure 54 that a large flow velocity in half-cycle I yields a minor wake in the subsequent half-cycle II and not a large wake as expected. It may also be observed how the wake velocity according to the original paper depends on the subsequent flow velocity.
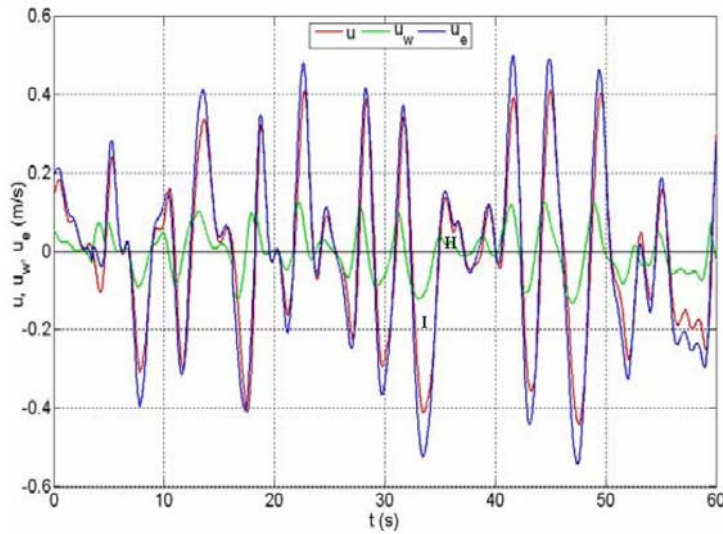
Figure 54: The wake effect in the Wake II Extended Model in the original paper for a flow condition with irregular waves without current. Adopted from [Aristodemo et al. 2007, p8].

The remaining parameters are described in the following. The wake should be computed in the pipe centre which gives

$$x = \frac{D}{2} \tag{3.2.47}$$

[Aristodemo et al. 2007, p4]

The time shift is given by the local half-cycle period and a phase shift

$$\tau_j = T_{loc,j} \frac{\phi_j}{180°} \tag{3.2.48}$$

where

$T_{loc,j}$ is the period of the jth half-cycle of the flow velocity [s]

ϕ_j is the phase shift between the flow and wake velocity during the jth half-cycle [deg]

[Aristodemo et al. 2007, p5]

The half-cycle phase shift depends linearly upon the local Keulegan-Carpenter number

$$\phi_j = a_0 + a_1 KC_{loc,j} \tag{3.2.49}$$

where

a_0, a_1 are empirical parameters [deg]

[Aristodemo et al. 2007, p5]

For the cases without and with current, respectively, the local Keulegan-Carpenter number is defined as

$$KC_{loc,j} = \begin{cases} \dfrac{2 \cdot \left| U_{\max,j} \right| T_{loc,j}}{D} & \text{Without current} \\[4ex] \dfrac{\left| U_{\max,j} \right| T_{loc,j}}{D} & \text{With current} \end{cases}$$

(3.2.50)

where

$KC_{loc,j}$ is the local Keulegan-Carpenter number of the jth half-cycle of the flow velocity [-] [Aristodemo et al. 2006, p3; Aristodemo et al. 2007, p5]

The empirical parameters a_0, a_1, C_D differ greatly for the case with and without current and can be found in Appendix F (Empirical Parameters of Wake Models). The wake effect for the Wake II Extended Model with current is illustrated in Figure 55 for the flow condition example for regular waves with current.
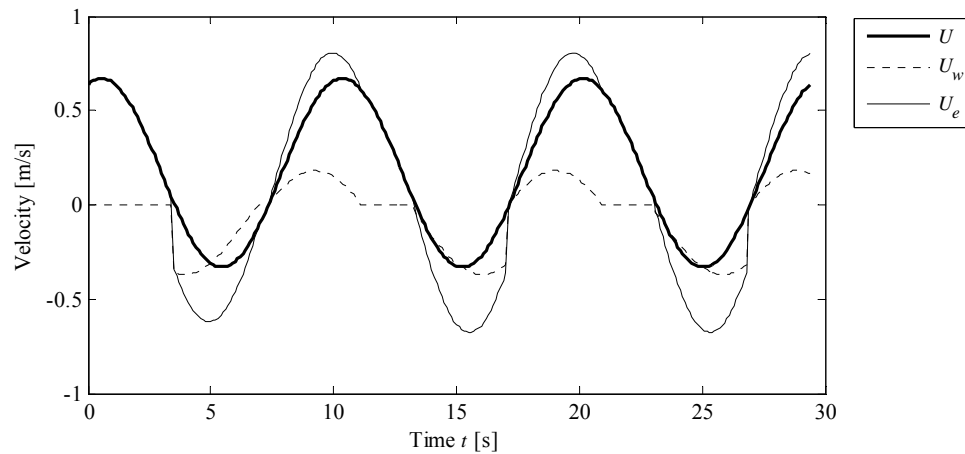

Figure 55: The wake effect in the Wake II Extended Model for flow condition example R-C.

3.2.3 COMPARISONS

In this section, the start-up and wake effect of the Wake Models and the hydrodynamic forces of the Morison Model and the Wake Models are compared. This serves as the basis for a preliminary evaluation of the considered models.

3.2.3.1. The Start-up Effect

As mentioned previously, the start-up effect depends upon empirical parameters that attain different values in the Wake Models. The parameters depend upon the flow condition but are assumed constant throughout the flow regime. The transient parts of the drag and lift force coefficients as functions of the impulse ratio, defined by (3.2.29), are shown in Figure 56 and Figure 57 for the Wake Models. For the variation of the lift force coefficients, measurements are available from the PIT and PFMP [Lambrakos et al. 1987, p128].
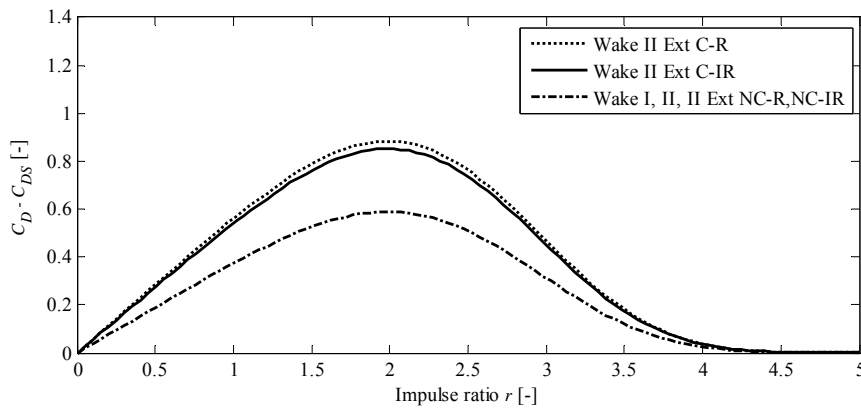
Figure 56: The transient drag force coefficient as function of the impulse ratio for the Wake Models.
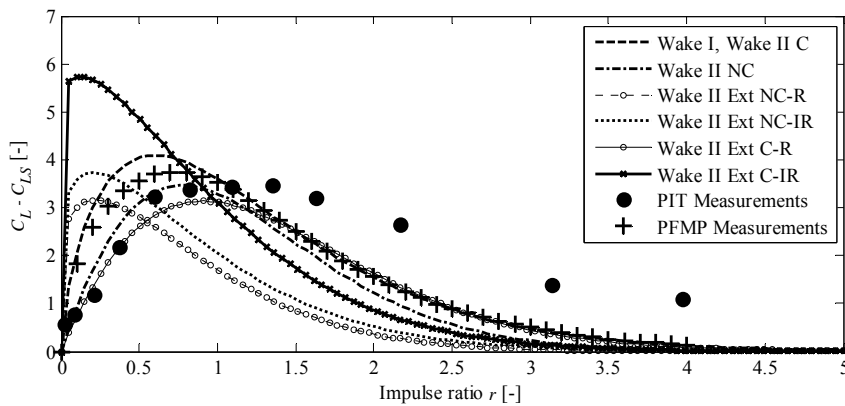

Figure 57: The transient lift force coefficient as function of the impulse ratio for the Wake Models.

From Figure 56, it can be seen that variation of the drag force coefficient is identical for the Wake I, II and II Extended Model without current. By comparison of Figure 56 and Figure 57, it may be seen that the time variation is modelled much larger for the lift force coefficient than the drag force coefficient.

3.2.3.2. The Wake Effect

In this section, the wake effect of the Wake Models is compared. The comparison is based upon the flow condition examples with current as defined in the section on flow condition examples since these are of interest in the dynamic analysis in the project.

Regular Waves and Current

For the flow condition example of regular waves with current, the wake and effective velocities of the Wake Models are shown in Figure 58 and Figure 59.
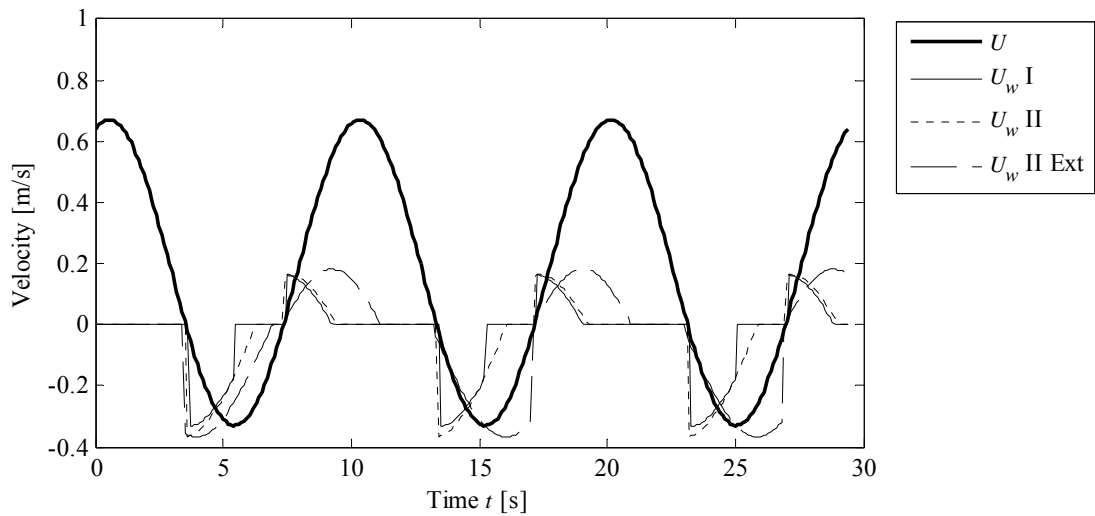
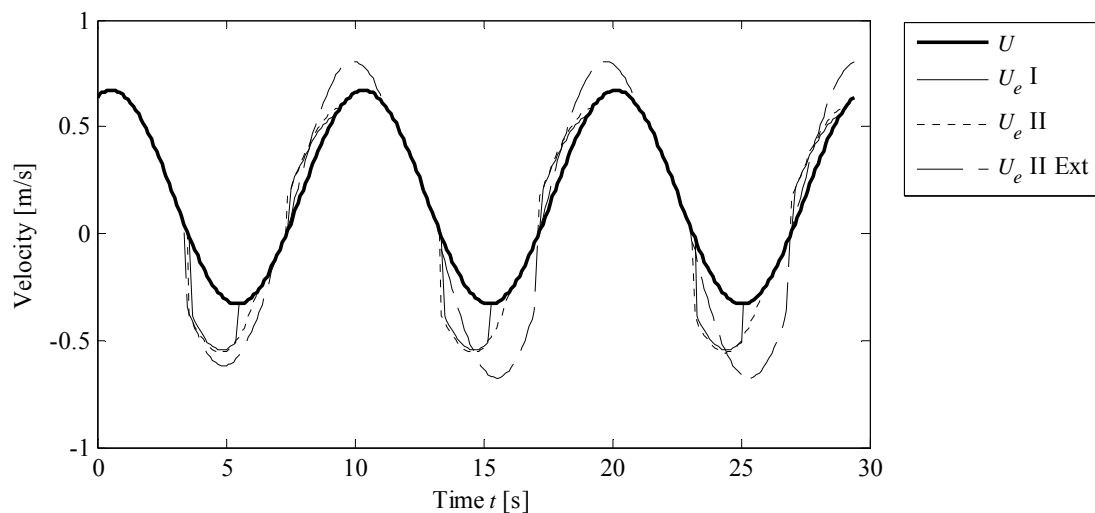*Figure 58: Ambient velocity and wake velocities of Wake Models for flow condition example R-C.*

Figure 59: Ambient velocity and effective velocities of Wake Models for flow condition example R-C.

It may be seen from Figure 58 that all of the Wake Models seem to estimate the same magnitude of the peaks of the wake velocity. Furthermore, the Wake I and II Models predict nearly identical phase and shape of the wake and effective velocity. Since the Wake II Extended Model predicts smaller phase shifts between the wake and flow velocity, its effective velocity is about 20 % greater than those of the other Wake Models for the considered flow condition example.

Irregular Waves and Current

For the flow condition example of irregular waves with current, the wake and effective velocities of the Wake I and II Extended Models are shown in Figure 60 and Figure 61. The two models predict wakes of nearly identical magnitude, but with different shapes and phases as in the case of regular waves with current.
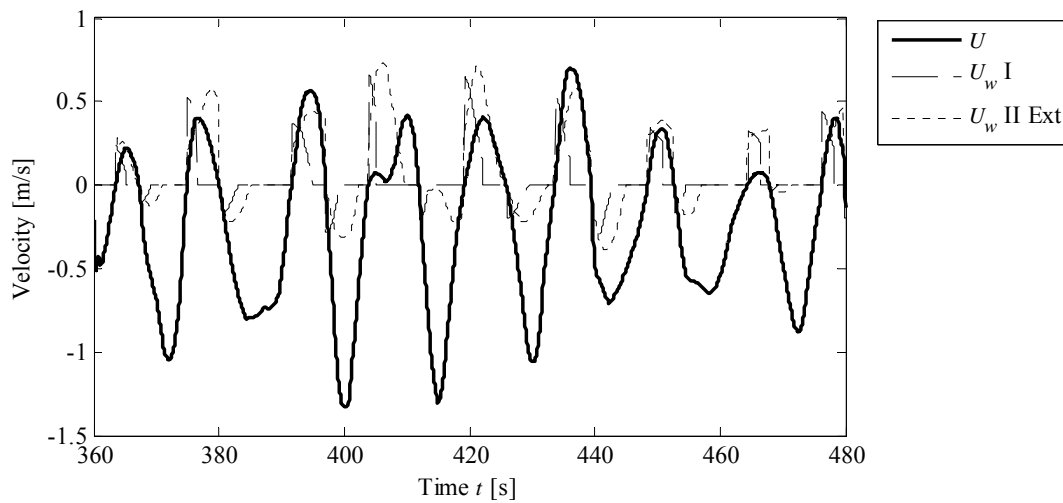
Figure 60: Ambient and wake velocities of Wake Models for flow condition example IR-C.
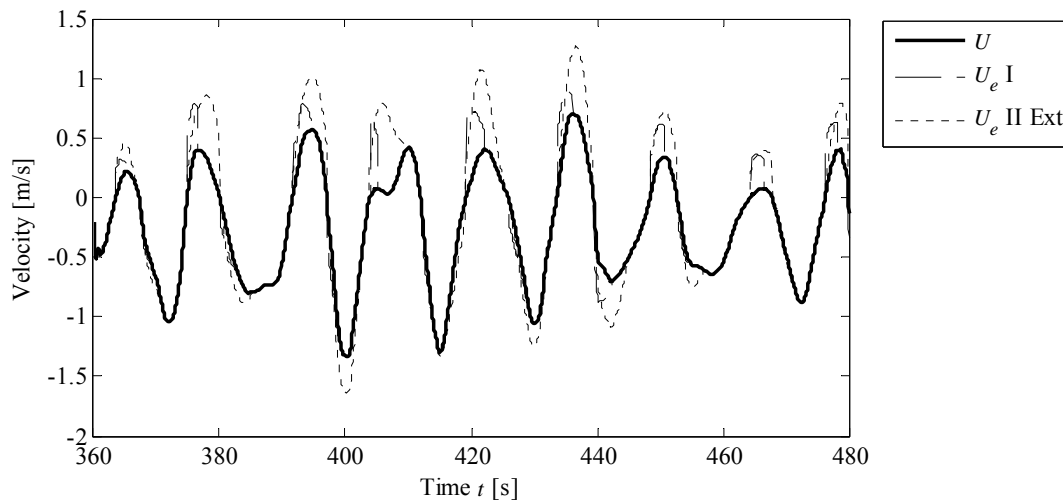

Figure 61: Ambient and effective velocities of Wake Models for flow condition example IR-C.

3.2.3.3. Hydrodynamic Forces

For the comparison of hydrodynamic forces of the Morison Model and the Wake Models, the flow condition examples with current are considered. For the Wake Models, the wake acceleration is determined by numerical differentiation of the wake velocity where the momentan acceleration or deceleration at the birth and death of a sudden wake has been nullified. The density of water is taken as $\rho_w = 1025 \frac{\text{kg}}{\text{m}^3}$.

Regular Waves and Current

For regular waves and current, the Morison Model is computed with $C_M = 3$, $C_D = 2$, $C_L = 2.7$ whereas the parameters of the Wake Models are given in Appendix F (Empirical Parameters of

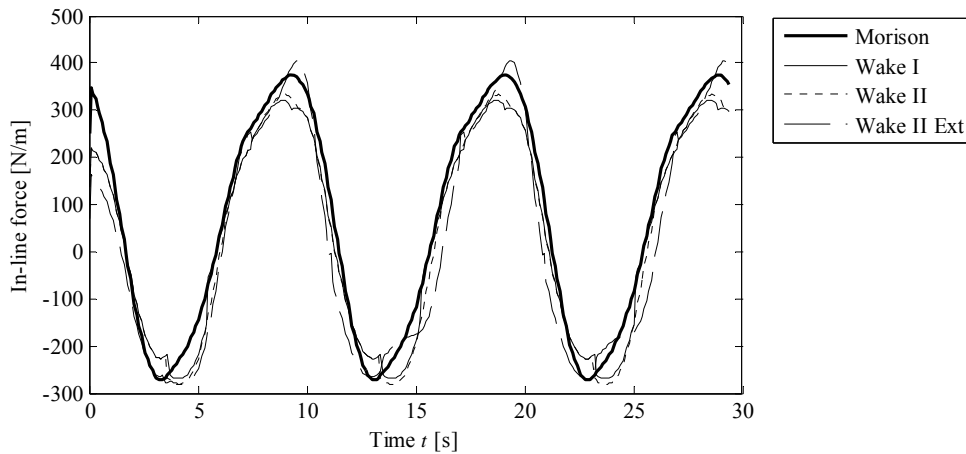Wake Models). The in-line and cross-flow force history is shown in Figure 62 and Figure 63, respectively.

Figure 62: In-line force history of Morison and Wake Models for flow condition example R-C.
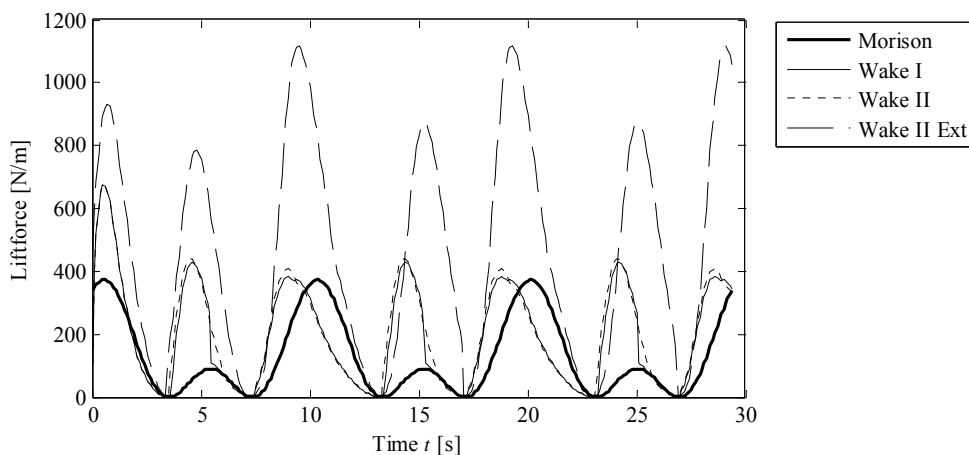

Figure 63: Cross-flow force history of Morison and Wake Models for flow condition example R-C.

It may be seen from Figure 62 that all the models provide nearly identical in-line forces. Figure 63 shows that the cross-flow force history of the Wake I and II Models is nearly identical and has considerably smaller peaks than the Wake II Extended Model. The cross-flow force history of the Morison Model is distinguished from the Wake Models by having a different phase of the primary cycle and a considerably lower peak of the second cycle.

Irregular Waves and Current

For the flow condition example of irregular waves and current, force measurements are provided from the PFMP, along with computations with the Morison and Wake I Model. [Lambrakos et al. 1987, p129-130].

In this section, the Morison and Wake I Model are each evaluated for two sets of force coefficients. The cases are shown in Table 14 where the remaining coefficients of the Wake I Model are given in Appendix F (Empirical Parameters of Wake Models). The cases are described below.

Table 14: Calibration basis and values of force coefficients for flow condition example IR-C. All coefficients are dimensionless.

Case	Force model	Calibration basis	In-line force coefficients			Lift force coefficient
			C_A	C_M	C_D	C_L
A	Morison Model	Computed Morison forces [Lambrakos et al. 1987, p129-130]	-	0.87	0.85	1.34
	Wake I Model	Appendix F (Empirical Parameters of Wake Models)	0.25	2.5	1.1 - 1.7 $(C_{DS}=1.1, \ \alpha_D=0.38)$	0.8 - 4.9 $(C_{LS}=0.8, \ \alpha_L=9.8)$
B	Morison Model	Measurements [Lambrakos et al. 1987, p129-130]	-	1.70	0.60	0.60
	Wake I Model	Measurements [Lambrakos et al. 1987, p129-130]	0.46	0.87	0.37 - 0.59 $(C_{DS}=0.37, \ \alpha_D=0.145)$	0.37 - 1.35 $(C_{LS}=0.37, \ \alpha_L=2.35)$

In case A, the force coefficients of the Morison Model have been fitted to the computed Morison forces that appear in the original paper [Lambrakos et al. 1987, p129-130]. The computed Morison forces of the original paper have been fitted to peak forces of several records from the PFMP which appear to have higher peaks than those in the flow condition example IR-C. The coefficients of the Wake I Model are evaluated at their default values which are given in Appendix F (Empirical Parameters of Wake Models). In case B, the force coefficients of the Morison and Wake I Model are fitted to the force measurements of the flow condition example IR-C alone.

The in-line and cross-flow force history for the cases are shown in Figure 64-Figure 67. Furthermore, single-sided spectrums of the force amplitudes are shown for case B in Figure 68 and Figure 69 based upon Fast Fourier Transforms of the force histories. The figures are commented below.
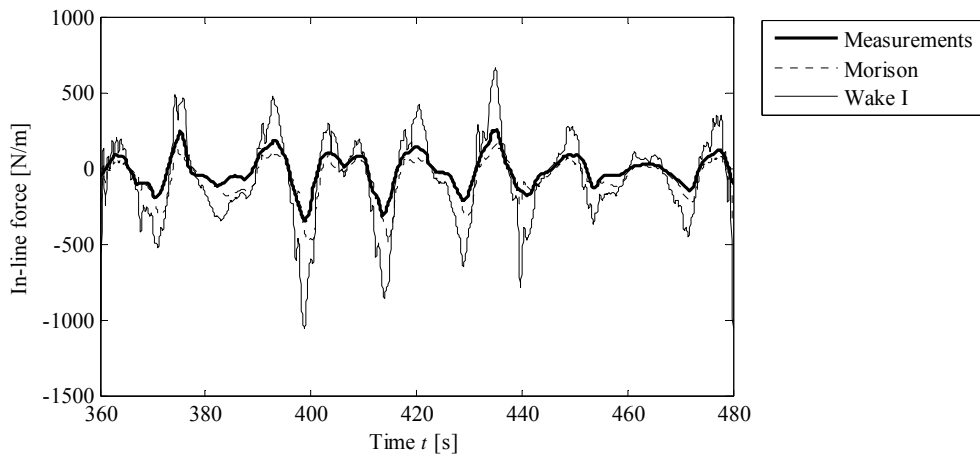
Figure 64: In-line force history of the Morison and Wake I Model for case A and flow condition example IR-C.
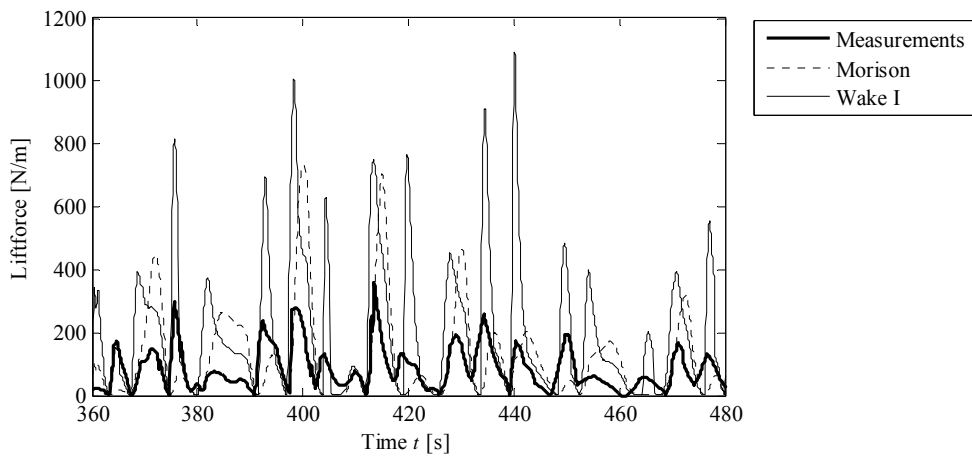

Figure 65: Cross-flow force history of the Morison and Wake I Model for case A and flow condition example IR-C.
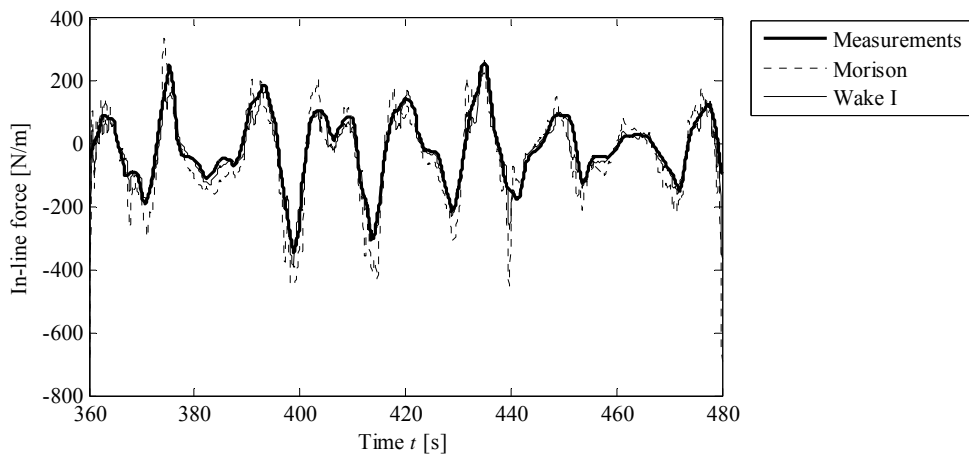

Figure 66: In-line force history of the Morison and Wake I Model for case B and flow condition example IR-C.
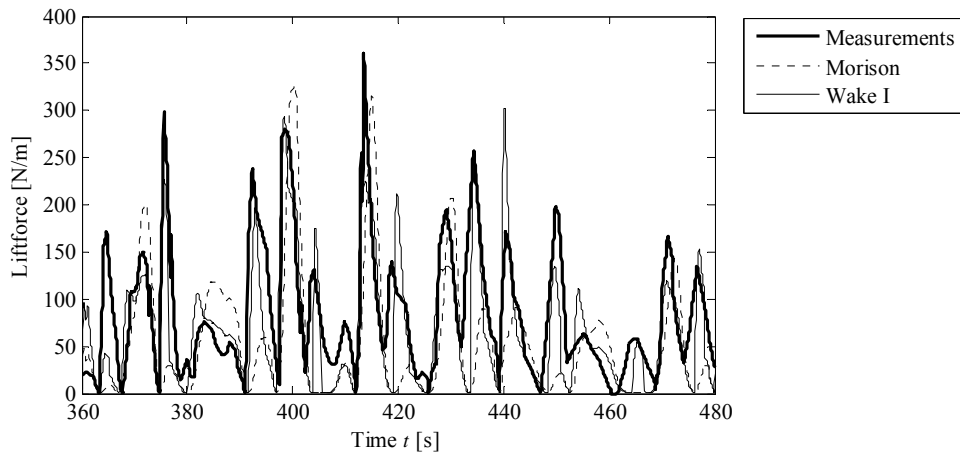
Figure 67: Cross-flow force history of the Morison and Wake I Model for case B and flow condition example IR-C.
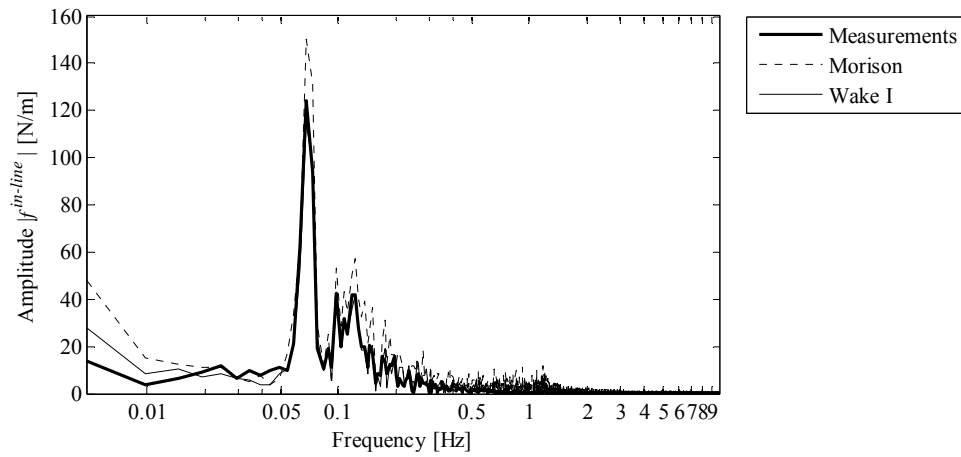
Figure 68: In-line force amplitude single-sided spectrum of the Morison and Wake I Model for case B and flow condition example IR-C.
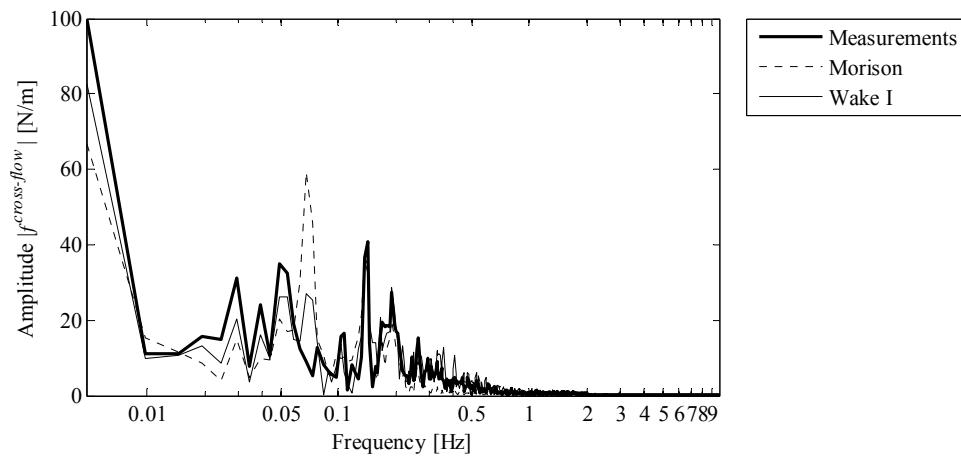
Figure 69: Cross-flow force amplitude single-sided spectrum of the Morison and Wake I Model for case B and flow condition example IR-C.

Several observations may be obtained from Figure 64 and Figure 65. First, the in-line and cross-flow forces of the Morison Model are overestimated compared to the measurements. This must be due to the fact that the force coefficients for the Morison Model have been fitted to peak values that exceed those of Figure 64 and Figure 65. The overestimation is greatest for the cross-flow force where the computed Morison cross-flow force may be more than 200 % greater than the measured cross-flow force.

When the force coefficients of the Morison Model are fitted to the maximum forces of the flow condition example IR-C alone, the phase and shape of the forces are predicted well for the in-line forces, but still poorly for the cross-flow forces. This may be seen by comparison of Figure 66-Figure 69.

Secondly, it may be seen that the Wake I Model with default empirical parameters has a poor prediction of the in-line and cross-flow force history. The cross-flow force is overestimated by more than 300 % compared to the measurements. In contrast, the model is able to predict the peaks, phase and shape of the in-line and cross-flow force when the parameters are fitted to the measurements. Compared to the Morison Model, the Wake I Model provides an improved description of the cross-flow force which is also evident from the cross-flow force spectrum in Figure 69.

Lastly, it may be seen from Figure 66 that the average in-line force is non-zero and nearly zero according to the Morison Model and measurements, respectively, which agrees with the results in the original paper. This attribute of the measurements for current-wave ratios below 0.5 may be explained by the paradox that although the presence of current increases the wake that is generated in the downstream direction, it is counteracted by the same wake when the ambient flow reverses. [Lambrakos et al. 1987, p122]

3.2.4 EVALUATION

It is concluded that the Morison Model can predict the peaks and the time-variation of the in-line force fairly accurately for pipelines above and upon the seabed. However, it requires an accurate determination of the corresponding force coefficients.

The Morison Model provides a poor prediction of the time-variation of the cross-flow force. In contrast, a much better prediction is provided for a pipeline above the seabed by the extended Morison Model that includes the effects of vortex shedding. If lock-in occurs, the cross-flow force oscillates at the lowest vertical eigenfrequency.

For a pipeline upon the seabed, a better description of the cross-flow force in comparison with the Morison Model is obtained by the Wake Models. The most versatile Wake Model appears to be the Wake I Model which has been calibrated against force measurements from the Pipeline Field Measurement Program. The Wake I Model is provided with a default set of empirical coefficients for all flow conditions but it appears to have been calibrated to provide a conservative fit. Due to the lack of measurements from the field location, the Wake I Model with the default set of coefficients is

chosen for the analyses for irregular waves. The Wake II and Wake II Extended Models have not been considered further due to limitations in their theoretical background or calibration basis.

Part 4

Soil Mechanics

The theory behind analytical modelling of soil springs has been studied. Analytical and numerical load-displacement curves have been compared. The latter has been made in Plaxis 8.2 which is a commercial geotechnical FEM-program.

The concept of transmitting boundary conditions has been discussed considering the modelling of a finite soil domain. Transmitting boundary elements (TBE) are developed for a plane, straight Bernoulli-Euler beam with constant axial force upon a Winkler foundation. An analytical formulation of TBE is derived and cast into an element formulation to be used in the finite element modelling of the pipeline free-span.

The dynamic response of the soil has been studied with respect to the phenomenon of liquefaction. An overview of the theory of liquefaction is given and the liquefaction problem is evaluated considering a pipeline free-span.

4.1 SOIL SPRINGS

To make a Winkler model of a pipeline free-span, the soil surrounding the pipeline is modelled as springs. An analytical approach to spring modelling of the soil will be described in this chapter with general reference to [LICengineering 2005]. In [LICengineering 2005], assumptions and simplifications have been made to make load-displacement curves based on simple analytical models. These assumptions have significant impact on the shape of the load-displacement curves and this chapter will clarify whether the analytically determined load-displacement curves are in agreement with the shape of numerically determined load-displacement curves. The numerical models are made in Plaxis which is a commercial geotechnical non-linear FEM-program.

In principle, the soil should be modelled with springs in various directions. The first assumption is that this can be simplified to springs that act independently in three directions. Movements in various directions are described by interaction between the following springs:

- Axial springs
- Vertical springs
- Lateral springs

To clarify whether the interaction between the springs gives satisfactory results when the pipe moves in various directions, numerical load-displacement curves have been made for diagonal movement of the pipe.

Structural and Soil Data

In order to compare the analytically and numerically determined load-displacement curves, the following conditions for pipeline and soil are chosen. Table 15 shows the relevant structural data determined for a water-filled 20" Multiphase Pipeline where the pipeline data is taken from Chapter 1.1 (Design Conditions).

Table 15: Structural data for the pipeline.

Parameter	Symbol	Value	Unit
Submerged pipe weight	W_{pipe}	2.607	kN/m
Diameter incl. coating	D	0.620	m
Trenching depth	d_b	1.620	m

The soil is assumed to be cohesionless. This is convenient for the analytical spring models and a reasonable assumption for typical marine soil. A small value of cohesion ($c = 0.2\,\text{kPa}$) is applied in

the numerical models for the sake of stability. Parametric analysis has been made to verify that this small value of cohesion does not have significant impact on the load-displacement curves for any of the failure modes. Parametric analysis has also been made for Poisson's ratio for values in the range of 0.2-0.4. The stiffness of the soil is assumed to be relatively low. The effect of this assumption will be discussed where this has a significant impact on the results. The analyses are performed with three different values of the friction angle to compare its effect on the spring models. All calculations are based on associated plasticity which means that the angle of friction and the angle of dilatation have equal values. Table 16 shows the soil conditions implemented in the following analyses.

Table 16: Soil conditions.

Parameter	Symbol	Sand	Unit
Material model	Model	Mohr-Coulomb	-
Type of analysis	Type	Drained	-
Saturated soil weight	γ_{sat}	20	kN/m^3
Effective soil weight	γ'	10	kN/m^3
Young's modulus	E	10 000	kPa
Poisson's ratio	ν	0.3	-
Cohesion	c	0 (0.2)	kPa
Angle of friction	φ'	25,30,35	Deg
Angle of dilation	ψ	25,30,35	Deg
Pipe-soil friction	k, R_{inter}	0.7	-

4.1.1   AXIAL SPRINGS

The axial springs are modelled to determine the resistance of the soil when the free-span of the pipe is affected by hydrodynamic loads which cause axial forces to develop in the pipe when large deformations occur. The axial stiffness is determined by considering two failure modes as the pipeline strains longitudinally:

- **O-failure:** This failure mode occurs when the soil fails around the entire perimeter of the pipe.
- **U-failure:** This failure mode occurs when the soil fails along the bottom pipe perimeter and vertically up to the seabed. This is likely to dominate when the trenching depth is relatively small.

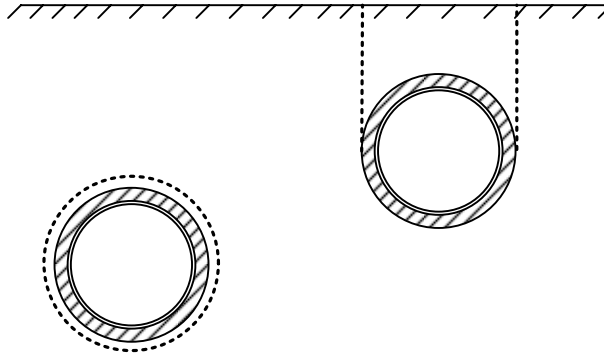Figure 70 shows the two axial failure modes.

Figure 70: Axial failure modes: O- failure (left) and U-failure (right).

Since the failure modes will be determined by assuming kinematically admissible but not statically admissible failure mode, the soil will in both situations pose too strong behaviour compared to the unknown exact solution. Therefore, the maximum axial friction force is determined as the minimum value of the friction force from O-failure or U-failure, i.e.

$$f_{axial} = \min \begin{cases} f_{O-failure} \\ f_{U-failure} \end{cases} \tag{4.1.1}$$

where

f_{axial} is the maximum axial friction force [kN/m]

$f_{O-failure}$ is the friction force during O-failure [kN/m]

$f_{U-failure}$ is the friction force during U-failure [kN/m]

Each failure mode is explained in detail in the following. The axial springs will not be verified by numerical analysis. The analytical calculations of axial springs are performed in Matlab and can be found in [DVD/Soil Springs/axial_spring.m].

4.1.1.1. O-failure

In this section, the friction force for the O-failure is determined analytically. Figure 71 (left) shows the variation of the effective normal stress along the failure line which develops around the pipeline perimeter. Figure 71 (right) shows a Mohr's diagram of the effective stress state at a failure point.
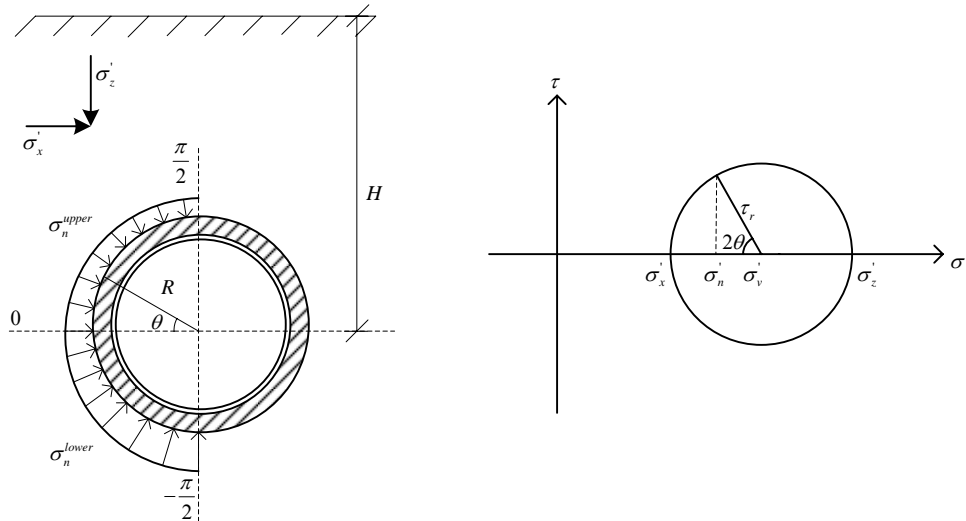
Figure 71: Effective normal stress variation for O-failure (left) and Mohr's diagram of effective stress state at a failure point (right)

The axial friction force per unit length is determined by polar integration of the effective normal stress around the upper and bottom pipe perimeter and exploiting vertical symmetry

$$f_{O-failure} = f_{O-failure}^{upper} + f_{O-failure}^{lower}, \qquad \begin{aligned} f_{O-failure}^{upper} &= 2\int_{0}^{\pi/2} \mu\sigma_n' R\,d\theta \\ f_{O-failure}^{lower} &= 2\int_{-\pi/2}^{0} \mu\sigma_n' R\,d\theta \end{aligned} \qquad (4.1.2)$$

where

μ is the friction coefficient between pipe and soil, determined as $\mu = \tan(k\varphi')$ [-]

k is the friction factor [-]

σ_n' is the effective normal stress at a failure point [kPa]

R is the outer radius of the pipe, including coating [m]

θ is the angle between horizontal and a failure point [rad]

Trigonometric considerations of Figure 71 (right) show that a failure point satisfies the following criterion which determines the effective normal stress

$$\sigma_n' = \sigma_v' - \tau_r \cos 2\theta \qquad (4.1.3)$$

where

σ_v' is the effective mean stress [kPa]

τ_r is the radius of Mohr's circle [kPa]

The effective mean stress is calculated as

$$\sigma_v' = \frac{1}{2}(\sigma_z' + \sigma_x') \qquad (4.1.4)$$

where

σ_z' is the effective vertical stress [kPa]

$\sigma_x{}'$ is the effective horizontal stress [kPa]

The radius in Mohr's circle is calculated as

$$\tau_r = \frac{1}{2}\left(\sigma_z{}' - \sigma_x{}'\right) \tag{4.1.5}$$

The effective horizontal stress is approximated from a state of rest which is a fair assumption for normally consolidated friction soil when the pipe strains axially

$$\sigma_x{}' = k_0 \sigma_z{}' \tag{4.1.6}$$

where

k_0 is the soil pressure coefficient for friction soil at rest, $k_0 = 1 - \sin\varphi'$ [-]

φ' is the effective angle of friction [deg]

[Ovesen et al. 2007, pp274-275]

The vertical stress along the perimeter for the upper quarter of the submerged pipeline is calculated by the submerged weight of the soil

$$\sigma_z^{upper}{}' = \gamma'\left(H - R\sin\theta\right), \qquad\qquad 0 < \theta < \pi/2 \tag{4.1.7}$$

where

γ' is the submerged weight of the soil [kN/m^3]

H is the distance between the seabed and the centre of the pipe [m]

The weight of the pipe is assumed to contribute to the vertical stresses on the lower part of the pipe. The reuction from the soil suppressed by the pipe is taken into account. Considering this, the vertical stresses for the lower part of the soil is assumed to be

$$\sigma_z^{lower}{}' = \gamma'H - R\sin\theta\cdot\left(2\gamma_p' - \gamma'\right), \qquad -\pi/2 < \theta < 0 \tag{4.1.8}$$

where

γ_p' is the equivalent weight of the submerged pipe per unit length [kN/m^3]

The equivalent weight of the submerged pipe is

$$\gamma_p' = \frac{W_{pipe}}{\pi R^2} \tag{4.1.9}$$

where

W_{pipe} is the weight of the submerged pipe per unit length [kN/m]

The vertical stresses along the pipe are now defined. By use of (4.1.3)-(4.1.9) in (4.1.2), the friction force on the upper and lower part of the pipe, respectively, is given as

$$f_{O-failure}^{upper} = \mu\cdot\left(\frac{\pi}{2}\gamma'RH\left(1+k_0\right) - \frac{2}{3}\left(2+k_0\right)\right) \tag{4.1.10}$$

113

$$f_{O-failure}^{lower} = \mu \cdot \left(\frac{\pi}{2} \gamma' R H \left(1 + k_0\right) + \frac{4}{3\pi} W_{pipe} \left(2 + k_0\right) - \frac{2}{3} \gamma' R^2 \left(2 + k_0\right) \right) \qquad (4.1.11)$$

By combination of (4.1.2), (4.1.10) and (4.1.11), the friction force on the entire pipe for O-failure is

$$f_{O-failure} = \mu \cdot \left(\pi \gamma' R H \left(1 + k_0\right) + \frac{4}{3\pi} W_{pipe} \left(2 + k_0\right) - \frac{4}{3} \gamma' R^2 \left(2 + k_0\right) \right) \qquad (4.1.12)$$

The derivation of (4.1.13) and (4.1.14) can be found in [DVD/Soil Springs/axial_spring.mws].

4.1.1.2. U-failure

In this section, the friction force for U-failure is determined analytically. The failure mode is shown in Figure 72 where the effective normal stresses along the failure lines have also been sketched.
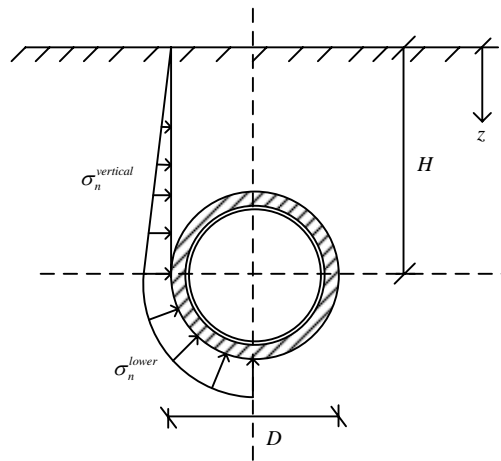

Figure 72: Effective normal stresses along failure lines for U-failure.

The friction force during U-failure is determined as

$$f_{U-failure} = f_{O-failure}^{lower} + f_{U-failure}^{upper} \qquad (4.1.15)$$

The friction force for the lower part of the pipe is identical to the friction force for O-failure in (4.1.11). The effective normal stresses along the vertical failure line is defined by

$$\sigma_n^{U-failure}{}' = k_0 \gamma' z \qquad (4.1.16)$$

where

z is the depth of a failure point from the seabed [m]

The friction force above the centreline of the pipe is determined by integration of normal stresses along the vertical failure lines and multiplying by $\tan(\varphi')$

$$f_{U-failure}^{upper} = 2 \tan \varphi' \cdot \int_0^H \sigma_n^{U-failure}{}' dz = \gamma' k_0 H^2 \tan \varphi' \qquad (4.1.17)$$

By inserting (4.1.11) and (4.1.17) into (4.1.15), the friction force for U-failure is

$$f_{U-failure} = \mu\left(\frac{\pi}{2}\gamma'RH\left(1+k_0\right)+\frac{4}{3\pi}W_{pipe}\left(2+k_0\right)-\frac{2}{3}\gamma'R^2\left(2+k_0\right)\right)+\gamma'k_0H^2\tan\varphi' \quad (4.1.18)$$

4.1.1.3. Axial Load-Displacement Curve

Regardless of the failure mode, the maximum axial friction force is assumed to be established at an axial displacement

$$\delta_{axial} = 2.5\,\text{mm} \quad (4.1.19)$$

When defining the axial load-displacement curve, the soil is assumed to behave as a linear elastic-ideal plastic material with identical strength for both positive and negative values of pipe displacements. The magnitude of the axial resistance and the axial load-displacement curves are shown in Figure 73 for the conditions mentioned in Table 15 and Table 16. The maximum axial resistances have been determined for O-failure since U-failure is only governing at a trenching depth identical to 0-0.4 m depending on the angle of friction of soil.
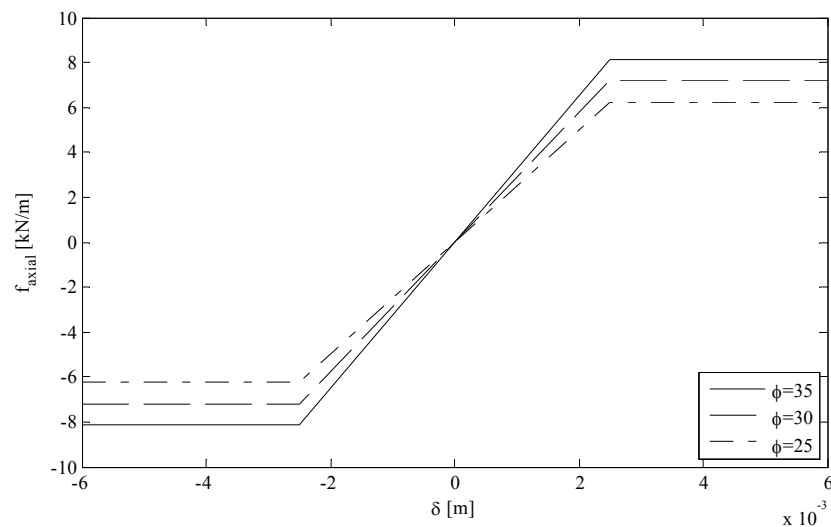

Figure 73: Load-displacement curve for axial displacement of pipe.

4.1.2 VERTICAL SPRINGS

The vertical springs are modelled to determine the resistance of the soil when the free-span of the pipe is affected by the cross-flow hydrodynamic force. The vertical springs are determined by calculating load-displacement curves for upward and downward movements of the pipe, respectively. Analytical and numerical models have been made for each of these two movements. The analytical calculations of vertical springs are made in Matlab and can be found in [DVD/Soil Springs/vertical_spring.m].

4.1.2.1. Downward Spring

Analytical Spring Model

The analytical load-displacement curve is based upon Terzaghi's formulation for bearing capacity of a strip foundation of infinite length with a central vertical load. In cohesionless soil, Terzaghi's formulation for maximum bearing capacity for a buried pipeline can be written as

$$f_{downward} = D \cdot \left(\frac{1}{2} \gamma' D N_\gamma + \gamma' d_b N_q \right) \qquad (4.1.20)$$

where

   D is the outer pipe diameter including coating [m]

   d_b is the trenching depth [m]

   N_γ, N_q are factors for bearing capacity [-]

[Ovesen et al. 2007, p223]

The factors for bearing capacity are determined respectively as

$$N_\gamma = \frac{1}{4}\left(N_q - 1\right)\cos\left(\varphi'\right)^{\frac{3}{2}} \qquad (4.1.21)$$

$$N_q = e^{\pi \tan \varphi'} \frac{1 + \sin \varphi'}{1 - \sin \varphi'} \qquad (4.1.22)$$

[Ovesen et al. 2007, p224]

The factors for the bearing capacity are based upon static or kinematic admissible failure modes which are shown in Figure 74. It is not possible to determine an exact value for N_γ that satisfies the criteria for a kinematic and static admissible failure mode which means that the formulation in (4.1.20) is only an approximation to the bearing capacity.
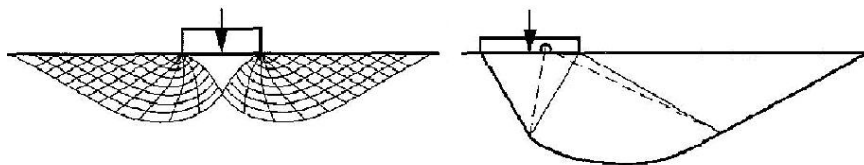

Figure 74: Static admissible failure mode (left) and kinematic admissible failure mode (right). [Ovesen et al. 2007, p223]

The maximum downward resistance is assumed to occur at a displacement equal to 10% of the pipe diameter, i.e.

$$\delta_{downward} = 0.1D \qquad (4.1.23)$$

In the analytical downward load-displacement curves, it is assumed that the soil behaves as a linear elastic-ideal plastic material.

Numerical Model

A pipeline buried in soil is modelled in Plaxis. The pipeline is applied a displacement downward in order to calculate the downward load-displacement curve. The numerical model can be found in [DVD/Soil Springs/downwardspring.plx]. Figure 75 shows the shear strain increments in the soil just before soil collapse.
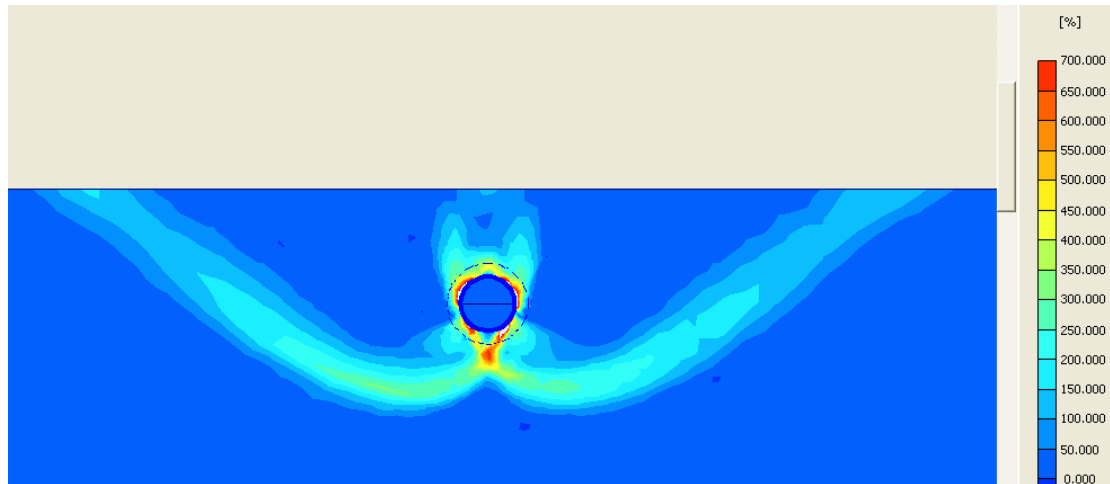

Figure 75: Shear strain increments in soil for downward displacement of pipeline.

Figure 75 verifies the failure modes assumed in the analytical analysis by showing that the failure lines in the soil have a shape like a logarithmic spiral.

Load-Displacement Curves - Downward

In Figure 76, the analytical and numerical load-displacement curves are shown for comparison. The conditions for the pipeline and the soil in each analysis are given in Table 15 and Table 16.
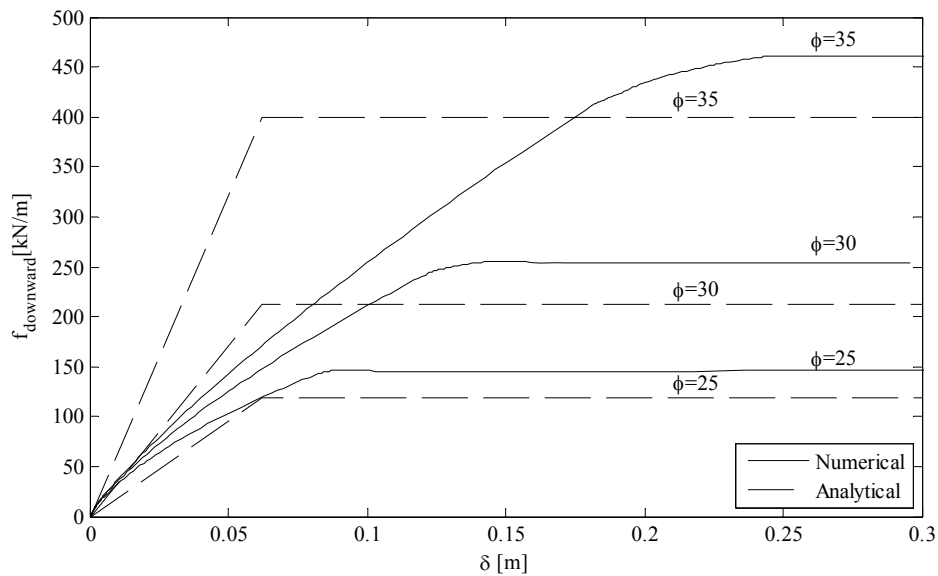
Figure 76: Load-displacement curves for downward displacement of pipeline.

Figure 76 shows relatively good agreement between the analytical and numerical load-displacements curves. The maximum resistances determined in the two types of analyses are of the same magnitude for all three values of φ' and the analytically determined resistances are conservative. The displacement of the numerically determined curves depends on the stiffness E of the soil. If E is increased, the slope of the first part of the curves increases. This means that the assumption made in the analytical solution that maximum resistance occurs at a displacement $\delta = 0.1D$ is inaccurate because the stiffness of the soil is not taken into account. In this case, the springs determined for higher values of φ' become too stiff. It is noticed that soil with a high value of φ' will in most cases tend to be more stiff than soil with low values of φ'. This tendency will decrease the difference between the analytical and numerical load-displacement curves.

4.1.2.2. Upward Spring

Analytical Spring Model

The vertical resistance per unit length is determined for three states of upward displacement of the pipe. State 1 is when the pipe is applied an initial displacement which is assumed to generate a resistance identical to the sum of the weight of the pipe and the weight of the soil above the pipe. State 2 is when the pipeline has been displaced enough to activate diagonal failure lines which provide a resistance corresponding to the weight of the cone between the failure lines above the pipeline. State 3 is when the pipe is assumed to have displaced through the seabed. At this state, the upward resistance equals the weight of the pipe. In Figure 77, the soil areas that contribute to the upward resistance are shown.
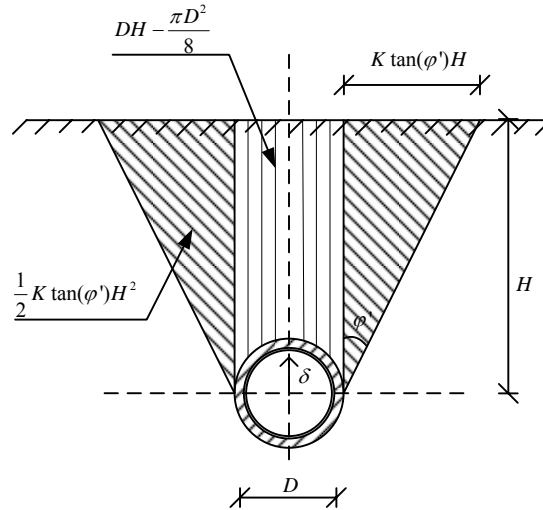
Figure 77: Soil areas that contribute to upward resistance.

The resistance for state 1 can be calculated as

$$f_{upward.1} = W_{pipe} + W_{soil} \qquad (4.1.24)$$

The weight of the soil above the pipe is

$$W_{soil} = \gamma' \left(H D - \frac{\pi}{8} D^2 \right) \qquad (4.1.25)$$

For convenience, the corresponding initial displacement is assumed to be zero

$$\delta_{upward.1} = 0 \qquad (4.1.26)$$

In order to calculate the upward resistance of state 2, the principle of virtual displacement can be formulated for the situation. Because associated plasticity is assumed, the internal work can be neglected. This means that only the weight of the soil and the pipeline contributes to the resistance. The diagonal failure lines are assumed to occur at an angle equal to φ' from the vertical axis. The resistance at state 2 can be written as

$$f_{upward.2} = W_{pipe} + \gamma' H D \left(1 - \frac{\pi D}{8H} + K \tan \varphi' \frac{H}{D} \right) \qquad (4.1.27)$$

where
  K is a factor, $K = 1$ for loose sand [-]

The displacement necessary to generate the resistance at state 2 is assumed to be the minimum of the following empirical values

$$\delta_{upward.2} = \min \begin{cases} \left(0.02 + 0.008 \dfrac{H}{D} \right) \cdot D \\ 0.1D \end{cases} \qquad (4.1.28)$$

The resistance of state 3 is assumed to be

$$f_{upward.3} = W_{pipe} \tag{4.1.29}$$

The pipe has to move all the way up to the seabed to reach state 3. This means that the displacement for this state has to be

$$\delta_{upward.3} = H \tag{4.1.30}$$

To give an overview of the resistance in the different states, the general shape of the analytically determined upward load-displacement curve is shown in Figure 78.
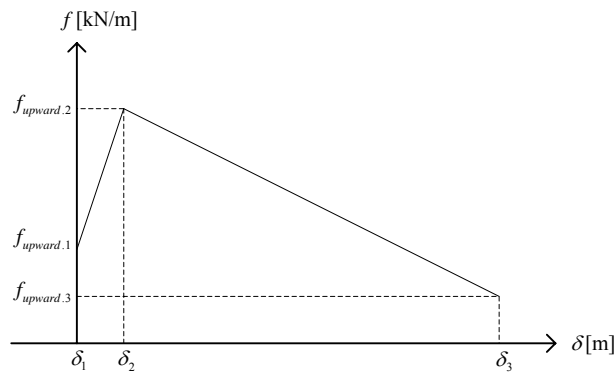

Figure 78: General shape of analytical load-displacement curve for upward displacement of the pipeline.

Numerical Model

A numerical model is made of the buried pipeline in the same way as the case for the downward spring. The numerical model can be found in [DVD/Soil Springs/upwardspring.plx]. The pipeline is applied a displacement in upward direction. In Figure 79, the shear strain increments are shown just before soil collapse.
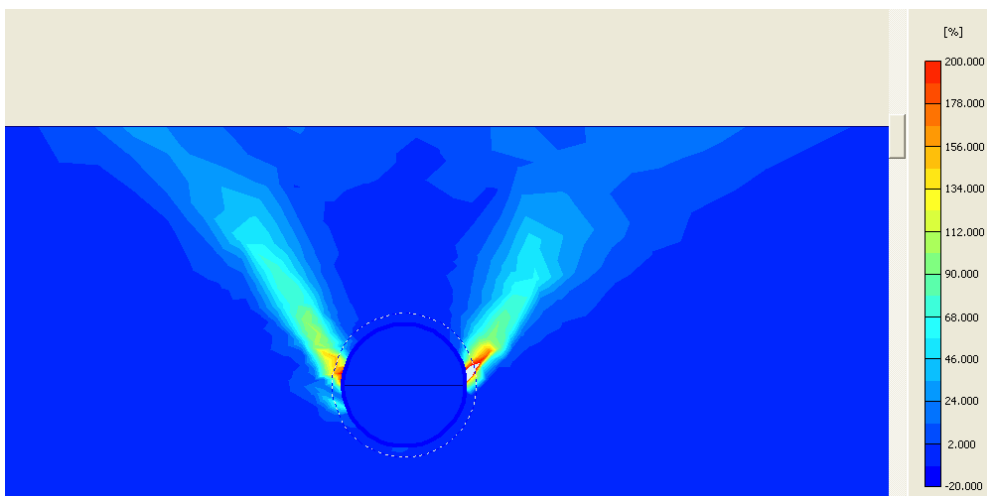

Figure 79: Shear strain increments in soil for upward displacement of pipeline.

Figure 79 shows that diagonal failure lines occur in the numerical analysis which is in good agreement with the assumed failure lines made for state 2 in the analytical analysis. However, the pipe is not allowed to move through the soil in the numerical model as assumed in state 3 in the analytical analysis. In Plaxis, soil collapse will happen before the pipe reaches the seabed. The result of this difference is discussed in the following section.

Load-Displacement Curves - Upward

Figure 80 shows the analytical and numerical load-displacement curves. Since soil collapse occurs in the numerical model before the pipe reaches the seabed, only the first part of the load-displacement curves are shown. The conditions for the pipeline and the soil in each analysis are given in Table 15 and Table 16.
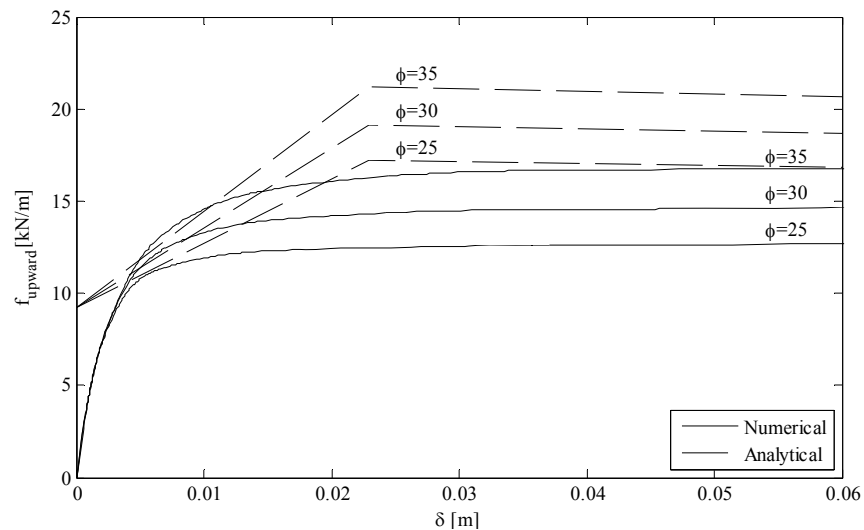
Figure 80: Load-displacement curves for upward displacement of pipeline.

It is seen from Figure 80 that the maximum resistances in the analytical and numerical models are in the same magnitude for all three values of φ'. In contrast to the downward resistance, the analytically determined upward resistances seem to be overestimated. In the first part of the curves, there seems to be large disagreement between analytical and numerical models. The assumption of a resistance at a displacement equal to zero in the analytical analyses seems to be in conflict with what happens in the numerical analyses.

In the numerical model, the soil underneath the pipe expands when the pipe is applied an upward motion. This expansion reduces the resistance for a given motion and a slope will occur in the numerical solution instead of the vertical line determined in the analytical solution. Although the basic assumptions for the two models are different, the stiffness for the two models are in the same ratio with high stiffness in the first part of the curves and rapidly decreasing stiffness for small displacements.

Again, the slope for the first part of the numerically determined load-displacement curves depends on the stiffness of the soil.

4.1.3 LATERAL SPRINGS

The lateral springs are modelled to determine the resistance of the soil when the free-span of the pipe is affected by the in-line hydrodynamic force. The analytical springs are based on anchor plate theory and compared to a numerical model made in Plaxis. The analytical calculations of lateral springs are made in Matlab and can be found in [DVD/Soil Springs/lateral_spring.m].

Analytical Spring Model

To calculate the lateral resistance, it is assumed that a pipeline buried in soil behaves similarly to an anchor plate with finite height and infinite length. The principle for determining the lateral resistance is first to determine the anchor resistance A_0 for a basic case and then to determine the lateral resistance for the buried pipeline by reducing A_0 so it fits the present case.

In the anchor plate theory, the basic case is defined as an anchor plate with an upper edge at the seabed and infinite length out of the plane. Figure 81 shows the failure mode for an anchor plate in the basic case.
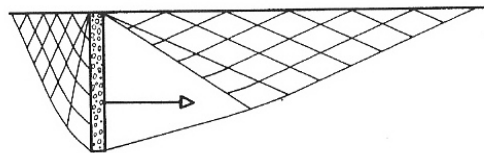

Figure 81: Failure mode for an anchor plate in the basic case.[Harremoës et al. 1980, p13.1]

Failure is assumed to happen all around the anchor plate. Figure 82 shows the forces acting on an anchor plate in the basic case.
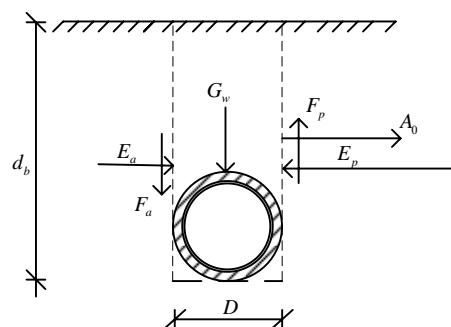

Figure 82: Forces for an anchor plate in the basic case.

The self-weight G_w can be determined as

$$G_w = W_{soil} + W_{pipe}$$

(4.1.31)

where

G_w is the self-weight per unit length on the anchor [kN/m]

On the active side, the anchor plate is assumed to be rough. The active vertical force F_a can be determined as

$$F_a = E_a \tan \varphi'$$ (4.1.32)

where

F_a is the active tangential soil pressure per unit length [kN/m]

E_a is the active normal soil pressure per unit length [kN/m]

The active pressure E_a can then be determined as

$$E_a = \frac{1}{2}\gamma'd_b^2 K_\gamma^{ar}$$ (4.1.33)

where

K_γ^{ar} is the active rough soil pressure coefficient for soil weight [-]

The active soil pressure coefficient for soil weight can be approximated as

$$K_\gamma^{ar} \approx K_p^{ar} + 0.007\left(e^{-9\sin\varphi'} - 1\right)$$ (4.1.34)

where

K_p^{ar} is the active rough soil pressure coefficient for load [-]

The active soil pressure coefficient for load is defined as

$$K_p^{ar} = \left(1 - \sin\varphi'\right)e^{\left(\varphi' - \frac{\pi}{2}\right)\tan\varphi'}$$ (4.1.35)

On the passive side of the anchor plate, the vertical force F_p is defined as

$$F_p = \frac{1}{2}\gamma'd_b^2 K_\gamma^p \tan\delta_\gamma, \qquad 0 \le \delta_\gamma \le \varphi'$$ (4.1.36)

where

F_p is the passive tangential soil pressure per unit length [kN/m]

K_γ^p is the passive soil pressure coefficient for soil weight [-]

$\tan\delta_\gamma$ is the passive friction coefficient between the soil and anchor plate [-]

Since the movement of the anchor plate is purely horizontal, the forces must satisfy vertical equilibrium which gives the following condition for determination of the passive friction coefficient

$$G_w + F_a - F_p = 0 \Leftrightarrow K_\gamma^p \tan \delta_\gamma = \frac{G_w + F_a}{\frac{1}{2}\gamma' d_b^2}, \qquad 0 \le \delta_\gamma \le \varphi' \qquad (4.1.37)$$

The passive soil pressure coefficient can be determined by Figure 83 which shows the passive soil pressure coefficients in the basic case for different angles of friction.
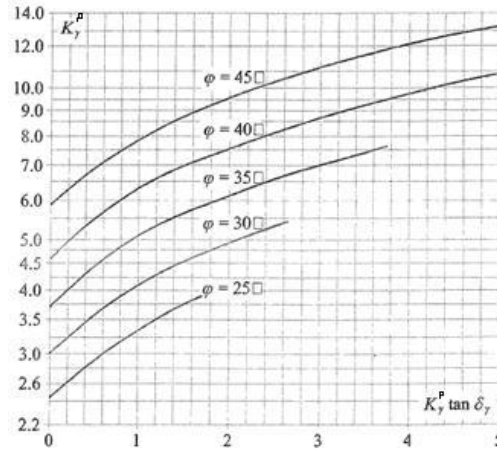

Figure 83: Passive soil pressure coefficients for an anchor plate in the basic case. [Ovesen et al. 2007, p349]

Once the passive soil pressure coefficient has been determined, the passive horizontal force E_p can be determined as

$$E_p = \frac{1}{2}\gamma' d_b^2 K_\gamma^p \qquad (4.1.38)$$

where

$\quad E_p \qquad$ is the passive normal soil pressure per unit length [kN/m]

The anchor resistance in the basic case A_0 can be determined by demanding horizontal equilibrium

$$A_0 = E_p - E_a$$
$$= \frac{1}{2}\gamma' d_b^2 (K_\gamma^p - K_\gamma^{ar}) \qquad (4.1.39)$$

The soil resistance for lateral movement of the pipe is determined by reducing the anchor resistance in the basic case. The reduction ratio A_s / A_0 for the pipeline is based on tests made on anchor plates with finite height and placed in a row. In Figure 84, the results of these tests are shown for a dense and loose soil respectively.
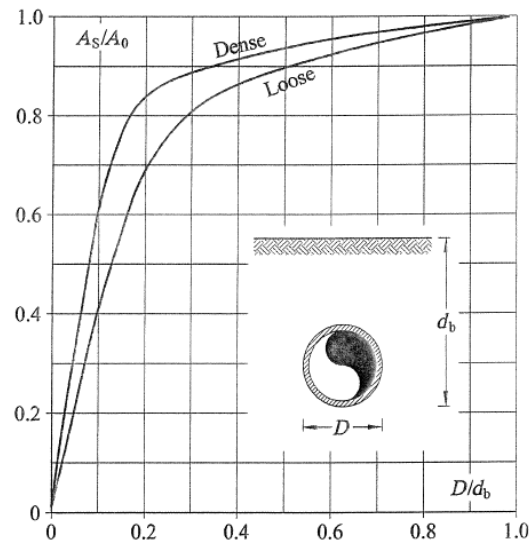
Figure 84: Graphical presentation of the reduction ratio A_s / A_0 [LICengineering 2005].

Finally, the lateral resistance per unit length can be determined as

$$f_{lateral} = \frac{A_s}{A_0} A_0 \qquad (4.1.40)$$

In the analytical lateral load-displacement curves, it is assumed that the soil behaves as an linear elastic-ideal plastic material. The maximum lateral resistance is assumed to occur at a lateral displacement calculated as

$$\delta_{lateral} = 0.02 \, d_b \qquad (4.1.41)$$

Numerical Model

A buried pipeline is modelled in Plaxis in the same way as the previous sections. In this case, the pipe is applied a lateral displacement in order to calculate lateral load-displacement curves. The numerical model can be found in [DVD/Soil Springs/lateralspring.plx]. Figure 85 shows the shear strain increments just before soil collapse.
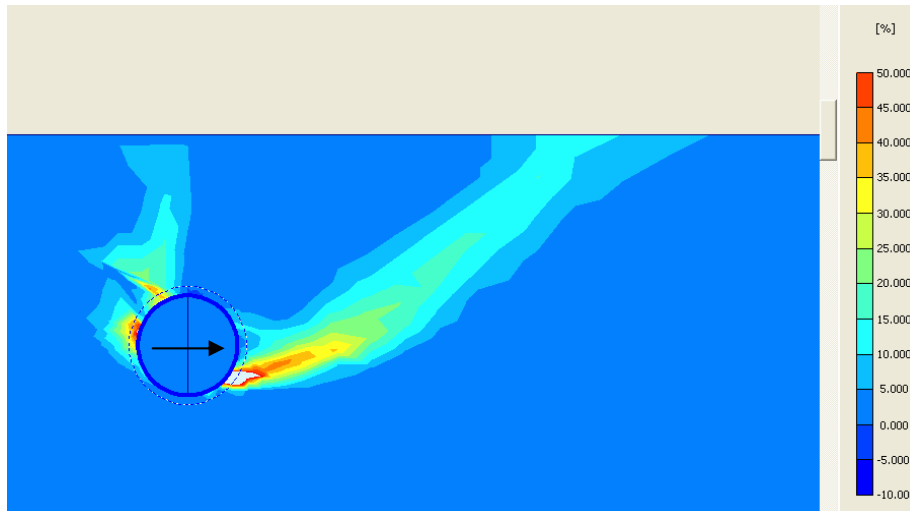
Figure 85: Shear strain increments for lateral displacement of pipeline.

The numerical failure mode is compared to the analytical failure mode for the basic case of an anchor plate whih is shown in Figure 81. The comparison shows good agreement between the general shapes of the failure lines.

4.1.3.1. Lateral Load-Displacement Curves

In Figure 86, the analytical and numerical load-displacement curves are shown. The conditions for the pipe and the soil in each analysis are given in Table 15 and Table 16.
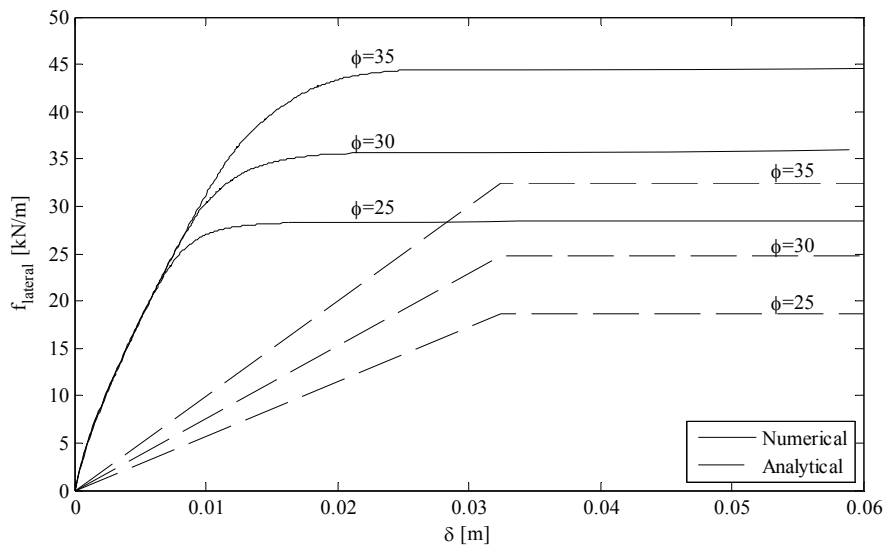
Figure 86: Load-displacement curves for lateral displacement of pipeline.

Comparison of the load-displacement curves in Figure 86 shows that the lateral resistances are in the same order of magnitude for the numerical and analytical models. The analytically determined resistances seem to be conservative. The maximum lateral resistance is assumed to occur at a high value of displacement in the analytical model. The analytically determined stiffness is therefore

significantly lower than the numerically determined stiffness. This occurs even though a relatively low stiffness for the soil is applied in the present case.

4.1.4   SPRINGS IN DIAGONAL DIRECTIONS

When the pipe moves in various directions, the Winkler model is based on the assumption that the corresponding spring stiffness can be determined by superposition of the load-displacement curves determined in the previous sections. This means that if the pipe moves in a downward diagonal direction, the corresponding soil resistance is calculated by superposition of load-displacement curves made for lateral and downward movement of the pipe. In this section, analytical load-displacement curves calculated by superposition are compared to numerical load-displacement curves for a buried pipeline that moves in diagonal directions. The numerical models can be found in [DVD/Soil Springs/diagonalup.plx; diagonaldown.plx].

Figure 87 shows the numerical and analytical load-displacement curves when the pipeline is applied a displacement in 45 degrees upward direction. This analysis is only made for soil with an angle of friction equal to 30 degrees.
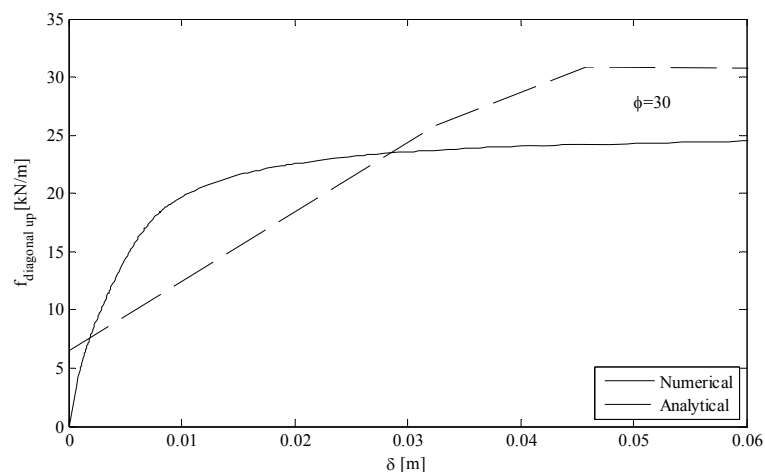
Figure 87: Load-displacement curves for 45 deg upward displacement of pipeline

Superposition of the analytical curves does not increase the difference between the analytical and numerical load-displacement curves compared to the analytical and numerical curves for upward and lateral pipe displacement, respectively. This can be seen by comparing Figure 87 with Figure 80 and Figure 86. The analytical curve shows larger resistance than the numerical curve because the analytical upward resistance is overestimated.

Figure 88 shows the load-displacement curves when the pipeline is applied a displacement in 45 degrees downward direction.
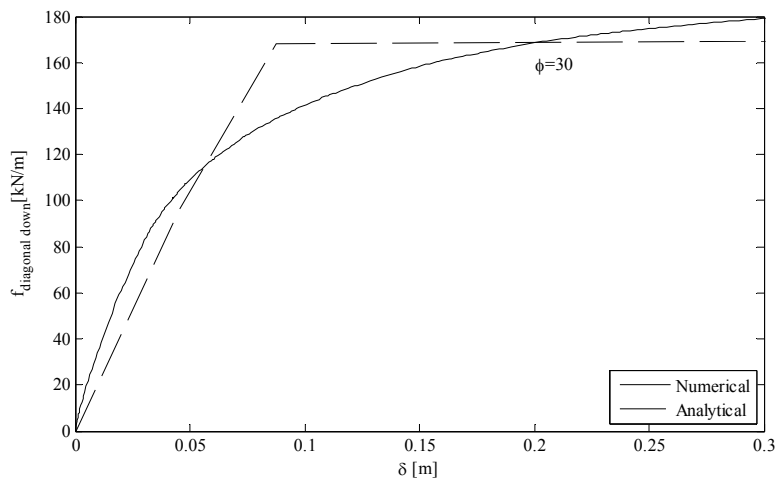
Figure 88: Load-displacement curves for 45 deg downward displacement of pipeline

Figure 88 shows good agreement between analytical and numerical load-displacement curves in the present case. There are no indications of increased difference between analytical and numerical load-displacement curves caused by superposition of the analytical curves.

4.1.5 EVALUATION OF SPRING MODELS

In the directions where numerical verification of springs has been carried out, analyses show relatively good agreement between maximum resistances determined by analytical and numerical methods. The analytical maximum resistances in upward direction have been shown to be non-conservative. Parametric study has shown that Poisson's ratios in the range of 0.2-0.4 has no significant impact on the load-displacement curves for any of the failure modes. Furthermore, the small value of cohesion $c = 0.2\,\text{kPa}$ that has been applied in the numerical models does not have significant impact on the load-displacement curves for any of the failure modes.

The displacements that correspond to the analytical resistances seem to be highly inaccurate in some of the analytical models compared to the numerical models. The stiffness of the analytical soil springs is sensible to the choice of displacement corresponding to the maximum bearing capacity, which must be estimated since the analytical solutions assume that the soil has rigid-plastic constitutive behaviour. In the upward and lateral directions, the analytically determined spring appear too slack and in the downward direction, the analytical spring appears to be too stiff. This means that although the stiffness of the soil in the numerical model is fitted to an analytical load-displacement curve in one direction, it will increase the difference between the numerical and analytical curves in some other direction.

The analyses have shown that some inaccuracy is implemented by assuming a Winkler model with soil springs. It is at this point too early to conclude if the inaccuracies in the analytical spring models have a considerable impact on the fatigue analysis of the free-span. Parametric studies in Chapter 5.2 (Parametric Study for Regular Waves) show that increased stiffness of the soil are favourable for the pipeline when considering fatigue damage.

4.2 TRANSMITTING BOUNDARY

In this chapter, the concept of a transmitting boundary is investigated. This is an important aspect in numerical soil dynamics. First, the concept is briefly introduced. Then, in two subsequent steps, transmitting boundary elements are developed for a plane, straight Bernoulli-Euler beam with constant axial force upon a Winkler foundation with linear springs. In the first step, an analytical formulation is derived. In the second step, this is cast into element formulation to be used in the Finite Element Method. Then follows a benchmark test on the implemented elements and an evaluation.

4.2.1 INTRODUCTION

The hydrodynamic forces that act upon the free-span of the pipe induce waves that travel through the soil domain until they dissipate completely. In general, the dispersion length is governed by the relationship between the load frequency and a so-called cut-on frequency which depends upon the pipeline and soil properties. When the load frequency is below the cut-on frequency, the waves will tend to reside relatively close to the load source and are therefore referred to as evanescent waves. When the load frequency exceeds the cut-on frequency, the waves will propagate a significant distance away from the load source before they vanish and are referred to as propagating waves [Andersen 2006, p70]. The two cases are illustrated in Figure 89 left and right, respectively, where the only difference is the magnitude of the load frequency.
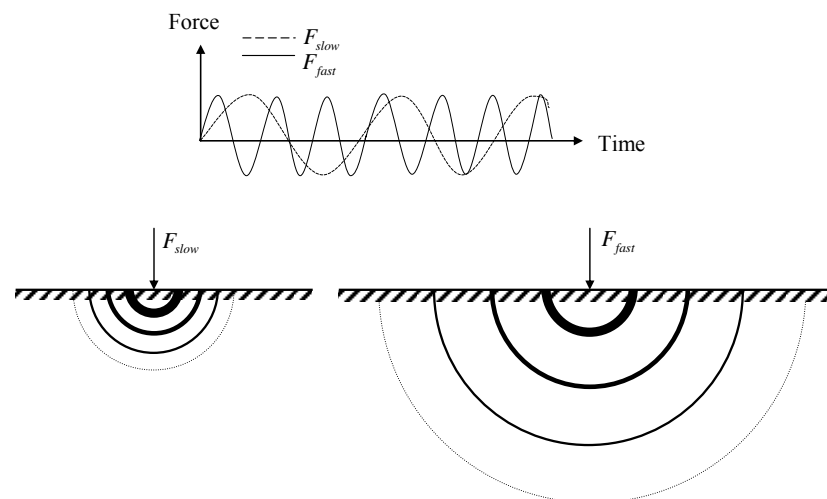

Figure 89: Waves in infinite soil domain that is dynamically loaded. Left: A low-frequent load induces evanescent waves. Right: A high-frequent load induces propagating waves.

In order to create a numerical model of the free-span pipeline by the Finite Element Method, the infinite domain of soil that supports the pipeline must be reduced to a finite domain. The core of the matter is to determine an appropriate size of the finite domain that is both computationally effective and accounts for the essential physical properties of the infinite soil domain. It is imperative that the boundary of the finite domain does not disturb the response of the rest of the model.

Two general approaches may be followed. The first approach is to use a large finite domain that allows all waves to vanish due to material damping before they reach the boundary. In case of propagating waves, a relatively large model is required which is not considered to be computationally effective. The second approach is to use a smaller finite domain and predict the response at the boundary. Thus, the boundary will absorb the residual waves and will be referred to as a transmitting boundary. The two approaches of modelling finite soil domains are illustrated in Figure 90 where the approach of a transmitting boundary is investigated in this project.
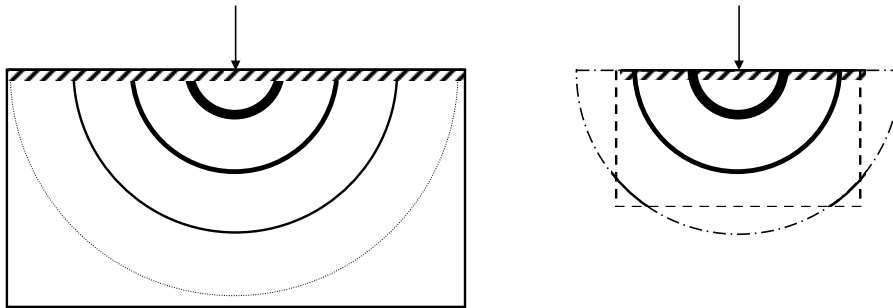
Figure 90: Finite soil domains that are dynamically loaded. Left: Large domain with reflecting boundary. Right: Small domain with transmitting boundary which is treated in this project.

When modelling a transmitting boundary, several methods exist. One intuitive approach is to encapsulate the domain of interest by a boundary zone that consists of highly damped material. The material damping should be calibrated in such a way that it is small enough to avoid reflecting the waves back into the domain of interest when the waves encounter the boundary zone and large enough to absorb the residual waves as they travel through the boundary zone. This is illustrated in Figure 91 left.

Another method is to encapsulate the domain of interest with transmitting boundary elements. These are derived by applying external stresses that are opposite-directed to the inner stresses that appear in the boundary in the absence of the remaining infinite domain. This is illustrated in Figure 91 right. In general, the latter method requires that the response is linear at the boundary which limits the minimum size of the domain.
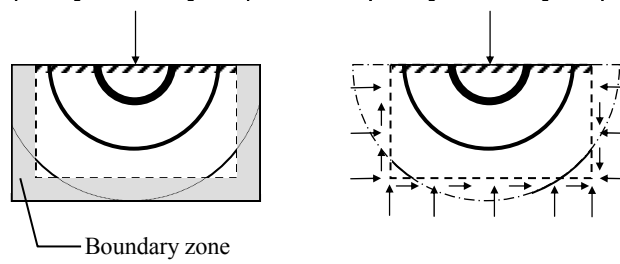
Figure 91: Small finite domains with transmitting boundary of highly damped material (left) or transmitting boundary elements (right).

The latter method is chosen in this project and is based upon a description of the pipeline as a Bernoulli-Euler beam upon Winkler foundation with linear springs. The description neglects material damping in the pipeline or soil but accounts implicitly for geometrical damping in the soil. The description includes stiffness adjustment due to an initial axial load but neglects contribution from transversal static loads. Thus, the transmitting boundary element includes the essential physical properties of the problem but requires some extension to be fully suited for practical use. It is emphasized that the transmitting boundary element in this project is a beam element while Abaqus only offers pre-defined transmitting boundary continuum elements. The latter has not been considered further.

4.2.2 ANALYTICAL FORMULATION

In this section, the analytic formulation is presented. First, the general presumptions for the beam are presented. Then an analytical solution of the transversal vibrations of the beam due to harmonic loading is derived. Finally, the section forces are written in terms of the displacements and rotations. Unless otherwise stated, all quantities are assumed to be real numbers. The derivations generally follow [Andersen pp66-67, pp96-98] but have been extended to include the stiffness reduction due to an initial axial load. A Maple worksheet with the derivations and supplementary verification may be found in [DVD/Transmitting Boundary/Analytic.mws].

4.2.2.1. General Presumptions

The analytical formulation is based upon a Bernoulli-Euler beam with a constant axial load upon Winkler foundation with linear springs. This is shown in Figure 92 and explained below.
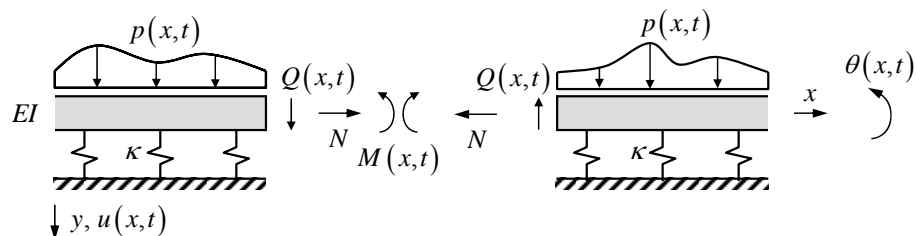

Figure 92: Sign conventions of external forces, section forces, displacements and rotations for a Bernoulli-Euler beam with constant axial load upon Winkler foundation.

The space coordinate along the beam axis is x. The time coordinate is t. The vertical displacement $u(x,t)$ is measured from the state of static equilibrium and defined positive in the downward direction. Likewise, the rotation $\theta(x,t)$ is measured from the state of static equilibrium and defined positive counter-clockwise. The external distributed load $p(x,t)$ is defined positive in downward direction. When cutting away the right side of the beam, the shear force $Q(x,t)$ and inner moment $M(x,t)$ are defined positive downward and counter-clockwise, respectively. When cutting away the left side of the beam, these are defined positive in the opposite directions. The constant axial force N is defined positive in tension.

Kinematic Relations

When neglecting shear strains, the only remaining measure of strain for the transversal displacement of a beam is the curvature $\beta(x,t)$. With the given directions of displacements and rotations and when also assuming strains to be infinitesimal, the curvature may be associated with the displacements through the following kinematical field conditions

$$\beta(x,t) \equiv \frac{\partial \theta(x,t)}{\partial x}, \qquad \theta(x,t) = -\frac{\partial u(x,t)}{\partial x} \tag{4.2.1}$$

where

u	is the downward displacement from the state of static equilibrium [m]
θ	is the clock-wise rotation from the state of static equilibrium [-]
β	is the curvature [m^{-1}]
x	is the position along the beam axis [m]
t	is time [s]

[Byskov 2002, pp118-119]

Static Relations

In order to derive the static relations, an infinitesimal part of the beam is shown in Figure 93. In order to capture the effects of adjusted stiffness due to the axial load, the strains are assumed to be infinitesimal but the rotations are assumed to be non-negligible.
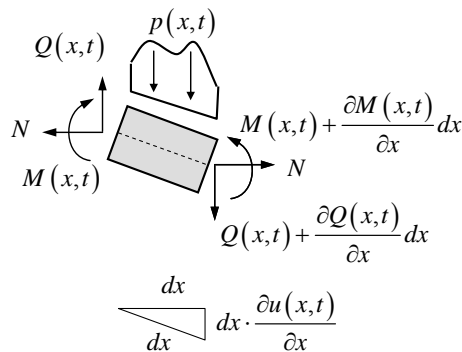

Figure 93: Infinitesimal part of the beam. Adopted from [Nielsen 2004, p116].

With the given directions of section forces and the mentioned strain assumptions, vertical and moment equilibrium of an infinitesimal beam element will yield the following static field conditions, respectively

$$\frac{\partial Q(x,t)}{\partial x} + p(x,t) = 0$$
$$\frac{\partial M(x,t)}{\partial x} - Q(x,t) + N\frac{\partial u(x,t)}{\partial x} = 0 \tag{4.2.2}$$

where

p	is the external downward distributed load [N/m]
Q	is the shear force [N]
N	is the inner normal force [N]
M	is the inner moment [Nm]

[Nielsen 2004, p116]

Constitutive Relation

Finally, the beam is assumed to behave like an isotropic linear elastic material which fulfils Hooke's law

$$M(x,t) = EI\beta(x,t) \tag{4.2.3}$$

where

E	is the Young's modulus [Pa]
I	is the second moment of area about the y-axis [m^4]

Static Equation of Equilibrium

For later reference, the kinematic, static and constitutive relations (4.2.1)-(4.2.3) are combined into some useful relations. The section forces are related to the second and third order spatial derivatives of the transversal displacements, respectively

$$M(x,t) = -EI\frac{\partial^2 u(x,t)}{\partial x^2} \tag{4.2.4}$$

$$Q(x,t) = -EI\frac{\partial^3 u(x,t)}{\partial x^3} + N\frac{\partial u(x,t)}{\partial x} \tag{4.2.5}$$

Secondly, the static equation of equilibrium is given by the following 4th order ordinary differential equation

$$EI\frac{\partial^4 u(x,t)}{\partial x^4} - N\frac{\partial^2 u(x,t)}{\partial x^2} = p(x,t) \tag{4.2.6}$$

4.2.2.2. Forced Transversal Vibrations during Harmonic Loading

In this section, the forced transversal vibrations of the beam during harmonic loading are determined. After establishing the dynamic equation of motion, it is solved. In the search for the solution, the wave numbers and amplitudes are determined.

Dynamic Equation of Motion

To establish the dynamic equation of motion for the beam, the distributed load $p(x,t)$ is assumed to be the resultant load of an external load, an inertia force and a transversal spring resistance

$$p(x,t) = f(x,t) - f_i(x,t) - f_\kappa(x,t), \quad f_i = m\frac{\partial^2 u(x,t)}{\partial t^2}, \quad f_\kappa = \kappa u(x,t) \tag{4.2.7}$$

where

$\quad f \quad$ is an external downward distributed load $\left[\frac{\text{N}}{\text{m}}\right]$

$\quad f_i \quad$ is the upward inertia distributed load $\left[\frac{\text{N}}{\text{m}}\right]$

$\quad f_\kappa \quad$ is the upward transversal spring distributed load $\left[\frac{\text{N}}{\text{m}}\right]$

$\quad m \quad$ is the beam mass per unit length $\left[\frac{\text{kg}}{\text{m}}\right]$

$\quad \kappa \quad$ is the transversal soil spring stiffness per unit length $\left[\frac{\text{N}}{\text{m}^2}\right]$

The beam is considered in the case when the only external load is a concentrated force that acts downwardly at $x = 0$ and varies harmonically with time. Thus, the external distributed load takes the following form

$$f(x,t) = \delta(x)F\exp(i\omega t), \quad F \in \mathbb{C}, \quad i^2 = -1 \tag{4.2.8}$$

where

$\quad F \quad$ is the complex force amplitude [N]

$\quad \omega \quad$ is the circular load frequency $\left[\frac{\text{rad}}{\text{s}}\right]$

$\quad i \quad$ is the imaginary unit [-]

$\quad \delta \quad$ is Dirac's delta function [-]

By use of (4.2.6)-(4.2.8), the forced transversal vibrations of the beam may be described by the following 4th order partial differential equation

$$EI\frac{\partial^4 u(x,t)}{\partial x^4} - N\frac{\partial^2 u(x,t)}{\partial x^2} + m\frac{\partial^2 u(x,t)}{\partial t^2} + \kappa u(x,t) = \delta(x)F\exp(i\omega t) \tag{4.2.9}$$

[Nielsen 2004, p118]

In the section where the concentrated force acts, i.e. $x = 0$, the static and kinematic quantities must fulfil some continuity conditions. The displacements, rotations and inner moments on both sides of the mid-section must be identical. In addition, the shear force should increase in magnitude over the section with the magnitude of the external concentrated force. This yields the following equations

where the quantities on the left and right-hand-side of the concentrated force are denoted with an upper index of minus or plus, respectively

$$u^-(0,t) = u^+(0,t) \qquad\qquad \text{Identical displacements}$$
$$\theta^-(0,t) = \theta^+(0,t) \qquad\qquad \text{Identical rotations}$$
$$M^-(0,t) = M^+(0,t) \qquad\qquad \text{Identical inner moments} \qquad\qquad (4.2.10)$$
$$Q^-(0,t) = Q^+(0,t) + \int_{x^-}^{x^+} f(x,t)\,dx \quad \text{Jump in shear force}$$

Solution of Dynamic Equation of Motion - Wave numbers

In order to solve (4.2.9), the form of the stationary displacement is guessed upon physical knowledge. First, the stationary displacement is assumed to be decomposed into its mutually independent spatial and time component

$$u(x,t) = U_x(x) \cdot U_t(t), \quad \{U_x, U_t\} \in \mathbb{C} \qquad\qquad (4.2.11)$$

where

U_x is the spatial component of the stationary displacement [m]

U_t is the time component of the stationary displacement [-]

The components are generally complex quantities but only their real part will be interpreted as the physical stationary displacement. Since the load varies harmonically, the beam will also vibrate harmonically with the load frequency but possibly out of phase. Thus, the time component of the stationary displacement can be described by

$$U_t(t) = \exp(i\omega t) \qquad\qquad (4.2.12)$$

For the determination of the spatial component of the stationary displacement, it is known that the waves, which are induced by the harmonic load will decay in magnitude after having travelled a distance away from the load source. Then the waves may either continue to propagate harmonically or dissipate completely. Thus, a particular solution to the spatial component of the stationary displacement has the following form with a complex non-zero amplitude and wave number

$$U_{x,p}(x) = U \exp(i k x), \qquad U \neq 0, \quad k \neq 0, \quad \{U,k\} \in \mathbb{C} \qquad\qquad (4.2.13)$$

where

U is a displacement amplitude [m]

k is a wave number $\left[\frac{\text{rad}}{\text{m}}\right]$

Since a wave number is generally complex, it may be decomposed into its real and imaginary parts

$$k = a \pm b i, \qquad b \geq 0, \quad \{a,b\} \in \mathbb{R} \qquad\qquad (4.2.14)$$

where

    a is the real part of a wave number $\left[\frac{\text{rad}}{\text{m}}\right]$

    b is the absolute imaginary part of a wave number $\left[\frac{\text{rad}}{\text{m}}\right]$

A particular solution of the spatial component (4.2.13) may be factorized by (4.2.14) which yields

$$U_{x,p}(x) = U \exp\left(i\,x \cdot (a \pm b\,i)\right) = U \exp\left(i\,x\,a \mp b\,x\right) = U \underbrace{\exp\left(i\,x\,a\right)}_{\text{harmonic}} \cdot \underbrace{\exp\left(\mp b\,x\right)}_{\text{exponential}} \qquad (4.2.15)$$

It is seen from (4.2.15) that the real and imaginary parts of a wave number determine the harmonic and exponential variation, respectively, of a particular spatial component of the stationary displacement. It will vary either purely harmonically, purely exponentially or combined harmonically and exponentially as shown in Table 17.

Table 17: Three cases for wave numbers and variation of particular spatial response.

Case	Wave number	Wave number components	Variation of spatial response
1	Pure real	$a > 0, \quad b = 0$ $a < 0, \quad b = 0$	Pure harmonic
2	Pure complex	$a = 0, \quad b > 0$	Pure exponential
3	Complex	$a < 0, \quad b > 0$ $a > 0, \quad b > 0$	Combined harmonic and exponential

In cases 2 and 3, (4.2.13) is physically valid only if it decays exponentially with the distance along the beam axis from the load source until it vanishes completely, i.e.

$$\begin{aligned} x \to -\infty &\Rightarrow U_{x,p}{}^{-}(x) \to 0 \\ x \to \infty &\Rightarrow U_{x,p}{}^{+}(x) \to 0 \end{aligned} \qquad (4.2.16)$$

In order to fulfil (4.2.16), a wave number with non-positive or non-negative imaginary parts must be associated with the left- or right-hand-side of the beam, respectively

$$k^{-} = a - b\,i, \qquad k^{+} = a + b\,i \qquad (4.2.17)$$

Substitution of (4.2.11)-(4.2.12) into (4.2.9) gives a 4th order linear ordinary differential equation

$$\left(EI \frac{\partial^4 U_x(x)}{\partial x^4} - N \frac{\partial^2 U_x(x)}{\partial x^2} + \left(\kappa - \omega^2 m\right) U_x(x) \right) \cdot \exp\left(i\,\omega t\right) = \delta(x)\,F \exp\left(i\,\omega t\right) \Leftrightarrow$$
$$EI \frac{\partial^4 U_x(x)}{\partial x^4} - N \frac{\partial^2 U_x(x)}{\partial x^2} + \left(\kappa - \omega^2 m\right) U_x(x) = \delta(x)\,F \qquad (4.2.18)$$

Further substitution of (4.2.13) into the homogeneous part of (4.2.18) yields the following 4th order characteristic polynomial

$$\left(EI(ik)^4 - N(ik)^2 + \kappa - \omega^2 m \right) \cdot U \exp(ikx) = 0 \Rightarrow$$

$$EI\,k^4 + N\,k^2 + \kappa - \omega^2 m = 0 \Rightarrow \qquad (4.2.19)$$

$$k^4 + c_1\,k^2 + c_2 = 0, \qquad c_1 = \frac{N}{EI}, \qquad c_2 = \frac{\kappa - \omega^2 m}{EI}, \qquad EI \neq 0$$

where

$\quad c_1 \qquad$ is the ratio of the axial force and the bending stiffness $\left[\mathrm{m}^{-2} \right]$

$\quad c_2 \qquad$ is the ratio of dynamic stiffness at a load frequency and the bending stiffness $\left[\mathrm{m}^{-4} \right]$

The roots of (4.2.19) are four arbitrary wave numbers k_1, k_2, k_3, k_4 which depend upon the coefficients c_1, c_2, and thus upon the beam, soil and load properties but not upon the load magnitude. The wave numbers must be ordered to fulfil (4.2.17).

Since (4.2.18) is a fourth order linear differential equation, its general solution must contain four unique particular solutions of the form (4.2.13) where each particular solution is associated with one of the wave numbers. The general solution of the spatial component of the stationary displacement may be defined piece-wisely for the left and right-hand-side of the beam by

$$U_x(x) = \begin{cases} U_x^-(x) = U_1 \exp(ik_1 x) + U_2 \exp(ik_2 x), & x \leq 0 \\ U_x^+(x) = U_3 \exp(ik_3 x) + U_4 \exp(ik_4 x), & x > 0 \end{cases} \qquad (4.2.20)$$

where

$\quad U_j \qquad$ is the jth displacement amplitude [m]

$\quad k_j \qquad$ is the jth ordered wave number $\left[\frac{\mathrm{rad}}{\mathrm{m}} \right]$

By use of (4.2.11)-(4.2.12) and (4.2.20), the stationary displacement is fully described by

$$u(x,t) = \begin{cases} u^-(x,t) = U_1 \exp(i\omega t + ik_1 x) + U_2 \exp(i\omega t + ik_2 x), & x \leq 0 \\ u^+(x,t) = U_3 \exp(i\omega t + ik_3 x) + U_4 \exp(i\omega t + ik_4 x), & x > 0 \end{cases} \qquad (4.2.21)$$

Solution of Dynamic Equation of Motion - Amplitudes

The amplitudes U_1, U_2, U_3, U_4 are determined from the continuity conditions (4.2.10) and the relations (4.2.1), (4.2.4)-(4.2.5) and (4.2.21). This yields the following system of linear equations

$$u^-(0,t) = u^+(0,t) \qquad\qquad \Rightarrow U_1 + U_2 = U_3 + U_4$$

$$\theta^-(0,t) = \theta^+(0,t) \qquad\qquad \Rightarrow ik_1 U_1 + ik_2 U_2 = ik_3 U_3 + ik_4 U_4$$

$$M^-(0,t) = M^+(0,t) \qquad\qquad \Rightarrow (ik_1)^2 U_1 + (ik_2)^2 U_2 = (ik_3)^2 U_3 + (ik_4)^2 U_4 \qquad (4.2.22)$$

$$Q^-(0,t) = Q^+(0,t) + \int_{x^-}^{x^+} f(x,t)\,dx \Rightarrow$$

$$\left((ik_1)^3 - \frac{N}{EI}ik_1 \right)U_1 + \left((ik_2)^3 - \frac{N}{EI}ik_2 \right)U_2 = \left((ik_3)^3 - \frac{N}{EI}ik_3 \right)U_3 + \left((ik_4)^3 - \frac{N}{EI}ik_4 \right)U_4 - \frac{F}{EI}$$

Equations (4.2.22) can be rewritten in matrix form

$$
\begin{bmatrix}
-1 & -1 & 1 & 1 \\
-ik_1 & -ik_2 & ik_3 & ik_4 \\
-(ik_1)^2 & -(ik_2)^2 & (ik_3)^2 & (ik_4)^2 \\
-(ik_1)^3 + \dfrac{N}{EI}ik_1 & -(ik_2)^3 + \dfrac{N}{EI}ik_2 & (ik_3)^3 - \dfrac{N}{EI}ik_3 & (ik_4)^3 - \dfrac{N}{EI}ik_4
\end{bmatrix}
\begin{bmatrix}
U_1 \\ U_2 \\ U_3 \\ U_4
\end{bmatrix}
=
\begin{bmatrix}
0 \\ 0 \\ 0 \\ \dfrac{F}{EI}
\end{bmatrix}
\quad (4.2.23)
$$

Equations (4.2.23) may be solved by Gauss elimination or matrix inversion. It may be seen from (4.2.23) that the amplitudes depend explicitly upon $c_1, \dfrac{F}{EI}$ and implicitly upon c_2 due to the wave numbers.

Solution of Dynamic Equation of Motion – Evanescent or Propagating Waves

In this section, the case of evanescent or propagating waves is investigated. The characteristic polynomial (4.2.19) may be rewritten as a second-order polynomial

$$
\tau^2 + c_1\tau + c_2 = 0, \qquad \tau = k^2 \tag{4.2.24}
$$

The roots of the first equation in (4.2.24) are determined by its discriminant

$$
d = c_1^2 - 4c_2 \tag{4.2.25}
$$

where

   d is the discriminant of the second-order polynomial $\left[\text{m}^{-4} \right]$

It appears that the cases of evanescent or propagating waves are separated by the case of resonance when (4.2.25) is exactly zero, i.e.

$$
\begin{array}{ll}
\text{Propagating waves:} & c_2 < c_{2,c} \\
\text{Evanescent waves:} & c_2 > c_{2,c}
\end{array}
, \qquad
c_{2,c} =
\begin{cases}
\frac{1}{4}c_1^2, & c_1 \le 0 \\
0, & c_1 > 0
\end{cases}
\tag{4.2.26}
$$

where

   $c_{2,c}$ is the critical value of c_2 $\left[\text{m}^{-4} \right]$

The domains of evanescent and propagating waves according to (4.2.26) are illustrated later in Figure 96. The coefficient c_2 may be rewritten in terms of the cut-on frequency

$$
c_2 \equiv \frac{\kappa - \omega^2 m}{EI} = \frac{\kappa \cdot \left(1 - \dfrac{\omega^2}{\omega_c^2} \right)}{EI}, \qquad \omega_c = \sqrt{\frac{\kappa}{m}}, \qquad m \ne 0 \tag{4.2.27}
$$

where

   ω_c is the circular cut-on frequency $\left[\frac{\text{rad}}{\text{s}} \right]$

From (4.2.27) it is seen that $c_2 < 0$ when the load frequency exceeds the cut-on frequency, i.e. $\omega > \omega_c$. According to (4.2.26), this always results in propagating waves. Furthermore, (4.2.26) also suggests that propagating waves may occur when the load frequency is below the cut-on frequency and a compressive axial force of sufficient large magnitude is present. In practice, however, buckling may prevent this from occurring.

To illustrate the case of evanescent or propagating waves, the physical spatial component of the stationary displacement for a beam that is subjected to harmonic loading is shown in Figure 94 and Figure 95. The load frequency is below and above the cut-on frequency, respectively. It may be noted that the amplitude of the propagating waves in Figure 95 remains constant because the analytic formulation neglects material damping of the pipeline and soil.
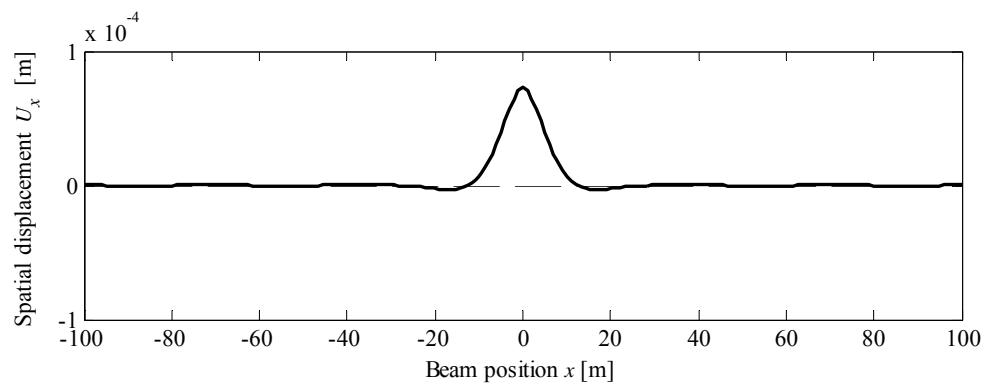

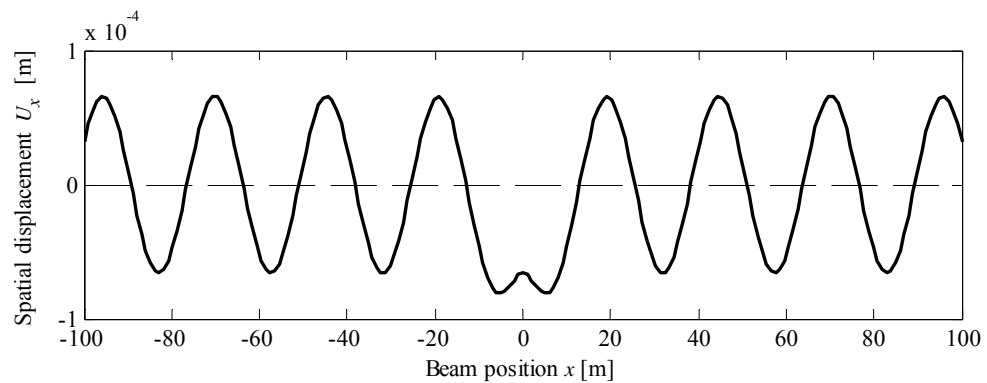*Figure 94: Example of the physical spatial component of stationary displacement for $\omega < \omega_c$.*

Figure 95: Example of the physical spatial component of stationary displacement for $\omega > \omega_c$.

4.2.2.3. Project Assessment

In this section, it is investigated whether the pipe in this project experiences evanescent or propagating waves. The assessment is based upon the most critical combinations of the extreme values of the properties of the pipeline, soil and load. These are given in Table 18 along with the coefficients c_1, c_2 at the most critical combinations. The sources of the values that are not obvious are commented below.

Table 18: Extreme values of pipeline, soil and load properties and coefficients c_1, c_2.

Parameter		Minimum	Maximum
Young's modulus	E [GPa]	210	340
Second moment of area	I [m^4]	0.0075	
Initial axial load	N [MN]	-4.2	0
Mass of side-span per unit length	$m \left[\frac{\text{kg}}{\text{m}} \right]$	1088	1270
In-line load frequency	f_y [Hz]	0.08	0.23
Cross-flow load frequency	f_z [Hz]	0.16	0.45
Lateral linear spring stiffness	$\kappa_y \left[\frac{\text{MN}}{\text{m}^2} \right]$	0.77	
Vertical linear spring stiffness	$\kappa_z \left[\frac{\text{MN}}{\text{m}^2} \right]$	3.43	
First coefficient	$c_1 \left[\text{m}^{-2} \right]$	-0.027	0
Second coefficient – Lateral	$c_{2,y} \left[\text{m}^{-4} \right]$	0.003	0.005
Second coefficient - Vertical	$c_{2,z} \left[\text{m}^{-4} \right]$	0.013	0.022

The minimum and maximum values of Young's modulus correspond to the stiffness steel and the equivalent stiffness of steel and concrete coating. The minimum and maximum values of the initial axial load correspond to the operational and water-filled state, respectively. The minimum and maximum values of the mass per unit length of the side-span correspond to the air-filled and water-filled state. The minimum and maximum values of the load frequencies correspond to the in-line and cross-flow frequency according to the Morison Model during sea state 5 and 1, respectively.

It is noted that the variation of $c_1 \in \left[-0.027\,\text{m}^{-2}; 0 \right]$ arises due to the potential variation of the bending stiffness and the initial axial load. Furthermore, the variation of $c_{2,y} \in \left[0.003\,\text{m}^{-4}; 0.005\,\text{m}^{-4} \right]$ and $c_{2,z} \in \left[0.013\,\text{m}^{-4}; 0.022\,\text{m}^{-4} \right]$ is dominated by that of the bending stiffness and is affected only to a small degree by the variation of the mass of the side-span and the load frequencies. The domains of evanescent and propagating waves and the possible outcomes of the coefficients c_1, c_2 are shown in Figure 96.
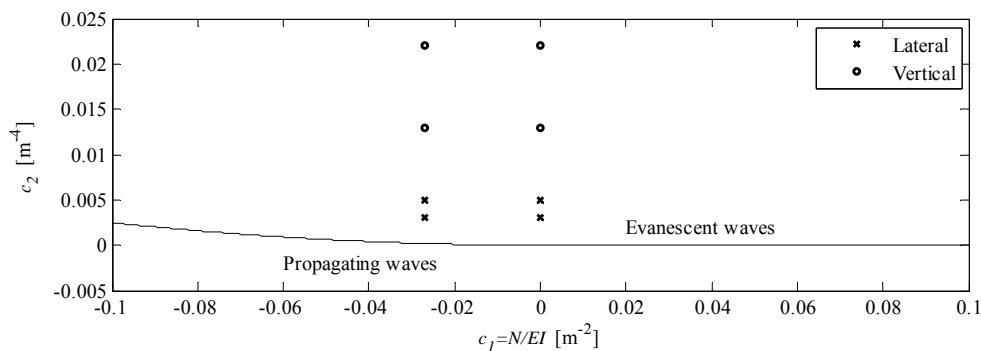

Figure 96: The domains of evanescent and propagating wave. The crosses and circles denote possible outcomes of the project parameters.

It is seen from Figure 96 that the possible outcomes of the project parameters lie within the domain of evanescent waves. Thus, waves will reside near the load source.

4.2.2.4. Section Forces during Harmonic Loading

In this section, different formulations of the section forces are derived. After introducing some relevant quantities, the section forces are written in terms of displacement spatial derivatives and eventually in terms of stiffness, damping and mass matrices which will be employed later in the element formulation. For the sake of space, the derivation is shown only for the left-hand-side of the beam in the first part of the section.

Quantities

The following vectors for section forces, general displacements and component displacements are introduced for the left-hand-side of the beam

$$\mathbf{f}^- = \begin{pmatrix} Q^-(x,t) \\ M^-(x,t) \end{pmatrix}, \quad \mathbf{x}^- = \begin{pmatrix} u^-(x,t) \\ \theta^-(x,t) \end{pmatrix}, \quad \mathbf{u}^- = \begin{pmatrix} U_1 \exp(i\omega t + i k_1 x) \\ U_2 \exp(i\omega t + i k_2 x) \end{pmatrix} \tag{4.2.28}$$

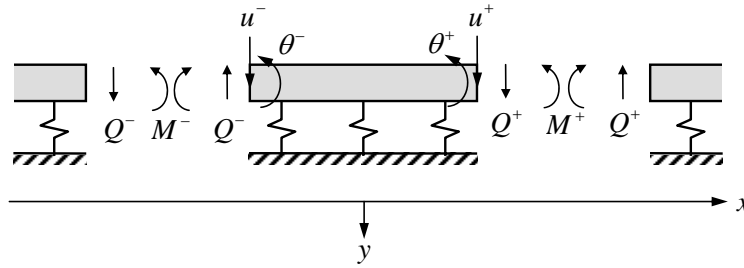The static and kinematic quantities are illustrated in Figure 97.

Figure 97: Static and kinematic quantities.

Section Forces in terms of Displacement Spatial Derivatives

By use of (4.2.4)-(4.2.5), the section force vector may be expressed in terms of the bending stiffness and the displacement spatial derivatives

$$\mathbf{f}^- = -EI \cdot \begin{pmatrix} \dfrac{\partial^3 u^-(x,t)}{\partial x^3} - \dfrac{N}{EI} \dfrac{\partial u^-(x,t)}{\partial x} \\ \dfrac{\partial^2 u^-(x,t)}{\partial x^2} \end{pmatrix} \tag{4.2.29}$$

Section Forces in terms of Stiffness and Damping

The section force vector may further be written in terms of the component displacement vector by use of (4.2.21) and (4.2.29)

$$\mathbf{f}^- = \mathbf{L_1}^- \mathbf{u}^-, \qquad \mathbf{L_1}^- = -EI \cdot \begin{bmatrix} (ik_1)^3 - \dfrac{N}{EI} ik_1 & (ik_2)^3 - \dfrac{N}{EI} ik_2 \\ (ik_1)^2 & (ik_2)^2 \end{bmatrix} \qquad (4.2.30)$$

Similarly, the general displacement vector may be written in terms of the component displacement vector

$$\mathbf{x}^- = \mathbf{L_0}^- \mathbf{u}^-, \qquad \mathbf{L_0}^- = \begin{bmatrix} 1 & 1 \\ -ik_1 & -ik_2 \end{bmatrix} \qquad (4.2.31)$$

The component displacement vector may be eliminated from (4.2.30) by left-multiplying (4.2.31) with the inverse of $\mathbf{L_0}^-$ and substituting the resulting equation into (4.2.30)

$$\mathbf{f}^- = \mathbf{B}^- \mathbf{x}^-, \qquad \mathbf{B}^- = \mathbf{L_1}^- \left(\mathbf{L_0}^- \right)^{-1} \qquad (4.2.32)$$

Now, the section force vector depends upon a frequency response matrix and the general displacement vector. The nature of this relation may be better understood by decomposing the frequency response matrix into its real and complex parts, so (4.2.32) becomes

$$\mathbf{f}^- = \mathrm{Re}\left(\mathbf{B}^- \right) \mathbf{x}^- + i\, \mathrm{Im}\left(\mathbf{B}^- \right) \mathbf{x}^- \qquad (4.2.33)$$

The first order time derivative of the general displacement vector in (4.2.28) is

$$\dot{\mathbf{x}}^- = i\omega \mathbf{x}^- \Leftrightarrow \mathbf{x}^- = \frac{1}{i\omega} \dot{\mathbf{x}}^-, \qquad \omega \neq 0 \qquad (4.2.34)$$

By use of (4.2.34), equation (4.2.33) may be rewritten as

$$\mathbf{f}^- = \mathbf{K}^- \mathbf{x}^- + \mathbf{C}^- \dot{\mathbf{x}}^-, \qquad \mathbf{K}^- = \mathrm{Re}\left(\mathbf{B}^- \right), \quad \mathbf{C}^- = \frac{i}{i\omega} \mathrm{Im}\left(\mathbf{B}^- \right) = \frac{1}{\omega} \mathrm{Im}\left(\mathbf{B}^- \right) \qquad (4.2.35)$$

Thus, the moment and shear force which constitute the section force vector are functions of stiffness and damping matrices and the given displacement and rotation at a section along the beam axis.

Section Forces in terms of Modified Stiffness, Damping and Mass

For reasons that will become clear later, an alternative expression for the force is necessary. The stiffness matrix can be rewritten as a linear combination of two matrices that fulfil

$$\mathbf{K}^- = \mathbf{K_1}^- + \mathbf{K_2}^- \qquad (4.2.36)$$

The second order time derivative of the general displacement vector in (4.2.28) yields

$$\ddot{\mathbf{x}}^- = (i\,\omega)^2\,\mathbf{x}^- \Leftrightarrow \mathbf{x}^- = \frac{1}{(i\,\omega)^2}\,\ddot{\mathbf{x}}^- = -\frac{1}{\omega^2}\,\ddot{\mathbf{x}}^- \tag{4.2.37}$$

By the use of (4.2.36) and (4.2.37), the spring force may be expressed in terms of a modified spring force and an inertia force

$$\mathbf{K}^-\,\mathbf{x}^- = \mathbf{K}_1^-\,\mathbf{x}^- + \mathbf{M}^-\,\ddot{\mathbf{x}}^-, \quad \mathbf{M}^- = -\frac{1}{\omega^2}\,\mathbf{K}_2^- \tag{4.2.38}$$

Thus, (4.2.35) may alternatively be written in terms of a modified stiffness, damping and mass matrix

$$\mathbf{f}^- = \mathbf{K}_1^-\,\mathbf{x}^- + \mathbf{C}^-\,\dot{\mathbf{x}}^- + \mathbf{M}^-\,\ddot{\mathbf{x}}^- \tag{4.2.39}$$

The equations for shear force and inner moment may be expanded into the following general form for the left- and right-hand-side where the matrix components are defined by either (4.2.35) or (4.2.39)

$$\begin{aligned}
Q^-(x,t) &= K^-_{11}\,u^-(x,t) + K^-_{12}\,\theta^-(x,t) + C^-_{11}\,\dot{u}^-(x,t) + C^-_{12}\,\dot{\theta}^-(x,t) + M^-_{11}\,\ddot{u}^-(x,t) + M^-_{12}\,\ddot{\theta}^-(x,t) \\
M^-(x,t) &= K^-_{21}\,u^-(x,t) + K^-_{22}\,\theta^-(x,t) + C^-_{21}\,\dot{u}^-(x,t) + C^-_{22}\,\dot{\theta}^-(x,t) + M^-_{21}\,\ddot{u}^-(x,t) + M^-_{22}\,\ddot{\theta}^-(x,t) \\
Q^+(x,t) &= K^+_{11}\,u^+(x,t) + K^+_{12}\,\theta^+(x,t) + C^+_{11}\,\dot{u}^+(x,t) + C^+_{12}\,\dot{\theta}^+(x,t) + M^+_{11}\,\ddot{u}^+(x,t) + M^+_{12}\,\ddot{\theta}^+(x,t) \\
M^+(x,t) &= K^+_{21}\,u^+(x,t) + K^+_{22}\,\theta^+(x,t) + C^+_{21}\,\dot{u}^+(x,t) + C^+_{22}\,\dot{\theta}^+(x,t) + M^+_{21}\,\ddot{u}^+(x,t) + M^+_{22}\,\ddot{\theta}^+(x,t)
\end{aligned} \tag{4.2.40}$$

Thus, the stiffness matrix is a function of c_1, c_2, EI while the damping and mass matrices are functions of c_1, c_2, EI, ω. In the case of evanescent waves, all components of the frequency response matrix are real and all components of the damping matrix will be zero too.

4.2.3   ELEMENT FORMULATION

In this section, the analytic formulation is cast into element formulation. After a brief presentation of the element topology, the external forces that should be applied to the element are determined. Finally, a correction strategy is presented in the case of non-positive definite element matrices.

Element Topology

The transmitting boundary element is derived for a two-nodal beam element which has three degrees of freedom at each node with the numbering and directions given in Figure 98. This corresponds to the beam elements that are used in the Matlab Model, see Chapter 5.1 (Winkler Model).
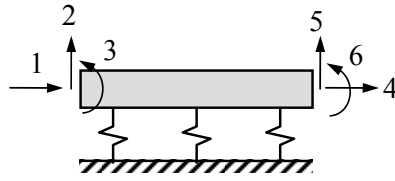
Figure 98: Degrees of freedom of two-nodal plane beam element.

Determination of Forces

When deriving the transmitting boundary element, the idea is to apply external forces which will yield the moment and shear force that would appear in the boundary in the absence of the remaining infinite beam. This may be done by applying external opposite-directed moments and vertical forces in the appropriate degrees of freedom of the beam element. By comparison of Figure 97 and Figure 98, the active external forces are given in Figure 99 for the left and right boundary element, respectively.
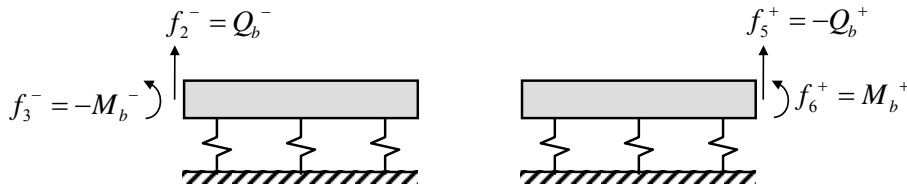

Figure 99: Active external forces that act upon left and right boundary element, respectively.

The relations between the active degrees of freedom in the analytical and element formulation are given in Figure 100. It is seen that the displacements are opposite-directed whereas the rotations have same direction.
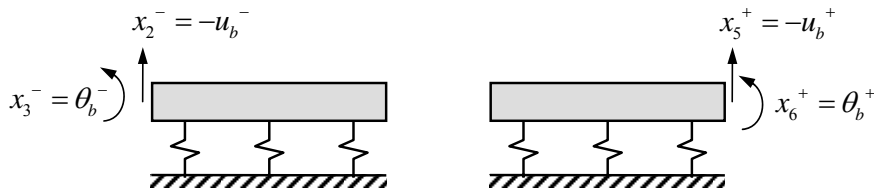

Figure 100: Relations between active degrees of freedom in the analytical and element formulation of left and right boundary element, respectively.

By use of Figure 99, Figure 100 and (4.2.40), the active external forces may be written in terms of matrices and the general displacements in the left and right boundary, respectively

$$
\begin{aligned}
f_2^- &= -K^-_{11} x_2^- + K^-_{12} x_3^- - C^-_{11} \dot{x}_2^- + C^-_{12} \dot{x}_3^- - M^-_{11} \dot{x}_2^- + M^-_{12} \dot{x}_3^- \\
f_3^- &= +K^-_{21} x_2^- - K^-_{22} x_3^- + C^-_{21} \dot{x}_2^- - C^-_{22} \dot{x}_3^- + M^-_{21} \dot{x}_2^- - M^-_{22} \dot{x}_3^- \\
f_5^+ &= +K^+_{11} x_5^+ - K^+_{12} x_6^+ + C^+_{11} \dot{x}_5^+ - C^+_{12} \dot{x}_6^+ + M^+_{11} \dot{x}_5^+ - M^+_{12} \dot{x}_6^+ \\
f_6^+ &= -K^+_{21} x_5^+ + K^+_{22} x_6^+ - C^+_{21} \dot{x}_5^+ + C^+_{22} \dot{x}_6^+ - M^+_{21} \dot{x}_5^+ + M^+_{22} \dot{x}_6^+
\end{aligned}
\qquad (4.2.41)
$$

Given the original element stiffness, damping and mass matrices $\mathbf{K}_e, \mathbf{C}_e, \mathbf{M}_e$, the equations of motion for the boundary element are

$$\mathbf{M}_e\, \ddot{\mathbf{x}}_e + \mathbf{C}_e\, \dot{\mathbf{x}}_e + \mathbf{K}_e \mathbf{x}_e = \mathbf{f}_e, \qquad \begin{aligned} \mathbf{x}_e &= \left(x_1, x_2, x_3, x_4, x_5, x_6 \right) \\ \mathbf{f}_e &= \left(f_1, f_2, f_3, f_4, f_5, f_6 \right) \end{aligned} \qquad (4.2.42)$$

By use of (4.2.41), the external force vector $\mathbf{f}_e$ may be defined in terms of the boundary element stiffness, damping and mass matrices for the left and right boundary, respectively

$$-\mathbf{f}_e = \mathbf{K}_b\, \mathbf{x}_e + \mathbf{C}_b\, \dot{\mathbf{x}}_e + \mathbf{M}_b\, \ddot{\mathbf{x}}_e,$$

$$\mathbf{A}_b^{\,-} = \begin{bmatrix} 0 & 0 & 0 & 0 & 0 & 0 \\ 0 & A_{11}^{-} & -A_{12}^{-} & 0 & 0 & 0 \\ 0 & -A_{21}^{-} & A_{22}^{-} & 0 & 0 & 0 \\ 0 & 0 & 0 & 0 & 0 & 0 \\ 0 & 0 & 0 & 0 & 0 & 0 \\ 0 & 0 & 0 & 0 & 0 & 0 \end{bmatrix}$$

$$\mathbf{A}_b^{\,+} = \begin{bmatrix} 0 & 0 & 0 & 0 & 0 & 0 \\ 0 & 0 & 0 & 0 & 0 & 0 \\ 0 & 0 & 0 & 0 & 0 & 0 \\ 0 & 0 & 0 & 0 & 0 & 0 \\ 0 & 0 & 0 & 0 & -A_{11}^{+} & A_{12}^{+} \\ 0 & 0 & 0 & 0 & A_{21}^{+} & -A_{22}^{+} \end{bmatrix}, \; A = K, C, M \qquad (4.2.43)$$

Summation of (4.2.42) and (4.2.43) yields the equations of motion in terms of the stiffness, damping and mass matrices of the final transmitting boundary element

$$\hat{\mathbf{M}}_e\, \ddot{\mathbf{x}} + \hat{\mathbf{C}}_e\, \dot{\mathbf{x}} + \hat{\mathbf{K}}_e \mathbf{x} = \mathbf{0},$$

$$\hat{\mathbf{C}}_e = \mathbf{C}_e + \mathbf{C}_\mathbf{b}, \qquad \hat{\mathbf{K}}_e = \mathbf{K}_e + \mathbf{K}_\mathbf{b}, \qquad \hat{\mathbf{M}}_e = \mathbf{M}_e + \mathbf{M}_\mathbf{b} \qquad (4.2.44)$$

The new set of equations of motion (4.2.44) may now be solved.

A transmitting boundary element for a plane Bernoulli-Euler beam upon Winkler foundation may be interpreted as a series of transversal and rotational springs, dampers and point masses that are attached to the beam-ends and to a mass-less and rigid beam as shown in Figure 101. The presence of the rigid beam enables coupling between nodal displacements and rotations and thus represents the off-diagonal terms of the boundary element matrices.
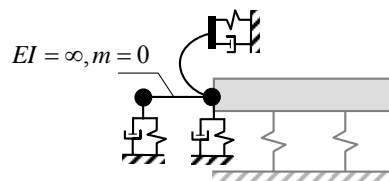

Figure 101: Interpretation of a transmitting boundary element for a plane Bernoulli-Euler beam upon Winkler foundation.

Positive Definiteness Correction

In order to obtain a stable FEM-scheme, the element matrices must fulfil some degree of positive definiteness. The definition of positive and semi-positive definiteness of a matrix $\mathbf{B}$ is

$$
\begin{array}{ll}
\text{Positive definiteness:} & \mathbf{a}\,\mathbf{B}\,\mathbf{a} > 0 \Leftrightarrow \quad \text{Eigenvalues of } \mathbf{B} \text{ are positive} \\
\text{Semi-positive definiteness:} & \mathbf{a}\,\mathbf{B}\,\mathbf{a} \geq 0 \Leftrightarrow \quad \text{Eigenvalues of } \mathbf{B} \text{ are positive or zero}
\end{array}
\,, \quad \mathbf{a} \in \mathbb{C}^n, \mathbf{a} \neq \mathbf{0}
$$

The final transmitting boundary element damping matrix $\hat{\mathbf{C}}_e$ has to be semi-positive definite while the element stiffness and mass matrices $\hat{\mathbf{K}}_e, \hat{\mathbf{M}}_e$ further have to be positive definite. This means that the boundary damping matrices $\mathbf{C}_b{}^-, \mathbf{C}_b{}^+$ must be semi-positive definite and that the following sub matrices of $\mathbf{K}_b{}^-, \mathbf{K}_b{}^+, \mathbf{M}_b{}^-, \mathbf{M}_b{}^+$ must be positive definite by comparison with (4.2.43)

$$
\mathbf{K}_s{}^- = \begin{bmatrix} K_{11}{}^- & -K_{12}{}^- \\ -K_{21}{}^- & K_{22}{}^- \end{bmatrix}, \;
\mathbf{K}_s{}^+ = \begin{bmatrix} -K_{11}{}^+ & K_{12}{}^+ \\ K_{21}{}^+ & -K_{22}{}^+ \end{bmatrix}, \;
\begin{bmatrix} M_{11}{}^- & -M_{12}{}^- \\ -M_{21}{}^- & M_{22}{}^- \end{bmatrix}, \;
\begin{bmatrix} -M_{11}{}^+ & M_{12}{}^+ \\ M_{21}{}^+ & -M_{22}{}^+ \end{bmatrix}
$$

For certain combinations of material properties and load frequency, the sub matrix $\mathbf{K}_s$ will not be positive definite since its upper-left component is non-positive, i.e.

$$
K_{s,11} \leq 0
$$

Only in this case should the element matrices be defined by (4.2.39). In order to fulfil (4.2.36) and positive definiteness, the sub matrices are modified in the following way so the non-positive component changes sign

$$
\mathbf{K}_1{}^- = \begin{bmatrix} -K_{s,11} & \tfrac{1}{2} K_{s,12} \\ \tfrac{1}{2} K_{s,21} & 2 K_{s,22} \end{bmatrix} \quad
\mathbf{K}_2 = \begin{bmatrix} 2 K_{s,11} & \tfrac{1}{2} K_{s,12} \\ \tfrac{1}{2} K_{s,21} & -K_{s,22} \end{bmatrix}, \tag{4.2.45}
$$

Stiffness Matrix Components

In this section, a brief presentation of the magnitude of the components of the stiffness matrix $\mathbf{K}_s{}^-$ is shown. This is important for determining the performance of the boundary elements when they are calibrated to one set of properties for the pipeline, soil and load. The components of the damping and mass matrices are not shown since they are zero in the case of evanescent waves.

The stiffness matrix is governed by the parameters EI, c_1, c_2. Given $EI = 255\,\mathrm{MNm}^2$, the contours in the domain of evanescent waves of the components of the stiffness matrix in the Matlab Model as function of c_1 and c_2 are shown in Figure 102-Figure 104. The limit between evanescent and propagating waves, according to (4.2.26), is given by the dashed curve. The crosses and dots denote the possible outcomes of the project parameters based upon Table 18.
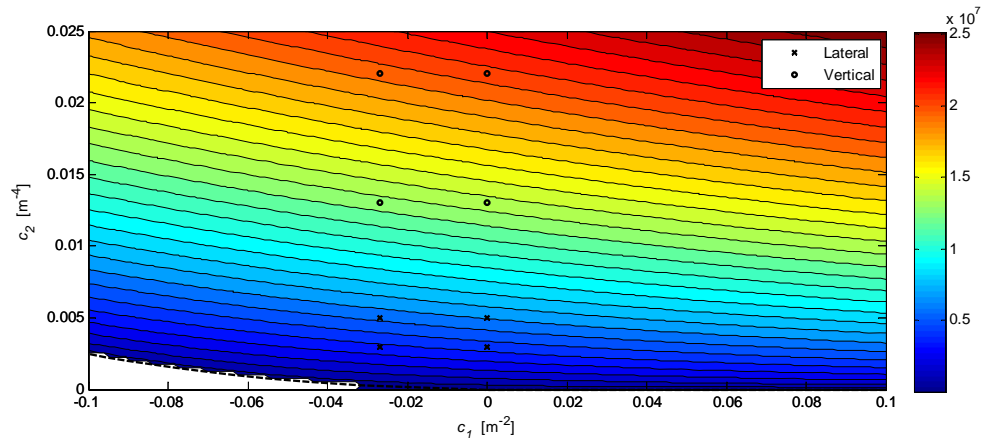
Figure 102: Contours of stiffness matrix component $K_{s,11}$ in N/m as a function of c_1 and c_2 for
$EI = 255 \, \text{MNm}^2$. *Contour step is* $0.84 \frac{\text{MN}}{\text{m}}$.
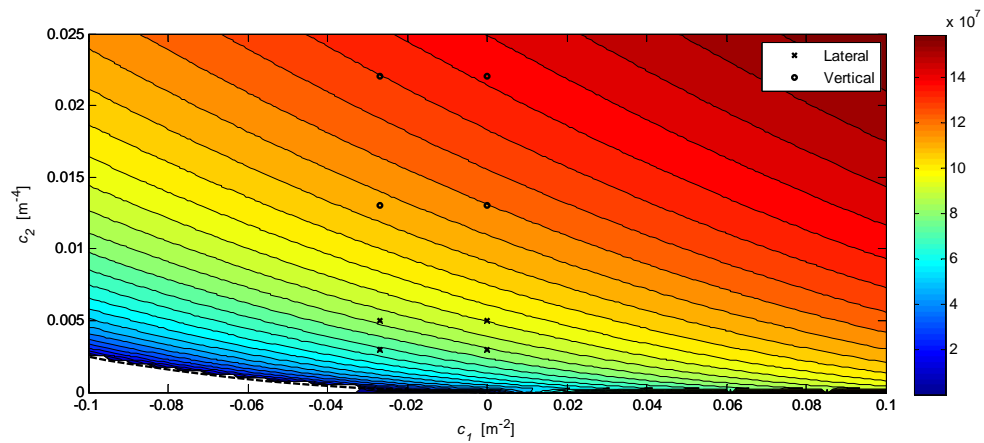

Figure 103: Contours of stiffness matrix component $K_{s,22}$ in Nm as a function of c_1 and c_2 for
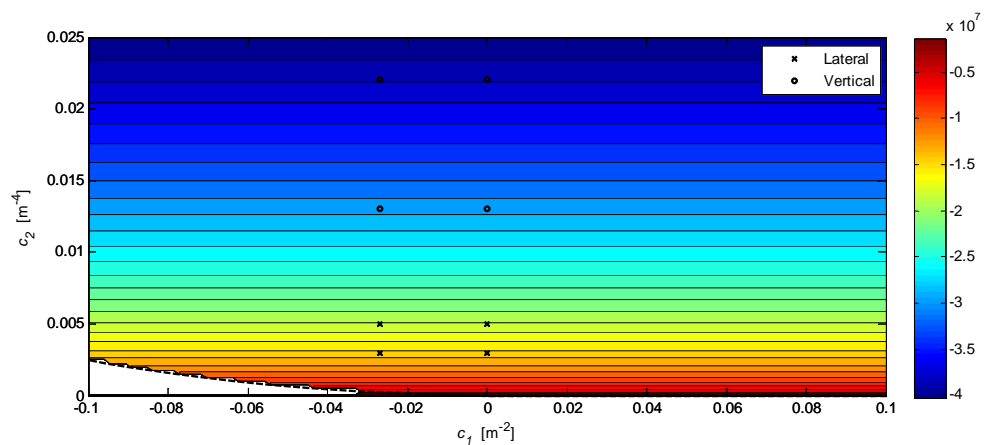$EI = 255 \, \text{MNm}^2$. *Contour step is* $1.3 \, \text{MNm}$.

Figure 104: Contours of stiffness matrix component $K_{s,12}$ in N as a function of c_1 and c_2 for
$EI = 255 \, \text{MNm}^2$. *Contour step is* $5.3 \, \text{MN}$.

Typical values of the stiffness matrix of the transmitting boundary element for the lateral and vertical direction in this project, respectively, are

$$\mathbf{K}_{s,y}^{-} \approx 10^{7} \cdot \begin{bmatrix} 0.4\,\tfrac{N}{m} & -1.4\,N \\ -1.4\,N & 8\,Nm \end{bmatrix} \qquad \mathbf{K}_{s,z}^{-} \approx 10^{7} \cdot \begin{bmatrix} 1.5\,\tfrac{N}{m} & -3\,N \\ -3\,N & 12\,Nm \end{bmatrix}$$

Transmitting Boundary Element in Abaqus

In order to implement the transmitting boundary element in Abaqus, the definitions of degrees of freedom are considered. The plane beam is considered in the vertical and lateral plane as shown in Figure 105 (a) and (b), respectively, while the three-dimensional beam element in Abaqus has six degrees of freedom at each node as shown in Figure 105 (c).
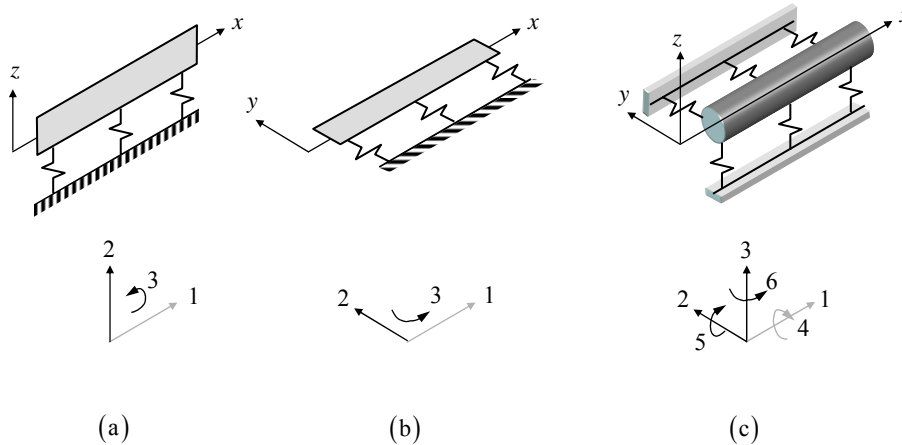

Figure 105: Degrees of freedom of beam element in vertical plane (a), lateral plane (b) and in Abaqus (c). Inactive degrees of freedom are shown in gray.

The relationships between the active degrees of freedom of the two models may be determined upon study of Figure 105 and are given in Table 19.

Table 19: Relationships between active degrees of freedom.

Matlab		Abaqus	Direction
Vertical	Lateral		
-	2	2	Same
2	-	3	Same
3	-	5	Opposite
-	3	6	Same

The transmitting boundary element is implemented in Abaqus as a user-defined linear element with a single node and four active degrees of freedom. A user-defined element is connected to the PIPE31-beam element in each end of the model. The matrices of the user-defined elements are derived from (4.2.43) for both the vertical and lateral plane. In the first case, the off-diagonal components of the boundary element matrices should change sign due to the opposite direction of the degrees of freedom according to Table 19. Thus, the final stiffness, damping and mass matrices for the left and right transmitting boundary element in Abaqus, respectively, are given as

$$-\mathbf{f}_a = -\left(f_{a,2}, f_{a,3}, f_{a,5}, f_{a,6}\right) = \mathbf{K}_a\,\mathbf{x}_a + \mathbf{C}_a\,\dot{\mathbf{x}}_a + \mathbf{M}_a\,\ddot{\mathbf{x}}_a,$$

$$\mathbf{x}_a = \left(x_{a,2}, x_{a,3}, x_{a,5}, x_{a,6}\right),$$

$$\mathbf{A}_a^- = \begin{bmatrix} A_{11,y}^- & 0 & 0 & -A_{12,y}^- \\ 0 & A_{11,z}^- & A_{12,z}^- & 0 \\ 0 & A_{21,z}^- & A_{22,z}^- & 0 \\ -A_{21,y}^- & 0 & 0 & A_{22,y}^- \end{bmatrix}$$

$$\mathbf{A}_a^+ = \begin{bmatrix} -A_{11,y}^+ & 0 & 0 & A_{12,y}^+ \\ 0 & -A_{11,z}^+ & -A_{12,z}^+ & 0 \\ 0 & -A_{21,z}^+ & -A_{22,z}^+ & 0 \\ A_{21,y}^+ & 0 & 0 & -A_{22,y}^+ \end{bmatrix} , \quad A = K, C, M$$

$$(4.2.46)$$

4.2.4 BENCHMARK TEST

A benchmark test has been performed to verify the results of the analytic and element formulation in Matlab and Abaqus. In the case of propagating waves, the benchmark test is limited to verification of the analytic solution and the Matlab Model since the implementation of user-defined damping matrices in Abaqus appears to be rather complicated.

The transmitting boundary elements are considered to be correctly implemented if the time history of the displacements and rotations at equivalent sections are identical for a small model with transmitting boundary elements at its beam-ends and a large model without transmitting boundary elements. The sections that are investigated are the mid-sections and another section where the response is linear and not negligible. The sections are shown in Figure 106 as the dashed lines (A) and (B), respectively, for the large and small model.
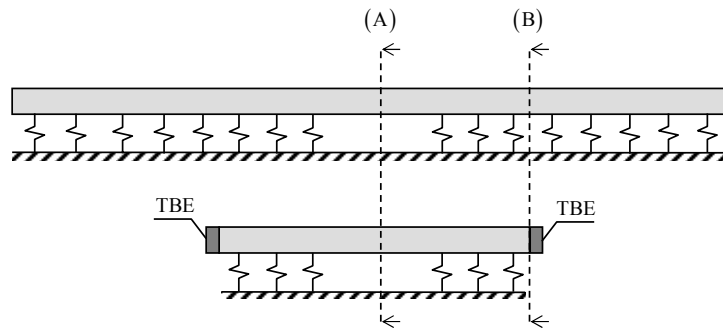

Figure 106: Investigated sections in benchmark test. Above: Large model without a transmitting boundary. Below: Small model with transmitting boundary elements (TBE) in the beam-ends. The mid-sections are denoted with (A) and the other sections are denoted with (B).

4.2.4.1. Tests For Evanescent Waves

In the case of evanescent waves, the benchmark test has been performed on four distinct cases with progressive complexity. The first case is a plane beam with linear soil springs, a plane harmonic concentrated load at the mid-section and without a free-span. The fourth case is a three-dimensional beam with non-linear soil springs and distributed harmonic loads in two dimensions along the free-

span. In all cases, the harmonic load has been applied with a magnitude that grows exponentially from zero to its maximum after some time. This has been done to avoid impulse response due to initial conditions. The details of the individual cases are given in Table 20. The analytical formulation and the models in Matlab are located in [DVD/Matlab Model] whereas the models in Abaqus are located in [DVD/Transmitting Boundary].

Table 20: Details of the investigated cases with progressive complexity for evanescent waves.

Case	Free-span	Load type	Spring behaviour	Models
E1	No	1-D Central	Linear	Analytic, Matlab
E2	Yes	1-D Central	Linear	Matlab, Abaqus
E3	Yes	2-D Distributed	Linear	Matlab, Abaqus
E4	Yes	2-D Distributed	Non-linear	Abaqus

All cases show nearly identical results between the large and small model with transmitting boundary elements. In the following, the benchmark results are shown for case E4 that compares a large 220-meter-model with 50-meter and 40-meter-models that have beam-ends that are fixed, free or attached to transmitting boundary elements.

The time history of the distributed loads is shown in Figure 107. The in-line load frequency is taken as 0.10 Hz and the cross-flow load frequency is taken as 0.20 Hz which are both below the cut-on frequencies. The maximum magnitude has been chosen large enough to induce non-linear displacements in the springs. Since the load varies harmonically, the response is expected to vary harmonically.
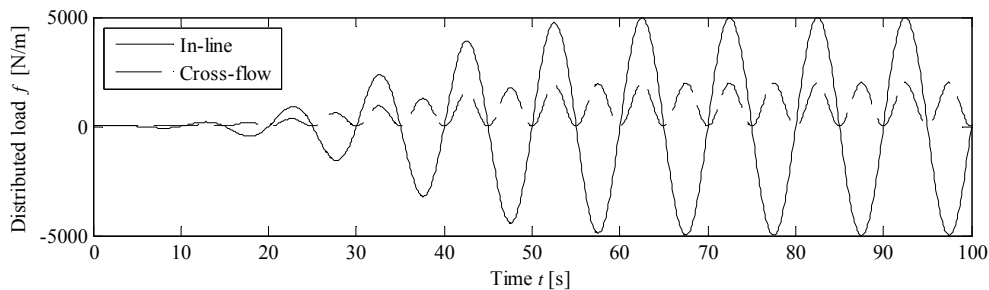

Figure 107: In-line and cross-flow distributed loads in case E4.

The time history of the lateral and vertical displacements at the mid-section are shown in Figure 108 and Figure 109, respectively. The vertical displacement for the small 40-meter model with free ends in Figure 109 terminates at $t \approx 50\,\text{s}$ due to numerical instability.
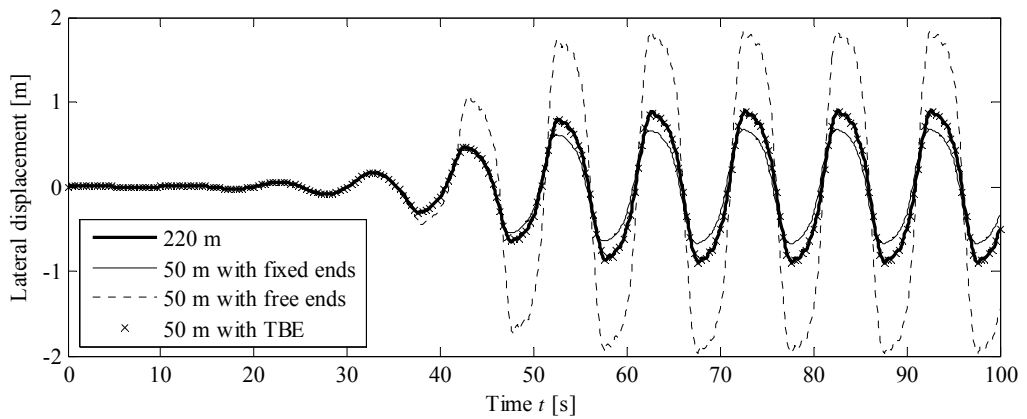
Figure 108: Lateral displacement at mid-section for varying boundary conditions in case E4.
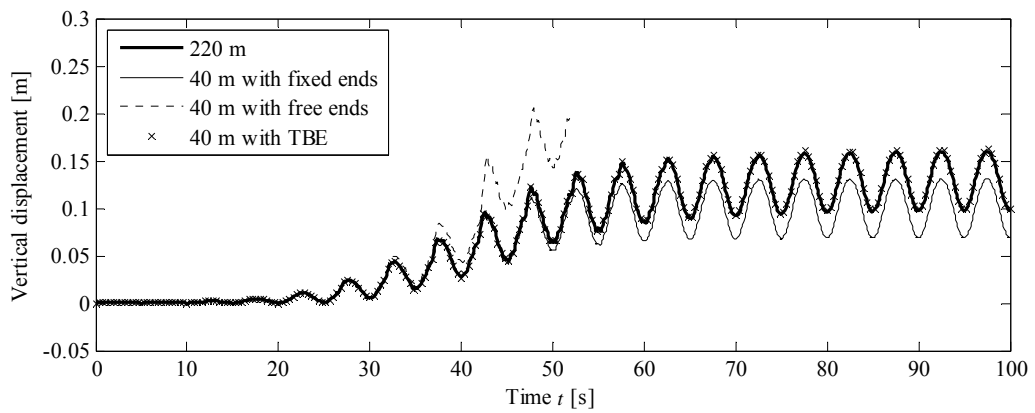

Figure 109: Vertical displacement at mid-section for varying boundary conditions in case E4.

It is seen from Figure 108 and Figure 109 that the small models with transmitting boundary elements correctly predict the history of the large model while the small models with free and fixed beam-ends provide upper and lower bounds on the magnitude of the displacement, respectively. The non-linearity of the vertical springs is evident due to the evolution of the average vertical displacement which is zero in the beginning of the analysis and about 0.12 m at the end of the analysis.

4.2.4.2. Tests For Propagating Waves

In the case of propagating waves, the benchmark test has been performed on three distinct cases whose details are given in Table 21. The latter case represents a plane beam with linear soil springs with a plane distributed harmonic load along the mid-span.

Table 21: Details of the investigated cases with progressive complexity of propagating waves.

Case	Free-span	Load type	Spring behaviour	Models
P1	No	1-D Central	Linear	Analytic, Matlab
P2	Yes	1-D Central	Linear	Matlab
P3	Yes	1-D Distributed	Linear	Matlab

Again, all cases show nearly identical results between the large and small model with transmitting boundary elements. In the following, case P3 will be illustrated which compares 220-meter models that have beam-ends that are fixed, free or attached to transmitting boundary elements.

A harmonic-ramp load has been applied at the load frequency 20 Hz which is above the cut-on frequency. The load history is shown in Figure 110.
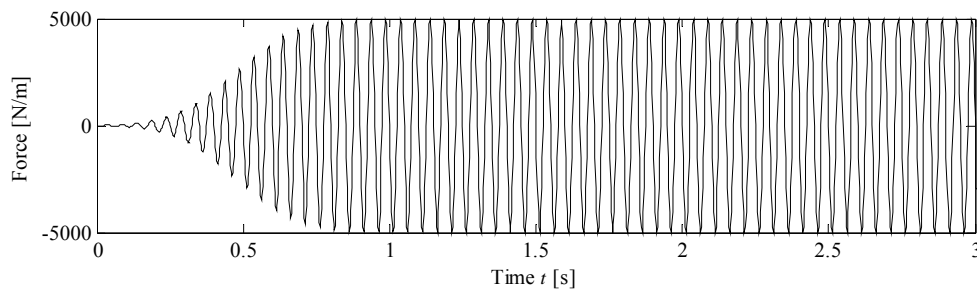

Figure 110: Distributed load in case P3.

The displacements at the end-section and mid-section are shown in Figure 111 and Figure 112, respectively.
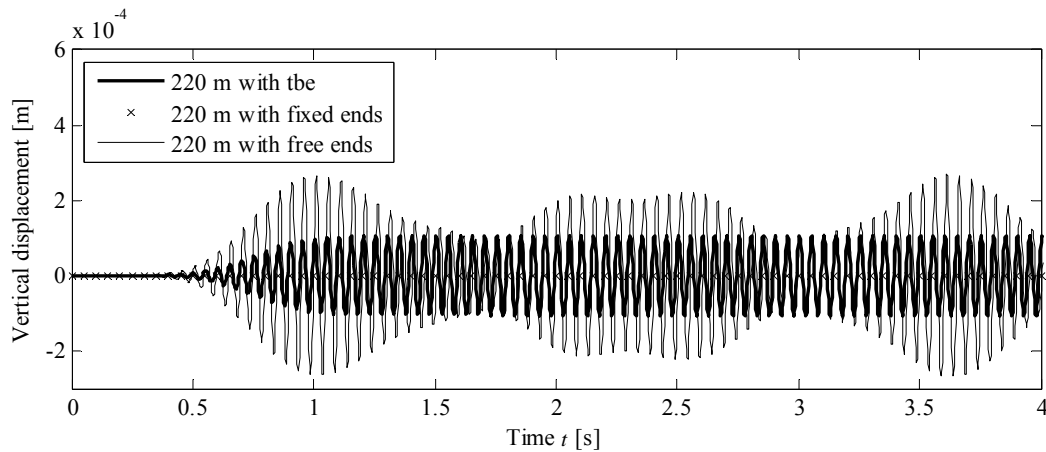

Figure 111: Vertical displacement at end-section for varying boundary conditions in case P3.
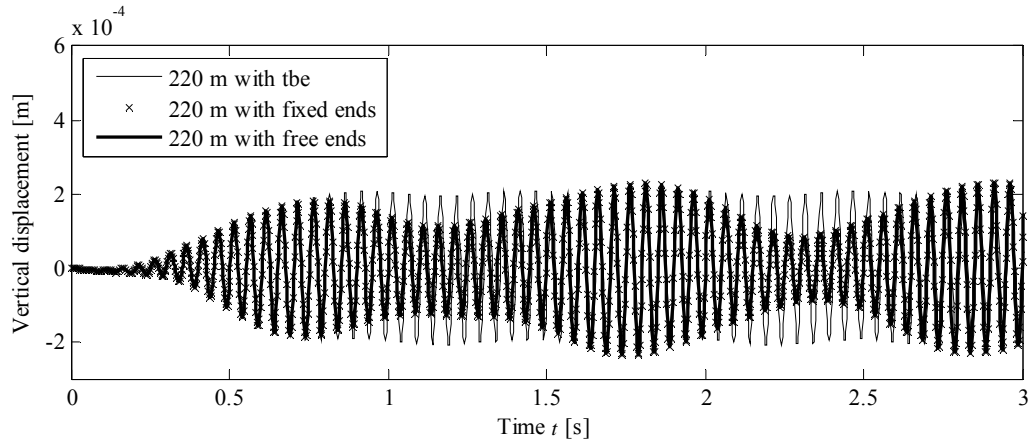
Figure 112: Vertical displacement at mid-section for varying boundary conditions in case P3.

It is seen from Figure 111 and Figure 112 that the model with transmitting boundary elements correctly provides a harmonic response with nearly constant amplitude. In contrast, the models with fixed or free ends exhibit wave interference where the waves are reflected back when they meet the boundary. It is seen that the first waves have travelled back to the mid-section at $t \approx 0.7\,\mathrm{s}$. Interestingly, the models with fixed or free ends experience identical response which has been verified by observation of the deformed shape of the entire pipeline.

4.2.5 EVALUATION

First, it is concluded that the properties of the pipeline, soil and load only provide evanescent waves in this project. This means that the waves in the pipeline that are induced by the hydrodynamic forces will reside relatively near the load source and will vanish before they reach the pipe-ends when the side-spans are wide enough. Thus, the implementation of a transmitting boundary in this project is hardly necessary.

Secondly, the transmitting boundary elements of this project may only be calibrated against a single load frequency but the hydrodynamic loads from irregular waves will act upon the pipe at a range of load frequencies. It has been estimated that a possible variation in the in-line load frequency 0.08-0.23 Hz and the cross-flow load frequency 0.16-0.48 Hz does not affect the coefficients c_1, c_2 that govern the boundary element stiffness matrices in the case of evanescent waves. Thus, the transmitting boundary elements are expected to perform satisfactorily during an analysis with irregular waves once they have been tuned to an arbitrary load frequency within the mentioned ranges. However, such an analysis has not been performed in this project.

Lastly, the efforts that are involved in deriving, verifying and implementing a transmitting boundary element may greatly exceed its computational gains. In practice, the method of using a boundary zone of highly damped material may be considered as an alternative. In the case of propagating waves, the damping matrices of the transmitting boundary elements appear to be difficult to implement in a commercial FEM-program such as Abaqus.

4.3 LIQUEFACTION

Liquefaction is a geotechnical failure concept which was initially developed to explain failure of soil due to cyclic excitation from earthquake. In this project, liquefaction is analysed in a different context, namely that soil at the pipe shoulders is exposed to cyclic excitation due to hydrodynamic loads at the free-span.

This chapter includes the following main subjects:

- Liquefaction mechanism
- Susceptibility for liquefaction
- Numerical modelling of liquefaction
- Liquefaction hazard assessment for a free-span

In the early state of this project, it was a part of the project scope to make a numerical model that describes liquefaction considering a pipeline free-span. Limitations in the pre-defined material models that are available in the used version of Abaqus have made this quest difficult and it has been considered to be beyond the project scope to implement a user-defined material model that would be able to adopt the liquefaction mechanism of the soil. The section on numerical modelling of liquefaction has instead become a presentation of the used material model, what it is missing to describe liquefaction and a suggested approach in case an appropriate material is available.

Since the numerical modelling of liquefaction failed, the liquefaction hazard for a free-span is evaluated in a qualitative matter based upon the knowledge of liquefaction mechanism and liquefaction susceptibility.

This chapter follows the traditional geotechnical sign-convention where stresses and strains are defined positive in compression.

4.3.1 LIQUEFACTION MECHANISM

Liquefaction is a concept of failure for saturated friction soil which is exposed to cyclic load during a limited period of time. Liquefaction happens when the soil is exposed to cyclic excitation causing collapse of the grain structure and development of excess pore pressure if drainage is prevented. This leads to reduced friction between the grains which decreases the bearing capacity of the soil. In the worst case, the soil begins to act like a fluid when the effective stresses decrease to zero. Figure 113 illustrates the collapse of the soil grain structure.
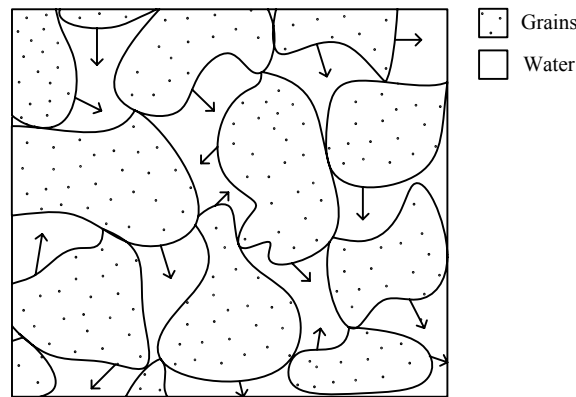
Figure 113: Collapse of grain structure in soil. The arrows indicate displacements of the grains.

The stresses in the soil are according to Terzaghi's effective stress principle composed by effective stresses and pore pressure. Because water is assumed not to sustain any shear stresses, the effective shear stresses are equal to the total shear stresses. The soil stresses can be described as

$$\boldsymbol{\sigma} = \begin{bmatrix} \sigma_{11} & \sigma_{22} & \sigma_{33} & \sigma_{12} & \sigma_{23} & \sigma_{31} \end{bmatrix}^{T}$$

$$\boldsymbol{\sigma} = \boldsymbol{\sigma}' + p_{w}\mathbf{I}, \qquad \boldsymbol{\sigma}' = \begin{bmatrix} \sigma'_{11} & \sigma'_{22} & \sigma'_{33} & \sigma'_{12} & \sigma'_{23} & \sigma'_{31} \end{bmatrix}^{T} \qquad (4.3.1)$$

$$\mathbf{I} = \begin{bmatrix} 1 & 1 & 1 & 0 & 0 & 0 \end{bmatrix}^{T}$$

where

$\boldsymbol{\sigma}$ is the total stress in the soil, defined as positive in compression [Pa]

$\boldsymbol{\sigma}'$ is the effective stress in the soil, defined as positive in compression [Pa]

p_{w} is the pore pressure [Pa]

T denotes matrix transpose

[Ovesen et al. 2007, p49]

Liquefaction is not a concept of how the total stresses vary with the external load but how the stress distribution between effective stresses and pore pressure changes over time.

Friction soil is however not always susceptible to liquefaction. If the soil may be drained, a densification of the soil will happen which will increase the bearing capacity of the soil. This is also what is exploited in the building industry when preparing loose friction soil for the foundation of structures.

The initial void ratio of the soil does also have an impact on how the soil reacts to cyclic excitation. Dense soil will tend to dilate during drained loading which will reduce the pore pressure during undrained conditions and increase the effective stresses. This will have the opposite effect of liquefaction and increase the bearing capacity of the soil momentarily, also known as stabilization.

4.3.1.1. Basic Concepts

Liquefaction may be divided into two main phenomena – flow liquefaction and cyclic mobility [Kramer 1996, p349]. The basic principles of the two phenomena are explained in the following:

- **Flow liquefaction:** This is a phenomenon of instability that occurs when the static shear stress exceeds the shear strength of the liquefied soil which results in instant failure of the soil. This is also why flow liquefaction is known to be the most dramatic effect of all the liquefaction-related phenomena. Flow liquefaction is often the reason why some slopes become unstable during an earthquake but the phenomenon has also caused instability of large structures.

- **Cyclic mobility:** This is a case of soil failure driven by the static and cyclic stresses exceeding the shear strength of the liquefied soil which can cause large incremental displacement of the soil. This phenomenon can cause severe damage to structures, roads etc. when the soil is exposed to an earthquake.

The susceptibility zones for flow liquefaction and cyclic mobility are illustrated in Figure 114.
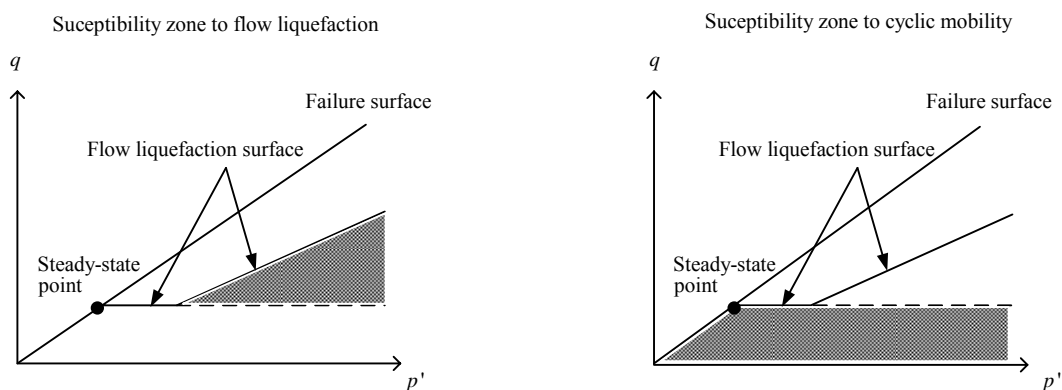

Figure 114: Susceptibility zones to flow liquefaction (left) and cyclic mobility (right), respectively. Adopted from [Kramer 1996, pp366-367]. q is the deviatoric stress and p' is the effective mean stress.

To understand the illustration in Figure 114, the definition of the flow liquefaction surface and the steady state point is explained in the following:

- **Flow liquefaction surface:** This describes the initiation of flow liquefaction in a stress space by a three dimensional surface. In practice, it is difficult to measure but it provides in conjunction with the steady-state concept a very useful framework for the conceptual understanding of the relationships between the various liquefaction phenomena [Kramer 1996 p361].

- **Steady-state point:** This describes a point that defines the residual shear strength of the liquefied soil. This mainly depends upon the initial void ratio of the soil and moves toward

the origin of the (q, p') -diagram if the soil is loose. In order to obtain flow liquefaction, the point of static shear stresses must be placed above the steady-state point in Figure 114.

4.3.2   SUSCEPTIBILITY FOR LIQUEFACTION

The primary parameters affecting the susceptibility for liquefaction have been summarized in this section. Table 22 shows the parameters that increase the susceptibility of flow liquefaction and cyclic mobility. Table 22 is compiled upon the theory of liquefaction in [Kramer 1996, pp348-422].

Table 22: Tendency of primary parameters that increase the susceptibility for liquefaction.

Parameter		Flow liquefaction	Cyclic mobility
Soil	Saturation	Must be fully saturated	
	Cohesion	Little or none	
	Type of grains	Round and well-sorted	
	Void ratio	Large (loose soil)	Large or small
	Drainage	Little	
	Consolidation ratio	Small	
	Earth pressure coefficients	Small	
	Initial stresses	Large	Small
Load or displacement	Amplitude	Large	
	Frequency	High	
	Excitation	Multi-directional	
	Time of sustained pressure	Short time	
	Load-displacement history	No previous cyclic excitation	

Since the parameters that influence the susceptibility for liquefaction are many and not of equal importance, it is a rather complex matter to evaluate whether liquefaction will be an issue considering a structural problem. However, Table 22 provides indication of how probable liquefaction will be by evaluating the parameters.

4.3.3   NUMERICAL MODELLING OF LIQUEFACTION

In this section, numerical modelling of liquefaction has been attempted. First, the key ingredients for numerical modelling of liquefaction are presented. These are important to know in order to understand their application scope and why the numerical modelling of liquefaction in this project has not been possible. Then follows a comparison of measured and predicted soil response. Finally, given an appropriate plastic model, an approach for a numerical model of liquefaction of the pipe free-span is suggested.

4.3.3.1. Key Ingredients

Several key ingredients are required for numerical modelling of liquefaction: An effective stress principle for the two-phase soil, an elastic model for elastic behaviour and an appropriate plastic model for describing the development of plastic strains. In addition, when considering locally drained conditions, a pore-fluid model is required to describe the flux through the soil and the

development of pore pressure. Abaqus offers all these except an appropriate plastic model that offers plastic strains during cyclic loading which is described later. The effective stress principle is given in (4.3.1) while the remaining ingredients are described in the following.

Darcy Flow and the Continuity Equation

In Abaqus, a pore-fluid model is seamlessly incorporated into the dynamic analysis by the use of continuum pore pressure elements. These elements have the conventional degrees of freedom at the nodes for general displacements or forces and an additional degree of freedom for pore pressure or flux.

The relationship between flux and pore pressure is described by Darcy's law which is a good model for flow at relatively low velocity through soil. Darcy's law in three dimensions is described as

$$v_i = -k \cdot \frac{\partial \Phi}{\partial x_i}, \qquad \Phi = z + \frac{p_w}{\gamma_w}, \qquad i = 1, 2, 3 \tag{4.3.2}$$

where

v	is the flux along the coordinate x_i of the pore-fluid per unit area [m/s]
k	is the hydraulic conductivity [m/s]
Φ	is the piezometric head [m]
z	is the elevation from a reference elevation [m]
γ_w	is the fluid weight [N/m^3]

[Ovesen et al. 2007, pp75-76; Dassault Systèmes 2007b, Section 2.8.4]

The conservation of pore-fluid is described by the continuity equation

$$\frac{\partial v_1}{\partial x_1} + \frac{\partial v_2}{\partial x_2} + \frac{\partial v_3}{\partial x_3} = 0 \tag{4.3.3}$$

[Ovesen et al. 2007, p76]

When performing soil procedures in Abaqus, the compressibility of the pore water in the soil may be considered. In practice, the pore water is usually assumed to be incompressible which is a good approximation when describing consolidation of soil.

Linear and Porous Elasticity

The elastic response may be modelled by different elastic models. With the geotechnical sign-convention of this section, a linear isotropic model provides

$$\frac{1}{K} \cdot (p_0 - p) = -\varepsilon_{vol}^{el}, \qquad p = \tfrac{1}{3} \cdot (\sigma_{11} + \sigma_{22} + \sigma_{33}) \tag{4.3.4}$$

where
K	is the bulk modulus [Pa]
p_0	is the initial total mean stress [Pa]
p	is the total mean stress [Pa]

σ is the total stress in the soil, defined as positive in compression [Pa]

ε_{vol}^{el} is the elastic volumetric strain, defined as positive in compression [-]

[Rice 1998, p3]

In contrast, a poroelastic material model allows the elastic bulk modulus to be pressure-dependent in a logarithmic fashion which is typical for soils [Zienkiewicz et al. 1999, p113]. Several definitions exist. In Abaqus, the following logarithmic model is available where the geotechnical sign-convention has been used

$$\frac{\kappa}{\left(1+e_0\right)} \cdot \ln\left(\frac{p_0 + p_t^{el}}{p + p_t^{el}}\right) = J^{el} - 1 = -\varepsilon_{vol}^{el} \qquad (4.3.5)$$

where

κ is a logarithmic bulk modulus [-]

e_0 is the initial void ratio [-]

p_t^{el} is the absolute total mean stress at large compaction [Pa]

J^{el} is a Jacobian for the elastic volume ratio of the current and reference states [-]

[Dassault Systèmes 2007, Section 17.3.1]

The relationship between pressure and elastic volumetric strain for linear and porous elastic materials is illustrated in Figure 115 where the bulk modulus is the slope of the curves.
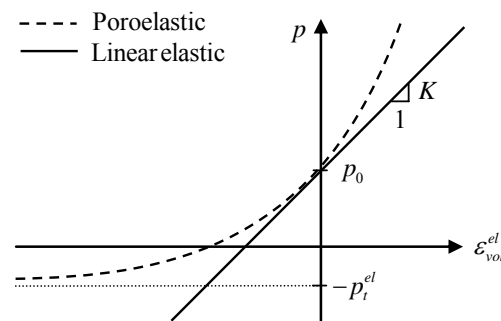

Figure 115: Relationship between pressure and elastic volumetric strain for linear and porous elastic materials.

The shear stiffness of the material can be computed either by assuming constant shear modulus or constant Poisson's ratio ν. The latter results in increased shear stiffness as the material is compacted.

The porous elastic material model in Abaqus may be combined with a few plastic models which are the extended and modified Drucker-Prager models and the modified Critical State model. The latter is described in the following.

Critical State Plasticity

The plastic response is modelled by a Critical State model which is also known as a Cam-Clay model. This is a classical plasticity model for soil that was originally developed at Cambridge University (1968). A Critical State model features an elastic model for elastic strains, a yield surface

and/or a plastic potential for the plastic strains and a hardening/softening rule that allows the yield surface to grow or shrink.

A Critical State model is based upon the critical state of the soil which is also known as the characteristic state or state of critical void ratio. This is defined as the state when the soil volume or pore pressure does not change under drained or undrained conditions, respectively. Triaxial experiments have shown that the critical state is a linear relationship between the deviatoric stress and mean pressure and the relationship is independent of the initial void ratio, stress path and drainage conditions [Ibsen 1993, pp27-33; Kramer 1996, pp355-357]. The linear relationship is given by the critical state line

$$q = M \, p', \qquad q = \sigma'_{11} - \sigma'_{33}, \quad p' = \tfrac{1}{3} \cdot \left(\sigma'_{11} + \sigma'_{22} + \sigma'_{33} \right) \qquad (4.3.6)$$

where

q	is the deviatoric stress [Pa]
p'	is the effective mean stress [Pa]
σ'	is the effective stress in the soil, defined as positive in compression [Pa]
M	is an empirical slope of the critical state line, usually equal to 1.2-1.3 [-]

The idea in a Critical State model is that the top-point of the yield surface intersects the critical state line. When assuming associated plasticity, the normal vector at the yield surface denotes the direction of the change in plastic strains. Thus, stress states at the yield surface that are above the critical state line result in dilation or decreasing pore pressure during drained or undrained conditions, respectively, which allows stabilization. In contrast, stress states at the yield surface that are below the critical state line result in compaction or pore pressure build-up during drained or undrained conditions, respectively, which allows liquefaction. The domains above and below the critical state line are usually refered to as the "dry" and "wet" zone, respectively. The characteristics are illustrated in Figure 116 for a compressive deviatoric stress where CSM denotes a Critical State model.
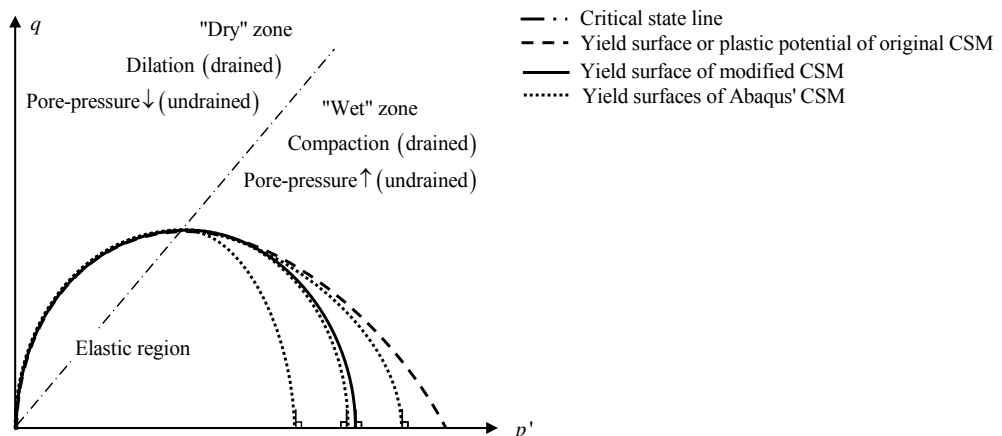

Figure 116: The critical state line and different formulations of the Critical State model.

As shown in Figure 116, the original Critical State model is based upon non-associated plasticity and an elliptic-like yield surface and plastic potential. The modified Critical State model is based upon

associated plasticity and an elliptic yield surface that is vertically symmetrical about the top-point. Abaqus uses the modified model but with a possible semi-elliptic yield surface where the end-cap of the yield surface in the wet zone may be moved. [Zienkiewicz et al. 1999, p120-124; Dassault Systèmes 2007, Section 17.3.1] In the remaining section, the modified Critical State model is illustrated in which the elastic response is modelled by linear elasticity.

The evolution of the yield surface may be illustrated by considering an initially loose and dense sample of the same specimen that is axially and monotonically strained from the same initial stress state during drained conditions. This is illustrated in Figure 117 left and right, respectively. The letters A-D denote stress states at progressive time instances while the numerals I, II, III denote the initial, intermediate and final yield surface.
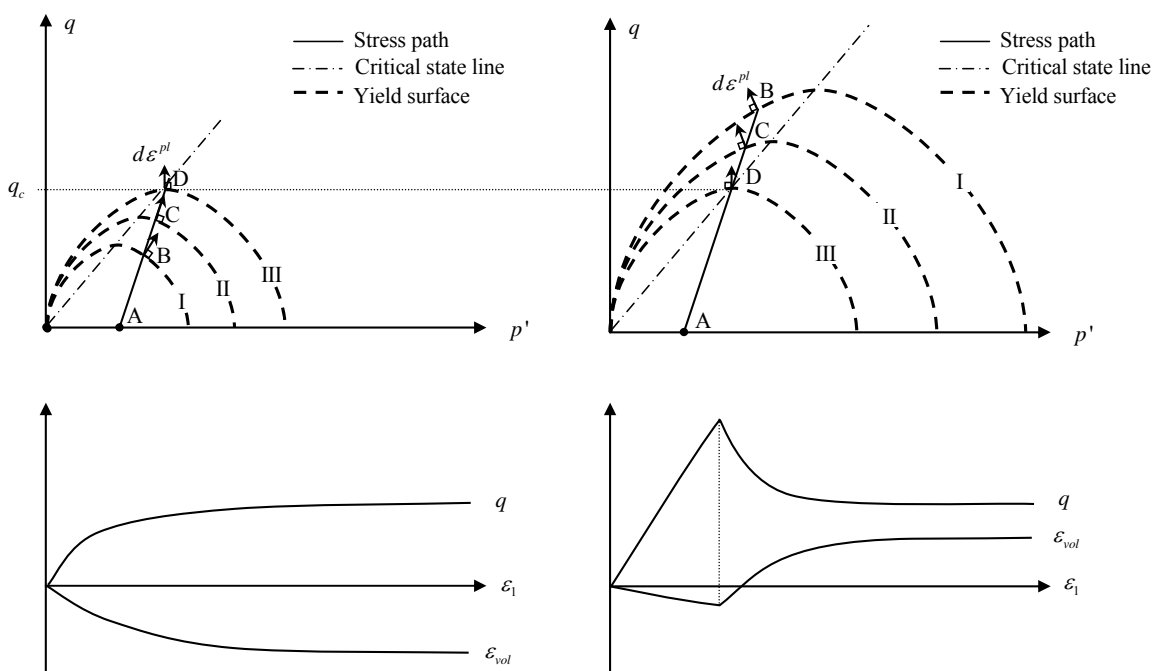

Figure 117: Schematized evolution of yield surfaces (top) and strain curves (bottom) in a Critical State model for an initially loose (left) and dense (right) sample of the same specimen during drained monotonic axial straining from the same initial stress state. Arrows indicate the direction of plastic strains. ε_{vol} denotes the total volumetric strain.

It is seen from Figure 117 left, that the initially loose sample has an initial yield surface of relatively little size. During axial straining, the sample will compact elastically along the path A-B and then compact elastoplastically along the path B-C until it reaches the critical state at point D with the shearing strength q_c. It is seen from Figure 117 right that the initially dense sample has an initial yield surface of relatively large size. During axial straining from the same initial stress state as the initially loose sample, the initially dense specimen will compact elastically from point A to B, where the stress state reaches the yield surface and experiences its ultimate shearing strength $q > q_c$. Once the yield surface has been reached, it shrinks as the sample dilates elastoplastically along path B-C until the critical state at point D is reached. It is observed that the Critical State model predicts that both an initially loose and dense sample that is strained from an identical initial stress state reach the same critical state but have varying ultimate shearing strengths.

4.3.4 COMPARISON OF MEASURED AND PREDICTED RESPONSE

In this section, comparisons are performed between measured and predicted soil response. The first qualitative comparison illustrates the soil behaviour under drained and undrained conditions and deals with the corresponding performance of a Critical State Model. The second quantitative comparison deals with measured and numerical response during undrained cyclic loading.

4.3.4.1. Undrained and Drained Monotonic Axial Straining

The soil response during drained and undrained conditions under monotonic axial straining has been illustrated in Figure 118 (top) and (bottom), respectively. In addition, the failure curves under drained conditions and the critical state line are shown. An initially loose or dense sample is taken to correspond to the predicted response for a normally or over-consolidated soil.
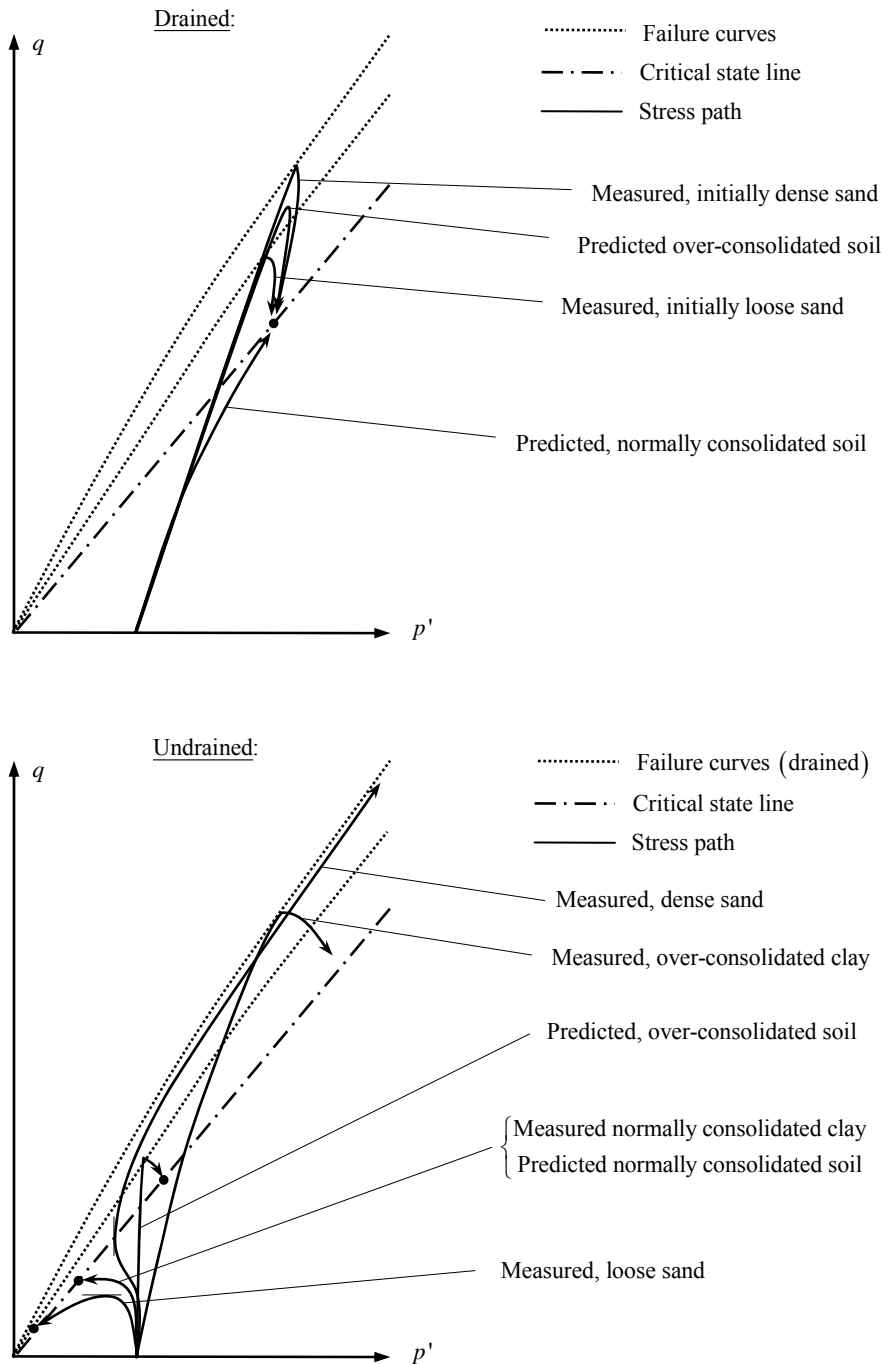
Figure 118: Schematized soil response according to measurements and predictions of the Critical State Model during monotonic, axial straining in drained (top) and undrained (bottom) conditions. Compiled upon study of [Zienkiewicz et al. 1999, pp118-127; Ibsen 1993, pp19-35; Andersen 2006b]

It may be seen from Figure 118 (top) that there is a reasonable agreement between measured and predicted response of sand during drained conditions. The difference in the stress path and the ultimate strength of sand between the measured and predicted response is less critical since the predicted response is conservative.

It may be seen from Figure 118 (bottom) that poor agreement is found between measured and predicted response during undrained conditions, except for a normally consolidated clay. The measured response of loose sand shows that flow liquefaction occurs when the deviatoric stress suddenly drops and the stress state ends at the steady-state point. In contrast, the predicted stress state ends at the critical state and thus overestimates the ultimate strength. For dense sand, measurements show that stabilization occurs where the shear strength continues to increase with the effective mean stress. The stress path appears to asymptotically follow the drained failure curve which explains the fact that drained strength parameters of a dense sample may be extracted from an undrained triaxial test. In contrast, the predicted response of dense sand results in a much smaller ultimate strength and a stress state that ends in the critical state. In this case, the predicted response is very conservative.

The comparison above concerns monotonic axial straining. A comparison during cyclic loading is performed in the next section.

4.3.4.2. Undrained Cyclic Loading

The measured and predicted response during undrained cyclic loading follows the experimental triaxial test program no. 8727 of the sand specimen "Lund no. 0" [Ibsen 1993b]. The model database of the numerical model may be found in [DVD/Liquefaction/triax_8727.cae]

The loads, boundary conditions and dimensions of the sample are defined in Figure 119. The numerical model is axisymmetrical in order to reduce the number of degrees of freedom without any loss in accuracy. The vertical displacements are restrained along the bottom surface of the numerical model while the lateral displacements are restrained along the centroidal axis of the sample. The boundary conditions along with identical height and diameter according to Danish laboratory traditions ensures a homogenous stress state in the sample which is important for an accurate estimation of the soil strength. [Ibsen 1993, pp13-16]
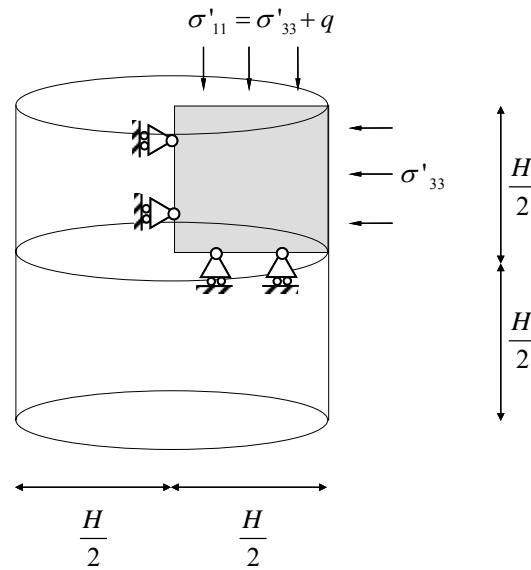
Figure 119: Loads, boundary conditions and dimensions of the sample. The gray part denotes the modelled part.

The material parameters of the sample are:

$$H = 0.070\,\text{m}, \qquad e_0 = 0.617, \qquad M = 1.18$$

The loose sample corresponds to a density index $D_R = 25\%$, i.e. a loose sample. The following porous elastic properties have been estimated where the shear stiffness is computed by Poisson's ratio:

$$\kappa = 0.0044, \qquad p_t^{el} = 0, \qquad \nu = 0.3$$

The triaxial test is performed in three steps: isotropic consolidation, anisotropic consolidation and finally undrained cyclic loading. The steps and the corresponding initial stresses, final stresses and numerical procedure are given in Table 23. The stress path from the end of the first step to the beginning of the second step has not been described in the experiment and is of minor importance.

Table 23: Description of steps and the corresponding initial and final stress states and numerical procedures. t denotes the time coordinate.

Step	Description	Initial stress state	Final stress state	Numerical procedure
1	Isotropic consolidation	$q = p' = 0$	$q = 0, \quad p' = 100\,\text{kPa}$	Specification of initial size of yield surface
2	Anisotropic consolidation	$q = q_s = 27\,\text{kPa}$ $p' = 32\,\text{kPa}$	$q = q_s = 27\,\text{kPa}$ $p' = p_s' = 41\,\text{kPa}$	Stationary soils procedure (drained)
3	Undrained cyclic loading with constant confining pressure σ'_3	$q = q_s + q_{cyc}$, $p' = p_s' + \frac{1}{3}q_{cyc}$, $q_{cyc} = 34\,\text{kPa} \cdot \sin\left(0.63\frac{\text{rad}}{\text{s}} \cdot t\right)$	-	Transient soils procedure (undrained)

The observed and predicted response during the undrained cyclic loading step is shown in Figure 120. In addition, the curve for drained failure (FC) at the given initial void ratio, the asymptotic undrained stress curve for a dense sample of the specimen (SC), the critical state line (CSL) and the

initial yield surface in the modified Critical State model are shown. The initial stress state is from the beginning of the undrained cyclic loading step.
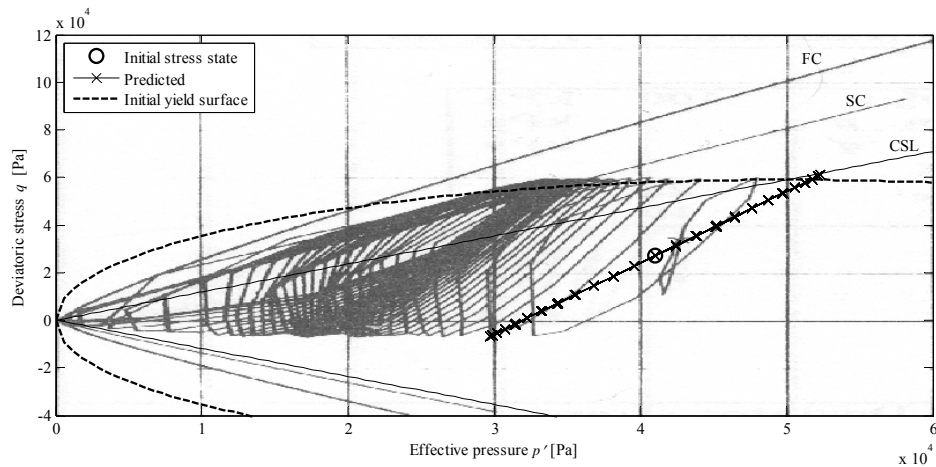

Figure 120: Measured and predicted response during cyclic loading. Measured response is from [Ibsen 1993b].

It may be seen from Figure 120 that the initial effective stress state is below the critical state line which indicates susceptibility for liquefaction. The first time the initial yield surface is touched in the numerical model, the yield surface is inflated and the pore pressure increases. However, since the effective stress path reverses before the critical state is reached, the subsequent response becomes elastic where the effective stress travels back and forth along the same path. In contrast, the measured response clearly shows the reduction of effective stresses due to pore pressure build-up.

It turns out that in a classical plasticity model, e.g. a Critical State, Mohr-Coulomb or Drucker-Prager model, plastic strains cannot develop within the yield surface. Since this is the domain where cyclic loading occurs, the classical plasticity models cannot reproduce liquefaction [Zienkiewicz et al. 1999, p129]. The development of cyclic plastic material models is currently a field of research.

Abaqus offers a plastic model specifically for cyclic loading which is illustrated in Figure 121. This is based upon nested yield surfaces where the inner yield surface follows the stress state and introduces plastic strains. Unfortunately, the yield surfaces in the material model are based upon deviatoric stresses alone and not the effective mean stress. This is well-suited for metals but a poor assumption for soil.
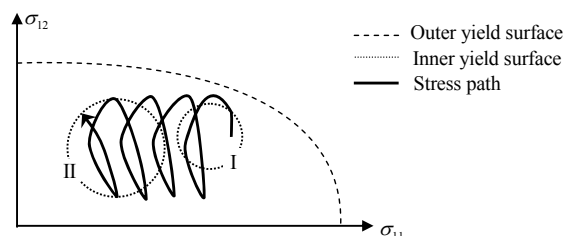

Figure 121: Schematized evolution of inner yield surface and pore pressure build-up during cyclic loading due to plastic strains in a plastic model with nested yield surfaces. I and II denote the initial and final inner yield surface. σ_{11} and σ_{12} denote a principal and deviatoric stress, respectively.

4.3.4.3. Suggested Modelling of Liquefaction Considering a Free-span

This section explains a possible set-up for numerical modelling of the pipeline free-span if sufficient material models had been available. The objective is to determine if the hydrodynamic loads affecting the pipeline free-span result in liquefaction of the soil near the free-span shoulder.

The numerical modelling of the liquefaction problem could be analysed as an equivalent two-dimensional problem. This procedure is explained in three steps:

- **Step 1** is to calculate the lateral and vertical displacements in a section near the shoulder of the free-span when the pipeline is affected by hydrodynamic load. This could be done in a three-dimensional Winkler Model as described in Chapter 5.1 (Winkler Model). The position of a possible section of interest is shown in Figure 122 as section A-A.
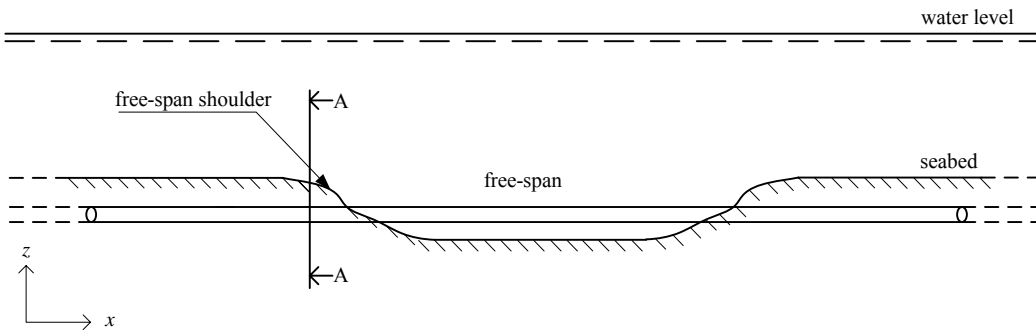

Figure 122: Position of section A-A where the displacements are extracted for the two-dimensional model.

- **Step 2** is to transfer the calculated displacements into a two-dimensional numerical model of the pipe and soil in section A-A. Figure 123 shows the principal geometry for the 2-dimensional model. The boundaries of the model should be drained and a pore-fluid model could allow locally undrained conditions.
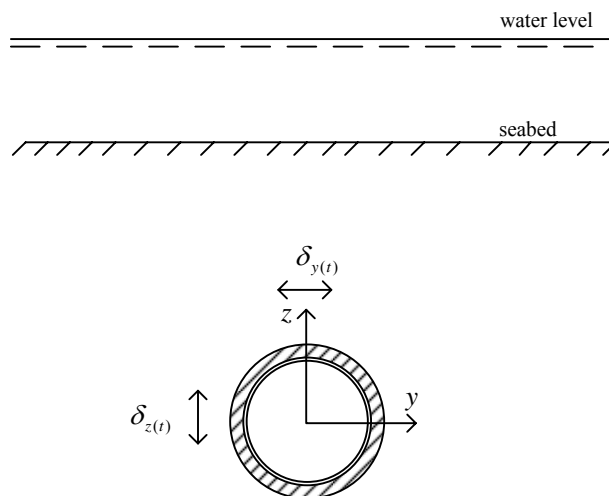

Figure 123: Principal two-dimensional model for liquefaction analysis.

- **Step 3** is to evaluate the effective stresses and pore pressure in the soil around the pipeline in section A-A to determine if excess pore pressure is present for the applied cyclic displacements. If excess pore pressure is present due to the cyclic excitation, the effect of this has to be evaluated considering either flow-liquefaction or cyclic mobility.

The above-mentioned procedure is based upon the assumption that the flow problem of the pore water can be considered to be a two-dimensional problem. This is considered to be a conservative approximation since the drainage distance towards the seabed will be largest in the two-dimensional model. It is noticed that if section A-A is placed at a further distance from the free-span, the error of considering the flow problem as two-dimensional will decrease.

4.3.5   LIQUEFACTION HAZARD ASSESSMENT OF A FREE-SPAN

One way of evaluating the liquefaction hazard is to make the analyses necessary to answer the three questions asked in [Kramer 1996 p351]:

1. Is the soil susceptible to liquefaction?
2. If the soil is susceptible, will liquefaction be triggered?
3. If liquefaction is triggered, will damage occur?

In this project, the liquefaction hazard for a pipeline free-span is evaluated in a qualitative manner because a numerical modelling of the liquefaction phenomenon has been considered too extensive for implementation in this project. The three questions above are discussed in the following.

4.3.5.1. Soil Susceptibility to Liquefaction

Since no soil analysis has been made in this project, the susceptibility to liquefaction is evaluated for typical marine soil. Table 22 serves as a general reference for the qualitative evaluation.

Marine soil will always be saturated and is typically a well-sorted friction soil with little or no cohesion. Furthermore, the soil is typically normally consolidated and even if the soil is pre-consolidated, this will be eliminated near the pipeline as the trenching of the pipeline disrupts the soil. All these factors make the soil more susceptible to liquefaction.

The initial stresses in the soil around the pipeline are small as the pipeline is typically installed in a small trenching depth. This reduces the risk of flow liquefaction in the soil whereas the soil becomes more susceptible to cyclic mobility. The drainage of the soil around the pipeline is considered to be large because friction soil is permeable and the drainage distance for the soil around the pipeline toward the seabed is small. The latter is an important aspect that will lower the risk of liquefaction radically.

4.3.5.2. Free-span Susceptibility to Liquefaction

This susceptibility evaluation is based on the knowledge of free-span behaviour from Chapter 5.2 (Parametric Study for Regular Waves) and the susceptibility influence for the governing parameters that are shown in Table 22.

The phenomenon of vortex lock-in described in Chapter 3.1 (Near-Wall Cylinder) becomes an important aspect when evaluating the free-span susceptibility to liquefaction. If the pipeline free-span is exposed to vortex lock-in, the hydrodynamic load amplitude increases rapidly as the load frequency remains constantly equal to the natural frequency of the free-span. If the phenomenon of vortex lock-in does not appear, the load frequency from the hydrodynamic loads decreases as the amplitude of the force increases. This is due to the fact that larger waves creating larger load amplitudes also have longer wave periods and thereby decreasing load frequencies.

The susceptibility to liquefaction has shown to be higher for increasing amplitude and frequencies of excitation which means that the free-span affected by vortex lock-in will also be more susceptible to liquefaction.

The relatively small pipe diameters and trenching depth will however limit the risk of triggering liquefaction for a pipeline free-span due to the fact that the short drainage distance toward the seabed will prevent the presence of excess pore pressure.

4.3.5.3. Free-span Consequence of Liquefaction

This section evaluates the scenario and consequences of flow liquefaction and cyclic mobility, respectively, for a pipeline free-span in general. If liquefaction appears, the worst case scenarios of the two phenomena have been discussed in the following.

Flow Liquefaction

The worst case scenario of flow liquefaction considering a pipeline free-span would be that the increased buoyancy from the liquefied soil at the shoulders exceeds the self-weight of the pipeline creating an upward static resultant force. The upward static force could drive the pipeline up towards the seabed and thereby increase the spanning length of the free-span. This scenario will be most probable for light-weight pipelines but still depends upon the mobilization of liquefaction in a rather large volume of soil near the free-span shoulder. The scenario causing flow liquefaction for a pipeline free-span is sketched in Figure 124.
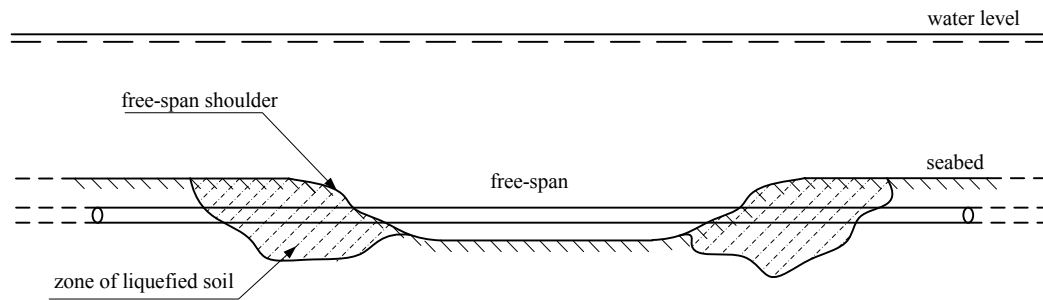
Figure 124: Sketch of the flow-liquefaction scenario.

The mobilization of a soil volume large enough to create flow liquefaction is considered to be unlikely and flow liquefaction is therefore considered to be the least probable liquefaction phenomenon for a pipeline free-span.

Cyclic Mobility

The consequence of cyclic mobility considering a pipeline free-span will be that the stiffness of the soil springs in the liquefied soil will be decreased radically. This will result in larger displacements and lower structural frequencies which could lead to increased stresses and larger dynamic amplification if the hydrodynamic load frequencies are lower than the structural frequencies. This could ultimately lead to either exceeding the bearing capacity or cause considerable damage on the pipeline. Cyclic mobility could also result in an increase in spanning length if the cross-flow force from wave and current exceeds the reduced bearing capacity of the soil in upward direction and drive the pipeline toward the seabed. The scenario causing cyclic mobility considering a pipeline free-span is sketched in Figure 125.
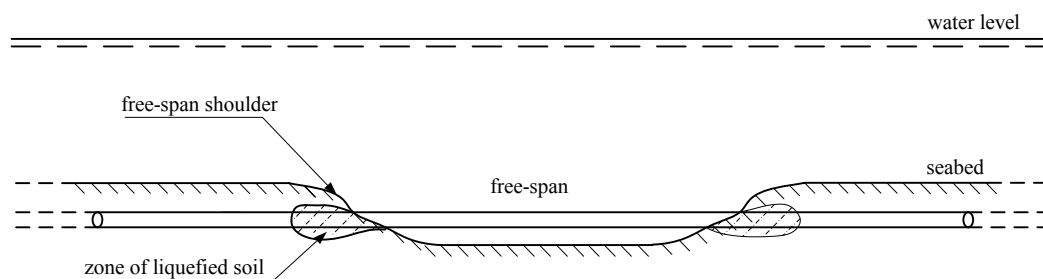

Figure 125: Sketch of the cyclic mobility scenario.

The free-span will be affected by cyclic mobility even though only a small volume of soil near the shoulder is mobilized to liquefaction. This will be the most probable phenomenon of liquefaction considering a pipeline free-span.

Part 5

Single-span Analyses

The pipeline free-span is modelled as a 3-dimensional beam model with non-linear soil springs using Abaqus 6.7 which is a commercial finite element program. A force feedback model that accounts for fluid damping of the free-span is implemented in the Abaqus Model by the use of user-defined FORTRAN subroutines. A 2-dimensional beam model with linear soil springs has been made in the commercial programming environment Matlab for benchmark testing of the Abaqus Model.

The Abaqus Model is used for free-span analyses in FLS and ULS. An extensive parametric study has been made to determine the parameters of greatest influence to the dynamic response and fatigue of the pipeline free-span. Maximum spanning lengths of the pipeline free-span has been determined when considering FLS and ULS.

5.1 WINKLER MODEL

In this chapter, a presentation is given of the single-span Winkler Model that has been created in two numerical models by the Finite Element Method. First, an overview of the features of the models is presented. Then, the common and specific properties of the models are described. Finally, the results of a benchmark test and a brief evaluation are presented.

5.1.1 OVERVIEW

The two numerical FEM-models of the Winkler Model are briefly described below:

- **Matlab Model:** This FEM-model has been created from scratch in the commercial programming environment MATLAB version 7.4.0 and will be referred to as the Matlab Model. The model is a 2-D model with optional material damping and optional adjustment of the stiffness due to a constant initial axial load. Since the model is entirely linear, relatively simple linear solvers for the static response, dynamic response and eigenvalues may be used. The purpose of this model is to explore the effects of a transmitting boundary and provide a verification basis for the more complex Abaqus Model. The code for the Matlab Model may be found in [DVD/Matlab Model/winklermodel.m].

- **Abaqus Model:** This FEM-model has been created in the commercial general-purpose FEM-program ABAQUS version 6.7 and will be referred to as the Abaqus Model. The model is a 3-D non-linear model with the capability to include effects of material damping, linear and non-linear soil springs, adjusted stiffness due to initial axial load and a feedback force. The internal non-linear solvers of Abaqus are used. An example of the model files for the Abaqus Model can be found in [DVD/Abaqus Model/Force Feedback/singlespan_example.inp].

An overview of the features of the two models is given in Table 24.

Table 24: Overview of features of FEM-models.

	Matlab Model	**Abaqus Model**
Dimensions	2-D	3-D
Spring material behaviour	Linear	Linear or non-linear
Possible material damping	Yes	Yes
Possible stiffness adjustment due to initial axial load	Yes – but only constant axial load	Yes
Possible feedback force	No	Yes

5.1.2 COMMON PROPERTIES

In this section, the common properties of the models are presented. These properties are geometry, boundary conditions, added mass and stiffness. Since the loads that are applied in the models are particular for the analyses, the loads are specified during each analysis.

5.1.2.1. Geometry

The geometry of the single-span pipeline is modelled as a free-span in the middle and two equally-sized side-spans that are covered by soil. For convenience, the soil strength is assumed to be constant along the side-spans which corresponds to a constant trenching depth along the side-spans. In reality, the trenching depth of the pipe will decrease near the pipe shoulder. Figure 126 shows a sketch of the geometry.
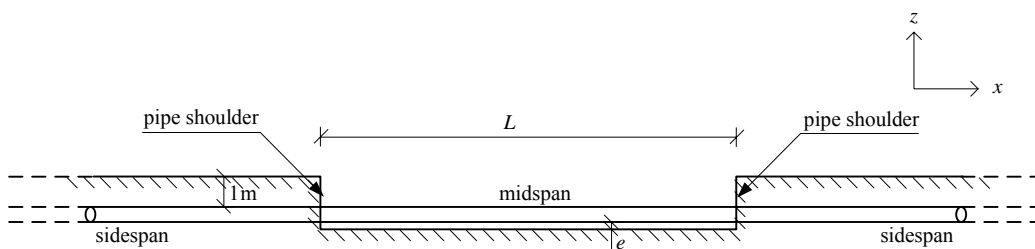

Figure 126: Geometry. The length of the free-span and the gap between pipeline and seabed are denoted with L and e, respectively.

The side-spans should be wide enough to allow fulfilment of static equilibrium. Since the pipeline experiences evanescent waves according to Chapter 4.2 (Transmitting Boundary), the side-spans should also be wide enough to allow complete dissipation of the evanescent waves. The latter is fulfilled when the lateral or transversal displacements vanish at the pipe-ends when they are free. It turns out that both conditions are fulfilled when the minimum length of a side-span is 17.5 m.

5.1.2.2. Boundary Conditions

In this section, the boundary conditions of the Matlab and Abaqus Model are presented. Since the pipeline experiences evanescent waves according to Chapter 4.2 (Transmitting Boundary) and the side-spans in the models are wide enough to allow dissipation of waves, all transversal displacements and rotations have vanished before reaching the boundary. Thus, the transversal and rotational boundary conditions at the pipe-ends will have no effect upon the static or dynamic response. However, in order to obtain reasonable transversal eigenmodes and eigenfrequencies for modes of higher order than the second-lowest mode, the transversal displacements and rotations at the pipe-ends are fixed.

In the derivation of the axial load according to Appendix A (Axial Force), the pipeline has been assumed to be fully axially restrained. In the Matlab Model, this restraint is not imperative. This is due to the fact that the load is applied as an initial condition, no other external axial loads are applied and the Matlab Model is linear. In contrast, the transversal displacements and rotations in the non-linear Abaqus Model may couple to the axial displacement and thus bring the axial boundary condition into effect. For simplicity, the axial displacement is fully restrained in the pipe-ends in both models. The boundary and initial conditions of the pipeline in the Matlab and Abaqus Model are illustrated in Figure 127.
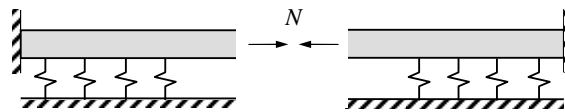

Figure 127: Boundary and initial conditions of the pipeline in the Matlab and Abaqus Model where N denotes an initial axial load.

5.1.2.3. Added Mass

In addition to the mass of the steel in the pipeline, these additional masses are applied in the FEM-models:

- Mass of content (internal fluid)
- Mass of coating
- Mass of marine growth
- Hydrodynamic added mass

In the following, only the hydrodynamic added mass is elaborated. This added mass arises in the case of considerable pipe acceleration. For the free-span, it corresponds to the added mass term in the in-line force for a slender structure in the Morison Model which is defined in **(3.2.2)**. Instead of implementing this force as an external inertia force in the equations of motion, it is implemented indirectly as an added mass on the free-span pipeline. This way of implementing the hydrodynamic inertia force is chosen for the sake of simplicity, computational performance and to allow identification of the experienced eigenfrequencies and modes of the system. However, it introduces an inertia force in the cross-flow direction.

For the side-spans, it is assumed that the additional mass for the soil around the pipe can be calculated as an equivalent hydrodynamic mass for soil. This is a crude but safe assumption since the added soil mass reduces the natural frequency of the system and thus brings it closer to the load frequency. The hydrodynamic mass is calculated as

$$m_h = C_A \frac{\pi}{4} D^2 \rho \qquad (5.1.1)$$

where

m_h is the hydrodynamic mass per unit length [kg/m]

C_A is the added mass coefficient [-]

D is the pipe outer diameter [m]

ρ is the density of ambient material $\left[\frac{\text{kg}}{\text{m}^3} \right]$

The added mass coefficient corresponds to the hydrodynamic mass for a pipeline in oscillatory flow and increases for the free-span with a decrease in the gap ratio, see Figure 128.
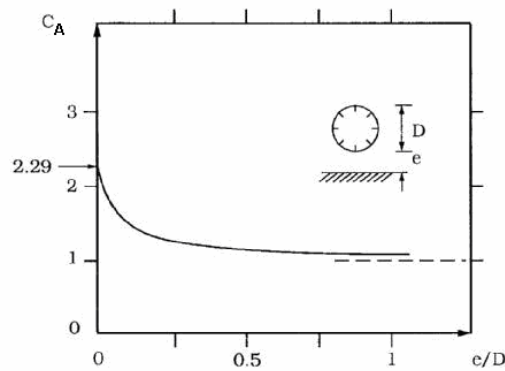

Figure 128: Hydrodynamic added mass coefficient for a cylinder in oscillatory flow near a wall. Adopted from [Sumer & Fredsøe 1997, p129].

The parameters for hydrodynamic added mass, the added masses and total added masses per unit length are shown in Table 25-Table 27, respectively. The calculations are based upon Chapter 1.1 (Design Conditions).

Table 25: Parameters for hydrodynamic added mass.

Parameter		Side-span	Free-span
Added mass coefficient	C_A [-]	1.0	2.29
Pipe outer diameter	D [m]	0.62	0.62
Density	ρ [kg/m²]	2000	1025

Table 26: Contributions of added mass per unit length in kg/m.

Added mass	Side-span	Free-span
Marine growth	-	55.2
Coating	289.2	289.2
Content – Air-filled	0.2	0.2
Content – Water-filled	182.4	182.4
Content – Operational	20.1	20.1
Hydrodynamic mass	603.8	708.7

Table 27: Total added mass per unit length in kg/m for the pipeline.

Functional state	Side-span	Free-span
Air-filled	893.2	1053.3
Water-filled	1075.4	1235.5
Operational	913.1	1073.2

The total added masses in Table 27 are implemented in both the Matlab and Abaqus Model. In the latter, they are implemented as so-called non-structural mass per unit length.

5.1.2.4. Stiffness

When considering the stiffness of the concrete coating, the axial and bending stiffness of the homogenous pipeline becomes

$$EA = E_{steel}A_{steel} + E_{concrete}A_{concrete} \tag{5.1.2}$$

$$EI = E_{steel}I_{steel} + E_{concrete}I_{concrete} \tag{5.1.3}$$

where

EA is the axial stiffness [N]

EI is the bending stiffness [Nm^2]

E_{steel} is the Young's modulus for steel [Pa]

$E_{concrete}$ is the Young's modulus for concrete [Pa]

A_{steel} is the cross-sectional area of the steel [m^2]

$A_{concrete}$ is the cross-sectional area of the concrete coating [m^2]

I_{steel} is the second moment of area of the steel [m^4]

$I_{concrete}$ is the second moment of area for the concrete coating [m^4]

A manual specification of the axial and bending stiffness or the use of an arbitrary section is less straight-forward in Abaqus. In contrast, it is easy to use a pipe section of a single material. Therefore, the pipe section is taken as that of the steel section with an equivalent Young's modulus instead of Young's modulus for steel. The equivalent value is calculated as the weighted sum of bending stiffness of the steel and the coating with respect to the second moment of area so it fulfils

$$EI = E_{equivalent}I_{steel} \tag{5.1.4}$$

where

$E_{equivalent}$ is an equivalent Young's modulus [Pa]

For simplicity, the same approach is used in the Matlab Model. The bending stiffness is modelled exactly at the expense of the axial stiffness that is overestimated according to (5.1.2). However, this is considered to be reasonable since the bending stiffness is considered to be the governing stiffness for the pipeline free-span. By use of the material properties from Chapter 1.1 (Design Conditions), the equivalent Young's modulus is

$$
\begin{aligned}
E_{equivalent} &= \frac{I_{steel}E_{steel} + I_{concrete}E_{concrete}}{I_{steel}} \\
&= \frac{0.75 \cdot 10^{-3}\,\text{m}^4 \cdot 0.21 \cdot 10^{12}\,\text{Pa} + 3.40 \cdot 10^{-3}\,\text{m}^4 \cdot 29.1 \cdot 10^9\,\text{Pa}}{0.75 \cdot 10^{-3}\,\text{m}^4} \\
&= 0.34 \cdot 10^{12}\,\text{Pa}
\end{aligned}
$$

For convenience, the true distribution of axial strain and normal stress due to axial compression and bending of the pipeline is shown in Figure 129 where Bernoulli-Euler beam theory has been assumed.
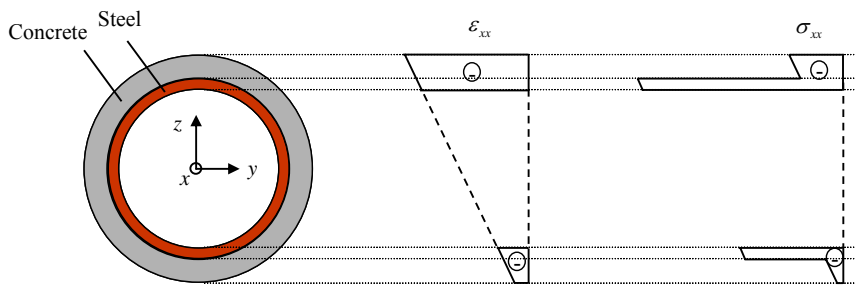

Figure 129: Cross-section (left) and true distribution of axial strain ε_{xx} (middle) and axial normal stress σ_{xx} (right) in the composite pipeline. The strains and stresses are defined as negative in compression.

5.1.3 MATLAB MODEL

In this section, the specific properties of the Matlab Model are presented. These are the elements, the mesh structure and resolution and fixed time increment.

5.1.3.1. Overview of Elements

The Matlab Model utilizes two-nodal 2-D Bernoulli-Euler linear elastic beam elements from the library of the CALMFEM v. 3.3 toolbox. This toolbox is developed at Lund University, Sweden [Department of Mechanics and Materials 1999]. The free-span is modelled as a series of regular beam elements while the soil at the side-span is modelled as a series of beam elements with an inherent Winkler foundation with linear transversal and axial springs. In the case of an initial axial load, the element stiffness matrices are adjusted. For clarity, the element stiffness and mass matrices are described in Appendix D (Element Matrices in Matlab Model).

5.1.3.2. Mesh

In this section, the mesh of the Matlab Model is presented. The mesh resolution should be small enough to be computationally effective and large enough to give an accurate physical description during both static and dynamic analyses.

For ease, the length and number of elements at each side-span and the mid-span may vary but is constant for all elements along a span as shown in Figure 130. This mesh structure will provide an accurate result when the number of elements is large enough.
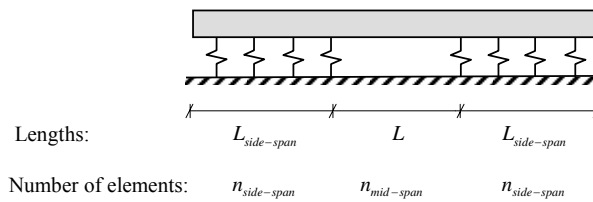

Figure 130: Mesh structure, element lengths and numbers in the Matlab Model.

In the following, the mesh resolution is investigated. The resolution during static analysis is assessed upon convergence analysis of the external work since the external work of a linear system of elements that are based upon kinematic admissible fields will converge towards a maximum as the resolution increases [Byskov 2002, pp519-521]. The external work is taken as

$$W_e = \frac{1}{2}\mathbf{x}^T\mathbf{f} > 0 \tag{5.1.5}$$

where

W_e is the external work [Nm]

$\mathbf{x}$ is the generalized displacements vector

$\mathbf{f}$ is the generalized load vector

The mesh resolution during dynamic analysis is assessed upon convergence analysis of the lowest and second-lowest eigenfrequencies that will converge towards minima as the resolution increases. In practice, the convergence analysis is carried out by a series of static and eigenfrequency analyses at different mesh resolutions and with the parameters for the pipeline that are given in Table 28.

Table 28: Parameters of the side-span and free-span during the convergence analysis.

Parameter		Side-span	Free-span
Length	L **[m]**	60	25
Mass per unit length	m **[kg/m]**	1107	1267
Bending stiffness	EI **[MNm^2]**	255	
Lateral linear spring stiffness	$\kappa_y \left[\frac{\text{MN}}{\text{m}^2} \right]$	0.77	
Axial linear spring stiffness	$\kappa_a \left[\frac{\text{MN}}{\text{m}^2} \right]$	0	
In-line distributed load	f_y **[N/m]**	0	4000
Initial axial load	N **[MN]**	-4.2 (compressive)	

The parameters in Table 28 correspond to a critical state for the pipeline during an operational state. The lateral direction is considered since it is the most slender transversal direction. The in-line distributed load along the mid-span corresponds in magnitude to the hydrodynamic drag force from maximum wave height during sea state 5. The compressive initial axial load corresponds in magnitude to the operational state, see Chapter 5.2 (Parametric Study for Regular Waves).

The contours of the external work, the lowest eigenfrequency and the second-lowest eigenfrequency as functions of the resolution are shown in Figure 131-Figure 133, respectively.
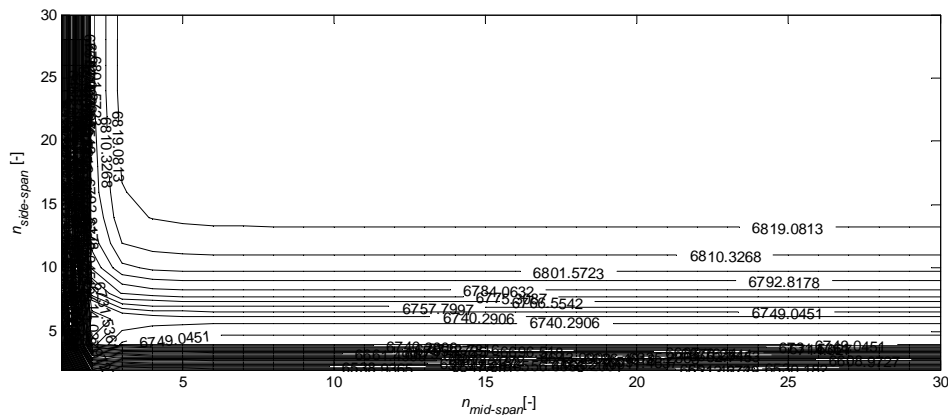

Figure 131: Contours of external work in Nm as functions of mesh resolution. Contour step is 8.76 Nm.
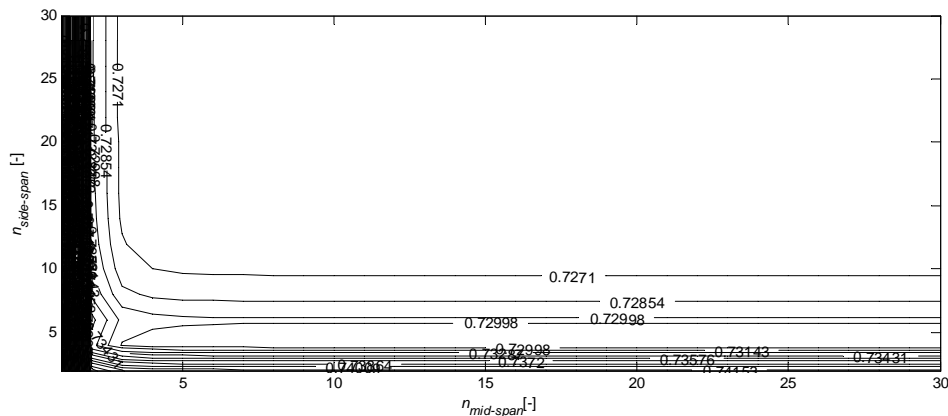

Figure 132: Contours of lowest eigenfrequency in Hz as functions of mesh resolution. Contour step is 0.0014 Hz.
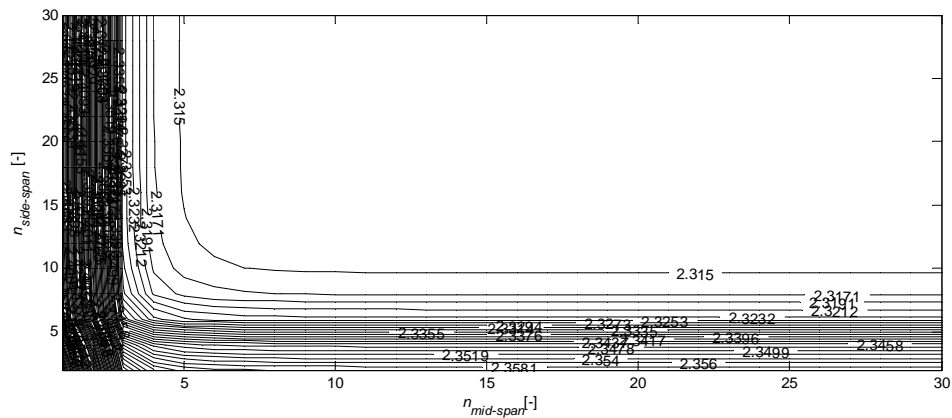
Figure 133: Contours of second-lowest eigenfrequency in Hz as functions of mesh resolution. Contour step is 0.0021 Hz.

It is seen from Figure 131 and Figure 132 that the external work and the lowest eigenfrequency has converged at a resolution with $n_{mid-span} \approx 4$ and $n_{side-span} \approx 14$. It is seen from Figure 133 that the second-lowest eigenfrequency has converged at a resolution with $n_{mid-span} \approx 6$ and $n_{side-span} \approx 13$. The reason why the second-lowest eigenmode compared to the lowest eigenmode requires a greater number of elements along the mid-span is due to its greater variation along the mid-span as illustrated in Figure 134.
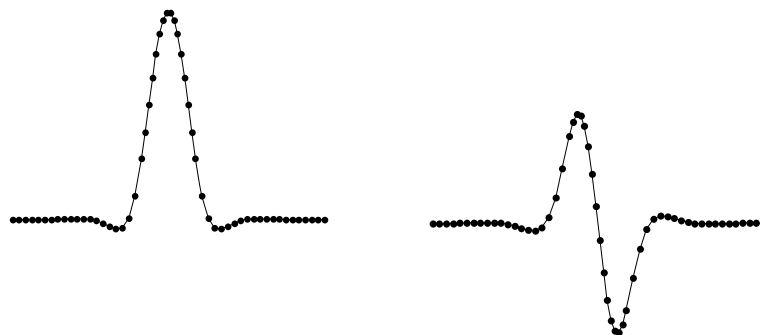

Figure 134: Illustration of lowest (left) and second-lowest (right) eigenmodes in Matlab Model. The dots indicate the nodes of the elements.

In general, higher order eigenfrequencies and eigenmodes require a higher mesh resolution. In order to avoid a poor description of these and to accommodate all states of interest, a mesh resolution with $n_{mid-span} = 15$ and $n_{side-span} = 20$ is considered to be sufficiently accurate and will be used in the Matlab Model.

5.1.3.3. Fixed Time Increment

In this section, the order of magnitude of the time increment in the Matlab Model is investigated. The time-domain dynamic analyses are performed by the Generalized Alpha Method where the

equations of motion are solved by implicit direct integration. The method is unconditionally stable for linear systems and is based upon a fixed time increment [Nielsen 2005, p54-61].

Since an unconditionally stable algorithm is used, the time increment has no influence on the stability of the algorithm. However, the time increment has a significant influence on the accuracy of the response. The time period should be chosen large enough to be computationally effective but small enough to avoid considerable period elongation and to avoid that a wave can travel unnoticed through an element. An estimate on the latter is determined by the Courant condition. In practice, the time increment is chosen as the largest fraction of the load period that provides a smooth response.

An estimate on the largest allowable ratio of the time increment and the element size due to wave propagation in the pipeline may be determined by the Courant condition

$$\frac{c \cdot \Delta t}{\Delta x} \leq 1 \qquad\qquad (5.1.6)$$

where

    c is a characteristic wave propagation speed [m/s]

    Δt is the time increment [s]

    Δx is a characteristic element size [m]

[Andersen 2006, p72]

The condition (5.1.6) states that for a large velocity, a small time increment or a large element size is needed. The velocity is related to the wave length and period in the following way

$$c = \frac{l}{T} = \frac{\omega}{k(\omega)} \qquad\qquad (5.1.7)$$

where

    l is a wave length [m]

    T is a wave period [s]

    ω is a circular wave frequency [rad/s]

    k is a characteristic wave number [rad/m]

The characteristic wave number is taken as the smallest absolute value of the wave numbers according to Chapter 4.2 (Transmitting Boundary). The wave numbers are functions of the load frequency and the properties of the pipeline and soil which are given in Table 29. These parameters correspond to an operational state.

Table 29: Parameters for Courant assessment.

Parameter		Value
Mass per unit length of side-span	m	1107 kg/m
Bending stiffness	EI	255 MNm^2
Lateral linear spring stiffness	κ_y	0.77 MN/m^2
Transversal linear spring stiffness	κ_z	3.43 MN/m^2
Initial axial load	N	-4.2 MN (compressive)

By use of **(4.2.19)**, (5.1.6)-(5.1.7) and the values in Table 29, the largest allowable ratio of the time increment and the element size for the lateral and vertical direction as function of the load frequency is shown in Figure 135.
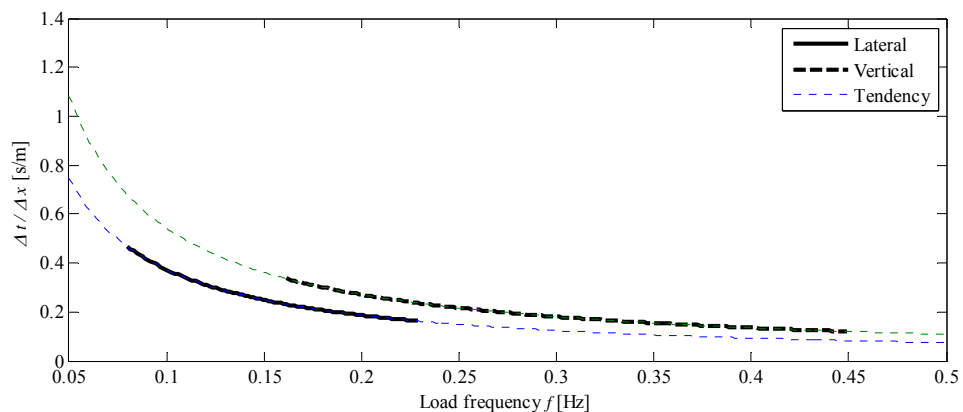
Figure 135: Largest allowable ratio of time increment and element size as function of load frequency due to the Courant condition.

It may be seen from Figure 135 that a smaller time increment or larger element size is required for the lateral direction compared to the vertical direction. This is due to the fact that waves that are induced by a harmonic load will have longer wave lengths and thus travel faster through the pipeline when the stiffness of its Winkler foundation is small.

5.1.4   ABAQUS MODEL

In this section, the specific properties of the Abaqus Model are presented. These are the elements, additional boundary conditions, the mesh, the time increment and the implementation of the feedback force.

5.1.4.1. Overview of Elements

The Abaqus Model uses two-nodal 3-D beam elements from the library of Abaqus/Standard v. 6.7. The pipeline at the side-spans and mid-span is modelled as a series of PIPE31-beam elements. The beam element at the side-span are attached to PSI34 (Pipe Soil Interaction) elements with non-linear material behaviour that has been investigated in the following section. The elements in the Abaqus Model are illustrated in Figure 136. The axial, lateral and vertical directions are given by the *x*-, *y*- and *z*-axis, respectively.
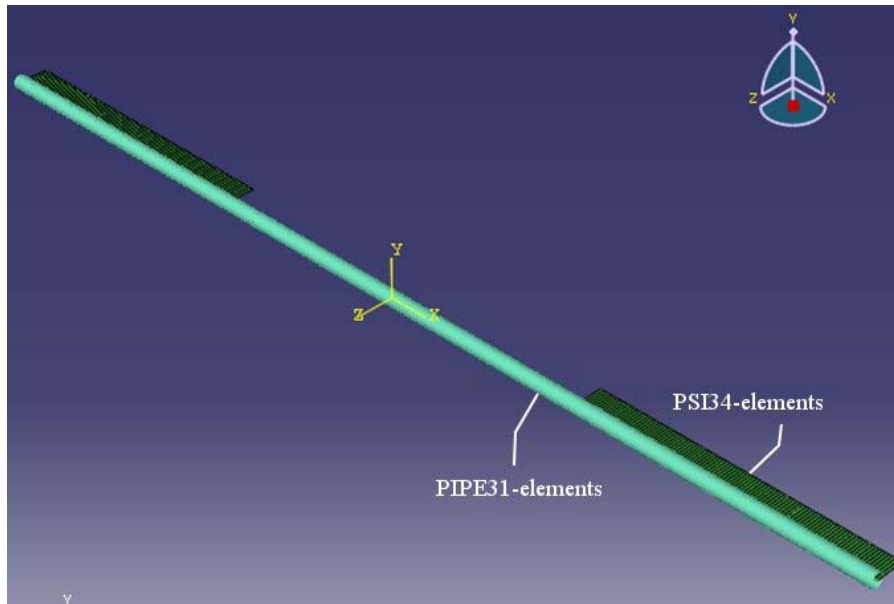
Figure 136: Elements in the Abaqus Model.

5.1.4.2. Constitutive Behaviour of the PSI-Element

Since the PSI-element is particular for Abaqus, its constitutive behaviour has been investigated. This has been done in a displacement-controlled numerical dynamic analysis in Abaqus with a single PSI-element. The material behaviour of the element has been defined as piece-wise non-linear, but differs from the non-linear soil springs in this project. The input file can be found in [DVD/Winkler Model/psi_element.inp].

The boundary conditions and reaction forces in the active plane of the element are illustrated in Figure 137. Two of the nodes of the element are subjected to a prescribed vertical displacement that varies in time where extension is defined as positive. The remaining two nodes that are furthest away from the prescribed boundary are restrained in the vertical direction and will yield opposite-directed vertical reaction forces. All nodes of the element are restrained in the axial and lateral direction.
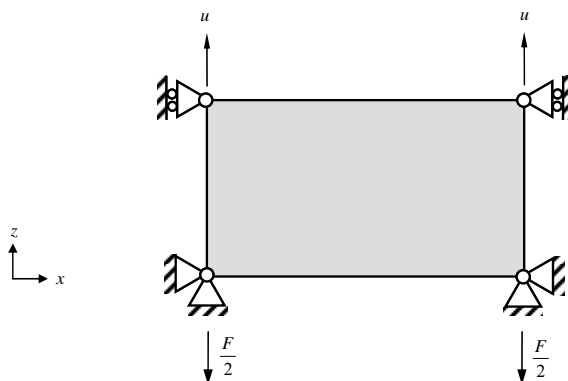

Figure 137: Active plane with boundary conditions and reaction forces of single PSI-element.

The time history of the prescribed displacement u and the total vertical reaction force F is shown in Figure 138. The definition of the load-displacement curve of the element and the actual load-

displacement pairs are shown in Figure 139. The letters A-N denote the pairs of load and displacement at progressive time steps.
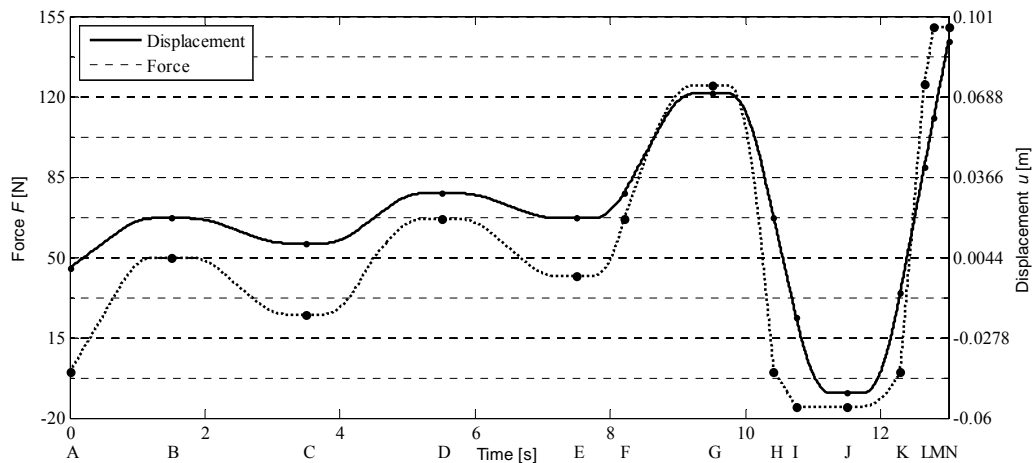

Figure 138: Time history of total vertical reaction force and prescribed vertical displacement.
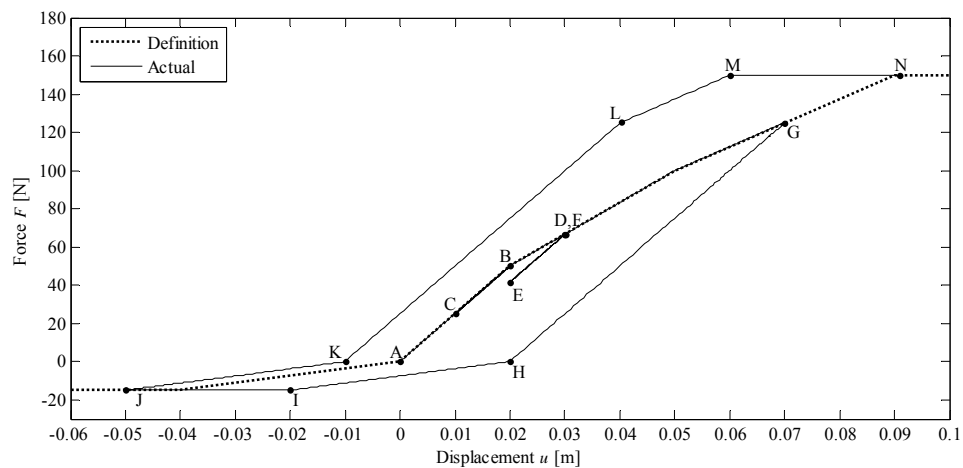

Figure 139: Definition and actual load-displacement for a PSI-element.

Several observations may be made from the results in Figure 138 and Figure 139. First, the PSI-element extends and compresses elastically between points B-C as expected for displacements within the elastic range A-B. However, when the element is extended beyond the initial elastic limit at point B, the element exhibits irreversible deformation that remains despite subsequent compression as seen from the path D-E. This has been found to be the case regardless of whether the piece-wise element load-displacement curve is monotonous or not. The plastic work of the element is indicated by the area of the nearly closed hysteresis loop from the path A-G-H-J-K-N.

Secondly, once the element has experienced a force beyond the initial elastic limit, the point of the elastic limit is moved. When the element is subsequently relaxed, the element will exhibit elastic behaviour until it reaches the same force again. This is clear by comparison of the relaxation point G and the secondary path K-L-M-N with the load-displacement curve that is defined for extension. Thus, one may say that the element experiences hardening.

Thirdly, the stiffness of the PSI-element along secondary elastic paths in the domain of extension, i.e. along paths D-E, E-F, G-H or K-L, is always based upon the initial slope of the load-displacement curve that is defined for extension, i.e. the path A-B. Equivalently, the stiffness along secondary elastic paths in the domain of compression is based upon the initial slope of load-displacement curve that is defined in compression which may be seen by comparison of paths H-I or J-K with the definition.

In conclusion, the constitutive behaviour of the PSI-element does not resemble that of a spring in a traditional sense but rather that of an element whose constitutive behaviour is elastoplastic with a hardening rule. The definition of the load-displacement curve is identified as a so-called backbone curve in the terminology of earthquake engineering [Kramer 1996, p242]. Thus, the PSI-element is considered to be a relatively simple way of modelling plastic soil behaviour compared to using traditional plastic continuum elements.

The plastic behaviour and the evolution of the elastic limit of the PSI-element are documented in the Abaqus User's Manual [Dassault Systèmes 2007, Sect. 26.13.1].

5.1.4.3. Additional Boundary Conditions

The Abaqus Model uses the boundary conditions at the pipe-ends as shown in Figure 127 but with additional restraints on the nodes of the PSI-elements since these are not restrained by default. The axial, lateral and vertical displacement of each node of a PSI-element that is away from the pipeline must be zero which are denoted with "A" in Figure 140. Recall that the displacements and rotations at the pipe-ends are fixed which are denoted with "B". The remaining nodes of the pipeline are free which are denoted with "C". The red contour indicates the boundary of a single PSI-element.
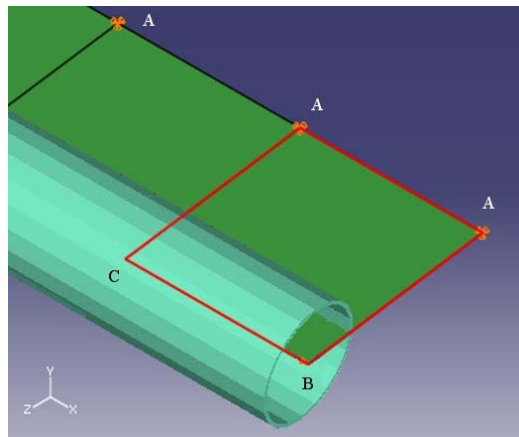
Figure 140: Boundary conditions in the Abaqus Model. A denotes zero-restraints on axial, lateral and vertical displacement. B denotes zero-restraints on all displacements and rotations. C denotes no restraints.

5.1.4.4. Mesh

The mesh of the Abaqus Model is subjected to higher performance requirements than the Matlab Model due to several reasons. First, the geometrical and material non-linearity of the Abaqus Model

requires a higher number of elements than the linear Matlab Model. Secondly, the Abaqus Model is used for a large series of analyses for parametric study and for dynamic analyses of great duration. Thus, it is of great interest to reduce the amount of the elements as much as possible.

In the Abaqus Model, the element size along the side-spans varies from large elements at the pipe-ends to small elements at the pipe shoulder. This is referred to as a biased discretisation. In addition, buffer zones with a high number of elements have been introduced at the mid-span close to the pipe shoulders in order to obtain a stable FEM-scheme. For the single-span pipeline, the Abaqus Model uses 70 PIPE-elements and 40 PSI-elements as illustrated in Figure 141.
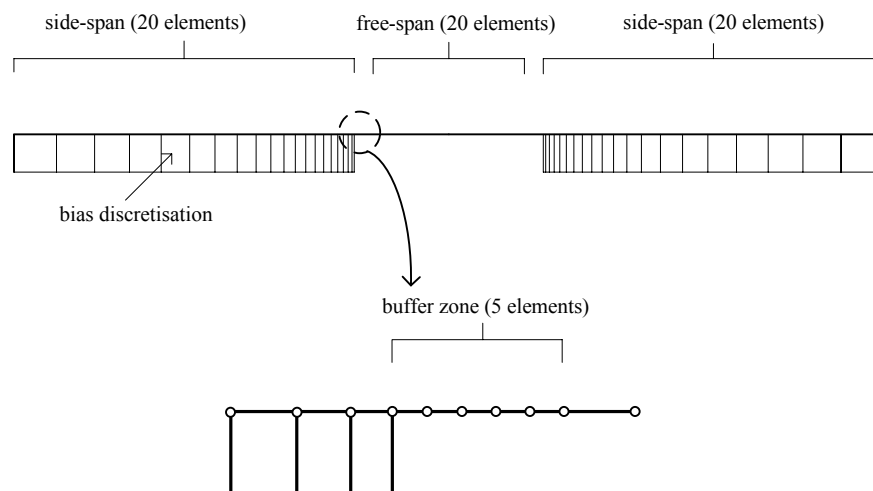

Figure 141: Schematized illustration of mesh in the Abaqus Model for the single-span pipeline.

5.1.4.5. Fixed or Variable Time Increment

In the Abaqus Model, time-domain dynamic analyses are performed by implicit direct integration in a similar fashion to that of the Matlab Model. However, the internal algorithm in Abaqus allows the use of a variable time increment that is adjusted regularly during the dynamic analysis. The time increment is large or small when the response changes slowly or rapidly, respectively [Dassault Systèmes 2007, Sect. 6.3.2]. A variable time increment is a great advantage in the dynamic analyses of great duration where it has been used. In order to obtain stable FEM-scheme, it has been necessary to set a limit upon the maximum value of the time increment.

5.1.4.6. Implementation of Feedback Force

In this section, the implementation of force feedback in the Abaqus Model is briefly presented. Force feedback is relevant when the pipe velocity is in the same order of magnitude as the flow velocity which is the case when the pipe is slender or experiences vortex lock-in. In this case, the hydrodynamic force that acts upon the free-span depends upon the pipe velocity that in turn depends upon the hydrodynamic force and so on. Since this process is recursive, the force is referred to as a feedback force.

For simplicity, an explicit solution method is chosen. This means that the hydrodynamic force at a time step is computed by the response at the previous time step. In practice, this will provide the correct force when the time increment is small enough.

Abaqus allows loads to be computed in user-defined subroutines that are written in FORTRAN. However, since Abaqus does not pass the response directly into the load subroutines, the feedback force is implemented through a library of user-defined subroutines. The response is extracted from a temporary results file that Abaqus can create during the analysis. Then, the response is saved into global variables and subsequently accessed by the load subroutine. The subroutines support the use of both fixed or variable time increment and a single-span or multi-span pipeline. The library of user-defined subroutines is located in [DVD/Abaqus Model/Force Feedback]. A flow chart and a description of the program execution steps and the file access are shown in Figure 142.
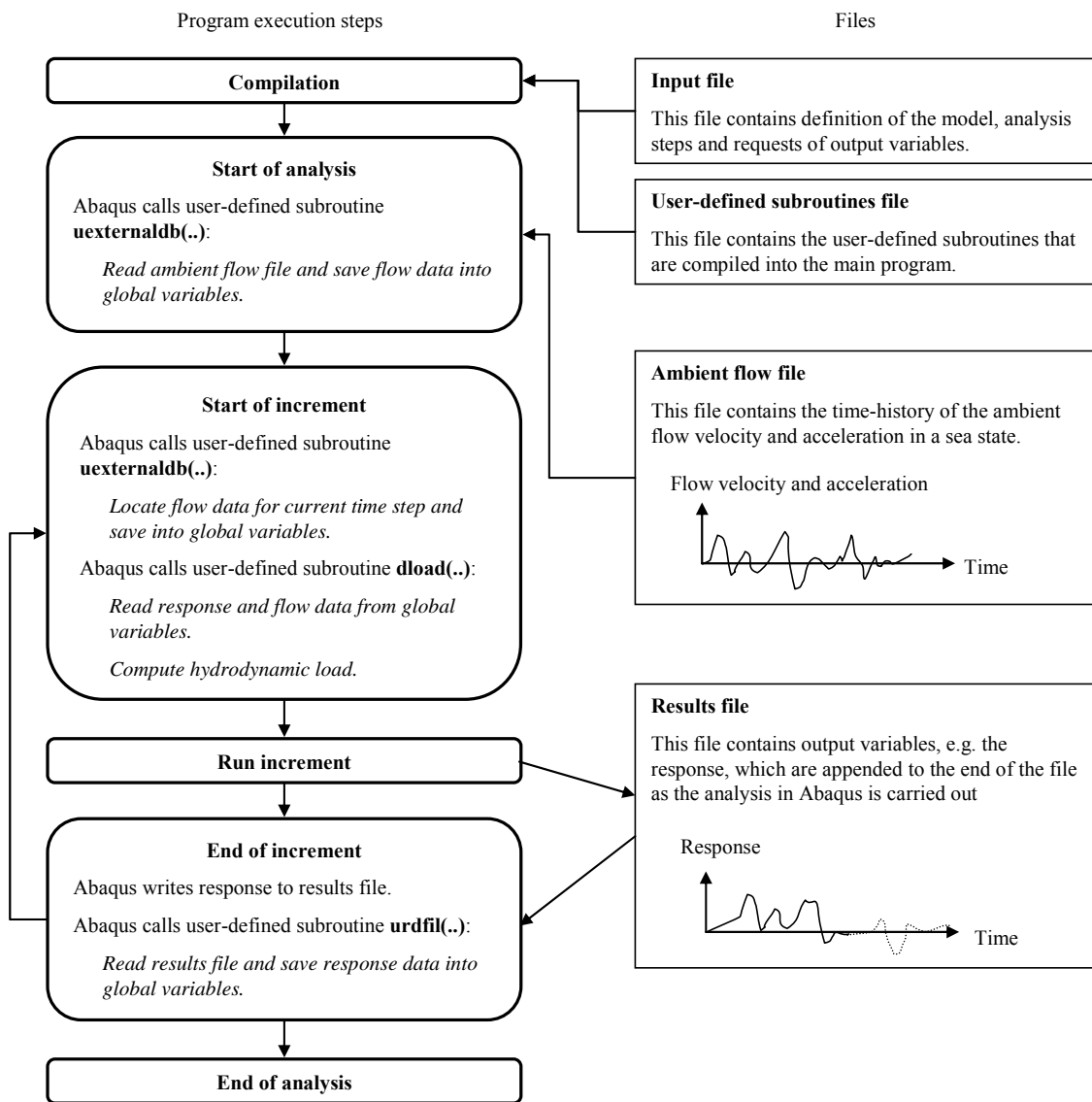

Figure 142: Flow chart of program execution steps and file access in implementing feedback force in the Abaqus Model.

5.1.5 BENCHMARK TEST

In order to verify the models, benchmark tests have been performed between the Matlab and Abaqus Models. Static and dynamic response is compared when simple loads are applied. The Abaqus Model is made with linear and non-linear springs in order to capture the effect of the non-linearity of the model.

5.1.5.1. Applied Loads

In this section, the loads that are applied in the benchmark test are described. A load may be static or dynamic where the dynamic load may be one of the following:

- **Impulse load:** This dynamic load acts suddenly in a very short time span and disappears just as suddenly. In practice, the duration is a few milliseconds for a maximum time history of a minute. The impulse load is useful for analysing transient response.

- **Harmonic load:** This dynamic load is a perfect sinusoidal wave. The harmonic load occurs for hydrodynamic forces and is also useful for analyzing dynamic amplification. Unless otherwise stated, the harmonic load takes the following form

$$\tilde{F}_y = F \sin(\omega t) \tag{5.1.8}$$

where

$\tilde{F}_y$ is the harmonic load [kN]

F is the load amplitude [kN]

ω is the circular load frequency [rad/s]

t is the time [s]

- **Harmonic-ramp load:** This dynamic load varies harmonically but its amplitude grows exponentially from zero to its maximum value after some time. The harmonic-ramp load is useful for analysing stationary response since vibrations due to initial conditions are avoided.

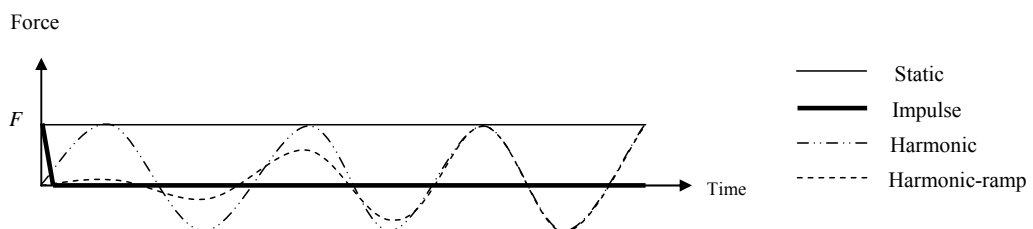The time history of the loads is illustrated in Figure 143.

Figure 143: Force history.

5.1.5.2. Static Response

The static displacements are tested for a concentrated load that is applied in the mid-section of the free-span of the pipeline. Comparison of the deformations is made for loads applied individually in three directions as:

- Axial load: $F_x = 10\text{kN}$

- Lateral load: $F_y = 10\text{kN}$

- Vertical load: $F_z = 10\text{kN}$

The corresponding displacements at the mid-section of the free-span are shown in Table 30.

Table 30: Displacements in mid-section free-span. The Abaqus Model has linear or non-linear springs.

Model	Axial displacement δ_x [m]	Lateral displacement δ_y [m]	Vertical displacement δ_z [m]
Matlab	$3.4 \cdot 10^{-5}$	$6.9 \cdot 10^{-3}$	$6.7 \cdot 10^{-3}$
Abaqus (linear)	$3.4 \cdot 10^{-5}$	$6.9 \cdot 10^{-3}$	$6.7 \cdot 10^{-3}$
Abaqus (non-linear)	$3.4 \cdot 10^{-5}$	$6.9 \cdot 10^{-3}$	$2.4 \cdot 10^{-3}$

There is good agreement between the deformation determined by the Matlab and the Abaqus Model with linear springs. The lateral displacements of the linear and non-linear model are identical since the stress state in the springs at the pipe shoulders is located at the linear part of the load-displacement curves. The upward vertical displacement decreases because the non-linear load-displacement curves increase the stiffness of the soil for small displacement in upward direction.

5.1.5.3. Modes and Frequencies

This test compares the eigenmodes and eigenfrequencies returned by the models. Figure 144 shows the four lowest eigenmodes that are returned by the Abaqus Model with linear springs and similar modes have been found in the Matlab Model. The modes 1-4 correspond to the four lowest eigenfrequencies and since the load frequency from the waves and current are also low, these will be the modes that have the largest impact on the response of the free-span. For reference with the undeformed state of the pipeline, see Figure 136.
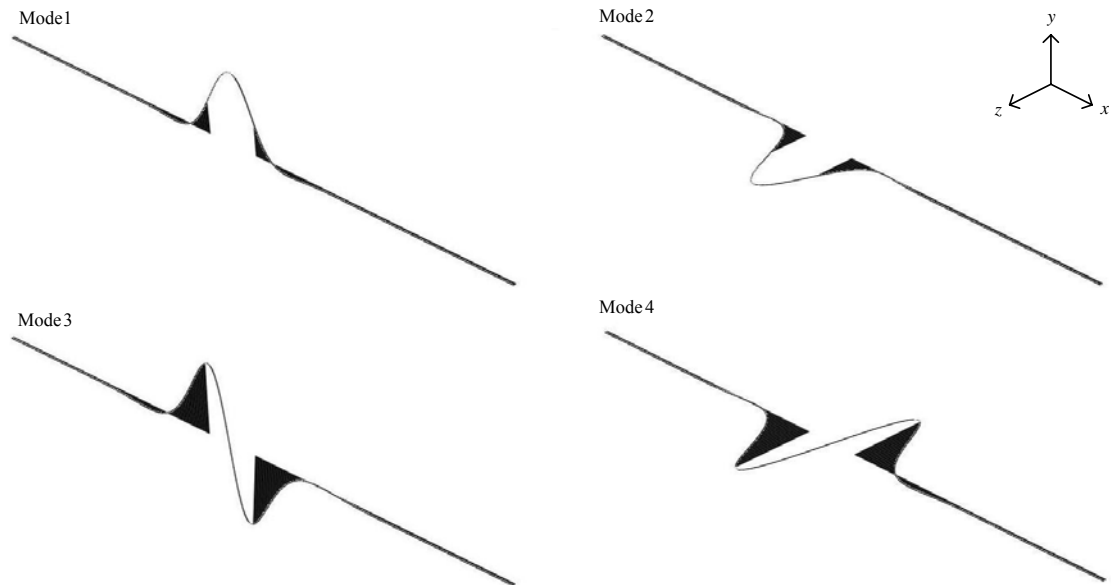
Mode 1

Mode 2

Mode 3

Mode 4

Figure 144: Eigenmodes for the models.

The corresponding eigenfrequencies are shown in Table 31.

Table 31: Eigenfrequencies.

Model	f_1 [Hz]	f_2 [Hz]	f_3 [Hz]	f_4 [Hz]
Matlab	1.60	1.64	3.45	3.56
Abaqus (linear)	1.60	1.64	3.44	3.55
Abaqus (non-linear)	1.60	3.32	3.44	8.98

There is a good agreement between the eigenfrequencies that are calculated in the linear models. In the Abaqus Model with non-linear springs, the vertical springs are modelled with significantly more stiffness for both upward and downward movements at the first part of the load-displacement curves. This gives rise to significantly higher vertical frequencies in the non-linear model.

5.1.5.4. Dynamic Response

The dynamic response of the Abaqus Model is tested by applying some simple dynamic loads to the model. The simple loads applied are chosen as:

- Impulse load in lateral direction
- Harmonic load in lateral direction

Impulse load

To verify dissipation due to damping, an impulse load acting in the lateral direction is applied as a concentrated force $F_y = 10\,\text{kN}$ in the mid-section of the free-span. The force is applied in 0.005 s and the decay of the corresponding vibrations of the pipe is calculated for a time period of 10 seconds. In both the Matlab and Abaqus Model, damping is implemented as Rayleigh damping

according to Appendix B (Rayleigh Damping). Figure 145 shows the lateral dynamic response in the mid-section of the free-span in the Abaqus Model with and without damping.
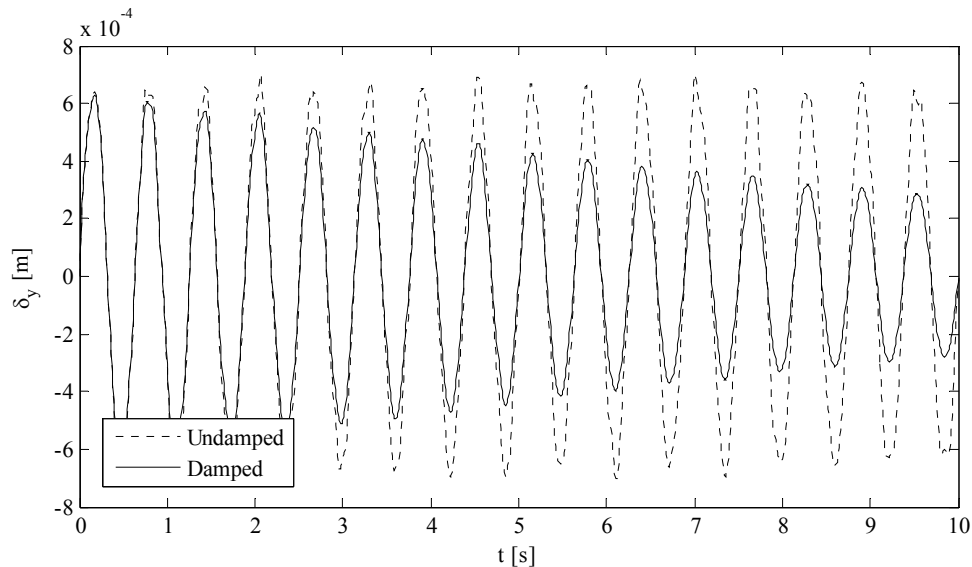

Figure 145: Lateral response in the mid-section of the free-span when an impulse load is applied

The Matlab Model shows dynamic response that is similar to that of the Abaqus Models. Since the lateral displacement is small, the Abaqus Model with linear springs and the Abaqus Model with non-linear springs show identical results.

Harmonic load

This test is made to identify dynamic amplification in the linear models and the non-linear Abaqus Model. The load is applied harmonically as a concentrated force that acts in the lateral direction in the mid-section of the free-span according to (5.1.8). In order to induce significant dynamic amplification, the circular load frequency is chosen to be equal to the first circular eigenfrequency, i.e. $\omega = 1.60 \cdot 2\pi \, \frac{\text{rad}}{\text{s}}$.

Similarly to the previous tests, the load amplitude is chosen as $F_y = 10 \, \text{kN}$. Figure 146 shows the lateral dynamic response in the mid-section of the free-span in the Abaqus Model with linear springs. The results are shown for a model with and without damping.
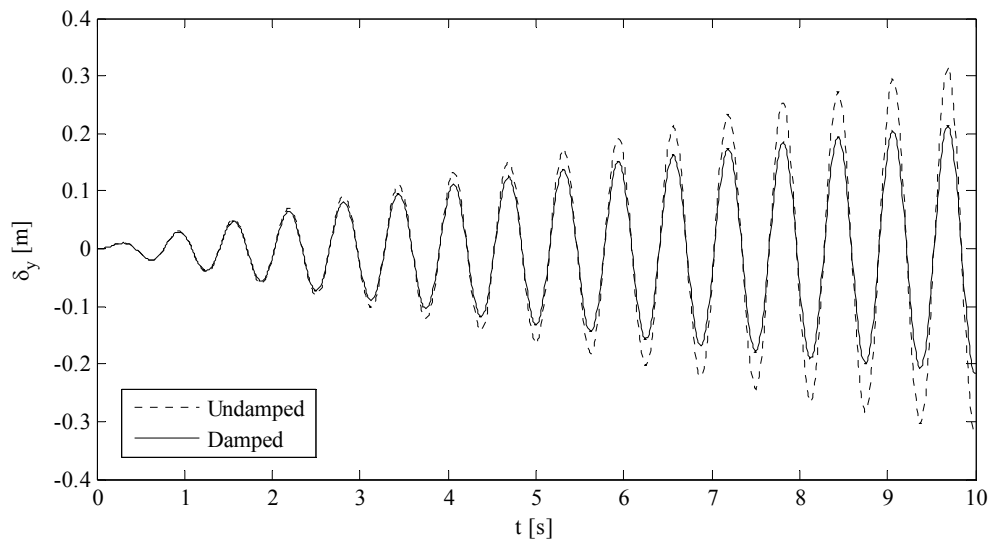
Figure 146: Lateral response in the mid-section of the free-span when a harmonic load is applied to the Abaqus Model with linear springs.

The Matlab Model shows results that are identical to the results for the Abaqus Model with linear springs. Figure 146 shows that considerable dynamic amplification occurs, especially for the undamped model. This is in good agreement with the theory of dynamics. At a time step that exceeds those shown in Figure 146, the damped response becomes stationary, i.e. harmonic with constant amplitude.

Because the dynamic amplification creates large displacements, some deviation is expected between the linear and non-linear model. Figure 147 shows the lateral dynamic response in the mid-section of the free-span in the Abaqus Model with non-linear springs.
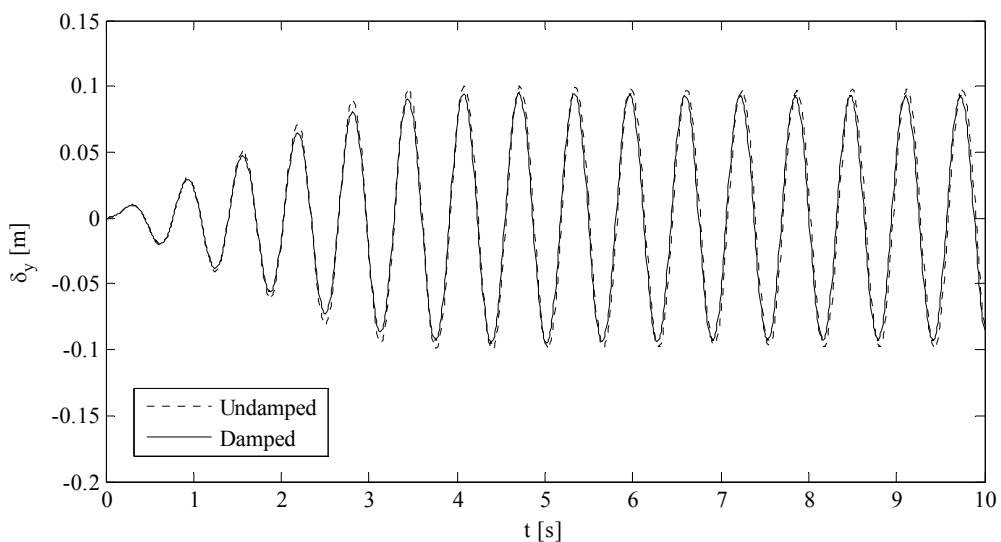

Figure 147: Lateral response in the mid-section of the free-span when a harmonic load is applied to the Abaqus Model with non-linear springs.

From Figure 147, it is seen that dynamic amplification ceases after $t > 3$ seconds and the dynamic response becomes stationary. When the displacement at the pipe shoulders reaches the non-linear part of the load-displacement curves at $t \approx 3$ seconds, the lowest eigenfrequency of the system decreases and damping is introduced due to plastic deformation according to the section on the constitutive behaviour of the PSI-element. As the difference between the load frequency and the eigenfrequency increases, the dynamic amplification ceases.

5.1.5.5. Evaluation

The strategy of creating two FEM-models – a relatively simple linear Matlab Model and a relatively complex non-linear Abaqus Model – has provided a verification basis for the non-linear Abaqus Model. In case of a linear system, the models show identical static and dynamic response. The latter is generally in agreement with the theory of dynamic systems. Thus, the results of the non-linear Abaqus Model are considered to be reliable.

The strategy has also provided insights into the differences between linear and non-linear dynamic systems. One of the main differences lies in the constitutive behaviour of the Winkler foundation. The Pipe Soil Interaction (PSI) elements that constitute the Winkler foundation of the Abaqus Model undergo plastic deformation when they exceed their elastic range. When subsequently relaxed, the PSI-elements do not return to their initial state. This deviates from the traditional understanding of a spring but is in better agreement with the plastic constitutive behaviour of soil.

This results in another important difference between the models. The possible change of the stiffness of the Winkler foundation in the Abaqus Model may change the eigenfrequencies of the non-linear system during a dynamic analysis. Thus, eigenfrequencies that are determined from the undeformed state could be misleading if they are not supplemented by eigenfrequencies that are determined from a deformed state after plastic deformation has occurred. This also applies when determining a reponse quantity by frequency-domain dynamic analysis. However, dynamic amplification is expected to decrease in magnitude during plastic deformation of the PSI-elements since they introduce damping during this process.

5.2 PARAMETRIC STUDY FOR REGULAR WAVES

This parametric study is performed to detect the governing parameters of the dynamic response and fatigue for the pipeline free-span in FLS. The Abaqus Model with non-linear springs described in Chapter 5.1 (Winkler Model) is used for the parametric study. The parametric study is divided into the following parts:

- Reference model
- Functional state
- Spanning length
- Damping
- Gap ratio
- Friction angle of soil
- Coating stiffness
- Wave height

The parametric study is ended with a brief evaluation on the damage effect of the above mentioned parameters. It is noticed that the parametric study is only valid for the project pipeline as different structural data or environmental conditions might change the tendencies found in this chapter. The parametric study will however give an idea of what to consider when parameters for free-span analyses have to be determined.

5.2.1 REFERENCE MODEL

In this section, the reference model for the parametric study is defined. The corresponding model files can be found in [DVD/Parametric Study of Regular Waves/singlespan.inp]. Figure 148 shows the design conditions and assumptions made in the reference model.
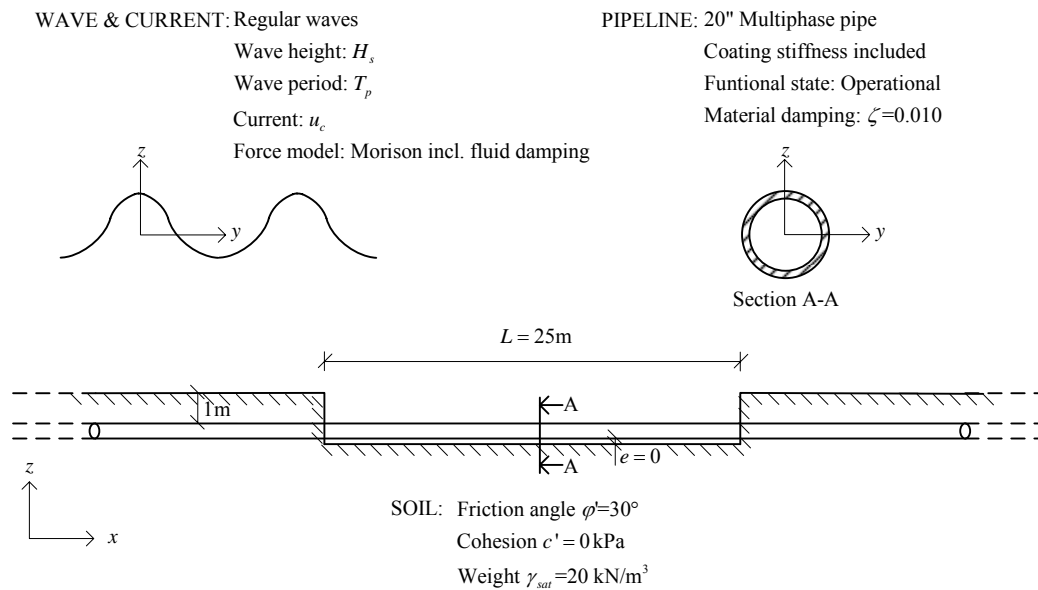
Figure 148: Design conditions and assumptions for the reference model.

The input parameters defining the numerical model are equal to those defined in Chapter 5.1 (Winkler Model). Only the loads that are applied to the model have to be redefined. The loads are divided into two separate parts:

- Static loads
- Dynamic loads

The loads are defined positive in the directions of the coordinate system *x*, *y*, *z* in Figure 148. The initial loads and stresses are defined positive in tension.

The analyses made for the reference model show the process of determining dynamic response and fatigue damage in the most critical areas of a pipeline free-span. The analyses are divided into the following sections:

- Structural study
- Frequency analysis
- Fatigue analysis

After the reference model is defined and analysed, the parametric study is initiated.

5.2.1.1. Static Loads

The static loads that have to be considered are:

- Self-weight (distributed load)
- Temperature load (axial load)
- Internal and external pressure (axial load)
- Poisson effect (axial load)

The self-weight is applied only at the free-span because the soil-springs at the side-spans are determined from the state of static equilibrium. The three contributions to axial load are applied at the total length of the pipeline. The physical interpretation of the axial loads is explained in Appendix A (Axial Force).

Self-Weight

The self-weight of the pipeline is the total submerged mass of the pipeline multiplied with gravity determined as

$$f_z = -m_{total} \cdot g \tag{5.2.1}$$

where

f_z	is the distributed load [N/m]
m_{total}	is the total submerged mass of the pipeline [kg/m]
g	is the gravity [N/kg]

Temperature Load

The temperature load emerges from the tendency of thermal expansion of the steel in the pipe-wall. If the pipe is assumed to be fully axially restrained, the temperature load creates an axial force in the pipeline determined as

$$F_x^{temp} = -E_{steel} \cdot \alpha \cdot \Delta T \cdot A_s \tag{5.2.2}$$

where

F_x^{temp}	is the axial force in the pipeline due to temperature [N]
E_{steel}	is the Young's modulus for steel [Pa]
α	is the expansion coefficient [1/°C]
ΔT	is the temperature difference [°C]
A_s	is the cross section area of the steel pipe [m²]

[DNV-RP-F105 2006, p31]

Internal and External Pressure

The pressure conditions inside and outside the pipeline result in an axial load. The internal and external pressure is defined in Chapter 1.1 (Design Conditions). The axial force due to pressure is determined as

$$F_x^{pressure} = -p_i A_i + p_e A_e \tag{5.2.3}$$

where

$F_x^{pressure}$	is the axial force in the pipeline due to pressure [N]
p_i	is the internal pressure [Pa]
A_i	is the internal cross section area of the pipe [m²]

p_e is the external pressure [Pa]

A_e is the external cross section area of the pipe including coating [m^2]

[DNV-RP-F105 2006, p31]

Poisson Effect

This axial force contribution is a result of the Poisson effect and the pressure difference. Assuming the pipe is fully axially restrained and thin-walled, the axial force due to the Poisson effect can be formulated as

$$F_x^{poisson} = 2\nu(p_i - p_e)A \qquad (5.2.4)$$

where

$F_x^{poisson}$ is the axial force in the pipeline due to the Poisson effect [N]

ν is the Poisson's ratio for steel [-]

A is the external cross section area of the pipe [m^2]

[DNV-RP-F105 2006, p31]

Total Static Load

The total axial force is determined as

$$\begin{aligned}
F_x &= F_x^{temp} + F_x^{pressure} + F_x^{poisson} \\
&= -E_{steel} \cdot \alpha \cdot \Delta T \cdot A_s - p_i A_i + p_e A_e + 2\nu(p_i - p_e)A
\end{aligned} \qquad (5.2.5)$$

The axial force during the operational state of the pipeline in the reference model is given in Table 32. The loads have been determined according to the parameters defined in Chapter 1.1 (Design Conditions).

Table 32: Contributions to the axial force that is defined as positive in tension.

Source		Axial force [MN]
Temperature	F_x^{temp}	-3.490
Pressure	$F_x^{pressure}$	-1.744
Poisson effect	$F_x^{poisson}$	1.192
Total	F_x	-4.042

In the Abaqus model, the axial load is implemented as an initial normal stress for the pipeline determined as

$$\sigma_x = \frac{F_x}{A_s} \qquad (5.2.6)$$

where

σ_x is the initial axial stress in the pipeline [Pa]

The static loads are given in Table 33. The static loads affect the stiffness of the pipeline if it undergoes large deformation. To include this impact, large deformation formulation has been used in the Abaqus Model which is referred to as non-linear geometry in Abaqus.

Table 33: Static loads applied to the reference model.

Functional state	Distributed load f_z [N/m]	Initial normal stress σ_x [Pa]
Operational	$-2.06 \cdot 10^3$	$-169.3 \cdot 10^6$

5.2.1.2. Dynamic Loads

The dynamic load is assumed to act only at the free-span which means that the dynamic load due to change in pore pressure at the side-spans is not taken into account. In order to determine the dynamic load, the particle velocities from wave and current are determined for five different sea states according to Chapter 1.1 (Design Conditions). Figure 149 shows the in-line ambient flow velocity from wave and current at the centreline of the pipe section for sea states 1-5.
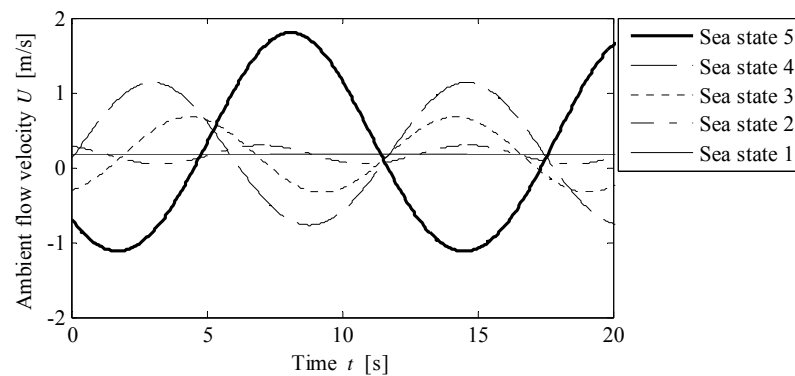

Figure 149: In-line ambient flow velocity at the centreline of the pipe section.

Figure 150 shows the in-line ambient flow acceleration at the centreline of the pipe section for sea states 1-5.
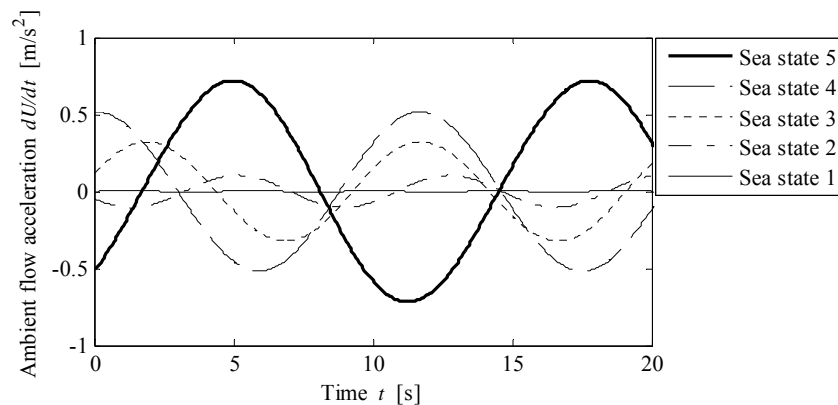

Figure 150: In-line ambient flow acceleration at the centreline of the pipeline section.

The dynamic loads in the in-line and cross-flow direction due to hydrodynamic forces are determined by the Morison Model according to Chapter 3.2 (Hydrodynamic Force Models). The Keulegan-Carpenter number and the force coefficients are shown in Table 34 for sea states 1-5.

Table 34: Keulegan-Carpenter number and force coefficients for sea states 1-5.

Sea state	KC	C_D	C_M	C_L
Sea state 5	31.0	1.3	2.1	2.5
Sea state 4	18.1	1.5	2.3	2.9
Sea state 3	8.0	1.9	2.3	3.1
Sea state 2	1.5	1.8	2.6	4.4
Sea state 1	0.0	1.5	3.1	4.49

Figure 151 and Figure 152 show the dynamic loads in the in-line and cross-flow direction, respectively, for sea state 1-5. It is noticed that a load ramp is implemented for $t = 0\text{-}13\,\text{s}$ to reduce the impact of initial conditions.
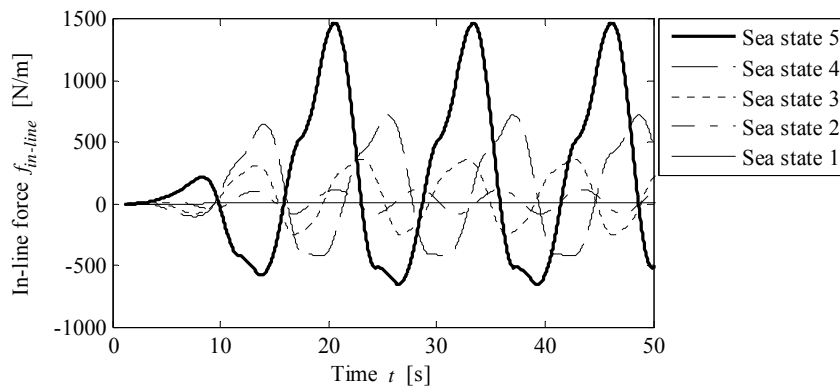

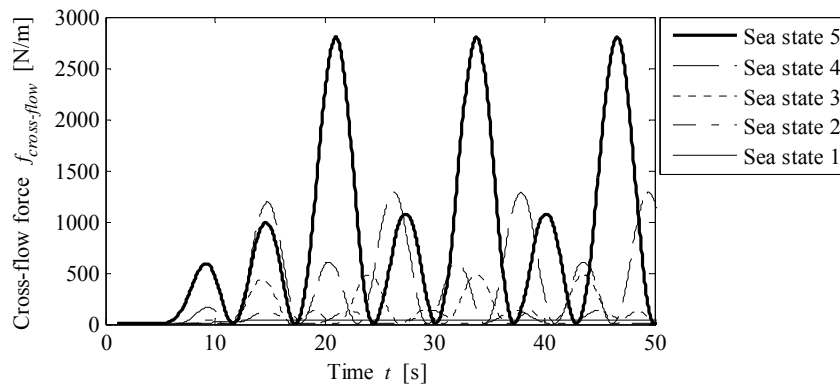*Figure 151: In-line force in the reference model for sea states 1-5.*

Figure 152: Cross-flow force in the reference model for sea states 1-5.

It is seen from Figure 151 and Figure 152 that the magnitude of the loads varies greatly for the different sea states.

5.2.1.3. Structural Study

This is a structural study of the pipeline free-span to determine the most critical areas for damage analyses along the pipeline. For simplicity, the stresses are based upon the effective stresses of the homogeneous pipe instead of the true stresses in the pipe-wall according to Appendix A (Axial Force). This has no effect for the determination of fatigue damage which is assumed to depend upon the amplitudes and not the mean value of the stresses according to Chapter 2.1 (Fatigue). The variation of the Von Mises stresses and normal stresses are examined when the dynamic load is determined for sea state 5. These stress variations will show the critical areas for yielding and fatigue, respectively.

Only four section points are analysed in the pipe section and they are chosen so they represent the stress response for vertical and lateral displacements of the pipeline. The location of the section points is shown in Figure 153.
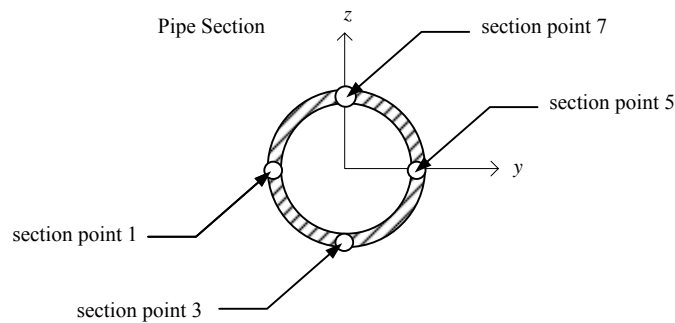

Figure 153: Location of section points in the pipe section.

The odd section point definition for the pipe element is determined by Abaqus. For some reason, intermediate points 2, 4, 6 and 8 are not available in Abaqus for this particular element.

Von Mises Stresses

Figure 154 shows the peak of the Von Mises stresses along the pipe during one wave period of sea state 5. The maximum Von Mises stress is calculated in section point 1.
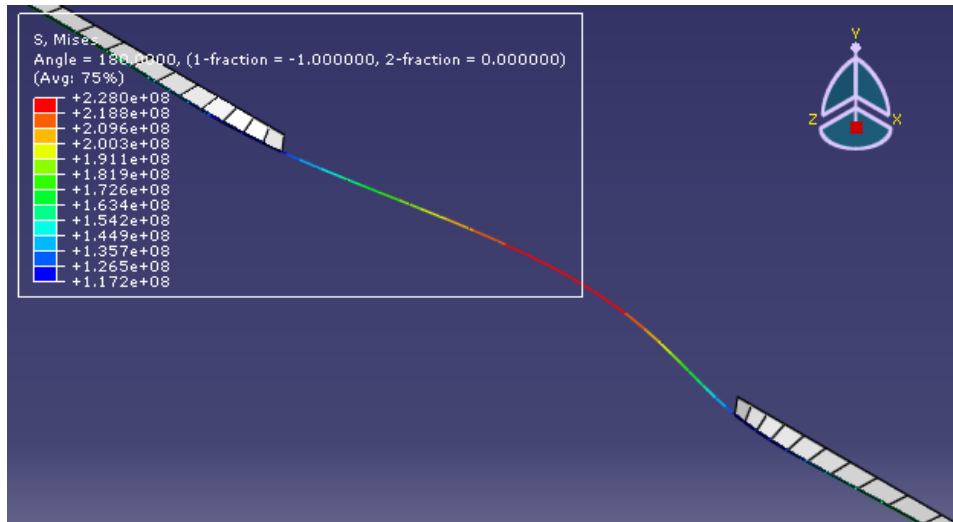
Figure 154: Maximum Von Mises stresses along the pipeline in section point 1 for sea state 5.

Figure 154 shows that the maximum Von Mises stress during a wave period is found in the centre of the pipeline mid-section.

Normal Stresses

To illustrate the difference of normal stresses along the pipeline, three sections have been examined. Figure 155 shows the location of these three sections.
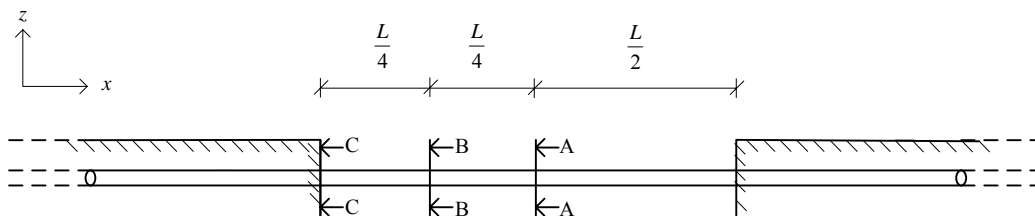

Figure 155: Sections along the pipeline where the normal stresses are examined.

Figure 156 and Figure 157 show the stress response for lateral and vertical excitation, respectively, in the three sections along the pipeline.
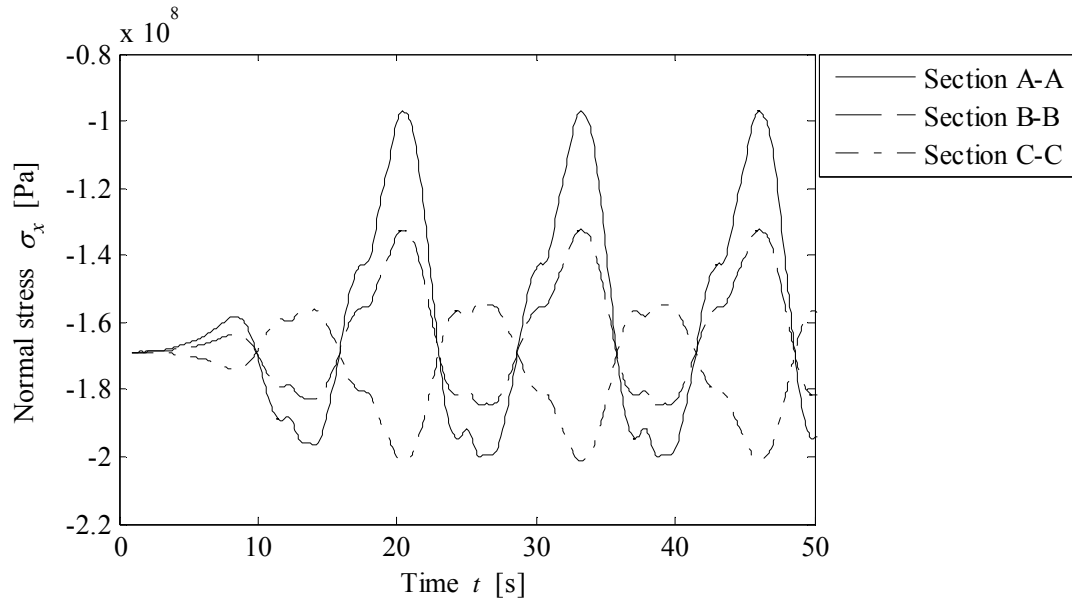
Figure 156: Normal stress in the three sections along the pipeline. Normal stresses are taken in section point 5 representing the stress response for lateral excitation.
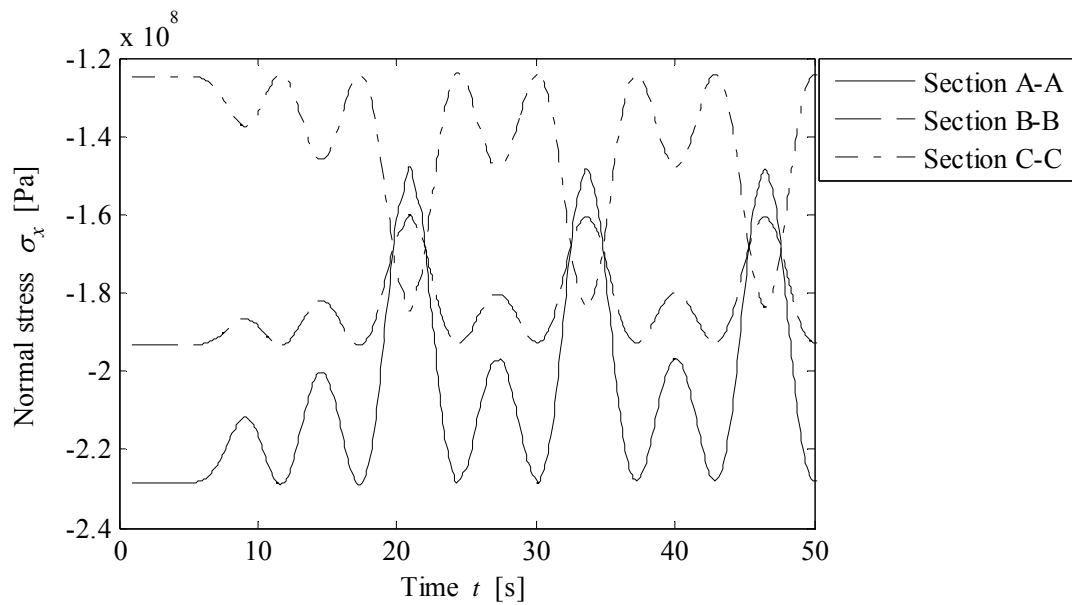

Figure 157: Normal stress in the three sections along the pipeline. Normal stresses are taken in section point 7 representing stress response for vertical excitation.

Figure 156 and Figure 157 show that the largest normal stress ranges are found in section A-A. Thus the damage analyses of the pipeline should be performed at the centre of the mid-span.

5.2.1.4. Frequency Analysis

The frequency analysis is performed to compare the eigenfrequencies with the load frequencies because this is known to have great influence on the dynamic response. Table 35 shows the load frequencies for sea states 1-5, respectively.

Table 35: Load frequencies for in-line and cross-flow force for sea states 1-5.

Sea state	In-line frequency $f_{in-line}$ [Hz]	Cross-flow frequency $f_{cross-flow}$ [Hz]
Sea state 5	0.08	0.16
Sea state 4	0.09	0.17
Sea state 3	0.10	0.20
Sea state 2	0.13	0.26
Sea state 1	0.23	0.45

Table 36 shows the four lowest eigenfrequencies for the reference model.

Table 36: The four lowest eigenfrequencies for the reference model.

Rank	1	2	3	4
Frequency [Hz]	0.73	1.23	2.31	3.81
Direction	Lateral	Vertical	Lateral	Vertical

To compare the dynamic response along the pipe, the normal stresses are calculated in the three sections defined in Figure 155. This will show if the critical cross section along the pipe depends on the load frequencies.

Figure 158 and Figure 159 show the stress response for lateral and vertical excitation, respectively, when a distributed in-line load $f_y = 1000\,\text{N/m}$ or cross-flow load $f_z = 1000\,\text{N/m}$, respectively, is applied to the free-span as a harmonic load with various load frequencies.
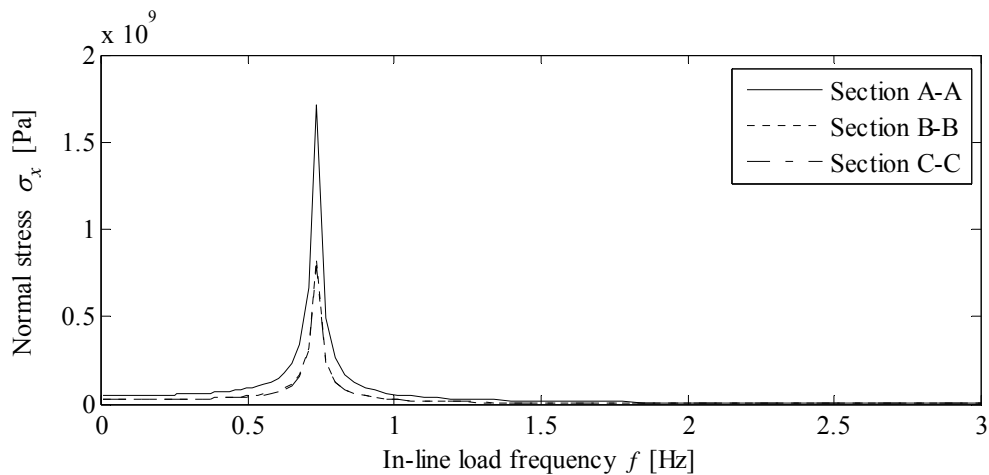

Figure 158: Normal stresses for varying in-line load frequencies and sections. Normal stresses are taken in section point 5 representing the stress response for lateral excitation.
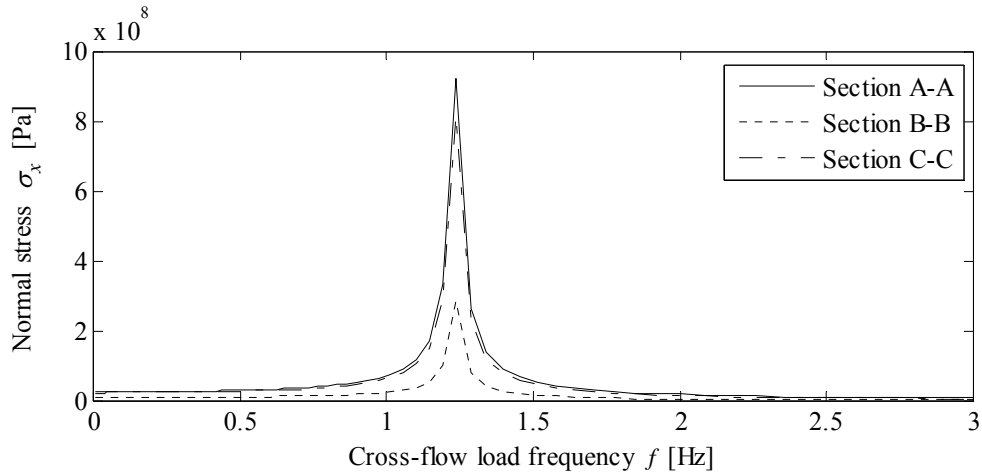
Figure 159: Normal stresses for varying cross-flow load frequencies and sections. Normal stresses are taken in section point 7 representing stress response for the vertical excitation.

It is seen from Figure 158 and Figure 159 that the stress response for all 3 sections peak at the same load frequency similar to the lowest eigenfrequency in the lateral and vertical direction, respectively. Figure 158 and Figure 159 also show that the load frequencies in the in-line and cross flow direction shown in Table 35 are not within the critical range of the frequency response.

5.2.1.5. Fatigue Analysis

The damage of the pipeline free-span is determined according to Chapter 2.1 (Fatigue). Because the load emerges from regular waves, some simplified methods are used when determining stress ranges and cycles. The simplifications are showed in the following.

Stress Ranges

The stress ranges in section A-A for lateral and vertical excitation during sea states 1-5 are shown in Figure 160 and Figure 161, respectively.
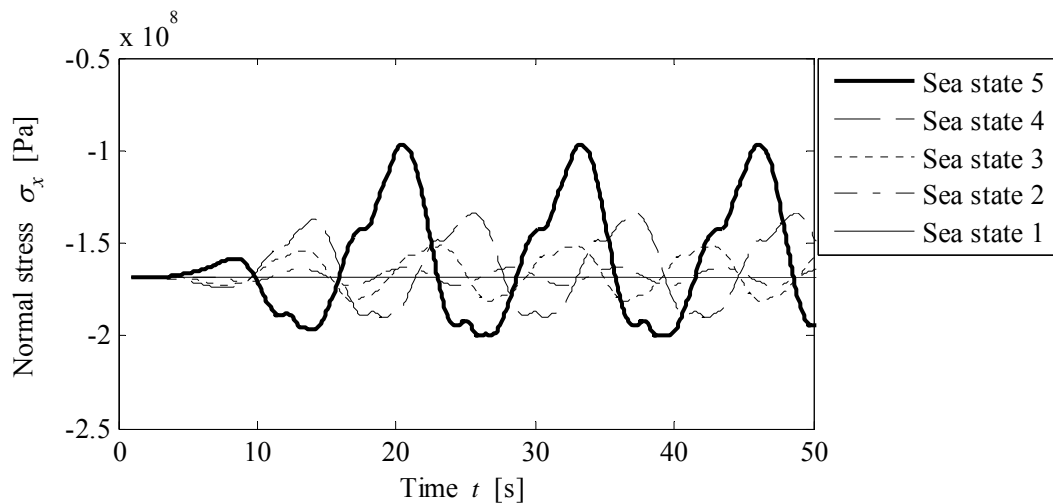

Figure 160: Stress ranges in section A-A for lateral excitation during the sea states 1-5.
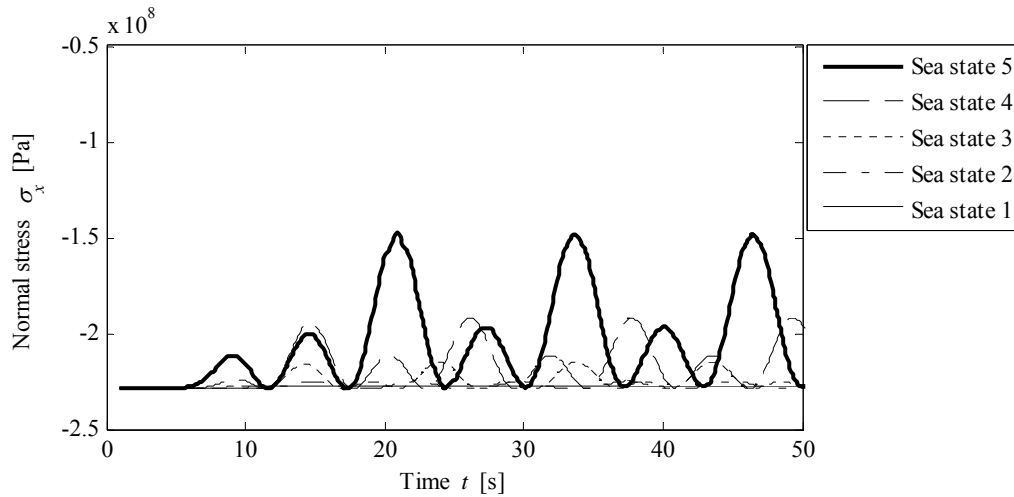
Figure 161: Stress ranges in section A-A for vertical excitation during the sea states 1-5.

In order to reduce calculation time, the stress ranges within one period T_p is determined when the initial conditions no longer affect the dynamic response and the response has become stationary.

Yield Stress Limit

The maximum Von Mises stresses are calculated in section A-A during sea state 5. The peak of Von Mises stress is shown in Figure 154 where the maximum Von Mises stress is determined as

$$\sigma_{mises} = 228\,\text{MPa} \leq f_{yd} = 415\,\text{MPa} \quad \text{OK!} \tag{5.2.7}$$

Stress Cycles

Because the stress ranges are determined within one wave period, the number of stress cycles for each sea state is found as

$$n_i = \frac{T_i}{T_{p,i}}, \qquad i = 1, 2, 3, 4, 5 \tag{5.2.8}$$

where

n_i is the number of stress cycles [-]

T_i is the duration of the individual sea state [s]

$T_{p,i}$ is the peak wave period of the individual sea state [s]

i is the number of sea state [-]

The duration of the sea states and the peak wave period can be found in Chapter 1.1 (Design Conditions).

Damage

The damage caused by the stress ranges is determined in the mid-section A-A. The damage caused by lateral and vertical excitation is determined in section point 5 and 7, respectively. Table 37 shows the damage contributions from each sea state and the total damage calculated for the reference model is shown at the bottom of the table.

Table 37: Damage in the mid-section in the reference model for sea states 1-5.

Sea state	Damage	
	$D_{lateral}$ [-]	$D_{vertical}$ [-]
Sea state 5	0.012	0.006
Sea state 4	0.004	0.001
Sea state 3	0.006	0.001
Sea state 2	0.000	0.000
Sea state 1	0.000	0.000
Total	0.023	0.008

Table 37 shows that only sea states 3-5 have significant impact on the total damage of the pipeline in the reference model. It is seen that sea state 5 which represents an environmental load from a 10 year storm causes more than 50% of the damage experienced by the pipeline.

The damage caused by vertical excitation is significantly lower than the damage caused by lateral excitation. The number of cycles is higher in the vertical direction and the stress ranges are lower than the stress ranges caused by lateral excitation, which shows that the magnitude of stress ranges in this case has the largest impact on damage.

The damage caused by lateral excitation has not reached the damage limit $D_{lim} = 0.1$ which is described in Chapter 2.1 (Fatigue). The damage in the diagonal of the pipe section caused by resulting motion could be higher than the damage detected in section point 5 and 7. For the sake of simplicity, the damage ratios compared in the following parametric study are only compared for lateral and vertical pipeline excitation, respectively.

5.2.2   EFFECT OF FUNCTIONAL STATE

This analysis is made to find the most critical functional state for the pipeline free-span considering fatigue damage. The functional states that are considered are:

1. Water-filled condition
2. Air-filled condition
3. Operational condition (reference model)

The design condition for each functional state is shown in Chapter 1.1 (Design Conditions). The functional state has an impact on the following input parameters:

- Static loads

- Added mass

The functional state have an impact on the load-displacement curves for the soil springs because the weight of the pipeline changes for different contents. However, this impact is considered to be limited and the load-displacement curves are determined for the water-filled condition in all functional states according to Chapter 4.1 (Soil Springs). The weight of the pipeline has the largest impact on the upward soil spring but calculations have shown that this impact is limited considering the dynamic behaviour of the global system of the pipeline free-span.

The static loads that are applied in the functional states have an impact on the global stiffness of the pipeline free-span. An analysis of stiffness reduction due to initial stresses has been made by comparing the dynamic response of a pipeline free-span in water-filled and operational state.

Static Loads

The distributed load changes because of the difference in contents for each functional state. The temperature and pressure also changes for each functional state, which has an impact on the axial force applied to the pipe. Table 38 shows the static loads for each functional state.

Table 38: Static loads for each functional state.

Functional State	Distributed load f_z [N/m]	Initial normal stress σ_x [Pa]
Water filled	$-3.65 \cdot 10^3$	0
Air filled	$-1.86 \cdot 10^3$	$3.52 \cdot 10^6$
Operational	$-2.06 \cdot 10^3$	$-169.3 \cdot 10^6$

Added Mass

The added mass is different for each functional state due to the density change of the pipeline's content. Table 39 shows the added mass for each functional state.

Table 39: Added mass for each functional state.

Functional State	Added mass for content [kg/m]	Total added mass [kg/m]	
		Side-span	Free-span
Water-filled	182.4	1075.4	1235.5
Air-filled	0.2	893.2	1053.3
Operational	20.1	913.1	1073.2

5.2.2.1. Stiffness due to Initial Stresses

The stiffness due to initial stresses is governed by the normal stress from the static load. If the pipeline is in tension, the stiffness due to initial stresses will contribute to the total stiffness of the pipe. The opposite will happen if the pipeline is in compression. The impact of stiffness due to initial

stresses will increase for increasing spanning lengths because the response of the pipeline goes from being dominated by beam behaviour to being dominated by cable behaviour.

The stiffness due to initial stresses is analysed for a pipeline in water-filled and operational condition. The air-filled condition is considered to be of minor importance. Figure 162 shows a sketch of the pipeline free-span for a pipeline in water-filled and operational condition.
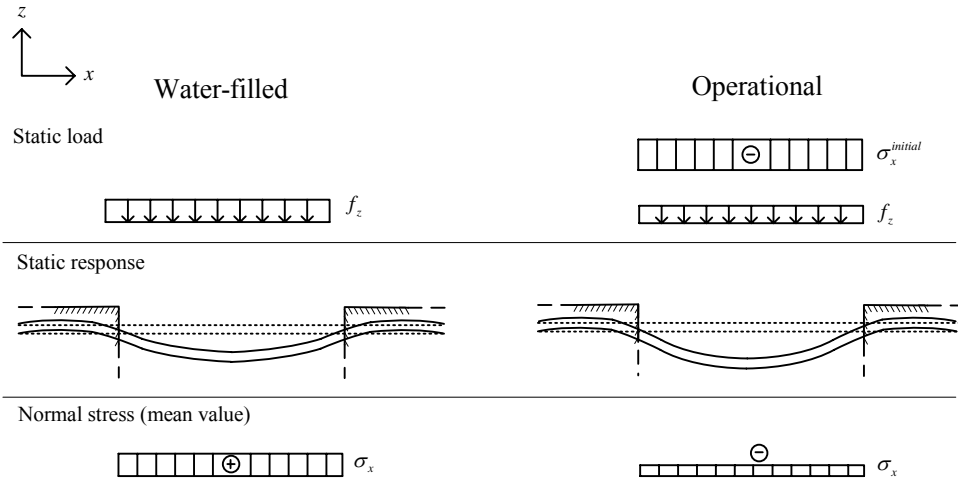

Figure 162: Initial conditions for water-filled and operational pipeline.

As Figure 162 implies, the geometrical stiffness of the operational state is lower than that of the water-filled state. This will cause larger deflection of the pipeline and increase the normal stresses in the pipeline section due to the increase of bending moment. Because the total stiffness of the pipeline is lower in the operational state, larger dynamic displacements and stress ranges are expected for this functional state.

Figure 163 shows the difference in lateral displacement in the centre of the mid-span for the water-filled and operational condition, respectively, during sea state 5.
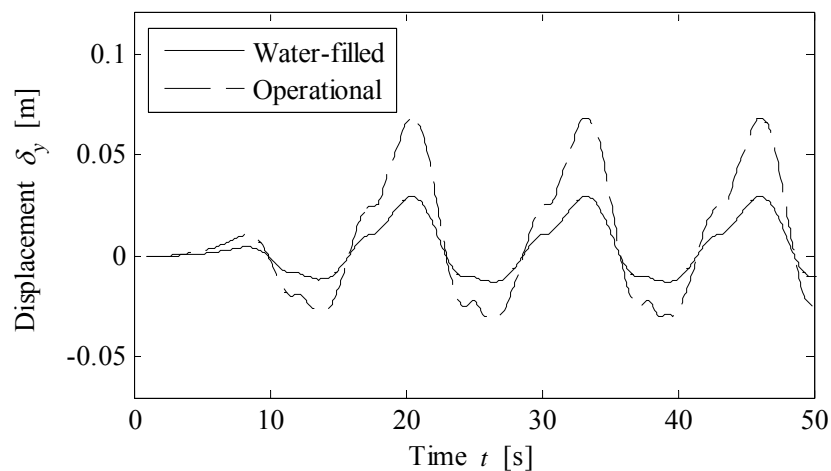

Figure 163: Lateral displacement in the centre of the mid-span for water-filled and operational condition in sea state 5.

It is seen that the geometrical stiffness has significant influence on the total stiffness of the pipeline because the axial pressure during the operational state causes the lateral displacements to increase radically.

5.2.2.2. Frequency Analysis

This section discusses the dynamic response influenced by the functional states. Table 33 shows the four lowest eigenfrequencies for each functional state.

Table 40: The four lowest eigenfrequencies for each functional state.

Functional state	Lateral f_1 [Hz]	Vertical f_2 [Hz]	Lateral f_3 [Hz]	Vertical f_4 [Hz]
Water-filled	1.03	1.50	2.53	3.85
Air-filled	1.11	1.61	2.72	4.15
Operational	0.73	1.23	2.31	3.81

To compare the dynamic response for each functional state, the normal stresses are calculated in the mid-section A-A. Figure 164 and Figure 165 show the normal stress response in section point 5 and 7 when a distributed in-line load $f_y = 1000\,\text{N/m}$ or vertical load $f_z = 1000\,\text{N/m}$, respectively, is applied. The load is applied to the free-span as a harmonic load with various load frequencies.
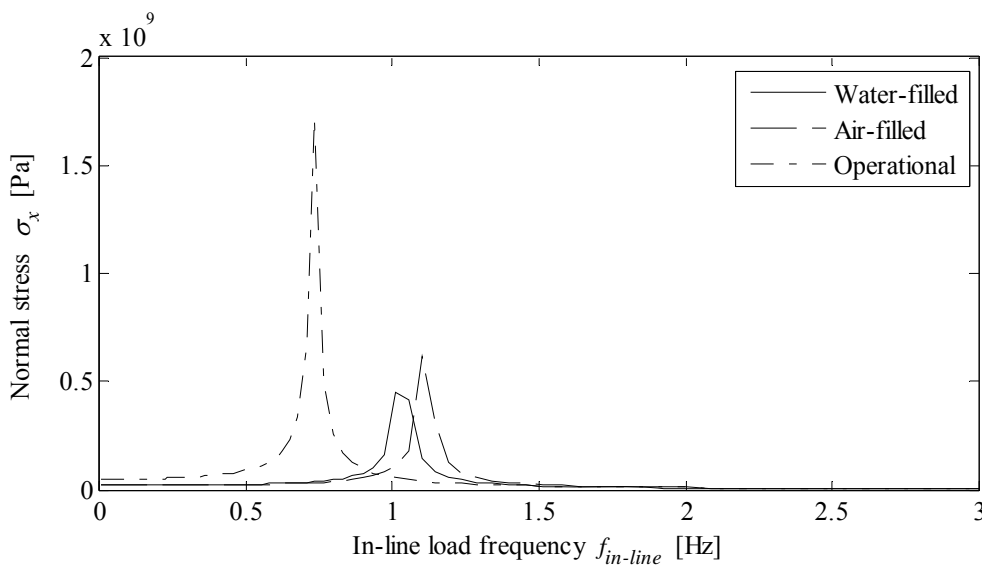

Figure 164: Normal stresses for varying in-line load frequencies and functional states. Normal stresses are taken in mid-section A-A in section point 5.
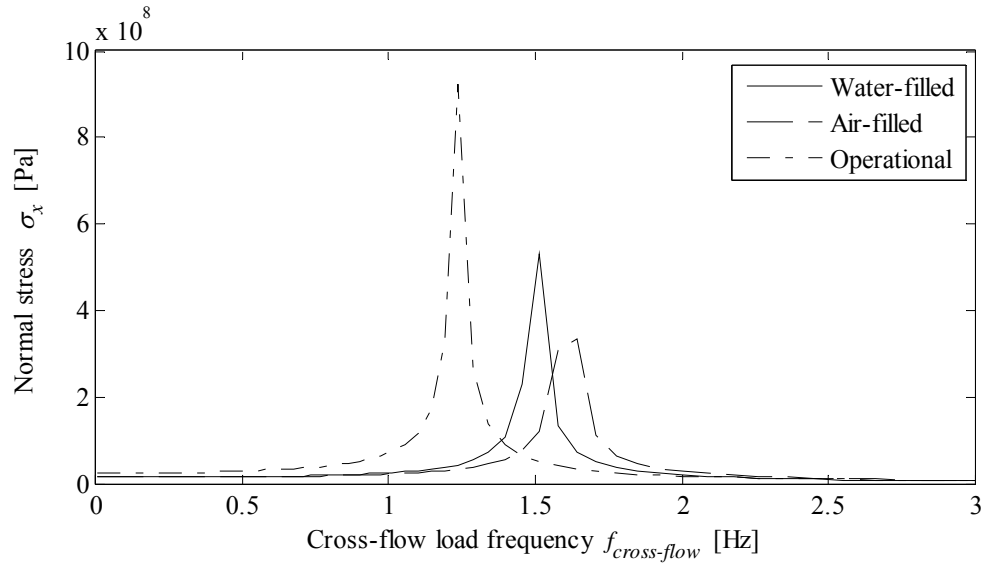
Figure 165: Normal stresses for varying cross-flow load frequencies and functional states. Normal stresses are taken in mid-section A-A in section point 7.

The load frequencies from the sea states are in the range of 0.08-0.45 Hz. Figure 164 and Figure 165 show that the operational state will result in the largest stress response in this range of load frequencies. Thus, the operational state is most likely to be the critical functional state when considering fatigue.

5.2.2.3. Fatigue Analysis

The fatigue analysis is made to find the difference in fatigue damage for the 3 functional states. Table 41 shows the fatigue damage for each functional state respectively.

Table 41: Damage ratios for the three functional states.

Functional state	Damage	
	$D_{lateral}$ [-]	$D_{vertical}$ [-]
Water-filled	0.001	0.001
Air-filled	0.001	0.001
Operational	0.023	0.008

It is seen that the operational pipeline is much more vulnerable considering fatigue compared to the two other functional states. This is mainly because of the loss of stiffness due to initial stresses in the operational state.

5.2.3   EFFECT OF SPANNING LENGTH

This analysis is made to determine the correlation between the spanning length and the damage of the pipeline. Frequency and damage analyses are made for spanning lengths in the range of 15-30 m.

5.2.3.1. Frequency Analysis

The frequency analysis is made to see if the load frequencies result in critical dynamic amplification for some of the spanning lengths. Table 42 shows the four lowest eigenfrequencies for the different spanning lengths.

Table 42: Eigenfrequencies for different spanning lengths.

Spanning length L[m]	Lateral f_1 [Hz]	Vertical f_2 [Hz]	Lateral f_3 [Hz]	Vertical f_4 [Hz]
30.0	0.45	0.82	1.79	2.76
25.0	0.73	1.23	2.31	3.81
20.0	1.10	1.89	2.95	5.41
15.0	1.61	3.00	3.63	7.92

The frequency response for the different spanning lengths is compared. Figure 166 and Figure 167 show the normal stress response in section point 5 and 7 when a distributed in-line load $f_y = 1000\,\text{N/m}$ or vertical load $f_z = 1000\,\text{N/m}$, respectively, is applied. The load is applied to the free-span as a harmonic load with various load frequencies.
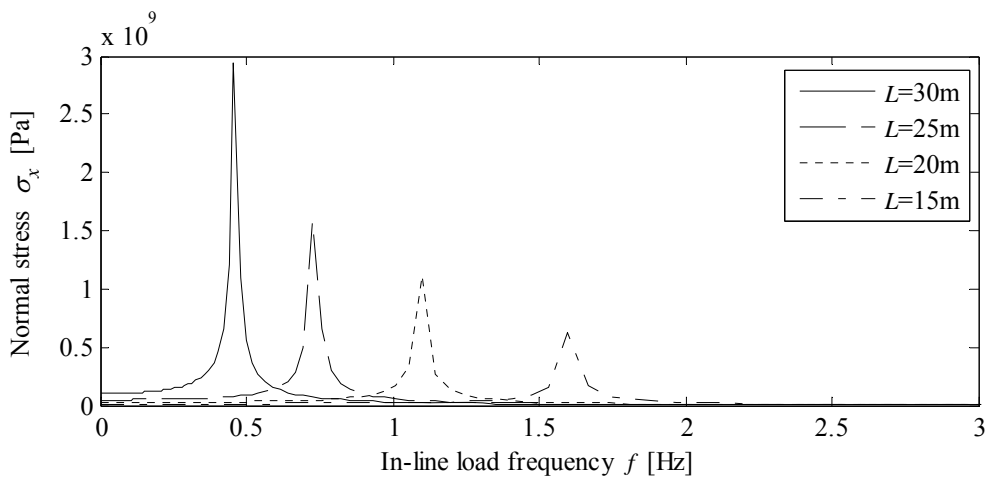

Figure 166: Normal stresses for varying in-line load frequencies and spanning lengths. Normal stresses are taken in mid-section A-A in section point 5.
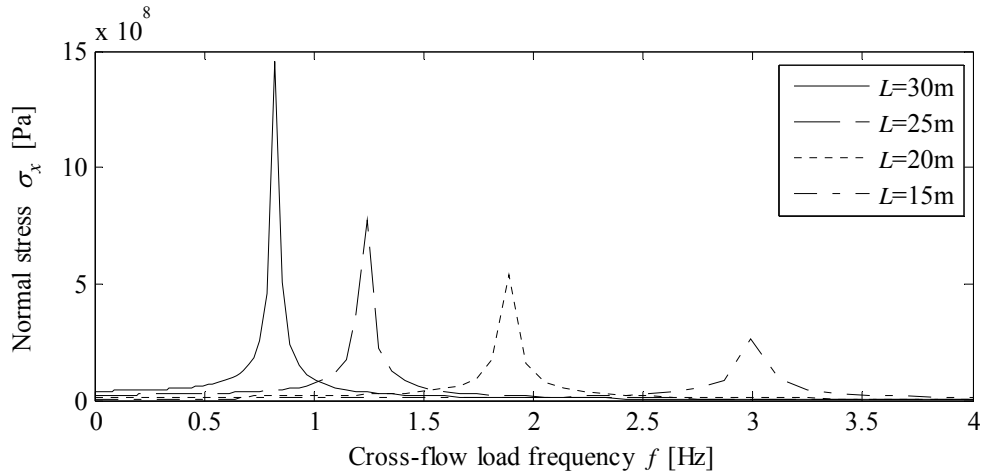
Figure 167: Normal stresses for varying cross-flow load frequencies and spanning lengths. Normal stresses are taken in mid-section A-A in section point 7.

Figure 166 and Figure 167 shows that the load frequencies approach the critical range of dynamic response for a spanning length $L = 30\,\text{m}$.

5.2.3.2. Fatigue Analysis

Table 43 shows the damage caused by lateral and vertical excitation as a function of the spanning lengths.

Table 43: Damage ratio of pipeline as a function of spanning lengths.

Spanning length $L\,[\text{m}]$	Damage	
	$D_{lateral}\,[-]$	$D_{vertical}\,[-]$
30.0	0.25	0.05
25.0	0.02	$8.4 \cdot 10^{-3}$
20.0	$3.3 \cdot 10^{-3}$	$1.4 \cdot 10^{-3}$
15.0	$0.5 \cdot 10^{-3}$	$0.2 \cdot 10^{-3}$

Table 43 indicates that the damage limit of $D_{limit} = 0.1$ is exceeded at a spanning length somewhere between 25-30m. This indicates that even though the damage ratio calculated at $L = 25\text{m}$ is low, the damage can increase to a significant value within a few meters extension of the spanning length.

Figure 168 illustrates the correlation between damage and spanning length by fitting curves according to the results shown in Table 43.
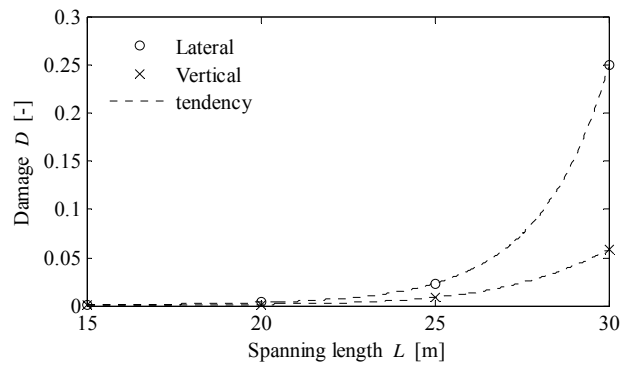
Figure 168: Correlation between damage and spanning length.

Figure 168 shows that the damage ratio increases rapidly when the spanning length exceeds $L = 25\text{m}$. Figure 168 also shows that a pipeline free-span of $L < 25\text{m}$ has hardly experienced any damage during 1 year of exposure.

Analyses of the dynamic response for the spanning lengths of $L = 30\text{m}$ show that the soil springs at the pipe shoulder exceed their maximum bearing capacity, which also decreases the resistance of the structural system.

5.2.4   EFFECT OF DAMPING

In this section, the damping influence of the dynamic response is analysed for fluid damping and material damping, respectively.

5.2.4.1. Fluid Damping

The fluid damping is included in the Morison Model according to Chapter 3.2 (Hydrodynamic Force Models). The fluid damping is relevant if the structure has a significant velocity compared to the ambient velocity. To determine if this is the case, Figure 169 shows the velocity of the pipe and the ambient flow for sea state 5.
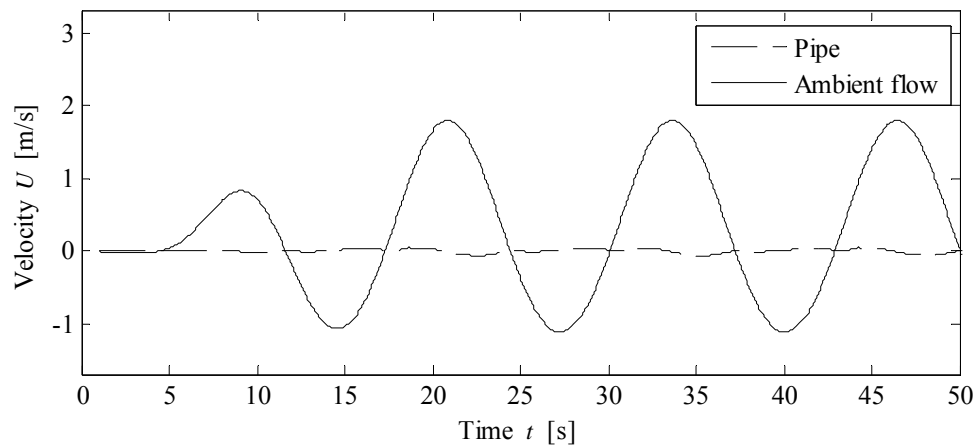
Figure 169: Velocity of pipe and ambient flow for sea state 5. The pipe velocity is shown for the mid-section A-A.

Figure 169 shows that the pipe velocity is small and insignificant compared to the velocity of the ambient flow for sea state 5. The same comparison has been made for sea state 1-4, which shows similar results. The pipe velocity increases when the load frequency is closer to the eigenfrequency. This could happen if the pipeline free-span experiences vortex lock-in, in which case fluid damping should be included.

To illustrate the fact that fluid damping does not affect the dynamic response of the pipeline, the stress ranges for lateral excitation are shown in Figure 170 for a dynamic model with and without fluid damping.
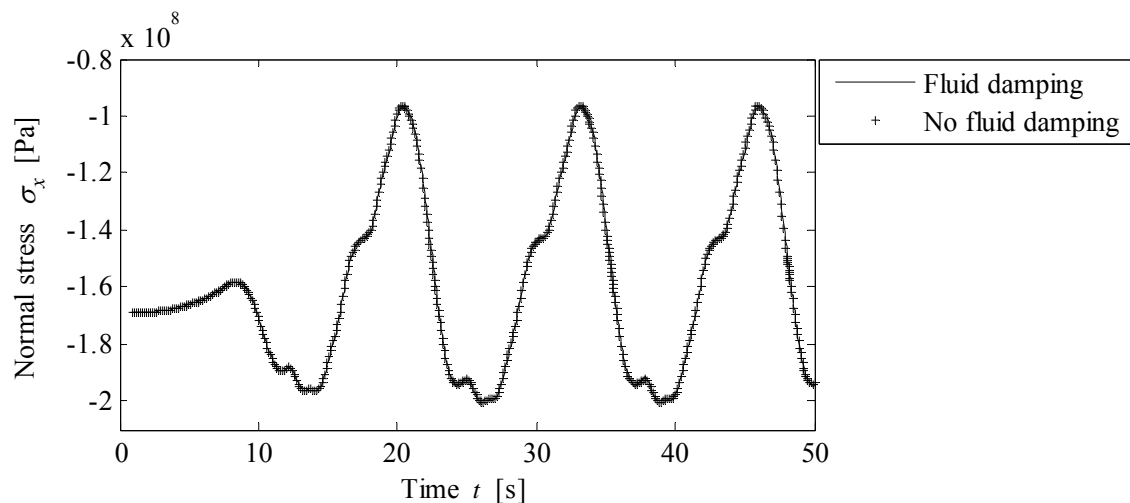

Figure 170: Stress ranges for lateral excitation in a dynamic model with and without fluid damping. Stress ranges are taken in the centre of the mid-span during sea state 5.

Because the stress ranges are unchanged for a dynamic model with and without fluid damping, the fluid damping will not have any influence on the fatigue of the pipeline.

5.2.4.2. Material Damping

The material damping is applied to the model as a Rayleigh damping according to Chapter 1.1 (Design Conditions). The dynamic response is compared for three different damping ratios:

- $\zeta = 0.005$

- $\zeta = 0.010$ (reference model)

- $\zeta = 0.015$

Figure 171 shows the stress ranges for lateral excitation in a dynamic model with three different damping ratios.
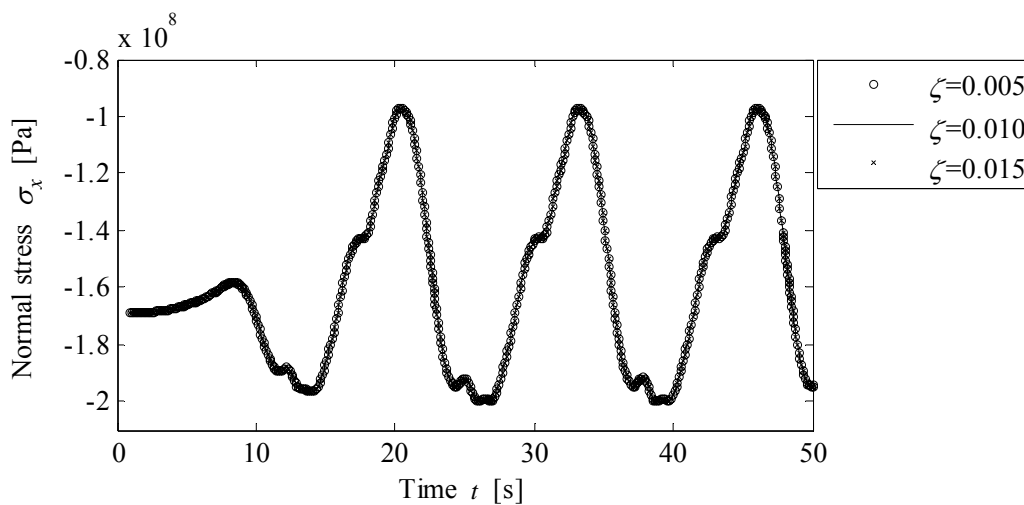

Figure 171: Stress ranges for lateral excitation in a dynamic model with different damping ratios. Stress ranges are taken in the centre of the mid-span. The ambient flow applied is sea state 5.

Figure 171 shows that the small change in damping ratios does not affect the calculated stress response of the model. The reason for this is that the velocity of the pipeline is small due to the difference in load and eigenfrequencies, which has been shown in Figure 169.

5.2.5 EFFECT OF GAP RATIO

In this section, the gap ratio's influence on the damage of the pipeline is investigated. Three gap ratios have been evaluated in this analysis:

- Large gap ratio: $e/D = 1$
- Small gap ratio: $e/D = 0.1$
- No gap ratio: $e/D = 0$ (reference model)

The gap ratio has great influence on the force coefficients that are applied in the force models, see Chapter 3.2 (Hydrodynamic Force Models), and the hydrodynamic mass that is applied to the free-

span, see Chapter 5.1 (Winkler Model). The following input parameters must be recalculated when the gap ratio is changed:

- Hydrodynamic mass and total added mass
- Hydrodynamic force coefficients C_M, C_D and C_L
- In-line and cross-flow forces per unit length of the pipe $f^{in-line}$, $f^{cross-flow}$

Added Mass

Table 44 shows the hydrodynamic mass and the total added mass for the three different gap ratios. The hydrodynamic mass is determined according to Chapter 5.1 (Winkler Model) which also describes why the hydrodynamic mass increases with decreasing gap ratio.

Table 44: Total added mass for the three different gap ratios.

Gap ratio e/D [-]	Hydrodynamic mass [kg/m]	Total added mass [kg/m]	
		Side-span	**Free-span**
1.0	309.5	913.2	399.2
0.1	464.2	913.2	668.7
0.0	708.7	913.2	1073.2

Force Coefficients and Dynamic Loads

Table 45 shows the force coefficients for the three gap ratios. The force coefficients are determined according to Chapter 3.2 (Hydrodynamic Force Models).

Table 45: Hydrodynamic force coefficients for different gap ratios.

Sea state	$\frac{e}{D}=1$			$\frac{e}{D}=0.1$			$\frac{e}{D}=0$		
	C_D	C_M	C_L	C_D	C_M	C_L	C_D	C_M	C_L
Sea state 5	1.0	1.3	0.5	1.1	1.7	1.4	1.3	2.1	2.5
Sea state 4	1.1	1.4	1.0	1.3	1.8	1.9	1.5	2.3	2.9
Sea state 3	1.4	1.4	1.9	1.6	1.8	2.3	1.9	2.3	3.1
Sea state 2	1.3	1.6	2.0	1.5	2.0	2.5	1.8	2.6	4.4
Sea state 1	1.0	1.9	2.1	1.2	2.5	2.6	1.5	3.1	4.49

Figure 172 shows the in-line force for sea state 5 for the different gap ratios. The in-line force is determined according to Chapter 3.2 (Hydrodynamic Force Models).
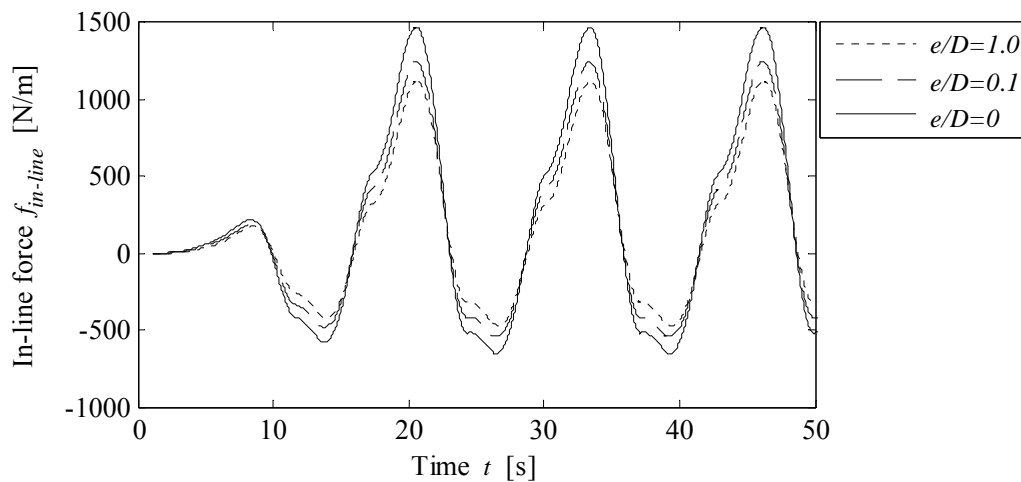
Figure 172: In-line force for sea state 5 for the different gap ratios.

The range between the maximum and minimum value of $f_{in-line}$ increases with approximately 34% for $e/D = 0$ compared to the case where $e/D = 1.0$. The damage of the pipeline free-span is expected to increase for smaller gaps due to this change in force. Also the cross-flow force increases when the gap ratio decreases but the comparison of the cross-flow force is not illustrated.

5.2.5.1. Frequency Analysis

The change in added mass also changes the eigenfrequencies of the pipeline free-span. Table 46 shows the change in the four lowest eigenfrequencies for different gap ratios.

Table 46: Eigenfrequencies for different gap ratios.

Gap ratio e/D [-]	Lateral f_1 [Hz]	Vertical f_2 [Hz]	Lateral f_3 [Hz]	Vertical f_4 [Hz]
1.0	1.06	1.80	3.07	5.50
0.1	0.88	1.41	2.70	4.60
0.0	0.73	1.23	2.31	3.81

It is seen from Table 46 that the eigenfrequencies of the pipeline free-span decreases as the gap ratio decreases, which is due to the increment of added mass. Because the load frequency are in the range of $0.08\,\text{Hz} - 0.45\,\text{Hz}$, the dynamic response will rise as the gap ratio decreases. This, held together with the findings in the previous analysis of the force, means that the largest stress ranges and most damage will be expected to appear at a gap ratio of $e/D = 0.0$.

5.2.5.2. Fatigue Analysis

Table 47 shows the damage caused by lateral and vertical excitation of the pipeline free-span with three different gap ratios.

Table 47: Damage for different gap ratios.

Gap ratio	Damage	
e/D [-]	$D_{lateral}$ [-]	$D_{vertical}$ [-]
1.0	$0.8 \cdot 10^{-2}$	$2.3 \cdot 10^{-4}$
0.1	$1.3 \cdot 10^{-2}$	$1.8 \cdot 10^{-3}$
0.0	$2.3 \cdot 10^{-2}$	$8.4 \cdot 10^{-3}$

To illustrate the influence of gap ratio considering damage of the pipeline, the results from Table 47 are shown in Figure 173. Tendency lines are shown according to the fatigue analysis for the three different gap ratios.
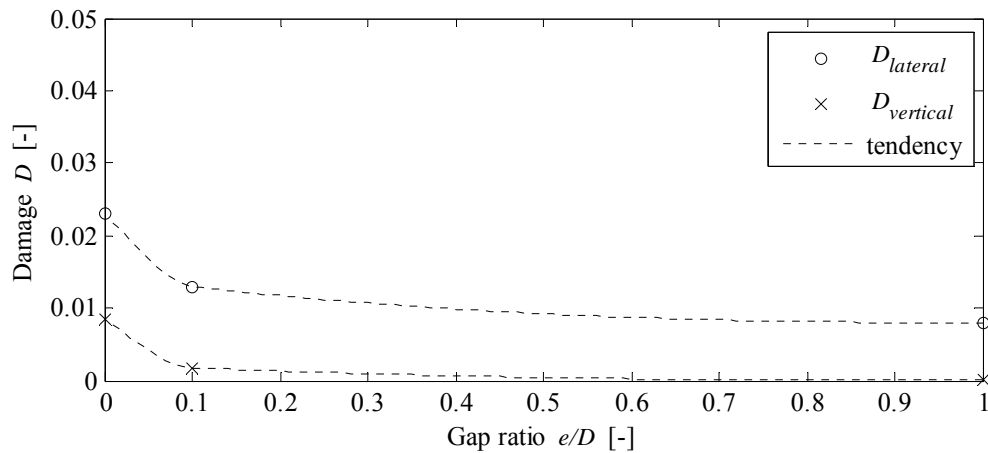

Figure 173: Damage for different gap ratios.

It is seen that the damage of the pipeline increases significantly for $e/D < 0.1$. For larger gap ratios, the change in damage is of minor importance. It is however highly conservative to calculate the damage of the pipeline assuming $e/D = 0$ because practical experiences have shown that that the gap ratio will increase to $e/D > 0.1$ within a short time after the erosion under the pipeline has started.

5.2.5.3. Vortex Lock-in

As explained in Chapter 3.1 (Near-Wall Cylinder) and Chapter 3.2 (Hydrodynamic Force Models), vortex lock-in must be considered when the gap ratio exceeds the value of 1.0. To ensure the damage estimate made has not been compromised by this phenomenon, the reduced velocity U_r is calculated for the case with a gap ratio $e/D = 1.0$. Inserting the maximum velocity for sea state 5 and the 1st eigenfrequency in the formula for the relative velocity gives

$$
\begin{aligned}
U_{r,1} &= \frac{U_{max,5}}{f_1 \cdot D} \\
&= \frac{1.80 \frac{m}{s}}{1.06 \, Hz \cdot 0.608 m} \\
&= 2.79
\end{aligned}
\tag{5.2.9}
$$

The reduced velocity in calculated in (5.2.9) is below the range of vortex lock in (4.8-8.0). It can be concluded that vortex lock-in will not appear in any of the sea states as the reduced velocity takes the highest value for sea state 5 and vortex lock-in does not cause additional damage in the present case. It is noticed that the lowest vertical eigenfrequency for a free-span with a gap ratio of 1.0 should be below the value of 0.62 Hz during sea state 5 before the free-span experiences vortex lock-in. This is kept in mind in the further analyses.

5.2.6   EFFECT OF FRICTION ANGLE OF SOIL

This is a parametric study of the friction angle's influence on the dynamic response and fatigue of the pipeline free-span. The analysis is made for three different frictions angles:

- $\varphi' = 25°$

- $\varphi' = 30°$ (reference model)

- $\varphi' = 35°$

The load-displacement curves for the soil springs are determined analytically for the three different frictions angles as shown in Chapter 4.1 (Soil Springs). The soil springs in the Winkler model are adjusted according to the load-displacement curves calculated for each friction angle. In this way, it is possible to compare the effect on frequency, dynamic response and fatigue of the pipeline free-span for different friction angles.

5.2.6.1. Frequency Analysis

Table 48 shows the four lowest eigenfrequencies of the pipeline free-span for the three different angles of friction.

Table 48: Eigenfrequencies for different friction angles.

Friction angle φ' [°]	Lateral f_1 [Hz]	Vertical f_2 [Hz]	Lateral f_3 [Hz]	Vertical f_4 [Hz]
25	0.66	1.23	2.14	3.81
30	0.73	1.23	2.31	3.81
35	0.78	1.23	2.49	3.81

The results in Table 48 show that the change in friction angle only has a minor influence on the lateral frequencies. The vertical frequencies are unchanged because of the high vertical soil stiffness which does not change significantly for different friction angles. The frequency response in both lateral and vertical direction will be similar for the three different friction angles and is for this reason not shown in this analysis.

5.2.6.2. Fatigue Analysis

Table 49 shows the damage caused by lateral and vertical excitation of the pipeline free-span in soil with three different friction angles.

Table 49: Damage for different friction angles

Friction angle	Damage	
φ' [°]	$D_{lateral}$ [-]	$D_{vertical}$ [-]
25	$3.3 \cdot 10^{-2}$	$12.4 \cdot 10^{-3}$
30	$2.3 \cdot 10^{-2}$	$8.4 \cdot 10^{-3}$
35	$1.6 \cdot 10^{-2}$	$0.6 \cdot 10^{-3}$

To illustrate the influence of the friction angle considering damage of the pipeline, the results from Table 49 are shown in Figure 173. Tendency lines are shown according to the fatigue analysis for the three different friction angles.
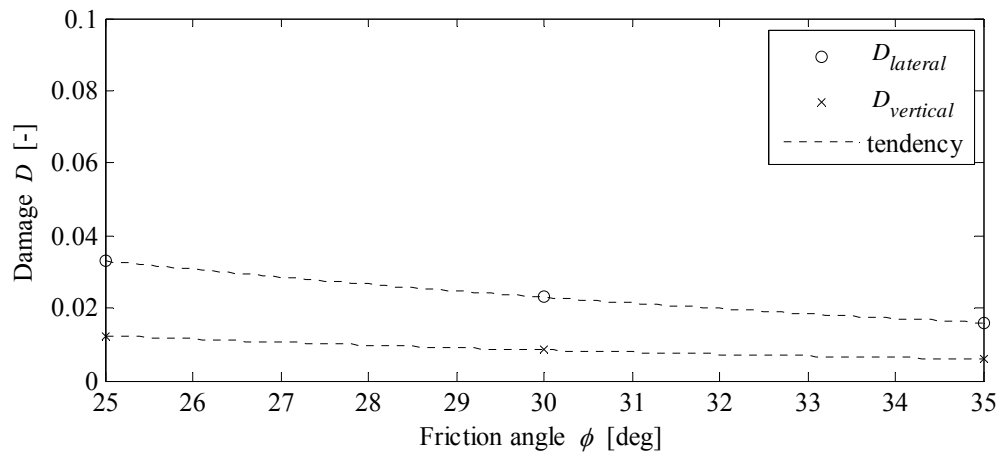

Figure 174: Damage for different friction angles

Figure 174 shows that the damage decreases for higher values of friction angles. The correlation between damage and friction angle is almost linear for both lateral and vertical excitation.

It is noticed that the correlation between damage and friction angle will not be linear if the spanning length or the forces affecting the pipeline free-span are increased so the soil springs near the pipe shoulders reach their non-linear area above the maximum bearing capacity. This will happen sooner for the soil with lower friction angles resulting in an instant and significant increase in damage.

5.2.7 EFFECT OF COATING STIFFNESS

If the contribution of the coating to the structural response is considered to be significant, appropriate models shall be used [DNV-RP-F105 p30]. This analysis will show the effect of including coating stiffness in the bending stiffness (EI) of the dynamic model. Frequency and damage analyses are made for a pipeline free-span with and without coating stiffness, respectively. The pipeline free-span is calculated with two different Young's moduli for the pipeline:

- Young's modulus for steel $E_{steel} = 0.21 \cdot 10^{12} \, Pa$
- Equivalent Young's modulus $E_{equivalent} = 0.34 \cdot 10^{12} \, Pa$ (reference model)

The effect of coating stiffness is included in the bending stiffness of the pipeline as described in Chapter 5.1 (Winkler Model).

5.2.7.1. Frequency Analysis

Table 50 shows the four lowest eigenfrequencies for the pipeline with and without coating stiffness, respectively.

Table 50:Eigenfrequencies for E_{steel} and $E_{equivalent}$.

Young's modulus E [GPa]	Lateral f_1 [Hz]	Vertical f_2 [Hz]	Lateral f_3 [Hz]	Vertical f_4 [Hz]
210	0.36	0.83	1.83	2.96
340	0.73	1.23	2.31	3.81

The frequency response for E_{steel} and $E_{equivalent}$ is compared. Figure 175 and Figure 176 show the normal stress response in section point 5 and 7 when a distributed in-line load $f_y = 1000\,\text{N/m}$ or vertical load $f_z = 1000\,\text{N/m}$, respectively, is applied to the free-span as a harmonic load with various load frequencies.
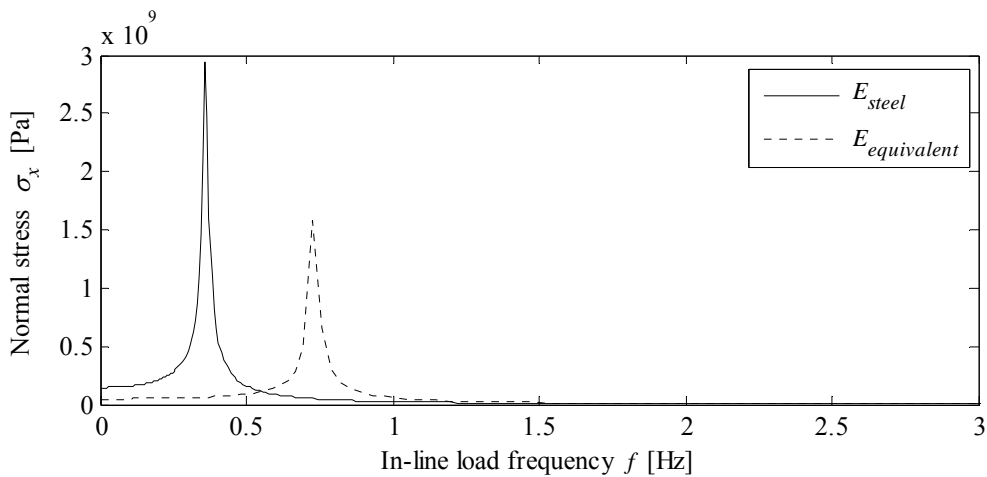

Figure 175: Normal stresses for varying in-line load frequencies. Normal stresses are taken in section point 5 in mid-section A-A for E_{steel} and $E_{equivalent}$, respectively.
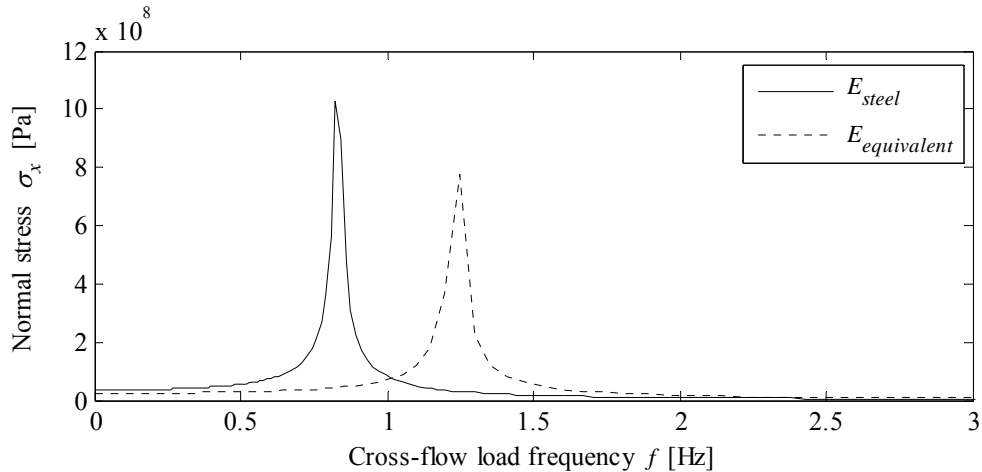
Figure 176: Normal stresses for varying in-line load frequencies. Normal stresses are taken in section point 5 in mid-section A-A for E_{steel} and $E_{equivalent}$, respectively.

It is seen that the eigenfrequency decreases significantly if coating stiffness is not included. This is a consequence of the initial normal stress which decreases the frequency of the pipeline free-span significantly as the free-span in principle is a beam-column.

Figure 175 and Figure 176 show that the dynamic response will increase for the model without coating stiffness as the load frequencies is known to be in the range of $0.08 - 0.45\text{Hz}$.

5.2.7.2. Fatigue Analyses

Table 51 shows the damage caused by lateral and vertical excitation of the pipeline with and without coating stiffness.

Table 51: Damage for E_{steel} and $E_{equivalent}$.

Young's modulus E [GPa]	Damage	
	$D_{lateral}$ [-]	$D_{vertical}$ [-]
210	0.46	$2.9 \cdot 10^{-2}$
340	$2.3 \cdot 10^{-2}$	$8.4 \cdot 10^{-3}$

It is seen that the damage increases significantly if the coating stiffness is not included. For a spanning length of $L = 25\text{m}$, the damage caused by lateral excitation of the model without coating is much higher than the damage determined for the model where coating stiffness is included. For the representative pipeline, it is considered to be highly conservative not to include coating stiffness.

5.2.8 EFFECT OF WAVE HEIGHT

This is a parametric study of the wave height's influence on the damage analyses. In this analysis, the significant wave height H_s and the maximum wave height H_{max} are chosen to represent the sea

states, respectively. The wave height affects the particle velocities and acceleration around the pipeline, which leads to the change of dynamic load from waves and current.

Changing the characteristic wave height entails that the following parameters have to be recalculated:

- In-line flow velocity and acceleration: $U, \dfrac{dU}{dt}$
- Hydrodynamic force coefficients: C_M, C_D, C_L
- In-line and cross-flow forces per unit length of the pipe: $f^{in-line}, f^{lift}$

H_s and H_{max} are taken from Chapter 1.1 (Design Conditions) where the method for determining the corresponding flow velocity and acceleration is also shown.

Force Coefficients and Dynamic Loads

Table 52 shows the difference in force coefficients for H_s and H_{max}, respectively. The force coefficients are determined according to Chapter 3.2 (Hydrodynamic Force Models).

Table 52: Force coefficients for H_s and H_{max}.

Sea state	H_s				H_{max}			
	KC	C_D	C_M	C_L	KC	C_D	C_M	C_L
Sea state 5	31.0	1.3	2.1	2.5	57.1	1.3	2.3	1.8
Sea state 4	18.1	1.5	2.3	2.9	33.6	1.4	2.4	2.5
Sea state 3	8.0	1.9	2.3	3.1	15.2	1.6	2.3	3.0
Sea state 2	1.5	1.8	2.6	4.4	3.0	2.2	2.4	4.4
Sea state 1	0.0	1.5	3.1	4.49	0.0	1.5	3.1	4.49

Figure 177 and Figure 178 shows the change in in-line and cross-flow force, respectively for H_s and H_{max}, respectively. The comparisons of forces are shown only for sea state 5.
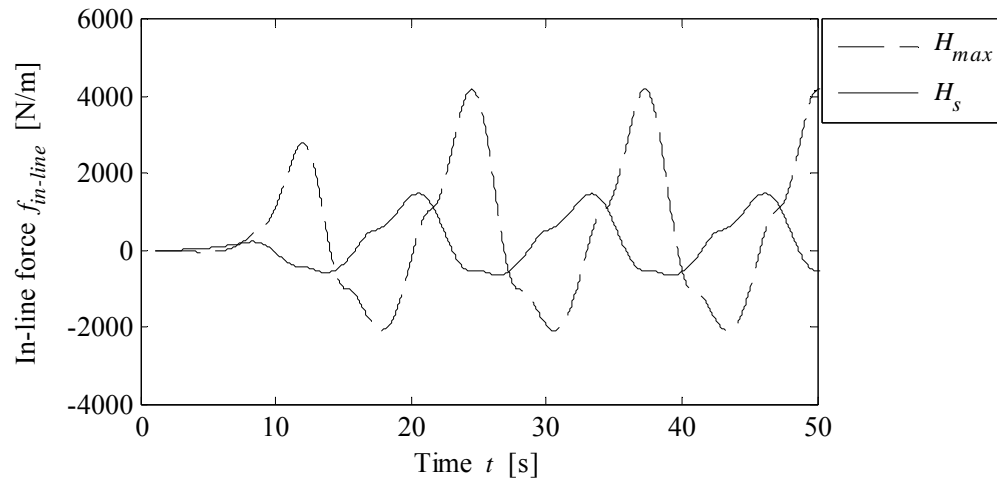
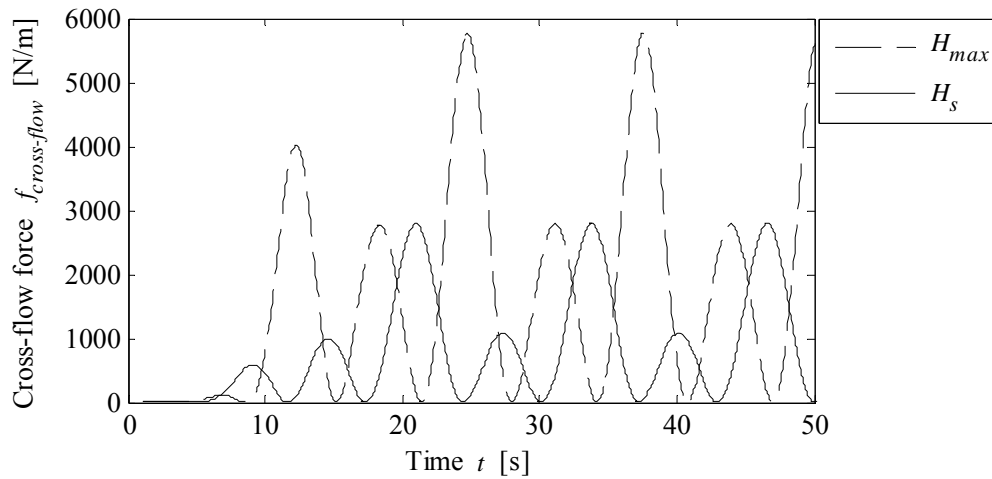Figure 177: In-line force for sea state 5 represented by H_s and H_{max}, respectively.

Figure 178: Cross-flow force for sea state 5 represented by H_s and H_{max}, respectively.

Figure 177 and Figure 178 show that the dynamic forces affecting the pipeline are increased significantly when the ambient flow is represented by H_{max} compared to H_s. The maximum values for $f_{in-line}$ and $f_{cross-flow}$ increase with a factor 2.8 and 2.0, respectively and the difference between the maximum and minimum value of $f_{in-line}$ increases with a factor 3.0. The main reason why the forces increase more than the ratio between H_{max} and H_s is that the ambient velocity is squared in the drag and lift term in the Morison Model, see Chapter 3.2 (Hydrodynamic Force Models).

5.2.8.1. Fatigue Analyses

Table 53 shows the damage caused by lateral and vertical excitation of the pipeline free-span when the sea states are represented by H_s and H_{max}, respectively.

Table 53: *Damage of pipeline free-span when the sea states are represented by* H_s *and* H_{max} , *respectively.*

Wave height	Damage	
	$D_{lateral}$ [-]	$D_{vertical}$ [-]
H_{max}	$1.5 \cdot 10^{-1}$	$8.8 \cdot 10^{-2}$
H_s	$2.3 \cdot 10^{-2}$	$8.4 \cdot 10^{-3}$

Table 53 shows that the damages for lateral and vertical excitation are increased by a factor 10, approximately, when the sea states are represented by H_{max} instead of H_s .

The analysis shows that it is important to consider the wave height chosen for the fatigue analyses. It is at this point too early to say which of the wave height that will give the most correct approximation of damage. Parametric studies in Chapter 5.3 (Parametric Study for Irregular Waves) show that H_s representing the sea states gives conservative damage results for the project pipeline. This means that choosing H_{max} to represent the sea states will be highly conservative in the present case.

5.2.9 EVALUATION

This serves to summarize the main findings of the parametric study of the pipeline free-span evaluated as a single-span that is affected by regular waves.

Because the pipeline does not experience vortex lock-in during all single-span analyses, the damage caused by lateral excitation has been shown to be more significant than the damage caused by vertical excitation. The cross-flow force has been determined by a force model that only applies upward loading which is an approximation since the real cross-flow force will affect the pipeline in both upward and downward direction.

The functional state has been found to be the most critical state when considering damage as the increased axial load results in reduced stiffness and eigenfrequency of the pipeline. Because the load frequencies from all sea state are lower than the eigenfrequency of the free-span, the reduced stiffness also results in increased dynamic amplification which is unfavourable for the pipeline when considering fatigue damage.

An evaluation of the damage contributions of the sea states has shown that sea state 5 causes more damage to the pipeline than sea states 1-4 all together. This means that the waves representing a 24-hour storm with a return period of 10 years cause more damage than smaller waves that are distributed over an entire year.

The damage calculated for the pipeline increases rapidly when the spanning length exceeds 25 m. The damage limit of $D_{lim} = 0.1$ is exceeded at an approximate spanning length of 27 m.

The effect of fluid and material damping has been shown to be of less significance to the dynamic behaviour for the project pipeline free-span. This is a result of the low dynamic amplification due to the difference in load frequency of the waves and eigenfrequency of the pipeline. In addition, the absence of vortex lock-in makes damping of less importance. These two effects result in low pipeline velocities compared to the ambient flow velocities which reduces the effect of damping.

The friction angle affects the strength and stiffness of the soil springs and has been shown to increase the damage of the pipeline as the friction angle is decreased. The damage influence has been shown to be minor since flat-sloped linear relationships have been found between the damage ratio of the pipeline and the friction angle of the soil.

The influence of coating stiffness has been shown to be significant to the dynamic response and the fatigue damage calculated for the pipeline free-span. The eigenfrequencies of the free-span decreases radically when coating stiffness is not included. The pipeline acts like a beam column because of the presence of axial force which increase the change in eigenfrequencies since coating stiffness is disregarded. It is considered to be very conservative not to include coating stiffness when determining the dynamic response and fatigue damage for the pipeline free-span.

The choice of wave height to represent the sea states has been shown to have a great influence upon the damage. Fatigue analysis has been made with the significant wave height H_s and maximum wave height H_{max} as representative wave heights. As expected, the damage ratio calculated for H_{max} is highest. It is however expected to give a more reasonable damage estimate when H_s is used as the representative wave height. This is explored further in Chapter 5.3 (Parametric Study for Irregular Waves).

5.3 PARAMETRIC STUDY FOR IRREGULAR WAVES

In practice, a spanning analysis of a pipeline free-span is conducted by assuming that the hydrodynamic forces are induced by regular waves. In nature, waves are irregular. In order to investigate the implications of this simplification, two analyses are performed with irregular waves on the reference model in Chapter 5.2 (Parametric Study for Regular Waves).

The irregular sea states 1-5 are modelled for 3.0 hours duration and the actual durations are given in Chapter 1.1 (Design Conditions). In order to reduce impulse vibrations at the beginning of the numerical analyses, the magnitude of the flow velocities and accelerations have been ramped from zero to their actual values during the first minute of modelled duration. For convenience, the ambient flow velocity history and acceleration history of the irregular sea states are shown in Appendix E (Irregular Sea States).

For the sake of simplicity, the effect of hydrodynamic damping induced by pipe vibrations is neglected. This is reasonable since it has been verified that the pipe velocity is of a considerably lower magnitude than that of the ambient flow velocity. As usual, the effect of hydrodynamic added inertia is taken into account by the use of hydrodynamic added mass. The diagrams of the hydrodynamic forces are without hydrodynamic added mass.

The critical fatigue stresses are determined by the normal stresses in the mid-section of the pipeline, where the magnitude of the normal stresses is largest. The normal stress has been considered to be an appropriate stress measure, since the magnitude of the shear stresses in the mid-section is small compared to that of the normal stresses. Recall that the shear stresses are non-zero in the mid-section because the Abaqus Model uses beam theory with large deformations.

The normal stresses are determined in section points 1 and 3 which are located in the lateral and bottom part of the pipe-section, see Figure 153. Thus, the section points correspond to the response that is induced by the in-line and cross-flow force, respectively. Since the response history is irregular, the Rain Flow Counting Method is used for determining stress ranges and cycles as described in Chapter 2.1 (Fatigue). The input files, output files and damage calculations can be found in [DVD/Parametric Study of Irregular Waves].

5.3.1 EFFECT OF REGULAR AND IRREGULAR WAVES IN THE MORISON MODEL

In this fatigue limit state analysis, the Morison Model for sea states 1-5 with irregular waves is considered and compared with the Morison Model with regular waves. For both regular and irregular waves, the force coefficients are taken from Table 34 in Chapter 5.2 (Parametric Study for Regular Waves).

5.3.1.1. Force History

The in-line and cross-flow force history for the irregular sea states 1-5 are shown in Figure 179 and Figure 180. By comparison with Figure 151 and Figure 152 in Chapter 5.2 (Parametric Study for Regular Waves), it may be seen that the magnitude of the peak in-line and cross-flow forces that are induced by the irregular sea states may be more than twice as large as those of the regular sea states.
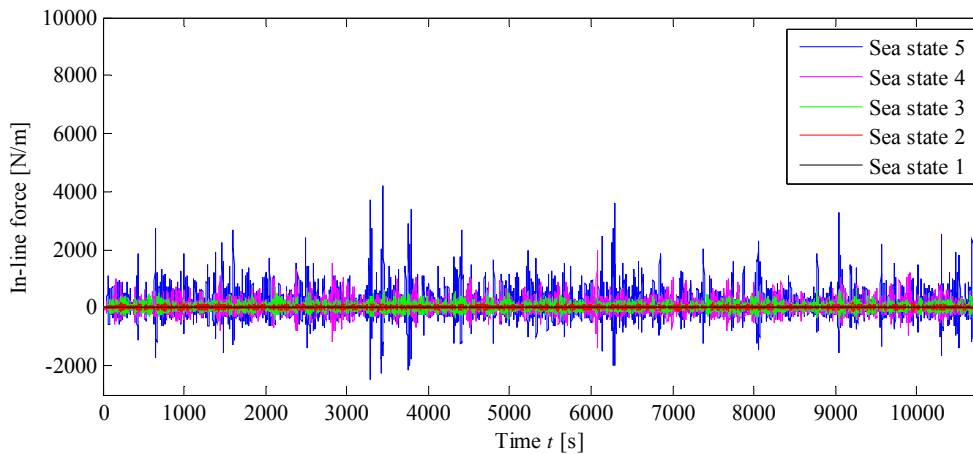

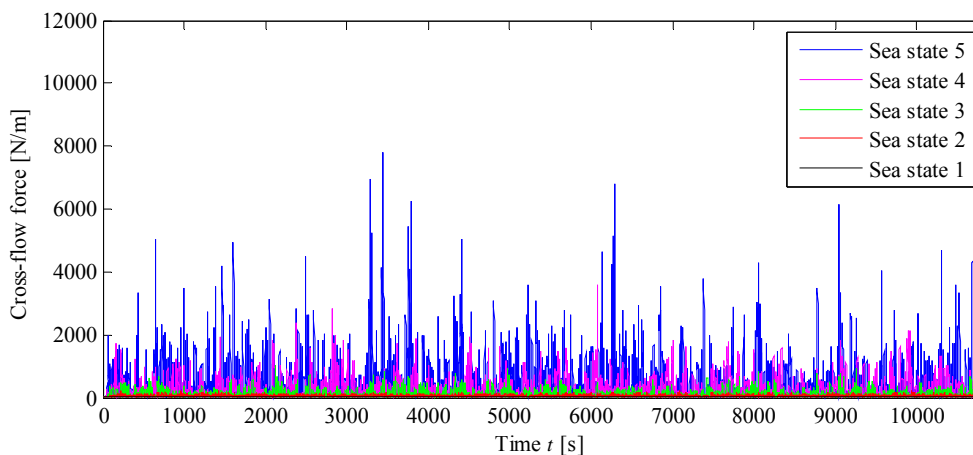*Figure 179: In-line force history during irregular sea states 1-5.*

Figure 180: Cross-flow force history during irregular sea states 1-5.

5.3.1.2. Stress History

The normal stress history for section points 1 and 3 during the irregular sea states 1-5 and the yield limit is shown in Figure 181 and Figure 182.
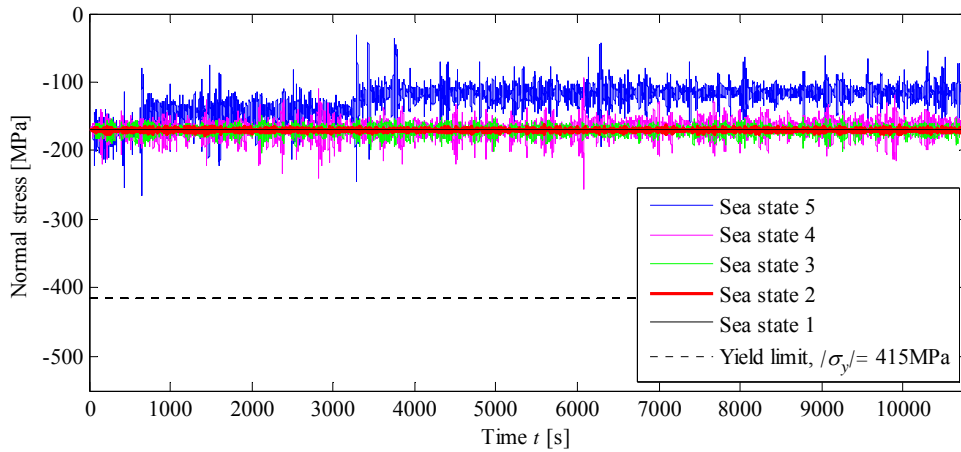

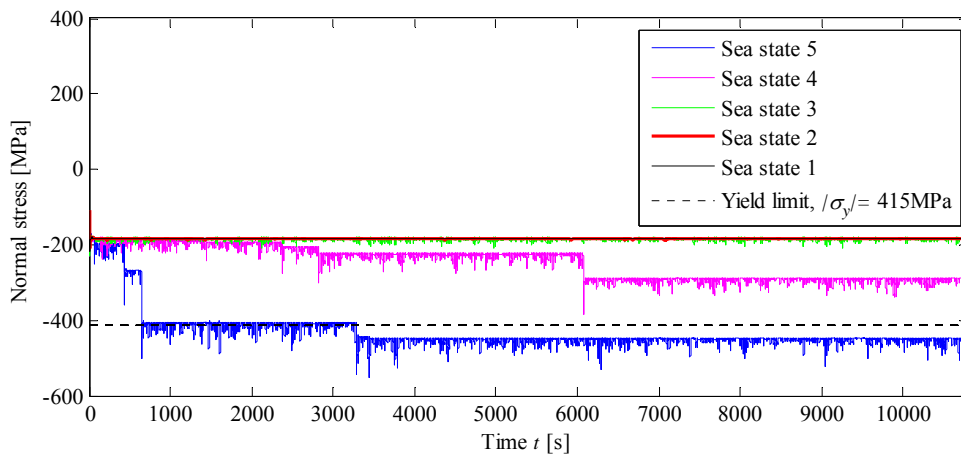*Figure 181: Normal stress history in mid-section in section point 1 during irregular sea states 1-5.*

Figure 182: Normal stress history in mid-section in section point 3 during irregular sea states 1-5.

Figure 181 and Figure 182 show sudden and large changes of the magnitude of the normal stresses. This is due to plastic deformation in the lateral and vertical soil springs during irregular sea states 5 and 4-5, respectively. By comparison with Figure 179 and Figure 180, it may be seen that this happens when a considerably large force hits the pipeline.

This observation is explained by the plastic constitutive behaviour of the soil springs. In the vertical direction, the cross-flow force extends the relatively slender vertical upward soil springs in the pipe shoulders beyond their elastic range. Once the springs have undergone plastic deformation, they remain extended as demonstrated in Chapter 5.1 (Winkler Model). When the cross-flow force diminishes, the pipe remains in the new configuration and the stresses fluctuate about this state. Interestingly, the pipe-span has an initial configuration of downward bending due to the static self-

weight but experiences configurations of increasing upward-bending each time plastic deformation occurs in the vertical soil springs. The occurrence of plastic deformation in the lateral soil springs may not be detected from the stress history since the in-line force can attain both negative and positive values and thus plastically extend and compress the lateral soil springs about the same state.

At $t \approx 650\,\text{s}$ during irregular sea state 5, the bottom of the pipeline experiences a compressive normal stress that exceeds the yield stress. Nevertheless, the fatigue analysis is carried out since it is primarily explorative in this parametric study. The magnitude of the tensile normal stress in the top of the pipe-section, i.e. section point 7, has been found to be below the yield stress.

5.3.1.3. Stress Ranges and Damage

The normal stress ranges and number of cycles for section points 1 and 3 during the irregular sea states 1-5 are shown in Figure 183 and Figure 184. The number of cycles has been scaled by the ratio between the actual and modelled duration of the irregular sea states. The figures also show the results from regular waves during sea state 5 and the maximum allowable number of cycles according to the S-N curves of DNV that have been described in Chapter 2.1 (Fatigue).
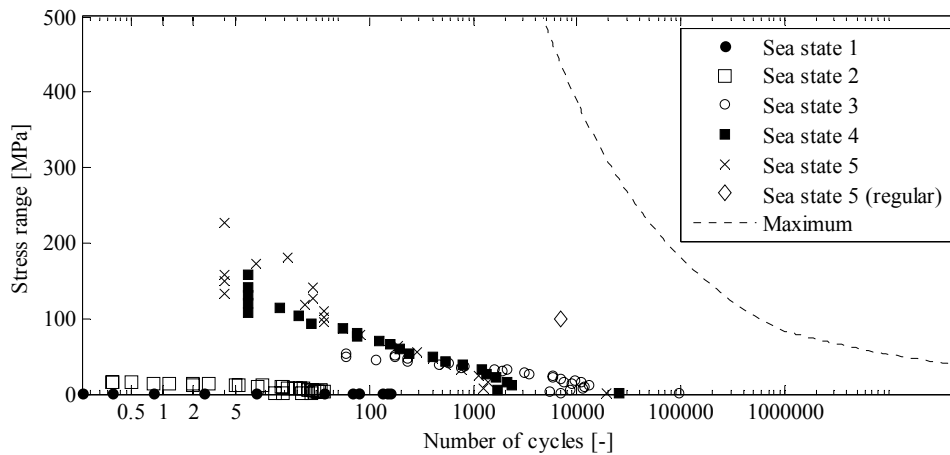

Figure 183: Normal stress ranges in mid-section in section point 1 as function of actual and maximum allowable number of cycles during irregular sea states 1-5 of actual duration.
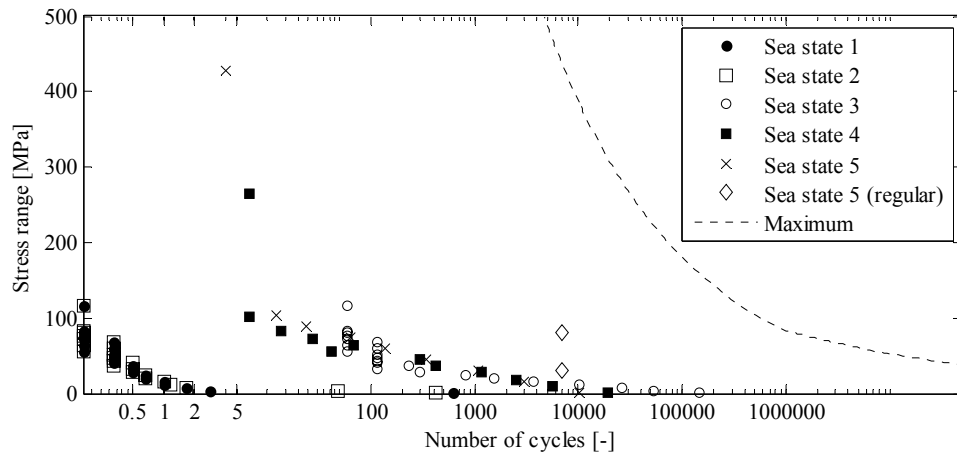
Figure 184: Normal stress ranges in mid-section in section point 3 as function of actual and maximum allowable number of cycles during irregular sea states 1-5 of actual duration.

It may be seen from Figure 184 that the Rain Flow Counting Method provides four cycles of the stress range 430 MPa in section point 3 during irregular sea state 5 of actual duration. By comparison with Figure 182, it is evident that this large stress range is based upon the major stress half-cycle due to the total plastic deformation during the entire modelled stress history and not the minor stress half-cycles due to the individual instances of plastic deformation.

The damage ratio for the irregular and regular sea states is given in Table 54 and Figure 185. The damage ratio for the regular waves is taken from Chapter 5.2 (Parametric Study for Regular Waves).

Table 54: Damage ratio during irregular and regular sea states 1-5 of actual duration.

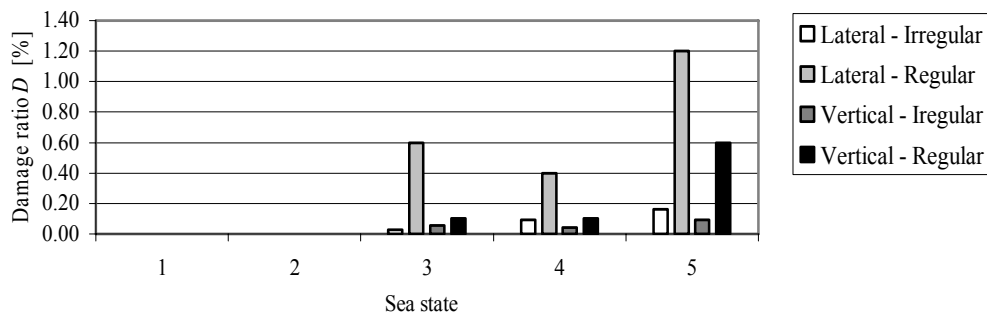| Sea state	Irregular		Regular	
	$D_{lateral}$ [-]	$D_{vertical}$ [-]	$D_{lateral}$ [-]	$D_{vertical}$ [-]
1	0	0	0	0
2	0	0	0	0
3	0.00029	0.00056	0.006	0.001
4	0.00092	0.00044	0.004	0.001
5	0.00160	0.00095	0.012	0.006
Total	0.00281	0.00195	0.023	0.008

Figure 185: Damage ratio in percent during irregular and regular sea states 1-5 of actual duration.

It is clear from Table 54 and Figure 185 that more damage is provided systematically by the regular sea states compared to the irregular waves – for some sea states nearly 8 times more damage. This may be explained by the many large stress cycles in the regular sea states that correspond to the significant wave height in contrast to the fewer but larger stress cycles in the irregular sea states due to extreme peaks and plastic deformation. Furthermore, most damage generally occurs in the lateral direction during the irregular sea states.

5.3.2   EFFECT OF IRREGULAR WAVES IN DIFFERENT FORCE MODELS

In this fatigue limit state analysis, the Morison Model with varying force coefficients and the Wake I Model are compared. This is done for the irregular sea state 5 which is governing sea state when considering fatigue damage. The coefficients of the models are given in Table 55 where the remaining coefficients of the Wake I Model are given in Appendix F (Empirical Parameters of Wake Models).

Table 55: Calibration basis and values of force coefficients for irregular sea state 5. All numbers are dimensionless

Case	Force model	Calibration basis	Gap ratio e/D	In-line force coefficients			Cross-flow force coefficient
				C_A	C_M	C_D	C_L
A	Morison Model	DNV and [Sumer & Fredsøe 1997, p183]	1	1.0	1.3	1.0	0.5
B	Morison Model	DNV and [Sumer & Fredsøe 1997, p183]	0	2.29	2.1	1.3	2.5
C	Morison Model	PFMP	0	2.29	3	2	2
D	Wake I Model	PFMP	0	0.25	2.5	1.1 - 1.7	0.8 - 4.9

Cases A and B show the Morison Model where the force coefficients have been determined for gap ratios 1 and 0, respectively, according to DNV and experimental results in [Sumer & Fredsøe 1997, p183]. These two cases may represent a typical choice when force data from the design location are unavailable. Case B is identical to the case with irregular sea state 5 in the fatigue analysis in the previous section.

Cases C and D cover the cases with the Morison and Wake I Model, respectively, when they have been fitted to measurements from the PFMP, see Chapter 3.2 (Hydrodynamic Force Models). In practice, the PFMP measurements are taken as the results of the Wake I Model at default parameters.

5.3.2.1. Force History and Spectrums

The in-line and cross-flow force history and single-sided amplitude spectrums for the cases are shown in Figure 186-Figure 189. The spectrums are based upon averaged Fast Fourier Transforms of subsets of the force histories and are not shown for the cross-flow force in cases A-B. Due to practical reasons, the cases appear in different order in the legends of the figures but the colours of each case are identical in the figures.
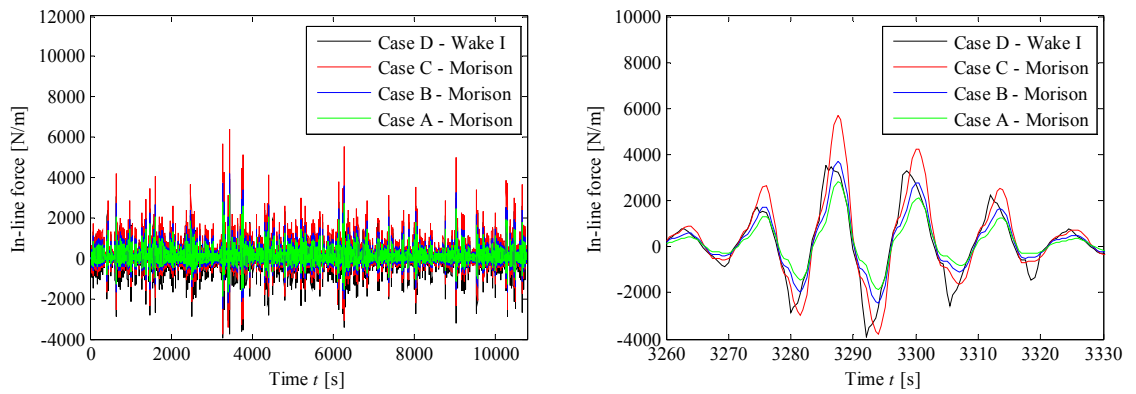
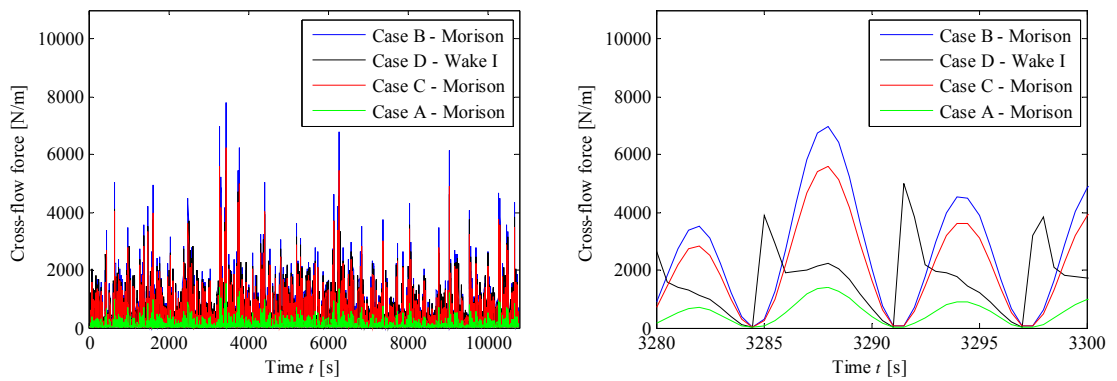*Figure 186: In-line force history during irregular sea state 5.*

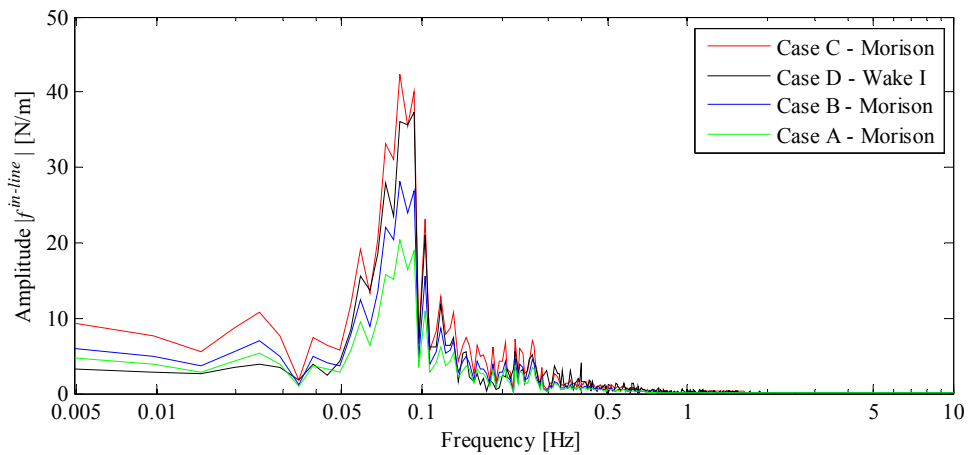*Figure 187: Cross-flow force history during irregular sea state 5.*

Figure 188: In-line force amplitude single-sided spectrum during irregular sea state 5.
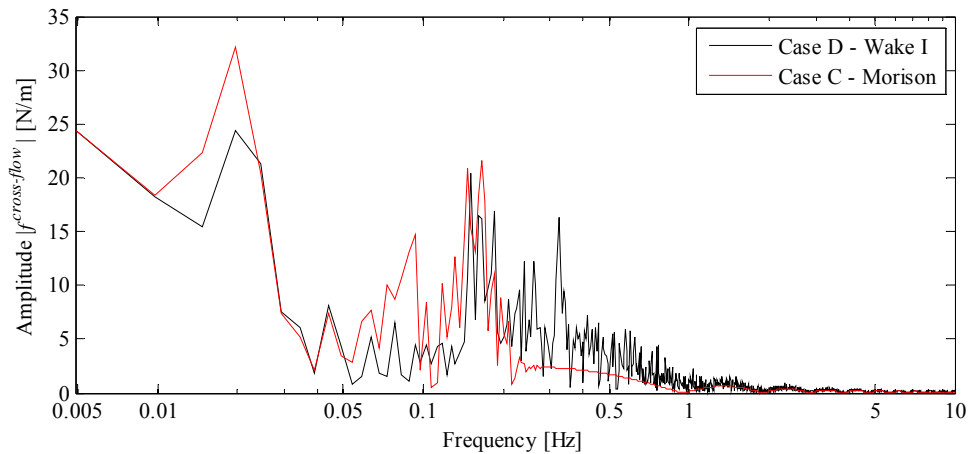
Figure 189: Cross-flow force amplitude single-sided spectrum during irregular sea state 5.

The in-line and cross-flow force in the Morison Model in case A are of considerably smaller magnitudes than those of the other cases. This may be seen in Figure 186-Figure 188 and illustrates the experimental observation that increasing gap ratio provides decreasing in-line and cross-flow force. This has been previously discussed in the context of regular waves.

As discussed in Chapter 3.2 (Hydrodynamic Force Models), the Morison Model is unable to predict an average in-line force equal to zero in the case of non-zero current-wave ratios below 0.5. Thus, in order to predict measured in-line force peaks that occur in the upstream direction, the in-line force peaks in the downstream direction are inevitably overestimated.

Thus, the Morison Model in case B underestimates the negative in-line force peaks, but estimates well the positive in-line force peaks in comparison with the Wake I Model. In contrast, the Morison Model in case C estimates well the negative in-line force peaks, but overestimates the positive in-line force peaks. This may be seen in Figure 186. Thus, the Morison Model in case B and C is expected to provide stress ranges in section point 3 of less and greater magnitude than those of the Wake I Model, respectively.

As seen in Figure 187 and Figure 189, the magnitude of the cross-flow force peaks of the Morison Model in case C is almost identical to the Wake I Model. However, as discussed in Chapter 3.2 (Hydrodynamic Force Models), the phase and shape of the Morison Model differ greatly from that of the Wake I Model. It is apparent from Figure 189 that the cross-flow force in both the Morison and Wake I Model is concentrated at the cross-flow frequency 0.16 Hz. But whereas the Morison Model has an additional considerable cross-flow force at the wave frequency 0.08 Hz, the Wake I Model has a considerable cross-flow force that is widely distributed at frequency ranges 0.16-0.50 Hz. Since the latter load frequencies are closer to and below the lowest eigenfrequency of the pipeline, the normal stress ranges in section point 3 that are provided by the Wake I Model are expected to be larger than those of the Morison Model.

5.3.2.2. Stress History

The normal stress history for section points 1 and 3 for the cases and the yield limit are shown in Figure 190 and Figure 191.
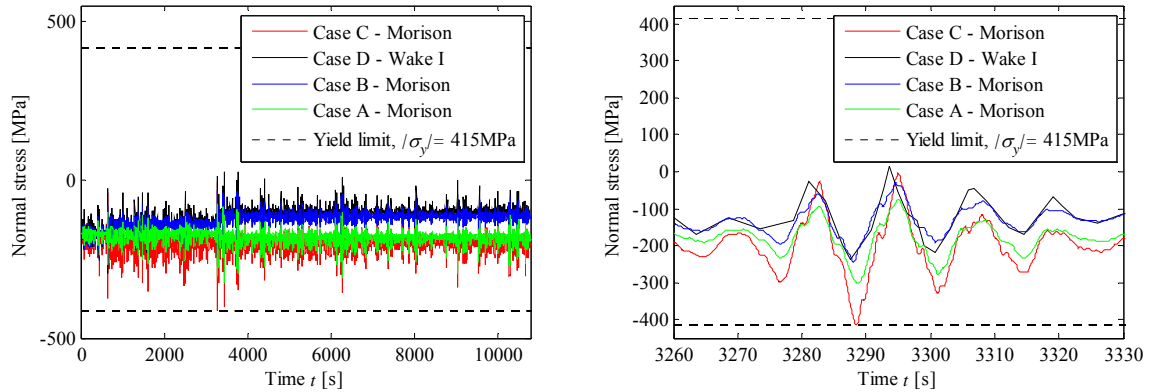

Figure 190: Normal stress history in mid-section in section point 1 during irregular sea state 5.
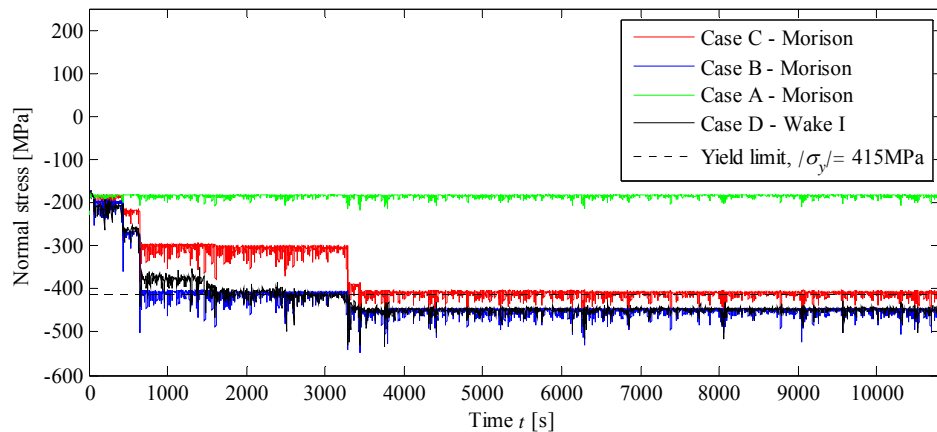

Figure 191: Normal stress history in mid-section in section point 3 during irregular sea state 5.

It may be seen from Figure 190 and Figure 191 that plastic deformation and yielding occurs in cases B-D. The largest stress amplitudes for lateral excitation are predicted by the Morison Model in case C.

5.3.2.3. Stress Ranges and Damage

The normal stress ranges as function of the actual and maximum allowable number of cycles for section points 1 and 3 during the irregular sea state 5 are shown in Figure 192 and Figure 193. The number of cycles has been scaled by 8 since this is the ratio between the actual and modelled duration of the irregular sea state 5.
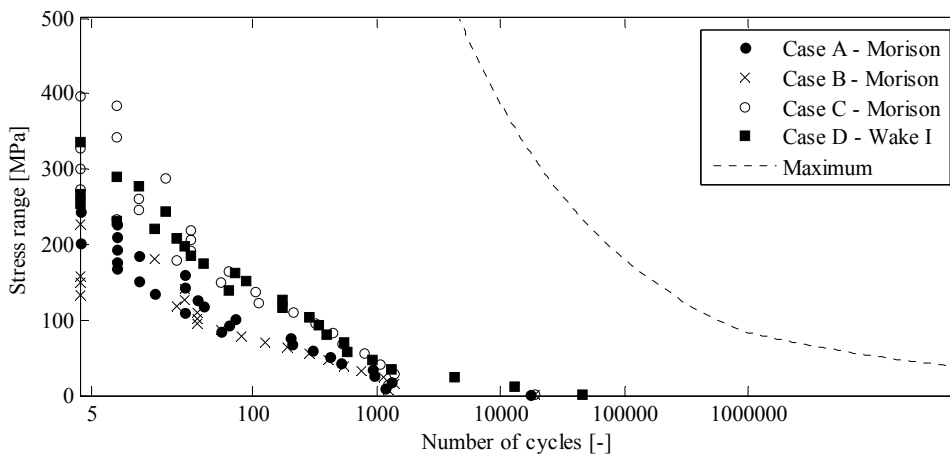
Figure 192: Normal stress ranges in mid-section in section point 1 as function of actual and maximum allowable number of cycles during irregular sea state 5 of actual duration.
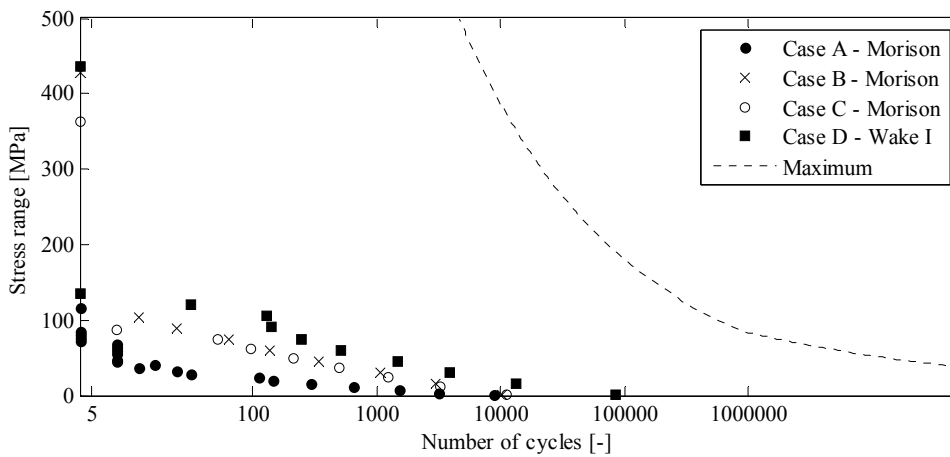

Figure 193: Normal stress ranges in mid-section in section point 3 as function of actual and maximum allowable number of cycles during irregular sea state 5 of actual duration.

It is seen from Figure 193 that the Wake I Model provides both larger stress ranges and a larger number of cycles in section point 3 than the Morison Model in cases A-C. This is attributed to the considerable cross-flow force at the high frequency ranges 0.16-0.50 Hz in the Wake I Model which has been discussed previously. For all stress ranges, the number of cycles is much smaller than the maximum number of cycles which results in small damage ratios. The resulting damage ratio is given in Table 56.

Table 56: Damage ratio during irregular sea state 5 of actual duration.

Case	Force model	Damage ratio	
		$D_{lateral}$ [-]	$D_{vertical}$ [-]
A	Morison Model	0.0028	0.00004
B	Morison Model	0.0016	0.00095
C	Morison Model	0.0118	0.00062
D	Wake I Model	0.0104	0.00260

It may be seen from Table 56 that most damage for lateral and vertical excitation is provided by the Morison Model in case C and the Wake I Model in case D, respectively. Furthermore, as discussed in a previous section, the Morison Model in case B and C indeed provides lower and upper bounds on the damage of the Wake I Model for lateral excitation.

By comparison of Table 54 and Table 56, it is seen that the damage for lateral excitation during sea state 5 is nearly identical for the Morison Model with irregular waves in case C and the Morison Model for regular waves. Thus, the difference in damage for lateral excitation during regular waves compared to irregular waves with identical in-line force coefficients in case B vanishes by the use of greater in-line force coefficients for the irregular waves. However, this overestimates the in-line force compared to that from maximum wave height which is given in Chapter 5.2 (Parametric Study for Regular Waves).

5.3.3   EVALUATION

First, it is concluded that different estimates of fatigue damage are obtained during severe sea states when considering impact from irregular and regular waves. This may be explained by the sensibility of fatigue damage to variation in the amplitude of stress cycles, the actual number of stress cycles and the maximum allowable number of stress cycles.

The impact from regular waves that are based upon the significant wave height provides a large amount of large-amplitude stress cycles in the pipeline. In contrast, impact from irregular waves provides few extreme stress cycles in the pipeline that correspond to the maximum wave height. In the latter case, the extreme loads introduce plastic deformation of the soil and considerable changes in the physical configuration of the pipeline but the total fatigue damage is negligible, nevertheless.

Thus, the conventional approach of using regular waves with the significant wave height for fatigue analysis is conservative for the project pipeline. It is considered to be an attractive approach when considering the additional computational resources that are involved in performing time-domain dynamic analyses with irregular waves of relatively long duration.

Secondly, different estimates of fatigue damage are obtained when predicting the hydrodynamic forces by the Morison Model and the Wake I Model with irregular waves. The difference appears to be relatively little when considering the fatigue of lateral section points of the pipe but considerably large for the top and bottom section points.

The latter is attributed to the difference in cross-flow force spectrums. When current is present, the cross-flow force of the Morison Model is distributed narrow-bandly about two peaks at the wave and cross-flow frequency. In contrast, the cross-flow force of the Wake I Model is concentrated at the cross-flow frequency and widely distributed at higher frequencies. Since the lowest eigenfrequency of the pipeline in the vertical direction is usually larger than the cross-flow frequency, the Wake I Model provides more dynamic amplification and larger stress cycles than the Morison Model.

5.4 BUCKLING ANALYSES

This chapter describes how to establish the maximum allowable spanning length in ultimate limit state (ULS) considering global and local buckling. The global buckling analysis has been made according to [DS412 1998] and [DNV No. 30.1 2004] as described in Chapter 2.2 (Buckling). The verification against local buckling analysis has been made according to [DNV-OS-F101], which is also described in Chapter 2.2 (Buckling). The main reason for making the buckling analysis is to determine if ULS is more critical to the pipeline free-span than the fatigue limit state (FLS). Because buckling is beyond the main focus of the project, some simplification has been made to ease the analysis.

5.4.1 REFERENCE MODEL

The buckling analyses are made according to a reference model whose design conditions and assumptions are shown in Figure 194.
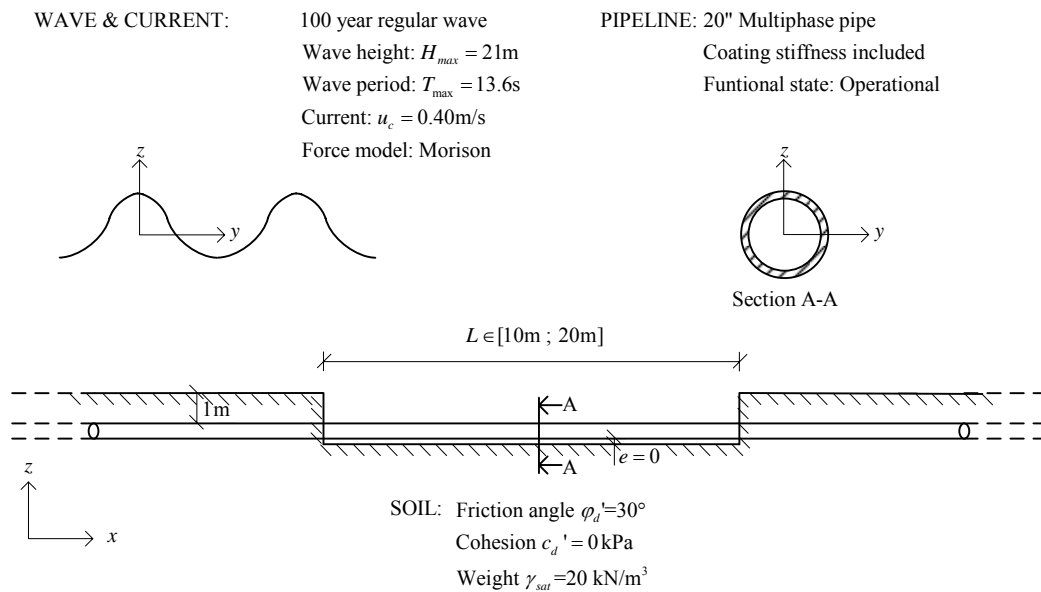

WAVE & CURRENT: 100 year regular wave   PIPELINE: 20" Multiphase pipe
                    Wave height: $H_{max} = 21\text{m}$ Coating stiffness included
                    Wave period: $T_{max} = 13.6\text{s}$ Funtional state: Operational
                    Current: $u_c = 0.40\text{m/s}$
                    Force model: Morison

Section A-A

$L \in [10\text{m} ; 20\text{m}]$

SOIL: Friction angle $\varphi_d' = 30°$
        Cohesion $c_d' = 0\,\text{kPa}$
        Weight $\gamma_{sat} = 20\,\text{kN/m}^3$

Figure 194: Reference model for buckling analysis.

A numerical model is made in the Abaqus Model similar to that of the fatigue analysis. The model is used to determine the section forces and critical buckling lengths, which are used as input to the buckling analysis according to the structural codes.

The calculation made in the Abaqus Model does not include the reduced stiffness due to axial force in the pipeline. The design procedures and the partial safety factors applied in the codes have already taken this in to account in ULS.

5.4.1.1. Design Loads

The characteristic loads from wave and current are established using the Morison Model for a 100 year regular wave with corresponding current, according to Chapter 1.1 (Design Conditions). The maximum in-line and cross-flow loads are used as equivalent static loads.

The force coefficients in the Morison Model have been determined according to Chapter 3.2 (Hydrodynamic Force Models) with the assumption that the pipeline is laying on the seabed. Table 57 shows the force coefficients that are used for the 100-year wave.

Table 57: Force coefficients used for ULS.

ULS sea states	C_D	C_M	C_L
Sea state 100	1.27	2.24	0.9

The magnitude of the characteristic load for self-weight, temperature and pressure is identical to the loads determined in Chapter 5.2 (Parametric Study for Regular Waves). The characteristic loads are transformed to design loads using the safety factors shown in Chapter 1.1 (Design Conditions). Table 58-Table 60 show the loads that are applied in the buckling analyses.

Table 58: Design axial load that is defined as positive in compression.

F_{sdx}	Characteristic load [MN]	Safety factors [-]	Design load [MN]
Temperature	3.490	1.0	3.490
Pressure incl. Poisson effect	0.552	1.05	0.580
Total	4.042	-	4.070

Table 59: Design in-line load.

f_{sdy}	Characteristic load [N/m]	Safety factors [-]	Design load [N/m]
Hydrodynamic in-line load	6329	1.3	8228

Table 60: Design cross-flow load.

f_{sdz}	Characteristic load [N/m]	Safety factors [-]	Design load [N/m]
Self weight	-2060	1.0	-2060
Hydrodynamic cross-flow load	4428	1.3	5756
Total	2368	-	3696

5.4.1.2. Design Material and Soil Parameters

The safety factors applied to the materials are shown in Chapter 1.1 (Design Conditions). It is noticed that the buckling length and section forces that are calculated in the Abaqus Model have all been determined using the safety factors given by DNV.

There has not been made any effort to change the friction angle and thereby the strength of the soil to a design value. This is a simplification that works in small favour for the free-span analysis in ULS when comparing the maximum allowable spanning lengths in FLS and ULS, respectively.

5.4.2 GLOBAL BUCKLING

The main purpose of this analysis is to determine the maximum spanning length considering global buckling. The practical procedure for the global buckling analysis is divided into the following steps:

1. Section forces and buckling length are determined in the Abaqus Model
2. Buckling resistance is determined according to [DS412 1998] and [DNV No. 30.1 2004]
3. Maximum spanning length considering buckling is determined

The computations that evaluate the pipeline's resistance against global buckling according to [DNV No. 30.1 2004] can be found in [DVD/Buckling/buckling_DNV.m] and the computations for the global buckling analysis according to [DS412 1998] can be found in [DVD/Buckling/buckling_DS412.m]. The input file for the Abaqus Model that is used to calculate section forces and critical buckling load can be found in [DVD/Buckling/singlespan_buckling.inp].

5.4.2.1. Section Forces

The section forces are determined in the numerical model. The maximum bending moments are found in the mid-section A-A of the free-span. Figure 195 shows the design moments for varying spanning lengths $L \in [10\,\text{m}; 20\,\text{m}]$.
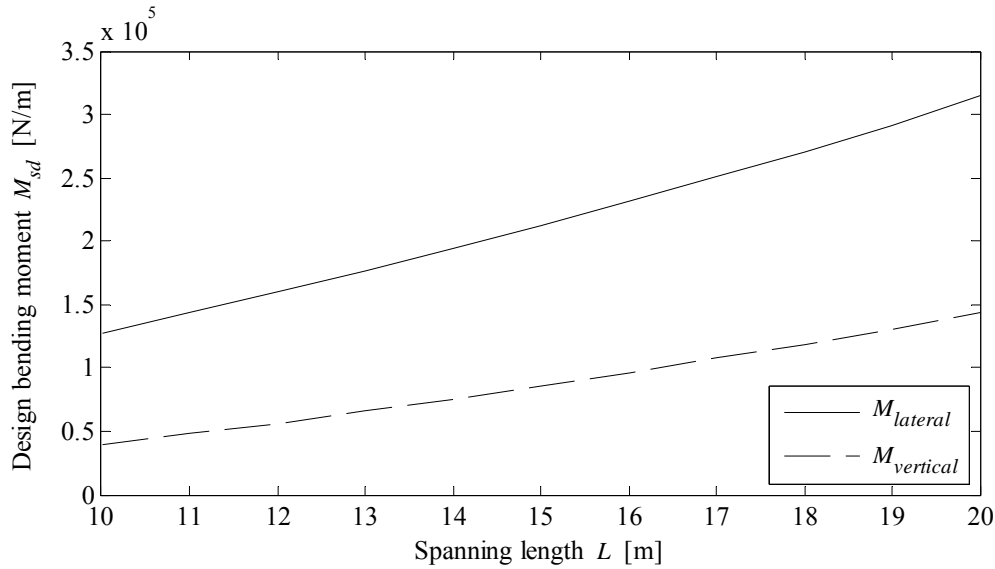
Figure 195: Design moment determined in the mid-section of the free-span.

The axial force equals the external axial design load given in Table 58.

5.4.2.2. Buckling Length

The buckling length is an essential parameter when global buckling is considered. The buckling length is determined in the Abaqus Model by an eigenvalue analysis. This is described in Appendix C (Buckling Eigenvalue Problem).

Critical Buckling Load

To determine the critical axial force that induces buckling of the pipeline free-span, the temperature load is defined as the perturbation load in order to define an incremental axial force that is uniformly distributed along the length of the pipeline.

Only the perturbation load is considered when determining the critical axial force and the initial temperature difference is $\Delta T = 1.0$. The load multipliers that are returned by the Abaqus Model are identical to the maximum allowable temperature difference before the pipeline free-span becomes instable.

The critical buckling force is determined as identical to the axial reaction force due to prevention of temperature expansion

$$F_{cr} = -F_x^{temp} = E \cdot \alpha \cdot \lambda_i \cdot \Delta T \cdot A_s, \quad \Delta T = 1°C \tag{5.4.1}$$

where

$\quad F_{cr}$ is the critical buckling load, defined as positive in compression [N]

$\quad F_x^{temp}$ is the axial force in the pipeline due to temperature, defined as positive in tension [N]

$\quad \lambda_i$ is the load multiplier for the ith buckling mode [-]

E is the Young's modulus [Pa]

α is the expansion coefficient $[1/°C]$

ΔT is the temperature difference $[°C]$

A_s is the cross-sectional area of the steel pipe $[m^2]$

The critical buckling load has been determined for varying spanning lengths $L \in [10\,m; 20\,m]$. Figure 196 shows the critical buckling load for the two lowest buckling modes which correspond to lateral and vertical buckling, respectively.
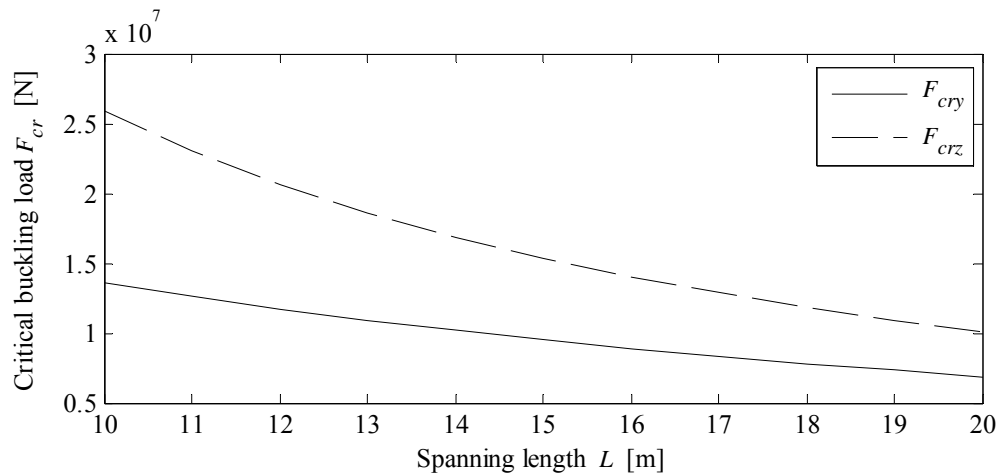

Figure 196: Critical buckling load for varying spanning lengths. Compression is positive.

Figure 196 shows that the vertical buckling resistance is higher than the lateral buckling resistance. This is because the stiffness of the vertical soil springs is higher than the lateral soil springs, see Chapter 4.1 (Soil Springs). As the spanning length increases, the buckling influence of the soil springs decreases, which reduces the difference between the lateral and vertical buckling resistance.

Buckling Length

By assuming that the critical buckling load F_{cr} is identical to the Euler load, the buckling length l_c can be found by the Euler formula for global buckling as

$$l_c = \sqrt{\frac{\pi^2 EI}{F_{cr}}}$$
(5.4.2)

where

l_c is the buckling length [m]

I is the second moment of the area about a given axis $[m^4]$

By combination of the critical buckling loads shown in Figure 196 and (5.4.2), one obtains the buckling length l_c for varying spanning lengths L, as shown in Figure 197.
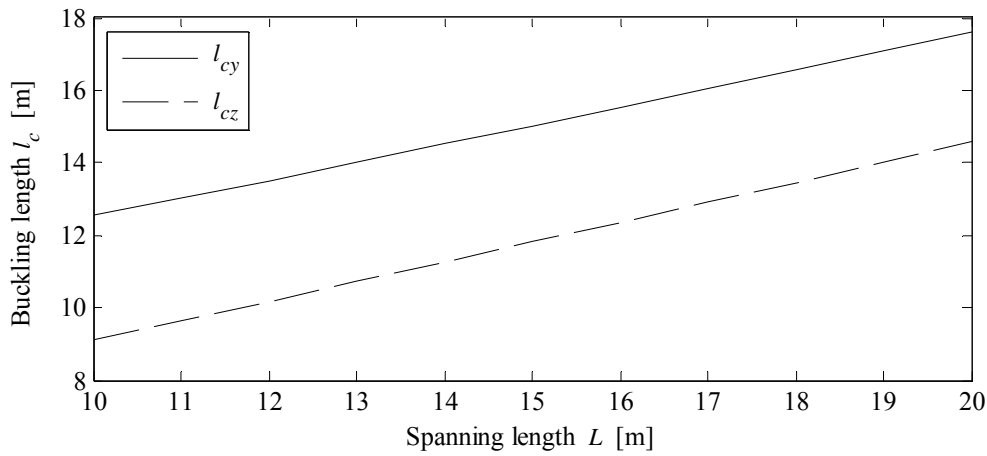
Figure 197: Buckling length for varying spanning lengths.

Figure 197 shows that the buckling length increases with the spanning length, but the ratio l_c / L increases as the spanning length decreases. This behaviour can be explained by studying the buckling modes for a pipeline free-span with spanning lengths of $L = 10\,\mathrm{m}$ and $L = 30\,\mathrm{m}$, respectively, which are shown in Figure 198.
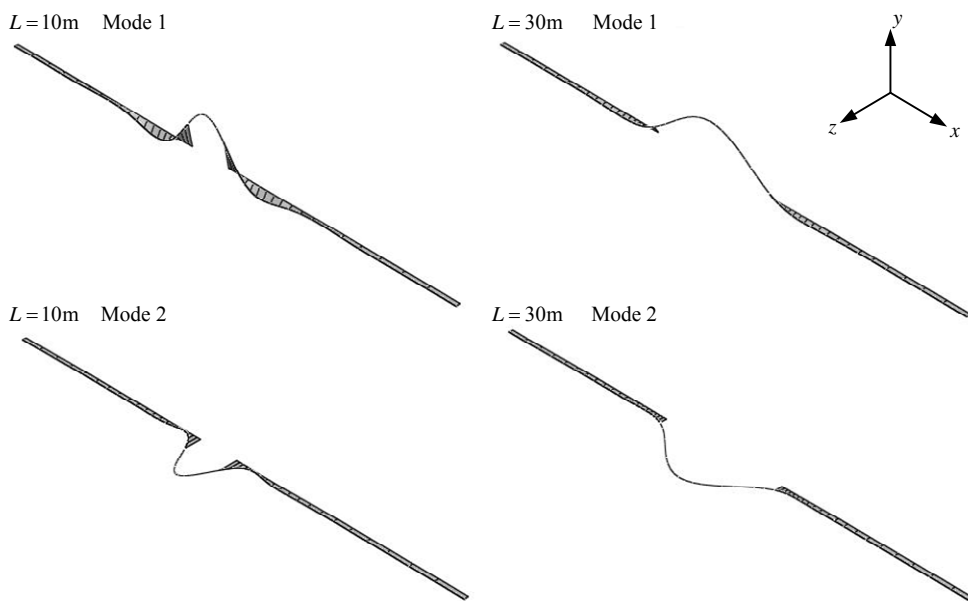
Figure 198: Buckling modes for $L = 10\,\mathrm{m}$ and $L = 30\,\mathrm{m}$, respectively.

The illustration of buckling modes in Figure 198 shows that for shorter free-span, the buckling mode propagate into the soil, since the global stiffness of the pipeline free-span increases when L decreases. The shorter free-span requires more strength of the soil in order to apply the same fixation of the pipeline as in the longer free-span. The buckling length is governed by the boundary of the pipeline free-span and so the ratio of l_c / L must increase when the spanning length decreases.

5.4.2.3. Buckling Resistance

Based upon the buckling length and section forces, the buckling resistance is determined in this section according to the analysing procedures of the structural codes. These have been explained in Chapter 2.2 (Buckling).

Global Buckling according to DS412

The global buckling is analysed for a beam-column using the following interaction formula, which is composed of a term for axial usage and two terms for bending usage about two axes

$$\overbrace{\frac{F_{sd}}{A_s\, f_{yd}\, \chi}}^{n_{max}} + \overbrace{k_y \frac{M_{sdy}}{W_y f_{yd}}}^{k_y m_y} + \overbrace{k_z \frac{M_{sdz}}{W_z f_{yd}}}^{k_z m_z} \leq 1.0 \tag{5.4.3}$$

where

n_{max}	is the axial usage [-]
F_{sd}	is the design axial compressive force [N]
A_s	is the cross section area [m^2]
f_{yd}	is the yield stress [Pa]
χ	is the reduction factor for buckling [-]
M_{sdy}	is the design bending moment about the strong axis (y-axis) [N/m]
M_{sdz}	is the design bending moment about the weak axis (z-axis) [N/m]
W_y	is the section modulus about the strong axis [m^3]
W_z	is the section modulus about the weak axis [m^3]
k_y	is the bending moment enhancement factor about the strong axis [-]
k_z	is the bending moment enhancement factor about the weak axis [-]
m_y	is the bending usage about the strong axis for infinitisimal deformation [-]
m_z	is the bending usage about the weak axis for infinitisimal deformation [-]

Figure 199 shows the usage ratio of each term in (5.4.3) for spanning lengths of $L \in [10\,\text{m}; 20\,\text{m}]$.
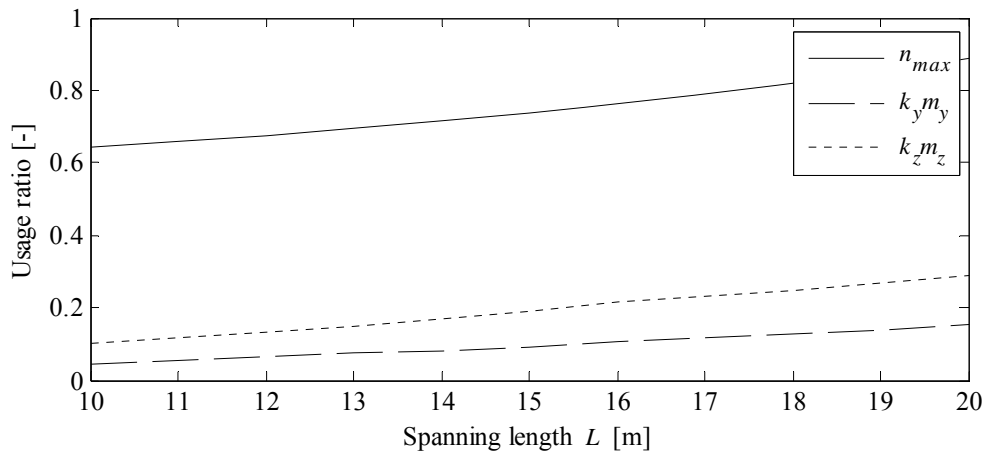
Figure 199: Usage ratio of the terms in the interaction formula according to [DS412 1998].

Figure 199 show that the governing term for buckling is the axial force. It is seen that none of the usage terms increase rapidly when the spanning length increases. It is noticed that the upper limit of the moment enhancement factors, i.e. $k = 1.5$, has been reached which diminishes the increase of the bending usage terms.

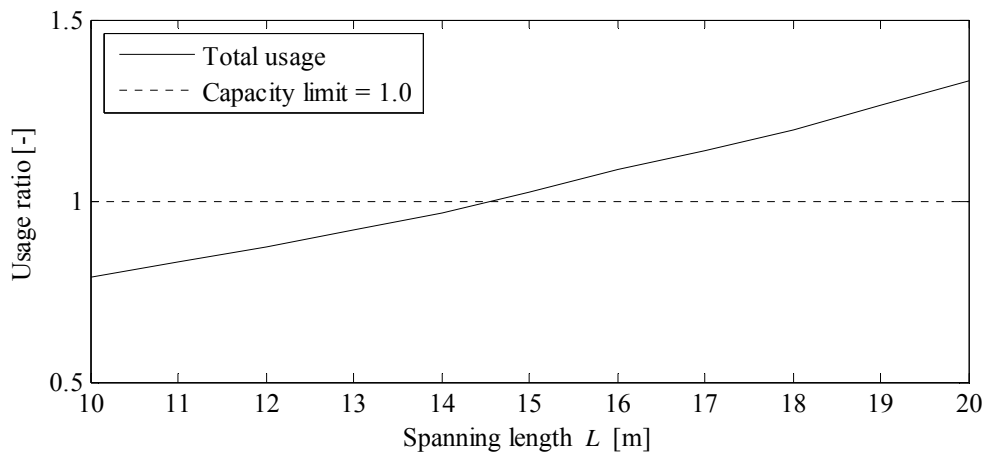Figure 200 shows the total buckling resistance according to [DS412 1998].

Figure 200: Buckling resistance for beam-column according to [DS412 1998].

Figure 200 shows that the approximate maximum spanning length of the pipeline free-span is $L_{max} = 14\,\text{m}$ as the total usage of the bearing capacity is exceeded at $L = 14.5\,\text{m}$.

Global Buckling according to DNV No. 30.1

The global buckling analysis according to DNV is also analysed using an interaction formula for a beam-column

$$\overbrace{\frac{\sigma_a}{\sigma_{acr}}}^{n_{max}} + \overbrace{\frac{\alpha'\sigma_{by}}{\left(1-\dfrac{\sigma_a}{\sigma_E}\right)f_{yd}}}^{k_y m_y} + \overbrace{\frac{\alpha'\sigma_{bz}}{\left(1-\dfrac{\sigma_a}{\sigma_E}\right)f_{yd}}}^{k_z m_z} = \eta \qquad (5.4.4)$$

where

η is the usage factor [-]

σ_a is the axial stress due to the compressive force F_{sdx} [Pa]

σ_{acr} is the characteristic buckling stress [Pa]

σ_{by} is the effective axial stress due to bending about the strong axis (y-axis) [Pa]

σ_{bz} is the effective axial stress due to bending about the weak axis (z-axis) [Pa]

σ_E is the Euler stress [Pa]

α' is a factor depending on the type of structure and reduced slenderness [-]

[DNV No. 30.1 2004]

By decomposition of the interaction formula into three terms similar to the procedure for DS412, the usage ratios are obtained as shown in Figure 201.
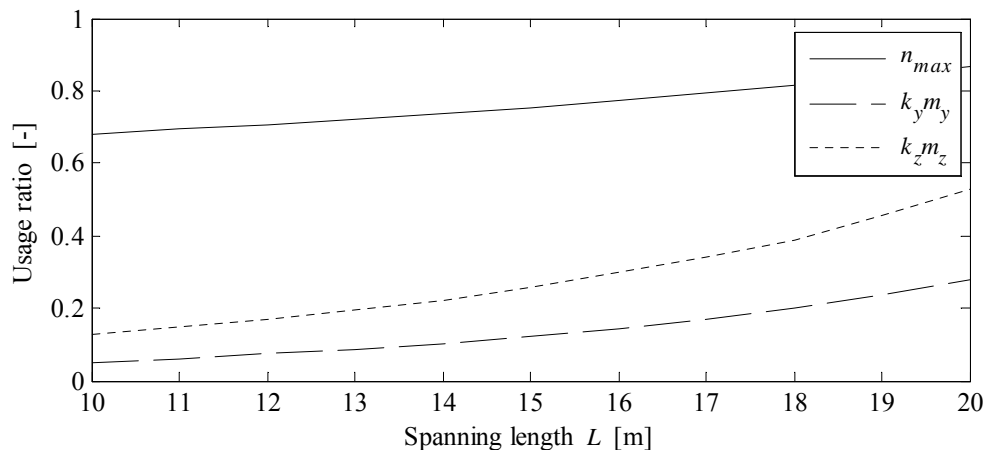

Figure 201: Usage ratio of interaction formula according to [DNV No. 30.1 2004]

Similar to the case for DS412, the interaction formula in DNV estimates the axial force to be the governing parameter for buckling. The usage of all three terms is a bit higher, since the material safety factors are higher in DNV compared to those of DS412. Furthermore, the bending usage terms increase more rapidly as the spanning length increases. This is because DNV does not specify any upper limit for the moment enhancement factors as in DS412.

Figure 202 shows the total buckling resistance according to [DNV No. 30.1 2004].
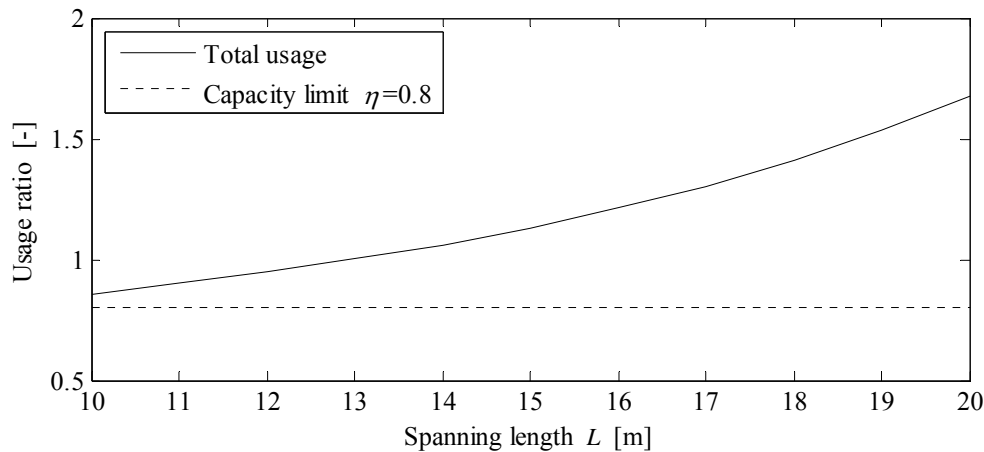
Figure 202: Buckling resistance for beam-column according to [DNV No. 30.1 2004].

It is seen from Figure 202 that the reduced capacity limit, $\eta = 0.8$, according to DNV result in a significant decrease in the maximum spanning length due to buckling. It predicts that the maximum allowable spanning length is $L < 10\,\mathrm{m}$. Since only limited access to the structural codes of DNV has been available, some parameters may have been misinterpreted, as the results do not seems to comply with the results from DS412.

5.4.3 LOCAL BUCKLING

The verification against local buckling analysis has been made according to [DNV-OS-F101] as described in Chapter 2.2 (Buckling). The computations that evaluate the pipeline resistance against local buckling can be found in [DVD/Buckling/localbuckling.m]. Figure 203 shows the usage ratio when considering local buckling.
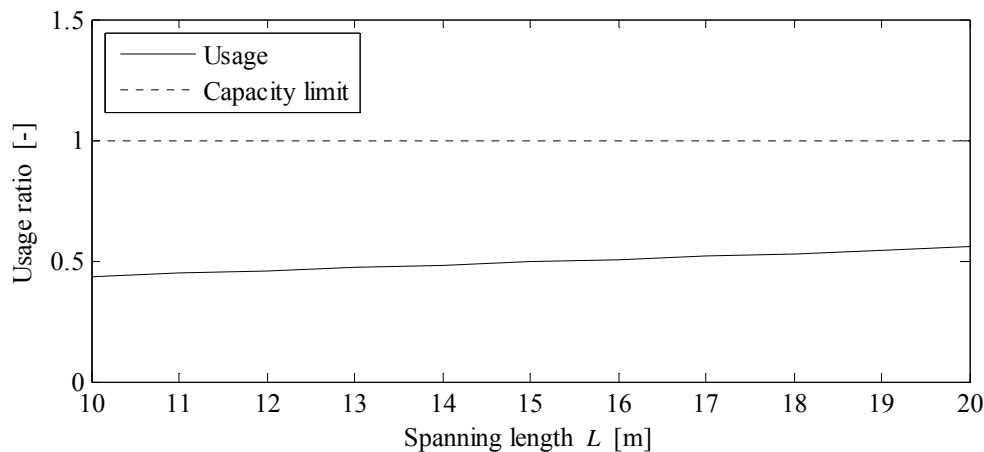

Figure 203: Local buckling according to [DNV-OS-F101]

Figure 203 shows that local buckling is not critical for spanning lengths $L \in [10\,\mathrm{m};20\,\mathrm{m}]$. It is seen that the usage ratio for local buckling increases with the spanning length as the stresses in the pipe-wall are increased due to increased bending. The increase in usage ratio as a result of increasing

spanning length is however considered to be small. It is concluded that local buckling is not governing for the maximum allowable spanning length.

5.4.4 EVALUATION

When comparing the buckling analysis according to DNV and DS412, the higher safety margin and the reduced usage factor of DNV provides a significantly lower maximum spanning length for the pipeline free-span. The results according to DS412 seem to be in best agreement with the estimated maximum allowable spanning length $L = 13\,\text{m}$ for a pipeline under similar conditions of the project pipeline [LIC-engineering 2005].

Regardless of the incoherent results, the global buckling analysis has shown that ULS is much more critical for the pipeline than FLS when considering the maximum allowable free-span. This is concluded since the buckling analysis in ULS predicts an approximate maximum spanning length of $L = 14\,\text{m}$ whereas the fatigue analysis in FLS predicts an approximate maximum spanning length of $L = 27\,\text{m}$ which is calculated in Chapter 5.2 (Parametric Study for Regular Waves).

It is also concluded that local buckling is not a problem for the pipeline free-span.

Part 6

Multi-span Analyses

Multi-span analyses have been made to examine the effect of potential interaction between two neighbouring free-spans. A parametric study of the governing parameters has been made considering the dynamic behaviour and fatigue of the neighbouring free-spans. It is a relatively new requirement that multi-span analysis has to be performed when neighbouring free-spans are detected. The objective for this part of the project is therefore also to outline some guidance to verification of a multi-span.

6.1   MULTI-SPAN ANALYSES

In the recent years, more focus has been given to the potential interaction between pipeline free-spans that are located near each other. In this project a multi-span analysis is performed in a force model in the Abaqus Model, which is similar to the procedure of the single-span analysis. It is noticed that [DNV-RP-F105] only provides procedures for multi-span analysis using a response model. So it is part of this project to outline some guidance rules for making multi-span analysis in a force model.

The multi-span analysis has been made with primary focus on Fatigue Limit State (FLS). The main purpose of this analysis is to determine an approximate length between two free-spans where interaction between the two spans no longer has a significant impact on the damage of the individual free-span. This will give an indication of when it will be sufficient to analyse neighbouring free-spans as individual single-spans.

A parametric study has been made in FLS of the parameters that are considered to have the greatest influence on the damage of pipeline. The considered parameters are the phase angle between the loads upon the neighbouring free-spans, the length of the mid-support, the friction-angle of the soil and the gap ratio. By comparing the results from the multi-span analysis with those of the single-span analysis, the consequence of interaction between two free-spans is evaluated.

In Ultimate Limit State (ULS), buckling analysis of the pipeline multi-span has been left out. Instead focus has been made on the stability of the soil bank acting as a mid-support between the two neighbouring free-spans. It is noticed that the ULS analyses do not refer to the same reference model as the analyses made in FLS.

6.1.1   REFERENCE MODEL (FLS)

In this section, the reference model for the multi-span analyses made in FLS is defined. The corresponding model files can be found in [DVD/Multispan/multispan_case1.inp; multispan_case2.inp]. The multi-span pipeline is assumed to consist of two neighbouring free-spans that are separated by a mid-support. Figure 204 shows the design conditions and assumptions made in the reference model for the multi-span pipeline.
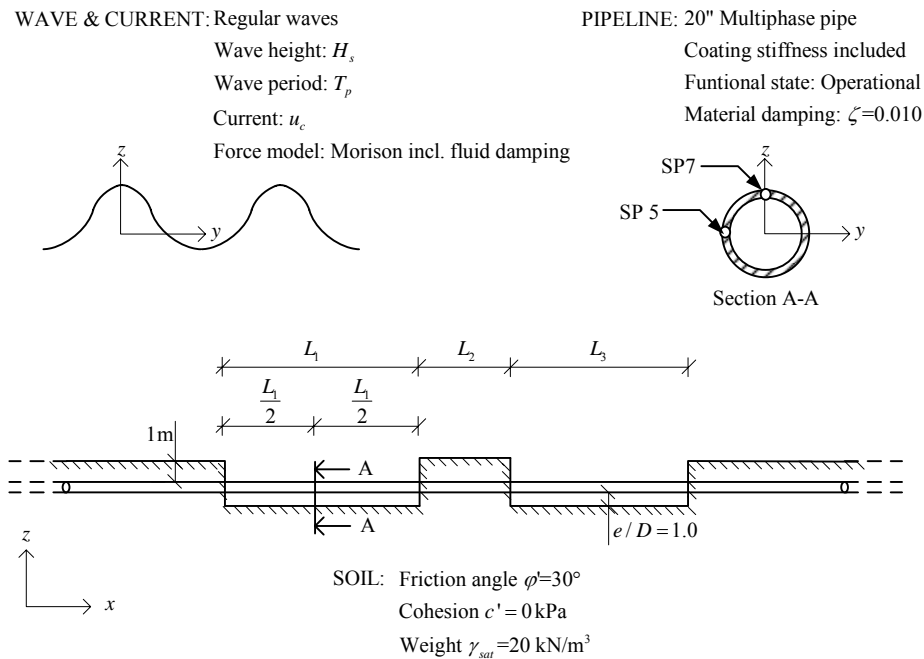
WAVE & CURRENT: Regular waves

Wave height: H_s

Wave period: T_p

Current: u_c

Force model: Morison incl. fluid damping

PIPELINE: 20" Multiphase pipe

Coating stiffness included

Funtional state: Operational

Material damping: $\zeta = 0.010$

SP7

SP 5

Section A-A

L_1 L_2 L_3

$\dfrac{L_1}{2}$ $\dfrac{L_1}{2}$

1m

A

A

$e/D = 1.0$

SOIL: Friction angle $\varphi' = 30°$

Cohesion $c' = 0\,kPa$

Weight $\gamma_{sat} = 20\,kN/m^3$

Figure 204: Reference model for multi-span in FLS.

The reference model in the multi-span analysis is compared to that of the single-span analysis with a spanning length equal to $L_1 = 25\,m$. In contrast to the reference model for the single-span, the gap ratio is $e/D = 1.0$ in the reference model for the multi-span. This difference has to be considered when comparing the results for the single-span and multi-span. The rest of the design conditions and assumptions are identical. From the single-span analysis, the assumption of no gap is known to be highly conservative since the wave load affecting the pipeline free-span will be overestimated, because the state of small gap will be of short duration as the gap increases rapidly due to scour.

The static and dynamic loads are determined similarly to the case for the single-span analysis with a gap ratio $e/D = 1.0$.

The hydrodynamic loads upon the neighbouring free-spans are assumed to act in opposite phase, i.e at a phase angle $\theta = 180°$. The following sections will clarify that this occurs together with one of the lowest eigenmodes of the multi-span pipeline, thus resulting in an upper bound solution to the damage. Another aspect, which will be discussed, is the physical fact that such a large phase angle cannot occur during the severe sea states when considering impact from 2D waves.

The damage ratio for lateral and vertical excitation is computed by the normal stresses in mid-section A-A in section point 5 (SP5) and section point 7 (SP7), respectively.
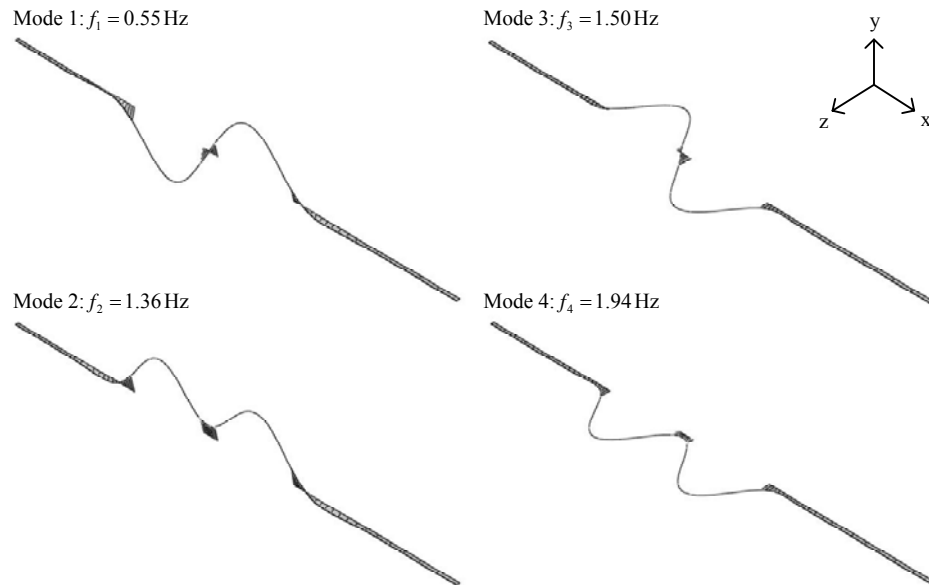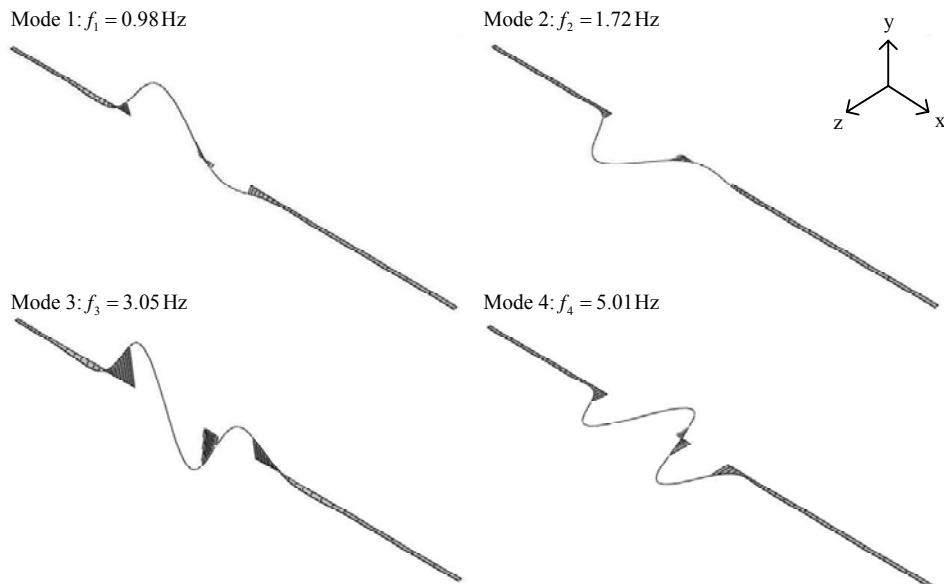
6.1.1.1. Definition and Eigenmodes of Basic Cases

The analyses are considered in two distinct cases, where the length of the mid-support and the side-spans are variable and constant, respectively. The cases are shown in Table 61.

Table 61: Basic cases for the multi-span analyses.

Case	L_1[m]	L_2[m]	L_3[m]
Case 1 – Symmetric free-spans	25	5-20	25
Case 2 – Asymmetric frees-spans	25	5-20	12.5

It is worthwhile to study the eigenmodes of the basic cases. For case 1 and 2 with $L_2 = 5\,\text{m}$, the four lowest eigenmodes of the multi-span are shown in Figure 205 and Figure 206, respectively.

Mode 1: $f_1 = 0.55\,\text{Hz}$

Mode 3: $f_3 = 1.50\,\text{Hz}$

Mode 2: $f_2 = 1.36\,\text{Hz}$

Mode 4: $f_4 = 1.94\,\text{Hz}$

Figure 205: The four lowest eigenmodes for case 1 and $L_2 = 5\,\text{m}$.

Mode 1: $f_1 = 0.98\,\text{Hz}$

Mode 2: $f_2 = 1.72\,\text{Hz}$

Mode 3: $f_3 = 3.05\,\text{Hz}$

Mode 4: $f_4 = 5.01\,\text{Hz}$

Figure 206: The four lowest eigenmodes for case 2 and $L_2 = 5\,\text{m}$.

For both cases, the lowest eigenfrequencies in lateral and vertical direction are obtained when the neighbouring free-spans vibrate in perfect opposite phase. This is shown in the upper-left and upper-

right part, respectively, of Figure 205 and Figure 206. Thus, the largest stress response in section A-A is expected when the loads on the free-spans are applied in perfect opposite phase.

In case 2, it is observed that the mode shapes of the widest free-span are similar to the mode shapes of a single-span. Eigenmodes 3-4 for case 2 are not considered to be critical for the pipeline since the corresponding frequencies are much higher than the load frequencies. Thus, these are not considered further.

6.1.2   EFFECT OF PHASE ANGLE

In this section, the effect of the phase angle upon the multi-span pipeline is investigated. First, physically valid values of the phase angle are discussed. Then, a fatigue analysis is performed for varying phase angles.

6.1.2.1. Physically Valid Phase Angles

In this section, a brief discussion has been made of the physically valid values of the phase angle between the wave loads upon the neighbouring free-spans of the multi-span pipeline. The discussion is limited to treat impact from 2D waves, since that of 3D waves has been considered too complex in practice.

In order to obtain a nonzero phase angle between the loads on the free-spans, the 2D wave front must attack the pipeline at a nonzero attack angle. This will reduce the perpendicular velocity against the pipeline and cause velocity variations along the free-spans. Figure 207 shows a plane sketch from above of the multi-span pipeline and the wave fronts.
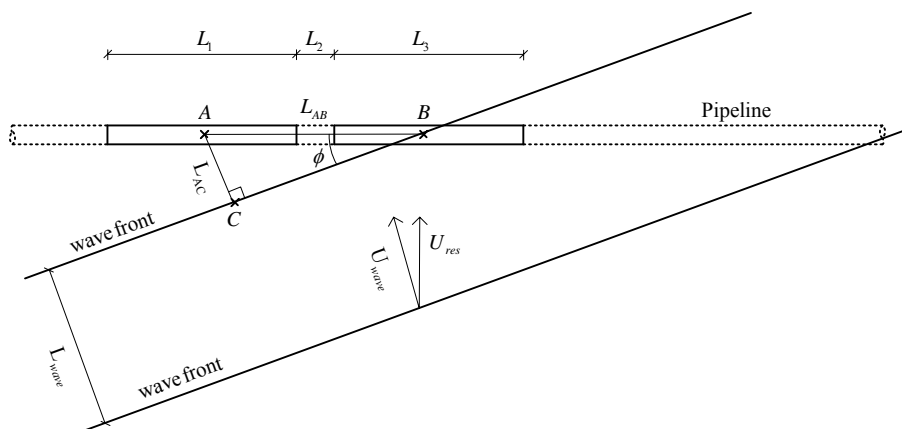

Figure 207: Plane view from above of multi-span pipeline and wave fronts of 2D waves.

An expression for the phase angle will be derived by trigonometric considerations of Figure 207. The phase angle between the wave loads of the two neighbouring free-spans can be formulated as

$$\theta = \frac{L_{AC}}{L_{wave}} \cdot 360° \qquad (6.1.1)$$

where

θ is the phase angle [deg]

L_{AC} is the distance between the wave front and the centre of the first side-span [m]

L_{wave} is the wave length [m]

The distance L_{AC} can be formulated as a function of the attack angle as

$$L_{AC} = L_{AB} \cdot \sin\phi = \left(0.5 \cdot \left(L_1 + L_3\right) + L_2\right) \cdot \sin\phi, \qquad \phi \in [0°; 90°[\qquad (6.1.2)$$

where

ϕ is the attack angle [deg]

L_{AB} is the distance between the centres of the side-spans [m]

By combination of (6.1.1) and (6.1.2), the phase angle θ can be described as

$$\theta = \frac{\left(0.5 \cdot \left(L_1 + L_3\right) + L_2\right) \cdot \sin\phi}{L_{wave}} \cdot 360°, \qquad \phi \in [0°; 90°[\qquad (6.1.3)$$

Figure 208 shows the maximum phase angle that can be obtained for case 1 with $L_2 = 20\,\text{m}$ and wave lengths that correspond to sea states 1-5. The wave lengths have been calculated by 5th order Stokes theory and include the effect of steady current U_c, as shown in Chapter 1.1 (Design Conditions).
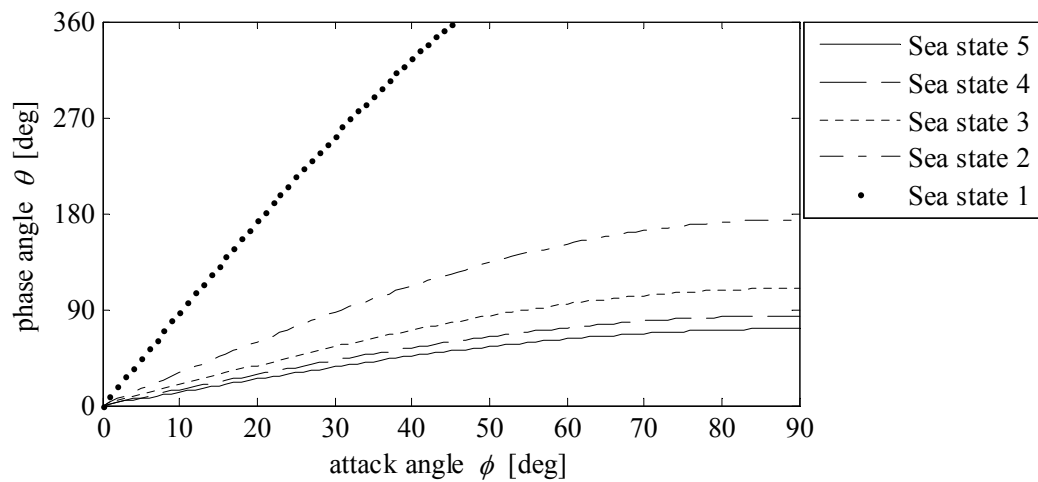

Figure 208: Phase angle as function of wave angle for case 1 and $L_2 = 20\,\text{m}$.

It may be seen from Figure 208 that in order to achieve a considerable phase angle for sea states 3-5, which cause most damage, the attack angle must be large. Furthermore, for case 1 and sea states 3-5, the maximum phase angle is $\theta < 180°$. This entails that a 2D wave will not be able to excite the free-spans in perfect opposite phase, i.e. $\theta = 180°$.

When increasing the attack angle, the velocity perpendicular to the pipe will decrease. This can be described as

$$U_{res} = U \cdot \cos\phi$$
$$U_{res} \to 0 \qquad \text{for} \quad \phi \to 90°$$

(6.1.4)

Conservatively, the reduction of the velocity according to (6.1.4) has been neglected in the following multi-span analysis based on the objective to obtain an upper bound solution to the impact of the pipeline.

In conclusion, it is highly conservative to calculate the damage of the pipeline multi-span by assuming that the wave load from a 2D wave affects the two neighbouring free-spans in perfect opposite phase.

6.1.2.2. Fatigue Analysis

In this section, the damage in case 1 with $L_2 = 5\,\text{m}$ is considered for varying phase angles $\theta \in \{0°; 90°; 180°\}$, where $\theta = 0°$ indicates that the loads are applied in phase. Figure 209 and Figure 210 show the damage ratio for lateral and vertical excitation, respectively.
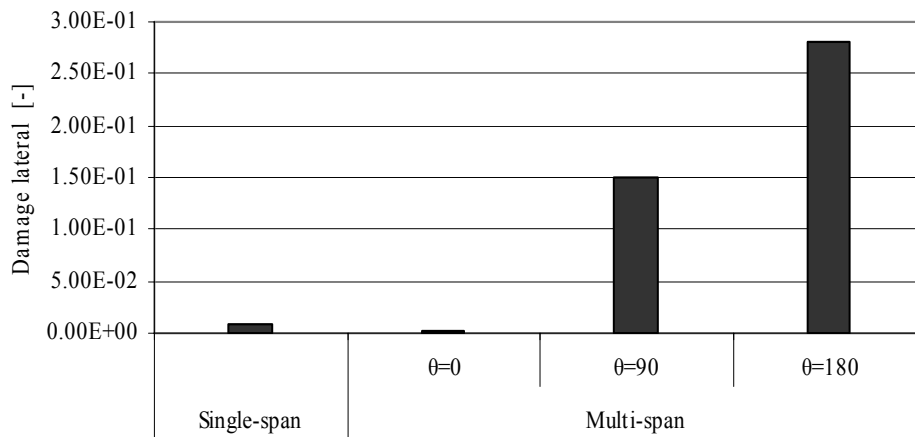

Figure 209: Damage caused by lateral excitation for varying phase angles $\theta \in \{0°; 90°; 180°\}$ in loads affecting case 1 with $L_2 = 5\,\text{m}$.
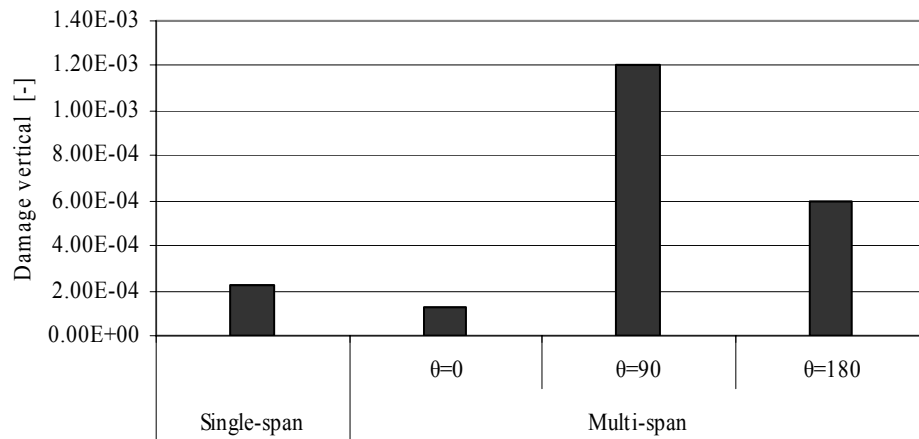
Figure 210: Damage caused by vertical excitation for varying phase angles $\theta \in \{0°;90°;180°\}$ in loads affecting case 1 with $L_2 = 5\,\mathrm{m}$.

It may be seen from Figure 209 that the damage caused by lateral excitation increases significantly when the load is applied out of phase. The damage in Figure 209 reaches a maximum at $\theta = 180°$, i.e. when the lowest eigenmode is excited according to Figure 205. It is seen that the damage for lateral excitation exceeds the allowable damage limit $D_{lim} = 0.1$ when $\theta = 90°$ and $\theta = 180°$.

From Figure 210 it may be seen that the damage caused by vertical excitation reaches a maximum at $\theta = 90°$. The damage caused by vertical excitation of the multi-span is much lower than the damage caused by lateral excitation since the multi-span pipeline does not reach the range of vortex lock-in and the magnitude of the cross-flow forces is lower than the in-line forces. As a result of this, the analysis of damage caused by vertical excitation is not considered further.

Figure 209 and Figure 210 show larger damage for the single-span compared to the multi-span affected by loads in phase. The frequency of the mode 2 is higher than the frequency of the single-span which decreases the dynamic amplification of the dynamic load. So the neighbouring free-pans work in advantage for the pipeline when they are excited in phase.

6.1.3 EFFECT OF LENGTH OF MID-SUPPORT

In this section, the effect of the length of the mid-support upon the eigenfrequencies and damage of the multi-span pipeline is investigated. The length of the mid-support is considered in the range $L_2 \in [5\,\mathrm{m};20\,\mathrm{m}]$ for both cases 1 and 2.

6.1.3.1. Frequency Analysis

Figure 211 shows the four lowest eigenfrequencies for cases 1 and 2, respectively. In addition, the two lowest eigenfrequencies of a single-span are shown with the dashed line. The single-span corresponds to analysing the free-spans individually as single-spans.
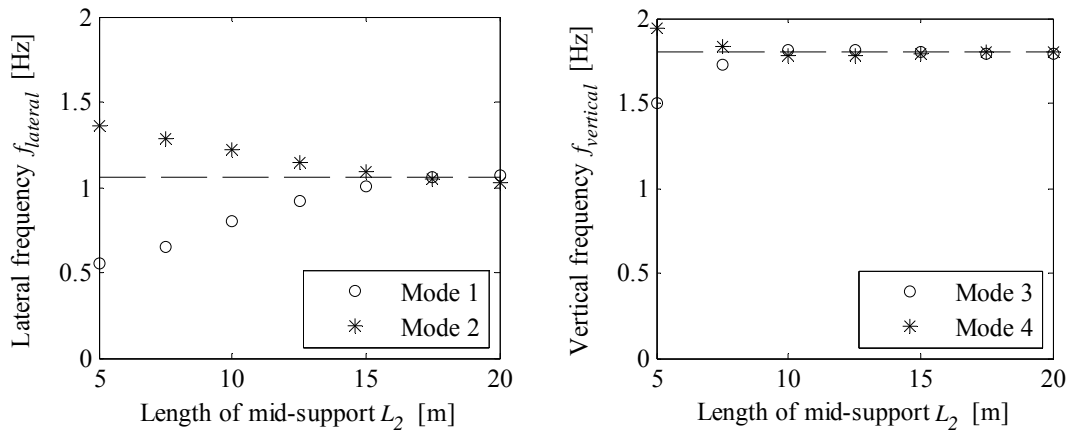
Figure 211: Eigenfrequencies for case 1. The dashed lines represent the lowest eigenfrequencies for a single-span.
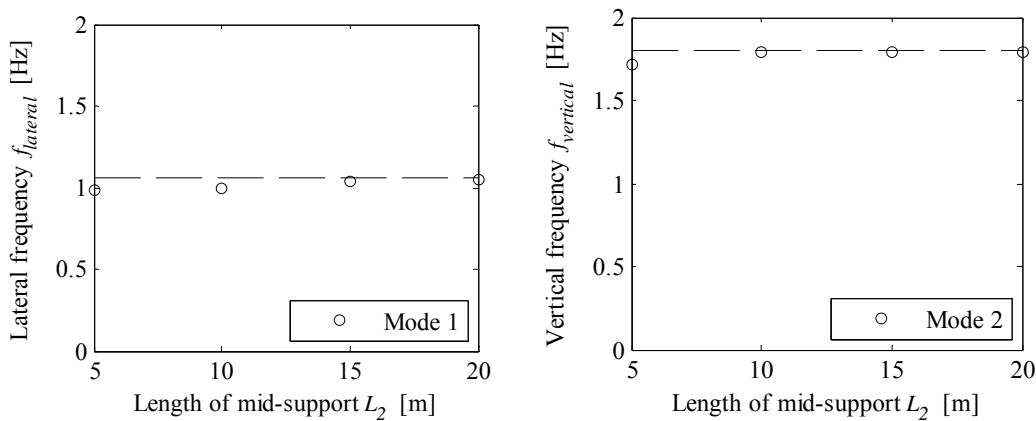

Figure 212: Eigenfrequencies for case 2. The dashed lines represent the lowest eigenfrequencies for a single-span.

For case 1, it is seen from Figure 211 that the eigenfrequencies of the multi-span differ from those of the single-span when the length of the mid-support decreases. The lowest lateral and vertical eigenfrequency begin to decrease at $L_2 < 15\,\text{m}$ and $L_2 < 10\,\text{m}$, respectively. The lowest eigenfrequency in lateral direction decreases to about half the frequency of the single-span for $L_2 = 5\,\text{m}$. The higher stiffness of the vertical soil spring prevent the same amount of deviation in the vertical eigenfrequencies.

For case 2, it is seen from Figure 212 that neither the lateral nor the vertical eigenfrequency of the multi-span deviate significantly from the corresponding eigenfrequencies for a single-span.

In conclusion, the frequency analysis of case 1 indicates that interaction occurs when the length of the mid-support is less than 15 m, given the present assumptions. The results for case 2 indicate that when one of the free-spans is considerably smaller than the other, interaction decreases.

6.1.3.2. Fatigue Analysis

The damage ratio caused by lateral excitation is shown in Figure 213 and Figure 214 for case 1 and 2, respectively. The damage for lateral excitation for a single-span is shown for comparison.
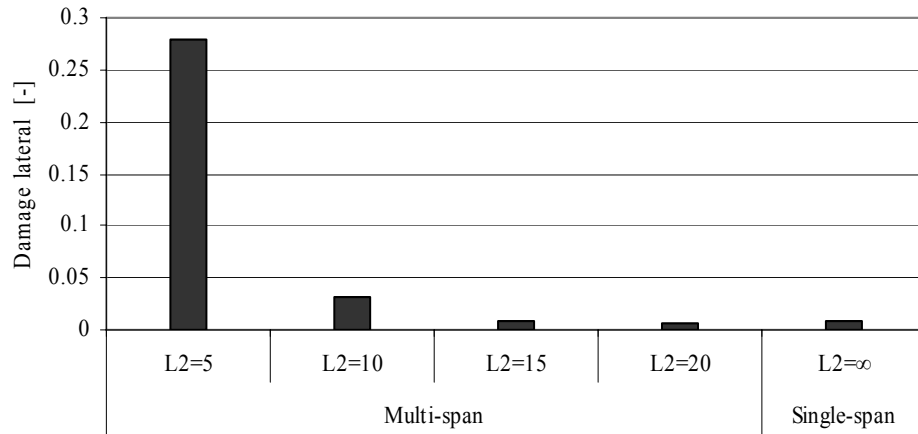

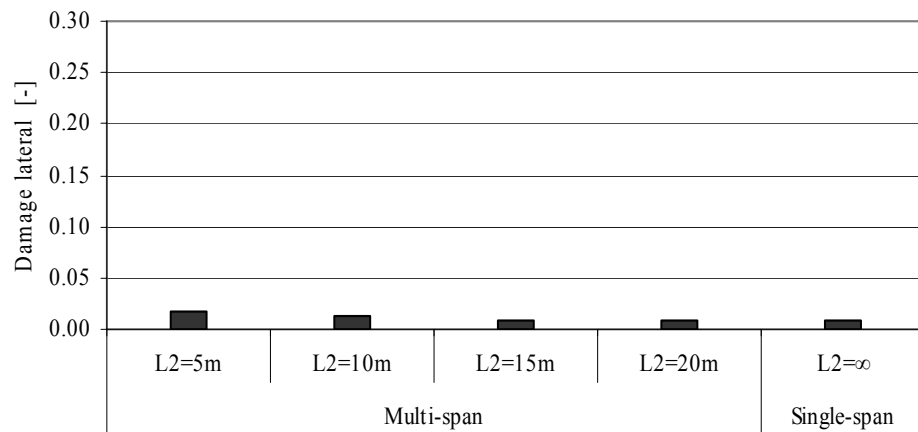*Figure 213: Damage for lateral excitation in case 1.*

Figure 214: Damage for lateral excitation in case 2.

Figure 10 shows that in case 1, the damage increases when the length of the mid-support is $L_2 \leq 15\,\mathrm{m}$. Furthermore, the maximum allowable damage ratio $D_{lim} = 0.1$ is exceeded for $L_2 = 5\,\mathrm{m}$.

Figure 214 show that in case 2, the damage also increases for $L_2 \leq 15\,\mathrm{m}$, but the damage does not reach the allowable damage ratio. The damage for lateral excitation that is calculated in case 2 is significantly lower than that of case 1.

It can be concluded that the length of the mid-support and the ratio between the lengths of the neighbouring free-spans are important parameters for the presence of interaction between the free-spans.

6.1.4   EFFECT OF FRICTION ANGLE OF SOIL

In this section, the effect of the friction angle of the soil upon the eigenfrequencies and damage of the multi-span pipeline is investigated for case 1. The friction angle is considered in the range $\varphi \in [25°; 35°]$.

6.1.4.1. Frequency Analysis

The lowest lateral and vertical eigenfrequencies of the multi-span pipeline for varying friction angles of the soil are shown in Figure 215, respectively. The frequency of a corresponding single-span with $\varphi = 30°$ is shown for comparison by the dashed line.
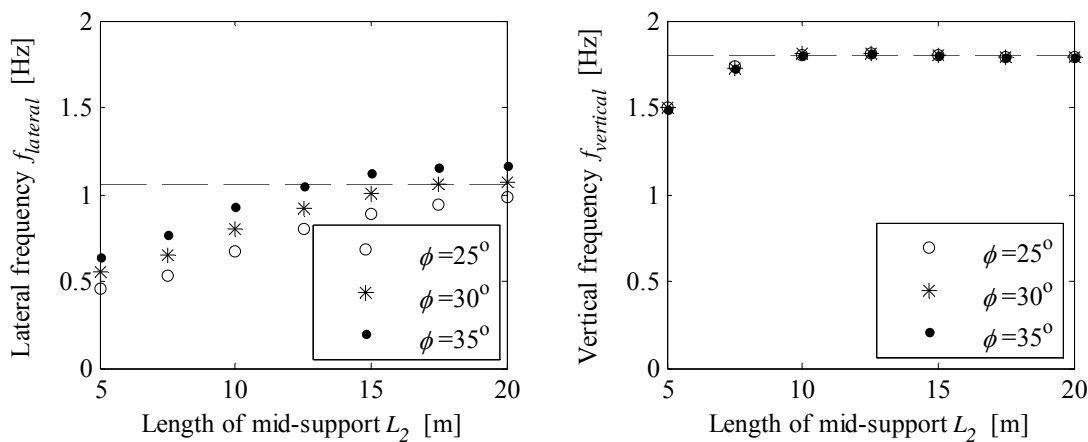

Figure 215: The lowest lateral and vertical eigenfrequency for case 1 and different angles of friction $\varphi \in [25°; 35°]$.

Figure 215 shows that neither the lateral nor the vertical eigenfrequency of the multi-span change significantly for different friction angles of the soil.

A decrease in the friction angle of the soil results in some decrease in the lateral eigenfrequency, whereas the vertical frequency of the multi-span is almost unaffected. The latter observation may be explained by the fact that the first part of the vertical spring curve does not change significantly when changing the angle of friction according to Chapter 4.1 (Soil Springs).

In conclusion, for friction angles in the range of $\varphi \in [25°; 35°]$, interaction occurs for $L_2 \leq 15\text{m}$.

6.1.4.2. Fatigue Analysis

The damage ratio caused by lateral excitation for varying friction angles of the soil is shown in Figure 216.
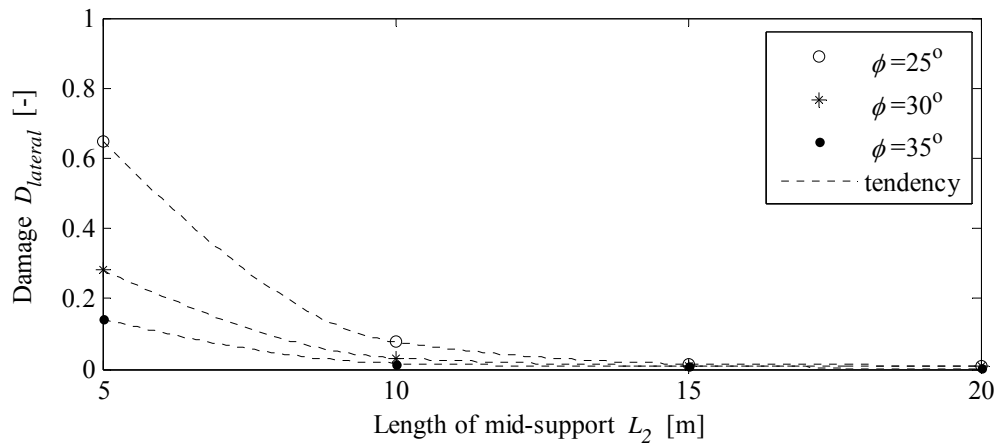
Figure 216: Damage caused by lateral excitation for varying friction angles in case 1.

Figure 216 shows that the damage ratio for the multi-span increases rapidly for decreasing angles when the length of the mid-support is short. Furthermore, compared to the single-span, the damage for the multi-span is considerably more dependent on the friction angle of the soil as the two neighbouring free-spans begin to interact. The strength of the mid-support has great influence on the structural system of the multi-span and as the friction angle decreases, so does the strength of the mid-support, especially when L_2 becomes smaller than 10m.

6.1.5   EFFECT OF GAP RATIO

In this final section, the effect of the gap ratio upon the eigenfrequencies and damage of the multi-span pipeline is investigated for case 1. The gap ratio is considered in the range $e/D = \{0;1\}$.

6.1.5.1. Frequency Analysis

Figure 217 shows the variation of the lowest lateral and vertical frequency, respectively, for a multi-span with no gap. The frequency of a corresponding single-span with no gap is shown for comparison by the dashed line.
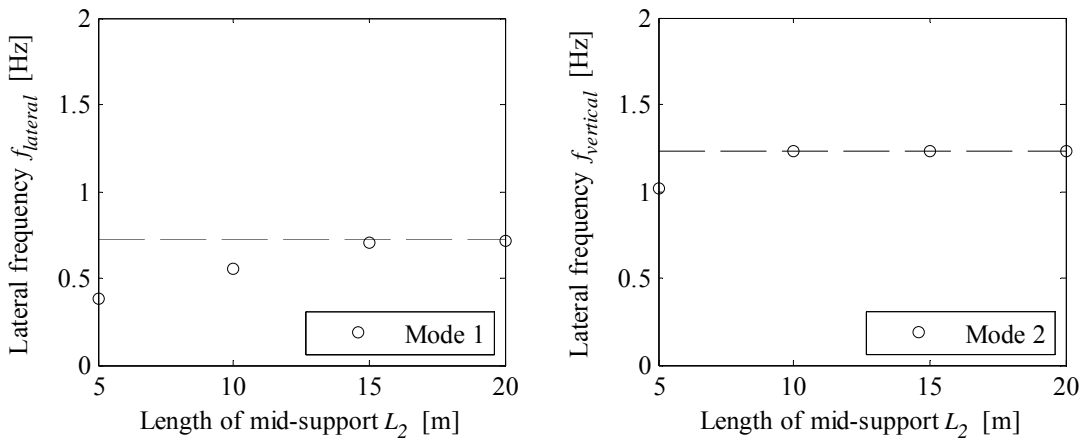
Figure 217: Eigenfrequency for case 1 with gap ratio $e/D = 0$.

The eigenfrequencies shown in Figure 217 indicate that interaction occurs for $L_2 < 15\,\mathrm{m}$. The eigenfrequencies are smaller compared to those of the multi-span reference model, but this has not resulted in interaction for longer mid-supports. Thus, the length of L_2 for initial interaction does not seem to depend directly upon the gap ratio.

6.1.5.2. Fatigue Analysis

The damage caused by lateral excitation for varying gap ratios is shown in Figure 218.
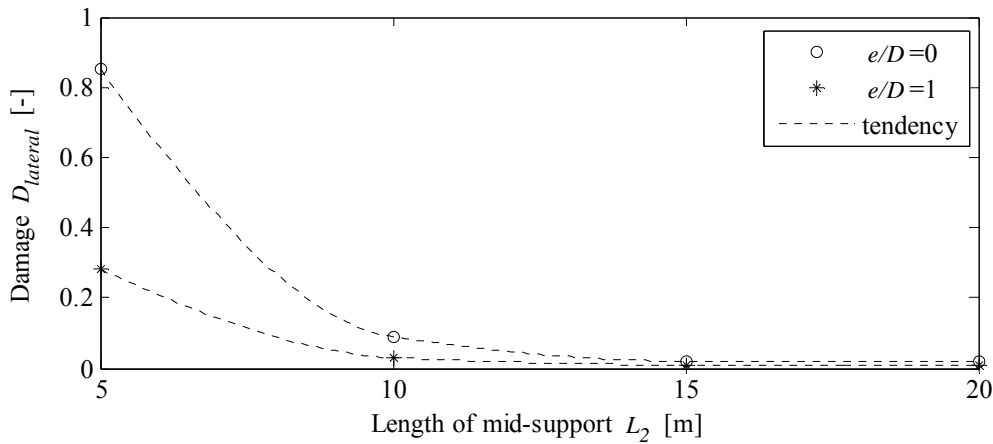

Figure 218: Damage for case 1 for varying gap ratios.

It is seen from Figure 218 that the damage due to interaction increases significantly when the gap ratio decreases. As the dynamic loads are increased and applied out of phase, the load frequency has become closer to the eigenfrequency of the multi-span. The combination of these factors result in increased damage. Figure 218 also indicates that interaction occurs for lengths of the mid-support $L_2 < 15\,\mathrm{m}$.

6.1.6 REFERENCE MODEL (ULS)

In this section the reference model for the ULS analyses is defined. The design conditions and assumptions are shown in Figure 219.
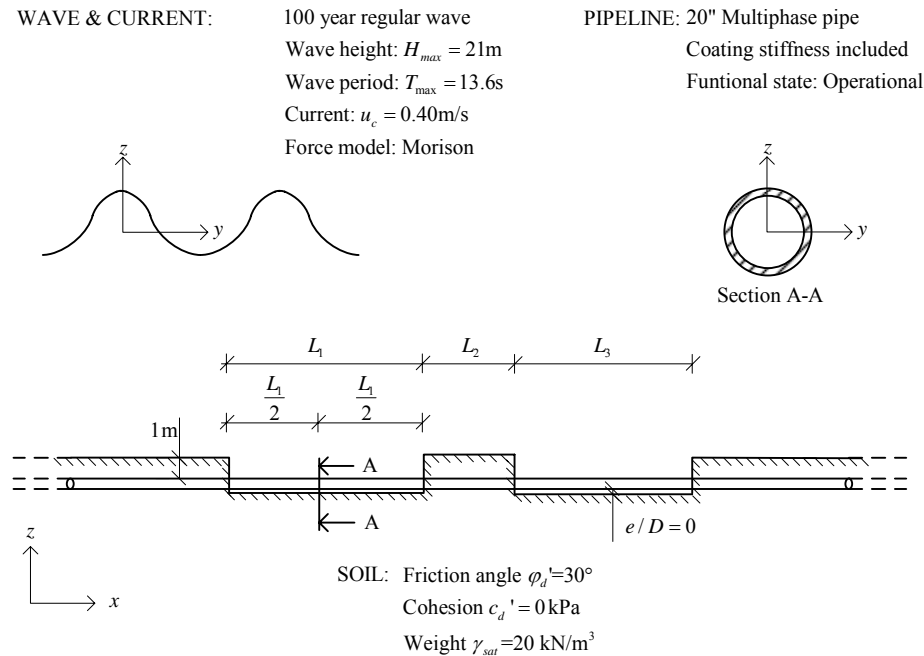

WAVE & CURRENT: 100 year regular wave   PIPELINE: 20" Multiphase pipe
                       Wave height: $H_{max} = 21$m   Coating stiffness included
                       Wave period: $T_{max} = 13.6$s   Funtional state: Operational
                       Current: $u_c = 0.40$m/s
                       Force model: Morison

Section A-A

$e/D = 0$

SOIL: Friction angle $\varphi_d' = 30°$
       Cohesion $c_d' = 0\,$kPa
       Weight $\gamma_{sat} = 20\,$kN/m^3

Figure 219: Reference model for multi-span in ULS.

The definitions of spanning lengths are identical to those defined in FLS which are shown in Table 61. The design conditions and assumptions made for the two neighbouring spans are identical to those made for a single-span in Chapter 5.4 (Buckling Analyses). The design loads acting on the system must therefore also be identical to those determined in Chapter 5.4 (Buckling Analyses).

6.1.7 FAILURE OF MID-SUPPORT

Failure of the mid-support happens as the length L_2 becomes so small that the forces from waves and current acting on the free-spans are able to pull the pipe through the soil bank that acts as mid-support. This will connect the two neighbouring free-spans to a single-span which will have a devastating effect on the pipeline. In the basic cases that are analysed in this project, failure of the mid-support will create a single-span with a spanning length that is above the maximum spanning length of both ultimate and fatigue limit state and will ultimately lead to failure of the pipeline.

6.1.7.1. Design Procedure

The analysis of failure is made as a static analysis. The length of the mid-support L_2 is decreased until failure of the mid-support is observed. This is done for the case of symmetrical and

asymmetrical multi-spans. Figure 219 shows the multi-span where the mid-support fails or restrain the pipeline.
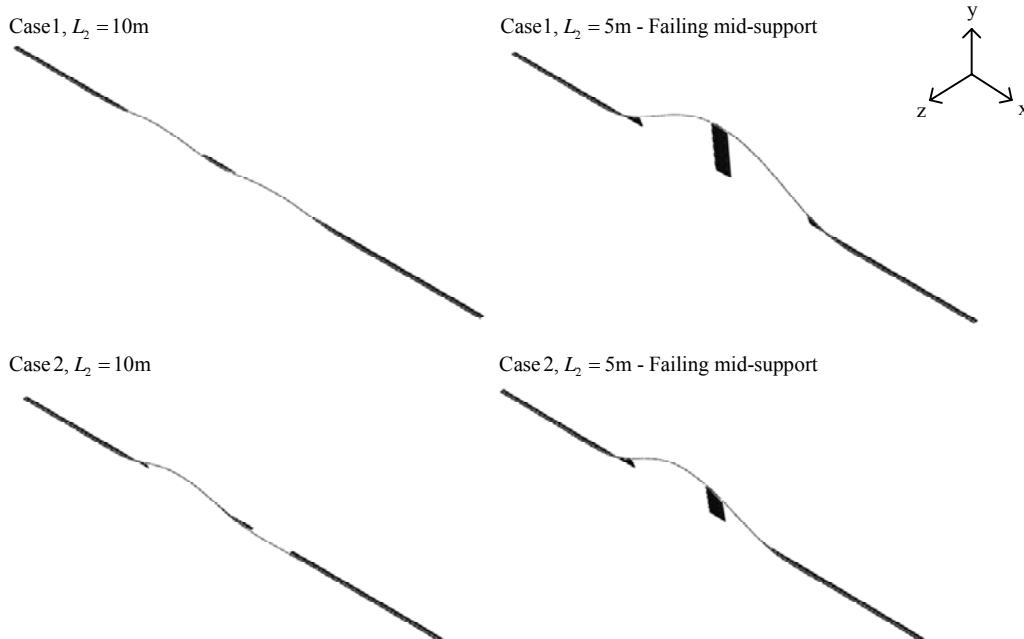

Figure 220: Deformed multi-span pipeline. Left) Restraining mid-support for case 1 and 2, respectively. Right) Failing mid-support for case 1 and 2, respectively.

Analysis has shown that the mid-support fails at $L_2 \approx 9\,\mathrm{m}$ for both case 1 and case 2, respectively. Surprisingly, the minimum length of the mid-support in case 2 is not longer than the minimum length found in case 1. The soil elements predict failure in case 2 as the pipeline is pulled through the soil from one side (the widest free-span). In case 1, the soil elements predict failure as the pipeline is pulled through the soil from both sides which apparently is not particularly worse than case 2. Frome these analyses it is concluded that the minimum length of the mid-support in case 1 and case 2 should be $L_2 \geq 10\,\mathrm{m}$.

6.1.8 EVALUATION

This evaluation partly serves to sum up the findings in the analyses of the project pipeline and partly to outline some guidelines for multi-span analyses in general.

Analyses in FLS

Frequency analysis shows that interaction between two neighbouring free-spans decrease the eigenfrequencies compared to the eigenfrequency of a single-span. Interaction has been shown to be most significant when the neighbouring free-spans have identical lengths and the length of the mid-support decreases. For neighbouring free-spans with spanning lengths of 25 m or less, frequency analysis has shown that interaction begins when the length of the mid-support becomes less than 15 m.

The lowest eigenmode of an interacting multi-span is obtained when the two neighbouring free-spans oscillate out of phase. If one of the neighbouring free-spans is reduced to half its length which creates an asymmetrical multi-span, the eigenmode where the free-spans oscillate in phase is suppressed.

In the analyses, the hydrodynamic forces from waves and current have been conservatively assumed to act out of phase in order to excite the lowest eigenmodes. The assumption is not physically valid for the severe sea states since the forces are also assumed to originate from two-dimensional waves. Since an upper bound of the damage has been sought, this has been ignored.

The multi-span pipeline does not experience vortex lock-in. Thus, damage due to vertical excitation is not critical. This means that the conclusions made in this project only concerns pipeline multi-spans without significant vortex lock-in.

The fatigue analysis has shown that the interaction between the two neighbouring free-spans increases the damage of the pipeline. The damage effect of interaction is largest for a symmetrical multi-span and for decreasing lengths of the mid-support. Similar to the frequency analysis, the fatigue analysis for neighbouring free-spans of L=25 m or less show that the damage starts to increase as the length of the mid-support becomes less than 15 m.

Parametric study has shown that a mid-support length of 15 m is sufficient to avoid significant effect of interaction for $e/D \in [0;1]$ and $\varphi \in [25°;35°]$. However, it has been shown that when interaction between the neighbouring free-spans is present, the gap ratio and friction angle has great effect on the consequences of interaction concerning fatigue damage. The fatigue analysis show that the acceptable damage ratio of $D_{\mathrm{lim}} = 0.1$ is reached for a mid-support length of approximately 10 m and neighbouring free-spans of 25 m but this result is highly dependent on the assumption made for e/D and φ.

Analyses in ULS

The failure analysis of the mid-support has shown that a minimum mid-support length of 10 m is required to avoid failure of the mid-support between two neighbouring free-spans of 25 m. The same minimum length is required for the asymmetrical multi-span with spanning length of 25 m and 12.5 m. The forces that act upon the widest free-span pull the pipeline through the soil of the mid-support from one side whereas two equally-sized free-spans pull the pipeline through the soil of the mid-support from both sides. The two situations seem to happen at almost the same length of the mid-support where the latter is the most critical case.

To complete the analysis in ULS, buckling analysis should be performed for the multi-span. This has been left out in this project. The buckling analysis for a multi-span can be made similar to the design procedure for the single-span described in Chapter 2.2 (Buckling). It is noticed that interaction between two neighbouring free-span can reduce the critical buckling length which is another reason to avoid interacting free-spans.

Guidelines to Multi-span Analyses

This section serves to outline some guidelines to a general verification procedure for multi-span analysis in FLS using a force model similar to that of the Abaqus Model in this project. The verification procedure is composed of three steps:

- **Step 1)** Frequency analysis is performed to determine if the distance between the neighbouring free-spans is above the length required for the neighbouring free-spans to interact. If no interaction is present, the free-spans can be regarded as individual single-spans. If interaction is present, continue to step 2.

- **Step 2)** Fatigue analysis of the pipeline is performed as an upper bound solution assuming the hydrodynamic forces act out of phase on the two neighbouring free-spans. If the multi-span is in the range of vortex lock-in, this should be taken into account in the hydrodynamic force model.

- **Step 3)** If the damage ratio that is determined in step 2 is not critical, restoration of the free-spans is planned. This could be rock-dumping from ships which prevents scour to cause free-span at the same location of the pipeline in the future. If critical damage ratio is exceeded, it may be considered either to perform more detailed computations or to plan damage inspection of the pipeline. The damage inspections will determine whether the pipeline should be repaired before the free-span is covered.

It is noticed that the risk of scour increasing the spanning lengths or decreasing the length of the mid-support should always be evaluated when determining the geometrical condition for the multi-span analysis. The risk of increasing spanning lengths due to scour is highly dependent on the weather conditions and the time between observation of a free-span until restoration.

A complete evaluation of a multi-span pipeline should be based upon ULS analyses that include a failure analysis of the mid-support and buckling analysis of the pipeline, in addition to FLS analyses.

APPENDICES

A   AXIAL FORCE

This section serves to clarify the various axial force contributions that affect the pipeline free-span. The use of conventional beam theory requires that the pipeline is homogeneous. In reality, however, the axial restraining of the pipeline and the presence of internal and external pressure due to the inner and surrounding fluid, respectively, renders the pipeline as a composite beam.

The composite beam is composed of a pipe-wall and internal fluid, as illustrated in Figure 221. In this context, the fact that the pipe-wall is a composite of steel and concrete is without relevance. In the pipe-wall, axial stresses exist due to temperature changes and installation. In addition, tractions that act perpendicularly upon the pipe-wall along the pipe section exist due to the internal and external pressure. In the internal fluid, compressive axial forces exist due to the internal pressure.
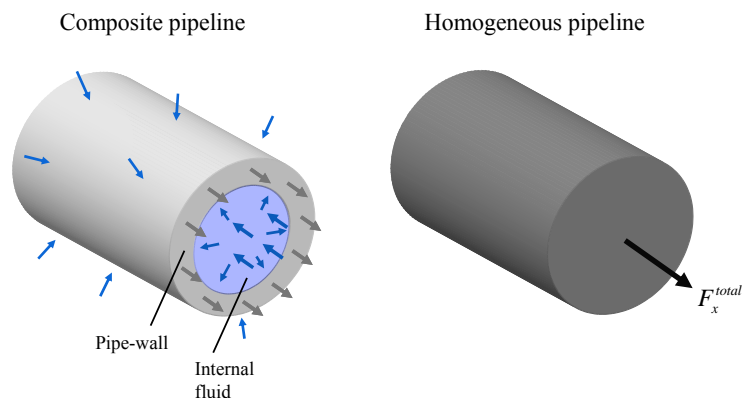

Composite pipeline   Homogeneous pipeline

F_x^{total}

Pipe-wall

Internal
fluid

Figure 221: Composite and homogeneous pipeline, respectively.

In order to abandon the composite description and instead treat the pipeline as homogenous, the external axial force of the homogeneous pipeline should have the following contributions

$$F_x^{total} = F_x^{install} + F_x^{temp} + F_x^{pressure} + F_x^{poisson} + F_x^{non-linear} \tag{A.1}$$

where

F_x^{total} is the total axial force in the homogenous pipeline [N]

$F_x^{install}$ is the initial axial force in the pipe-wall due to installation (lay-tension) [N]

F_x^{temp} is the axial force in the pipe-wall due to temperature [N]

$F_x^{pressure}$ is the axial force in the homogenous pipeline due to pressure [N]

$F_x^{poisson}$ is the axial force in the homogenous pipeline due to the Poisson effect [N]

$F_x^{non-linear}$ is the axial force due to large deformations [N]

[Braestrup et al. 2005, p105]

In this project, lay-tension from installation has been omitted because tension will be in favour for the pipeline free-span. The axial force contribution due to large deformations is implicit in the numerical model. The axial force due to installation and large deformations is not explored further in this section.

A.1   TEMPERATURE

The external axial force due to temperature arises from combined axial restraining and temperature change in the pipe-wall. All materials change volume when they are exposed to temperature changes. When the pipeline is exposed to rising temperature as the pipeline goes from the water-filled state to the functional state, the steel in the pipe-wall expands. The axial expansion for a part of the pipeline is shown in Figure 222.
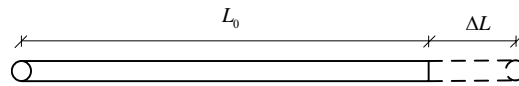

Figure 222: Expansion of a part of a pipeline.

The expansion is assumed to be proportional to the temperature and is written as

$$\Delta L = \alpha \cdot \Delta T \cdot L_0 \tag{A.2}$$

where

$\quad \Delta L \quad$ is the change in length [m]

$\quad L_0 \quad$ is the initial length [m]

$\quad \alpha \quad$ is the expansion coefficient [1/°C]

$\quad \Delta T \quad$ is the change in temperature [°C]

[Gottfredsen & Nielsen 1997, p160]

The axial strain due to temperature expansion of the pipeline may be formulated as

$$\varepsilon_x^{temp} = \frac{\Delta L}{L_0} \tag{A.3}$$

where

$\quad \varepsilon_x^{temp} \quad$ is the axial strain due to temperature, defined as positive in tension [-]

By use of (A.2) and (A.3), the initial length is eliminated from the formulation of axial strain due to temperature expansion

$$\varepsilon_x^{temp} = \alpha \cdot \Delta T \tag{A.4}$$

The axial strain due to normal stresses can be described by Hooke's law as

$$\varepsilon_x^{el} = \frac{1}{E_{steel}} \sigma_x \tag{A.5}$$

where

ε_x^{el} is the axial strain due to axial stresses [-]

σ_x is the normal stress [Pa]

E_{steel} is Young's modulus for steel [Pa]

When assuming that the pipeline is axially restrained so temperature expansion is prevented, the total axial strain must be zero. This can be formulated as

$$\varepsilon_x = \varepsilon_x^{temp} + \varepsilon_x^{el} = 0 \tag{A.6}$$

where

ε_x is the total axial strain [-]

ε_x^{el} is the axial strain due to normal stress [-]

Implementation of (A.4) and (A.5) into (A.6) provides the following normal stress due to prevention of temperature expansion

$$\sigma_x = -E_{steel} \cdot \alpha \cdot \Delta T \tag{A.7}$$

It is seen from (A.7) that the pipeline will experience additional normal stress as the temperature rises. The axial force due to temperature expansion can now be determined as

$$\begin{aligned} F_x^{temp} &= \sigma_x A_s \\ &= -E_{steel} \cdot \alpha \cdot \Delta T \cdot A_s \end{aligned} \tag{A.8}$$

[DNV-RP-F105 2006, p31]

A.2   PRESSURE

The axial force due to pressure arises from combined axial restraining and presence of internal and external pressure. It has been the object of some confusion in the past when the design stresses for pipeline or risers were to be determined. In this section, the pressure-induced axial force is described with general reference to [C. P. Sparks 1984, pp46-54].

According to DNV, the pressure-induced axial force is claimed to be

$$F_x^{pressure} = -p_i A_i + p_e A_e \tag{A.9}$$

[DNV-RP-F105 2006, p31]

In order to explain (A.9), it has been found favourable to distinguish between the axial force in the pipe-wall and the axial force induced by the fluid inside and outside the pipeline. This distinction has been made by introducing an effective axial force which is explained in the following.

A.2.1   Effective Axial Force

To explain the principle of effective axial force, the pipeline free-span is regarded as a composite column. In order to determine the global behaviour of a composite column, it is necessary to consider:

1. The total axial force that acts in the column section
2. The total bending stiffness (assuming elastic material)

In the absence of external pressure, the pipeline corresponds to a composite column of pipe and fluid. The effective axial force is determined as the sum of forces acting in the pipe-wall and fluid column, respectively

$$F_x^{eff} = F_x^{tw} - p_i \cdot A_i, \qquad p_i \geq 0 \tag{A.10}$$

where

$\quad F_x^{eff}$ is the effective axial force in the pipeline [N]

$\quad F_x^{tw}$ is the axial force in the pipe-wall (true wall) [N]

$\quad p_i$ is the internal pressure [Pa]

$\quad A_i$ is the internal cross section area of the pipe [m^2]

[C. P. Sparks 1984, p48]

When external pressure is present, the compressive force in the suppressed fluid column has to be deducted from the force acting in the pipeline section. This leads to the general formulation of effective axial force in the pipeline

$$\begin{aligned} F_x^{eff} &= F_x^{tw} - p_i \cdot A_i - \left(-p_e \cdot A_e\right), \qquad p_e \geq 0 \\ &= F_x^{tw} - p_i \cdot A_i + p_e \cdot A_e \\ &= F_x^{tw} + F_x^{pressure} \end{aligned} \tag{A.11}$$

where

$\quad F_x^{eff}$ is the effective axial force in the pipeline [N]

$\quad p_e$ is the external pressure [Pa]

$\quad A_e$ is the external cross section area of the pipe [m^2]

[C. P. Sparks 1984, p48]

Figure 223 illustrates the principle of determining the effective axial force in the pipeline.
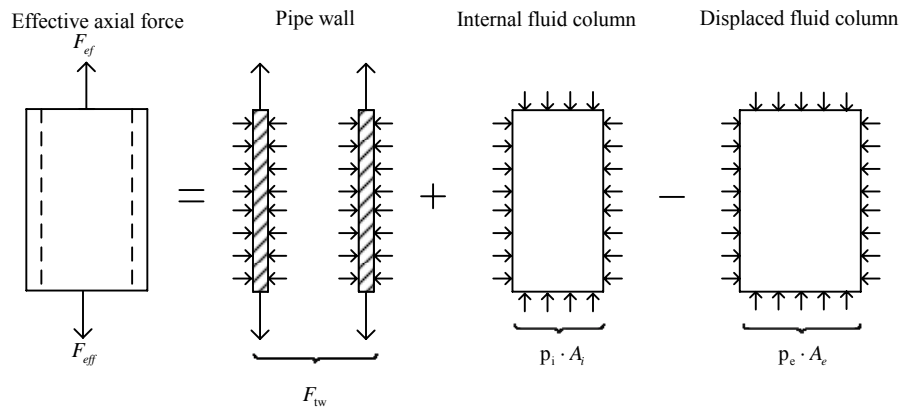
Figure 223: Illustration of effective axial force in pipeline. Big and small arrows indicate forces and stresses, respectively.

To avoid any confusion, it is noticed that the effective axial force defined in (A.11) is identical to the total axial force defined in (A.1) since the true-wall force F_x^{tw} is the sum of all forces acting in the pipe-wall

$$F_x^{tw} = F_x^{install} + F_x^{temp} + F_x^{poisson} + F_x^{non-linear} \qquad (A.12)$$

It is also noticed that the stiffness of the pipeline is governed only by the pipe-wall as the fluid columns has zero contribution to the total bending stiffness of the pipeline.

A.2.2   Buckling Example Due to Pressure

The hypothesis that effective axial force determines the global behaviour of the pipeline has been investigated by buckling experiments of two fluid-filled pipelines [C. P. Sparks 1984, p50]. Figure 224 shows the principle of the experiments. The two columns were identical except that the fluid in column 1 was subjected to internal pressure. In the pipe-ends, an external compressive force was applied axially upon the entire cross-section and the lateral displacements were constrained.
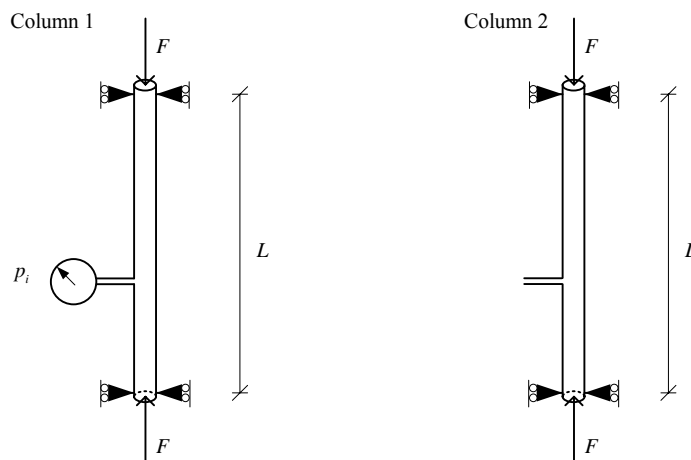

Figure 224: Principle of buckling tests of fluid-filled pipelines of length L with and without internal pressure p_i, respectively.

Measurements showed that buckling occurred in both pipes when the external force reached the Euler force

$$F = F_E = \frac{\pi^2 EI}{L^2}$$ (A.13)

where

    F is the applied force in the pipe-ends, defined as positive in compression [N]

    F_E is the Euler axial force load, defined as positive in compression [N]

    EI is the bending stiffness of the pipe [Nm^2]

    L is the length of the pipe [m]

This may be explained by the fact that the two columns experience an identical effective axial force that is equal to the same applied force. However, the axial forces in the pipe-wall and the inner fluid-columns are distributed differently in the two cases. In column 2, the external load is carried entirely by the pipe-wall while in column 1, the same external load is carried by both the pipe-wall and the fluid. Thus, internal pressure can induce global buckling of a pipeline.

A.3 POISSON EFFECT

The external axial force due to the Poisson effect arises from combined axial restraining, the Poisson effect and the presence of external and internal pressure. It may be explained in the following way: The tractions that act upon the pipe-wall due to internal and external pressure will tend to strain the cross-section in radial direction. Since this is prevented due to the Poisson effect and axial restraining, an axial reaction force arises. This is known as a plane strain state.

The axial force due to the Poisson effect can be determined by force equilibrium of a infinitesimal part of the pipe-wall as shown in Figure 225.
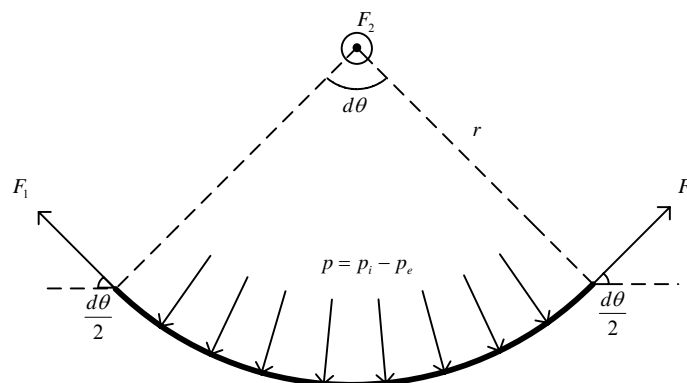

Figure 225: Infinitesimal part of the pipe-wall where r is the radius, $d\theta$ is an infinitisimal change of angle, F_1 is the hoop force and F_2 is the axial force.

By demanding vertical equilibrium of the forces affecting the infinitesimal part of the pipe-wall and assuming a thin-walled section, the hoop force F_1 can be determined as

$$-p \cdot r \cdot d\theta + 2F_1 \sin\left(\frac{d\theta}{2}\right) = 0, \quad p = p_i - p_e \quad \Rightarrow$$

$$-p \cdot r \cdot d\theta + 2F_1 \frac{d\theta}{2} = 0 \qquad\qquad\qquad \Rightarrow \qquad (A.14)$$

$$F_1 = p \cdot r = \frac{1}{2} p \cdot D$$

where

p is the difference in internal and external pressure [Pa]

r is the radius of the pipe-section [m]

$d\theta$ is an infinitesimal change of angle

F_1 is the hoop force [N]

The axial reaction force can be determined as

$$F_2 = v \cdot F_1 = v \frac{1}{2} pD \qquad\qquad (A.15)$$

where

F_2 is the axial reaction force [N]

In order to get the total force contribution from the Poisson effect along the entire pipe section, F_2 is multiplied with the circumference of the pipe section. The total force contribution from the Poisson effect is found as

$$
\begin{aligned}
F_x^{poisson} &= \pi D \cdot F_2 \\
&= \pi D v \frac{1}{2} pD \\
&= \frac{1}{2} \pi D^2 v \left(p_i - p_e \right) \\
&= 2v \left(p_i - p_e \right) A
\end{aligned}
\qquad (A.16)
$$

[DNV-RP-F105 2006, p31]

A.4   TOTAL AXIAL FORCE

Neglecting contributions due to installation and large deformations of the pipe, the total axial force can be written as

$$
\begin{aligned}
F_x^{total} &= F_x^{temp} + F_x^{pressure} + F_x^{poisson} \\
&= -E_{steel} \cdot \alpha \cdot \Delta T \cdot A_s - p_i A_i + p_e A_e + 2v(p_i - p_e)A
\end{aligned}
\qquad (A.17)
$$

B RAYLEIGH DAMPING

The global damping is implemented in the numerical models by Rayleigh's damping model which assumes that the damping matrix can be written as a linear combination of the mass and stiffness matrix as

$$\mathbf{C} = a_0\mathbf{M} + a_1\mathbf{K} \qquad\qquad\qquad (B.1)$$

where

    $\mathbf{C}$ is the damping matrix [-]

    $\mathbf{M}$ is the mass matrix [-]

    $\mathbf{K}$ is the stiffness matrix [-]

    a_0, a_1 are the Rayleigh coefficients [-]

[Nielsen 2004, p100]

When modal decoupling is assumed, the relation between the Rayleigh coefficients and the damping ratios can be written as

$$\zeta_i = \frac{1}{2\omega_i}\left(a_0 + a_1\omega_i^2\right), \qquad i = 1, 2, ..., n \qquad\qquad (B.2)$$

Where

    ς_i is the ith damping ratio [-]

    ω_i is the ith circular eigenfrequency [rad/s]

    i is the mode number [-]

    n is the number of degrees of freedom [-]

[Nielsen 2004, p100]

By use of (B.2), the Rayleigh coefficients can be calibrated perfectly for two eigenmodes by

$$\begin{bmatrix} a_0 \\ a_1 \end{bmatrix} = \frac{2\omega_1\omega_2}{\left(\omega_2^2 - \omega_1^2\right)}\begin{bmatrix} \omega_2 & -\omega_1 \\ -\dfrac{1}{\omega_2} & \dfrac{1}{\omega_1} \end{bmatrix}\begin{bmatrix} \zeta_1 \\ \zeta_2 \end{bmatrix} \qquad\qquad (B.3)$$

[Nielsen 2004, p100]

By assuming $\zeta_1 = \zeta_2 = \zeta_{global}$, the Rayleigh coefficients may be determined. The remaining modes will also experience damping but the damping ratio for these modes will not be equal to ζ_{global}. This is however considered to be a fair damping model as the dynamic behaviour of the free-span pipeline is dominated by the first two eigenmodes.

C BUCKLING EIGENVALUE PROBLEM

In Abaqus, the global buckling problem is solved by determining loads for which the global stiffness matrix becomes singular. The buckling load can be found by determining the non-trivial solution for the following system of linear equations

$$\mathbf{K}_0^{nm}\mathbf{v}^m = 0 \qquad\qquad (C.1)$$

where

$\mathbf{K}_0^{nm}$ is the global tangent stiffness matrix when the load is applied

$\mathbf{v}^m$ is the non-trivial generalised displacement vector

m, n denote the degrees of freedom [-]

[Dassault Systèmes 2007, Section 6.2.3]

This can be formulated as an eigenvalue problem by introducing a loading pattern Q^n determining the load which is scaled by load multipliers. The eigenvalue buckling problem is defined as

$$\left(\mathbf{K}_0^{nm} + \lambda_i \mathbf{K}_\Delta^{nm}\right)v_i^m = 0 \qquad\qquad (C.2)$$

where

$\mathbf{K}_0^{nm}$ is the global stiffness matrix in the base state incl. effects of pre-loads

$\mathbf{K}_\Delta^{nm}$ is the differential initial stress and load stiffness matrix due to the loading pattern Q^n

λ_i is the ith load multiplier

$\mathbf{v}_i^m$ is the ith normalised buckling mode, normalised so the maximum displacement is 1.0

[Dassault Systèmes 2007, Section 6.2.3]

It is noticed that the value of the loading pattern Q^n is not important since it is scaled by the load multiplier λ_i that is found in the eigenvalue problem. For ease, Q^n may be set to 1.0.

D ELEMENT MATRICES IN MATLAB MODEL

In this appendix, the element stiffness and mass matrices of the elements in the Matlab Model are given. The elements are based upon the theory of plane, straight Bernoulli-Euler beams. For convenience, the element matrices are presented for a beam whose axial axis is parallel with the global axial coordinate.

D.1 ELEMENT STIFFNESS MATRICES

In the Matlab Model, four element stiffness matrices are used. For the mid-span and side-span, the element stiffness matrices for a regular beam and beam upon Winkler foundation are used, respectively. In the case of large rotations, the presence of a tensile or compressive initial axial load of large magnitude may considerably increase or reduce the stiffness of the element, respectively. In this case, the element stiffness matrices are adjusted. An overview of the equations numbers and function calls of the element stiffness matrices are shown in Table 62 and the element stiffness matrices are given below.

Table 62: Overview of equation numbers and function calls for element stiffness matrices that are used for the mid-span or side-span, and with or without the effect of an initial axial load. All functions are pre-defined in the CALFEM toolbo, except the one that is marked with **.

Effect of initial axial load	Free-span		Side-span	
	Equation number	*Function call*	*Equation number*	*Function call*
No	(D.1)	Beam2e(..)	(D.3)	Beam2w(..)
Yes	(D.2)	Beam2g(..)	(D.4)	Beam2wg (..) **

D.1.1 Regular Beam

The element stiffness matrix of a regular beam is

$$
\mathbf{K}^e_{beam} =
\begin{bmatrix}
\frac{EA}{L} & & & & & \\
0 & \frac{12EI}{L^3} & & & \text{sym.} & \\
0 & \frac{6EI}{L^2} & \frac{4EI}{L} & & & \\
-\frac{EA}{L} & 0 & 0 & \frac{EA}{L} & & \\
0 & -\frac{12EI}{L^3} & -\frac{6EI}{L^2} & 0 & \frac{12EI}{L^3} & \\
0 & \frac{6EI}{L^2} & \frac{2EI}{L} & 0 & -\frac{6EI}{L^2} & \frac{4EI}{L}
\end{bmatrix}
\tag{D.1}
$$

where

$\mathbf{K}^e_{beam}$ is the element stiffness matrix of a regular beam

EA   is the element axial stiffness [N]

EI   is the element bending stiffness [Nm^2]

L   is the element length [m]

[Department of Mechanics and Materials 1999, Sect. 5.6-3; Nielsen 2004, p153]

D.1.2   Beam With Effect of Initial Axial Load

The element stiffness matrix of a beam with the effect of an initial axial load is

$$\mathbf{K}^e_{beam2} = \begin{bmatrix} \frac{EA}{L} & & & & & \\ 0 & \frac{12EI}{L^3}\phi_5 & & & \text{sym.} & \\ 0 & \frac{6EI}{L^2}\phi_2 & \frac{4EI}{L}\phi_3 & & & \\ -\frac{EA}{L} & 0 & 0 & \frac{EA}{L} & & \\ 0 & -\frac{12EI}{L^3}\phi_5 & -\frac{6EI}{L^2}\phi_2 & 0 & \frac{12EI}{L^3}\phi_5 & \\ 0 & \frac{6EI}{L^2}\phi_2 & \frac{2EI}{L}\phi_4 & 0 & -\frac{6EI}{L^2}\phi_2 & \frac{4EI}{L}\phi_3 \end{bmatrix}$$
(D.2)

where

$\mathbf{K}^e_{beam2}$ is the element stiffness matrix of the beam with the effect of an initial axial load

ϕ_j is the *j*th interpolation function

[Department of Mechanics and Materials 1999, Sect. 5.6-16]

The interpolation functions are determined by

$$N < 0: \quad \phi_1 = \frac{cL}{2}\cot\left(\frac{cL}{2}\right), \quad \phi_2 = \frac{c^2L^2}{12\cdot(1-\phi_1)}, \quad c = \frac{\pi}{L}\sqrt{\rho},$$

$$N > 0: \quad \phi_1 = \frac{cL}{2}\coth\left(\frac{cL}{2}\right), \quad \phi_2 = -\frac{c^2L^2}{12\cdot(1-\phi_1)}, \quad c = \frac{\pi}{L}\sqrt{-\rho}, \qquad \rho = -\frac{NL^2}{\pi^2 EI}$$

$$\phi_3 = \frac{1}{4}\phi_1 + \frac{3}{4}\phi_2, \quad \phi_4 = -\frac{1}{2}\phi_1 + \frac{3}{2}\phi_2, \quad \phi_5 = \phi_1\phi_2$$

where

N   is the initial axial load, defined as positive in tension [N]

c   is a coefficient [1/m]

ρ is the negative ratio of the axial load and the Euler load [-]

[Department of Mechanics and Materials 1999, Sect. 5.6-16]

D.1.3   Beam Upon Winkler Foundation

The element stiffness matrix of a beam upon Winkler foundation is

$$\mathbf{K}^e_{beam-winkler} = \mathbf{K}^e_{beam} + \mathbf{K}^e_{winkler},$$

(D.3)

$$\mathbf{K}^e_{winkler} = \frac{L}{420} \cdot \begin{bmatrix} 140\,\kappa_a & & & & & \\ 0 & 156\,\kappa_t & & & \text{sym.} & \\ 0 & 22\,\kappa_t\,L & 4\,\kappa_t\,L^2 & & & \\ 70\,\kappa_a & 0 & 0 & 140\,\kappa_a & & \\ 0 & 54\,\kappa_t & 13\,\kappa_t\,L & 0 & 156\,\kappa_t & \\ 0 & -13\,\kappa_t\,L & -3\,\kappa_t\,L^2 & 0 & -22\,\kappa_t\,L & 4\,\kappa_t\,L^2 \end{bmatrix}$$

where

$\mathbf{K}^e_{beam-winkler}$ is the element stiffness matrix of a beam upon Winkler foundation

$\mathbf{K}^e_{winkler}$ is the element stiffness matrix of the Winkler foundation

κ_a is the linear spring stiffness in axial direction [N/m^2]

κ_t is the linear spring stiffness in transversal direction [N/m^2]

[Department of Mechanics and Materials 1999, Sect. 5.6-12]

D.1.4   Beam With Effect of Initial Axial Load Upon Winkler Foundation

The element stiffness matrix of a beam with the effect of an initial axial load where the beam is placed upon a Winkler foundation is

$$\mathbf{K}^e_{beam2-winkler} = \mathbf{K}^e_{beam2} + \mathbf{K}^e_{winkler}$$

(D.4)

where

$\mathbf{K}^e_{winkler-axial}$ is the element stiffness matrix of a beam upon Winkler foundation with axial load

D.2   ELEMENT MASS MATRIX

For all of the elements, the consistent element mass matrix is used

$$\mathbf{M}^e = \frac{mL}{420} \cdot \begin{bmatrix} 140 & & & & & \\ 0 & 156 & & & \text{sym.} & \\ 0 & 22L & 4L^2 & & & \\ 70 & 0 & 0 & 140 & & \\ 0 & 54 & 13L & 0 & 156 & \\ 0 & -13L & -3L^2 & 0 & -22L & 4L^2 \end{bmatrix}$$

(D.5)

where

$\mathbf{M}^e$ is the consistent element mass matrix of the beam
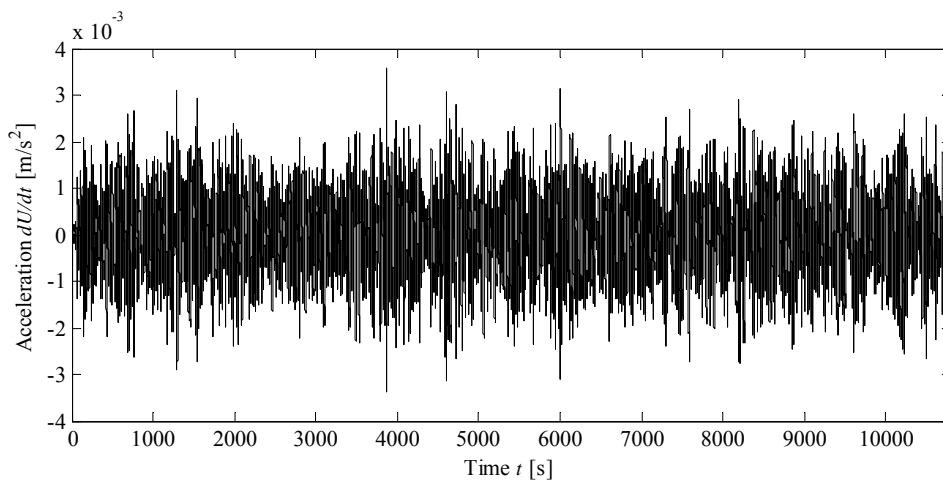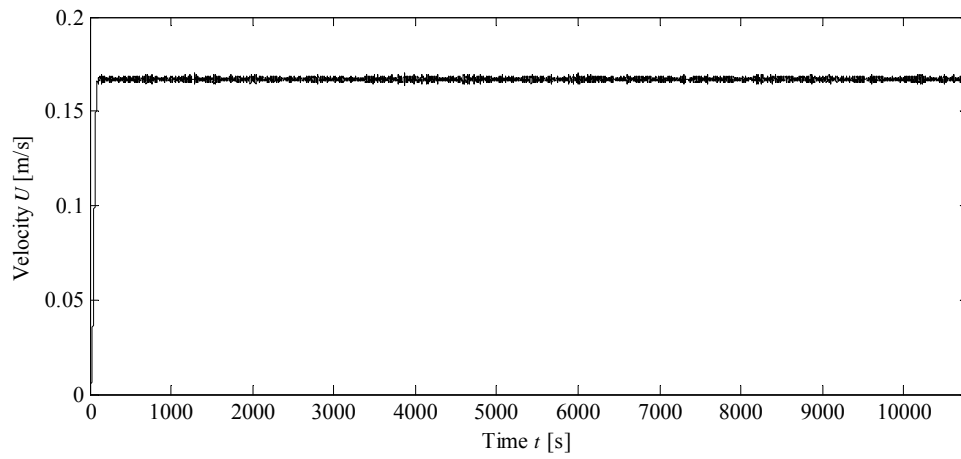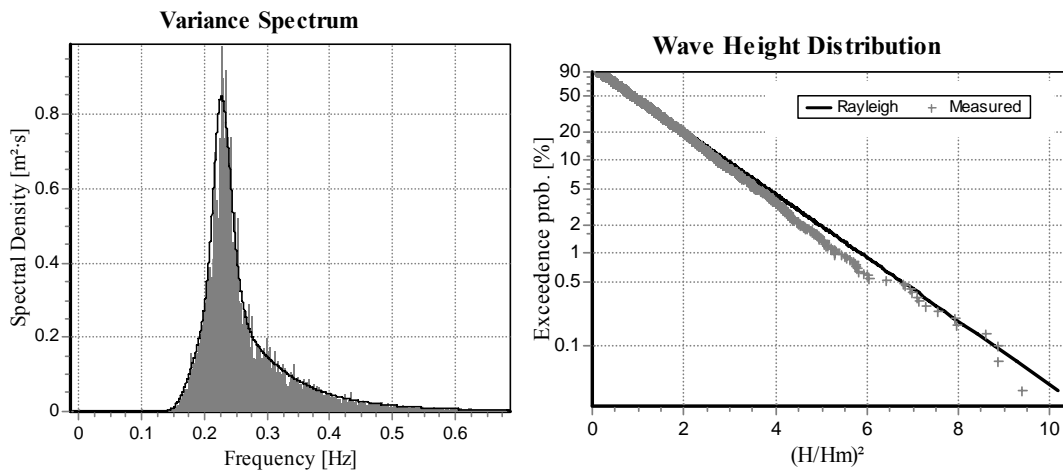m is the mass per unit length [kg/m]

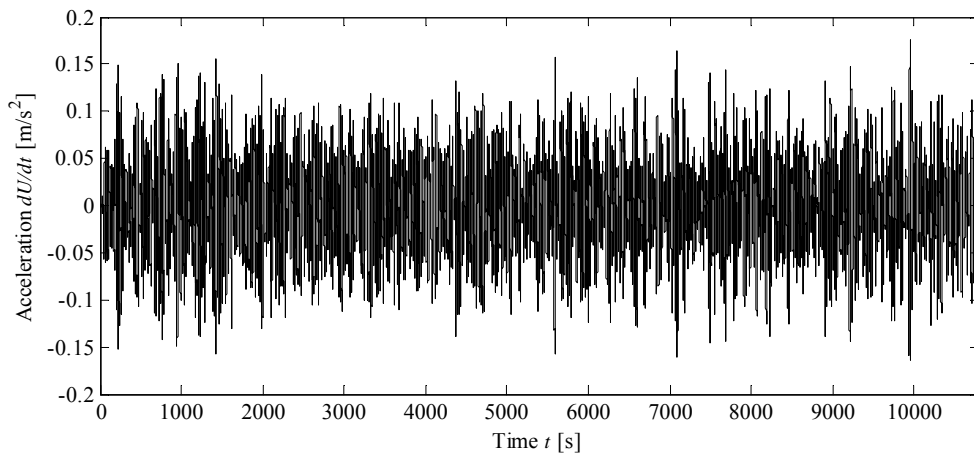[Department of Mechanics and Materials 1999, Sect. 5.6-21; Nielsen 2004, p153]

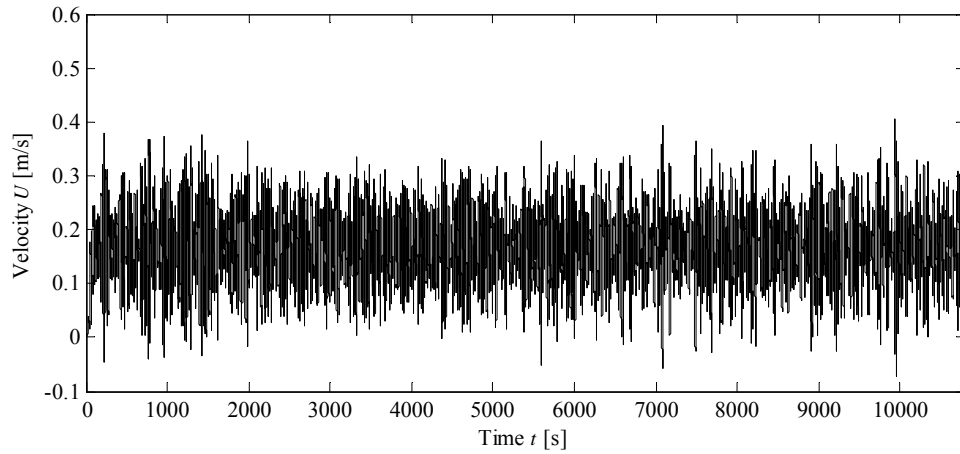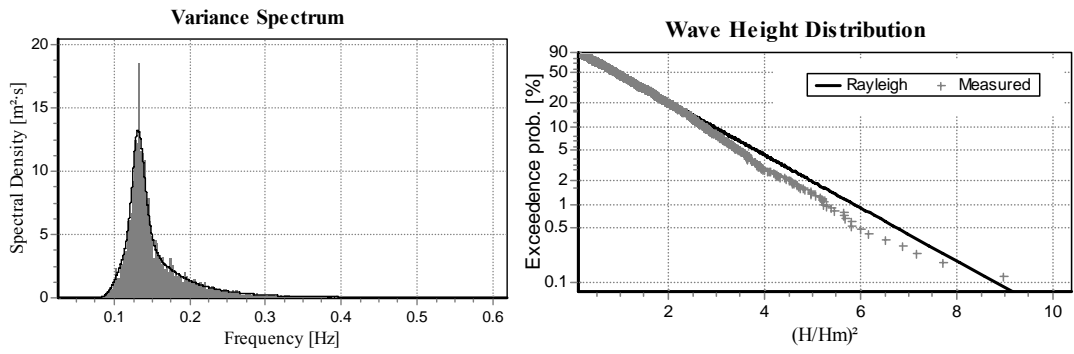# E   IRREGULAR SEA STATES

This appendix contains data sheets for the irregular sea states 1-5 that have been generated in WaveLab2. The variance spectrum shows the generated wave data compared to a standard JONSWAP spectrum. The diagrams of wave height distribution shows the generated wave height distribution compared to a Rayleigh distribution. The flow velocity history and acceleration history are evaluated at half an outer pipe diameter above the seabed. The sea states are modelled for 3.0 hours and the actual durations are given in Chapter 1.1 (Design Conditions).
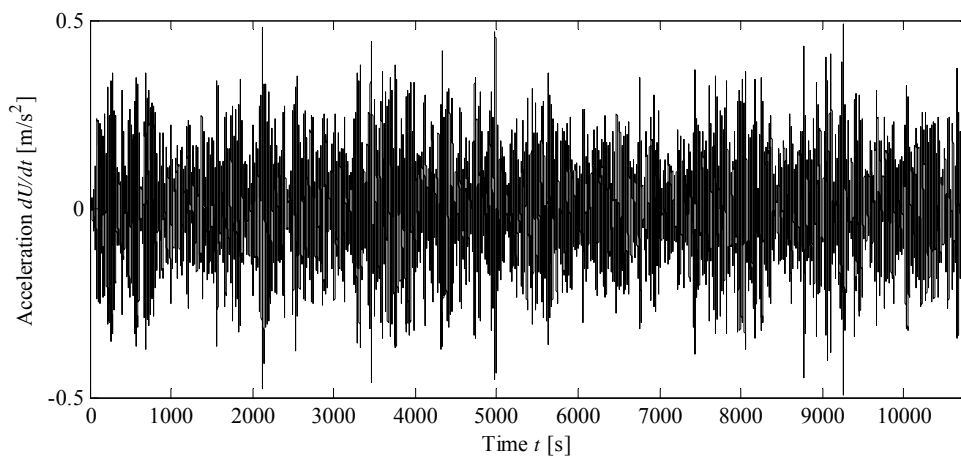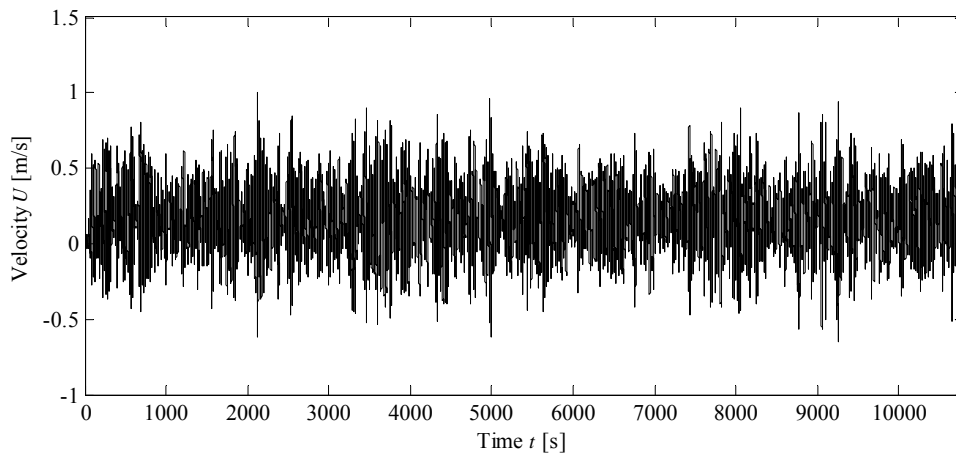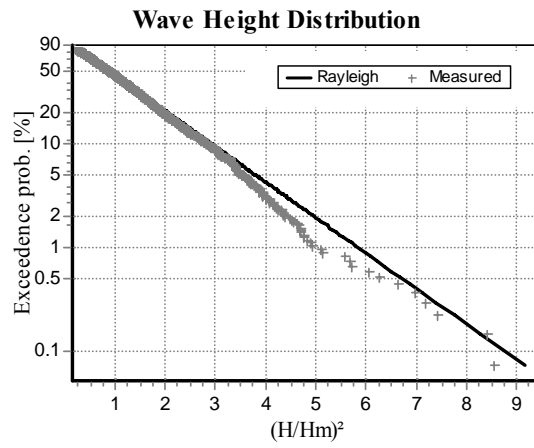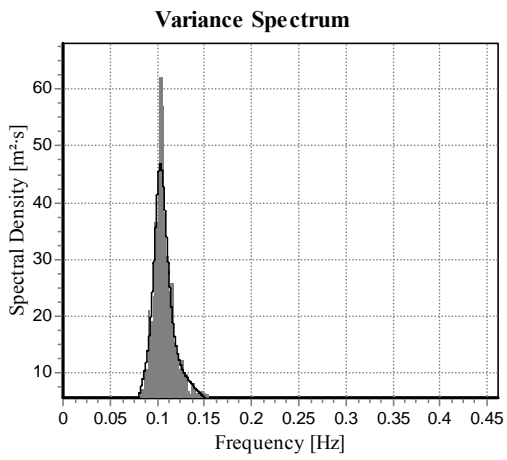
E.1 IRREGULAR SEA STATE 1

Variance Spectrum

Wave Height Distribution

E.2 IRREGULAR SEA STATE 2

Variance Spectrum

Wave Height Distribution

E.3   IRREGULAR SEA STATE 3

Variance Spectrum

Wave Height Distribution
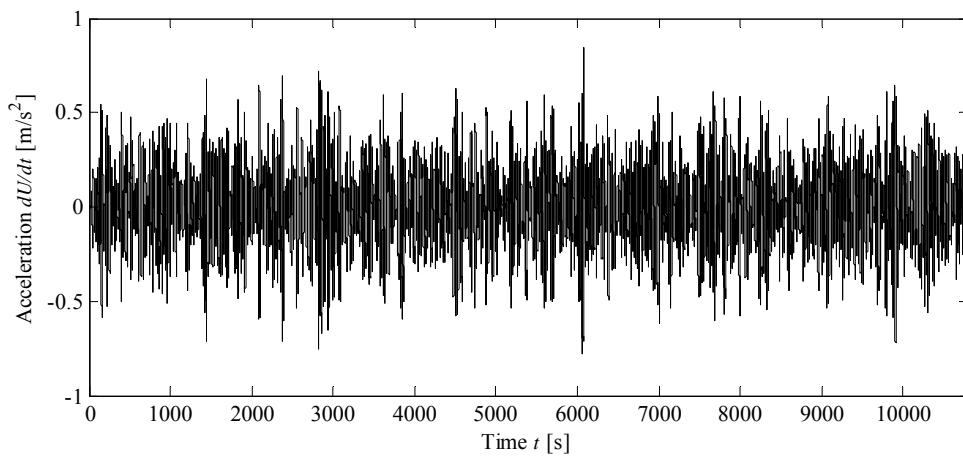
E.4   IRREGULAR SEA STATE 4

Variance Spectrum
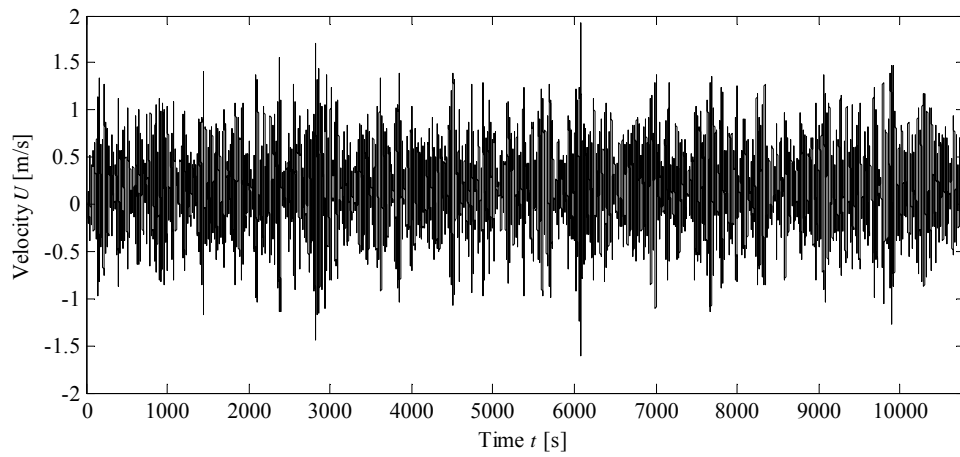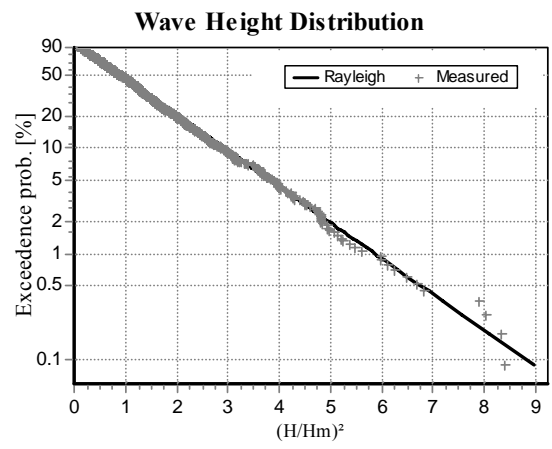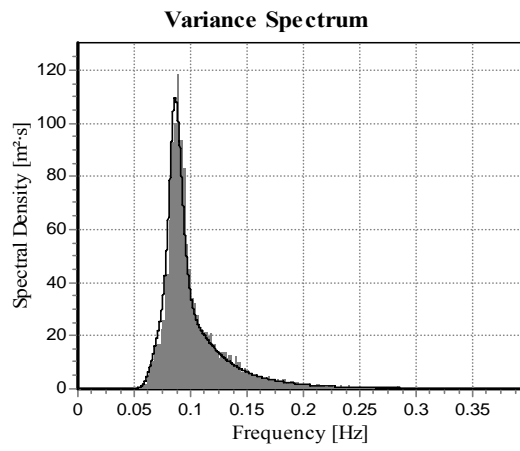

Wave Height Distribution

E.5 IRREGULAR SEA STATE 5

Variance Spectrum

Wave Height Distribution
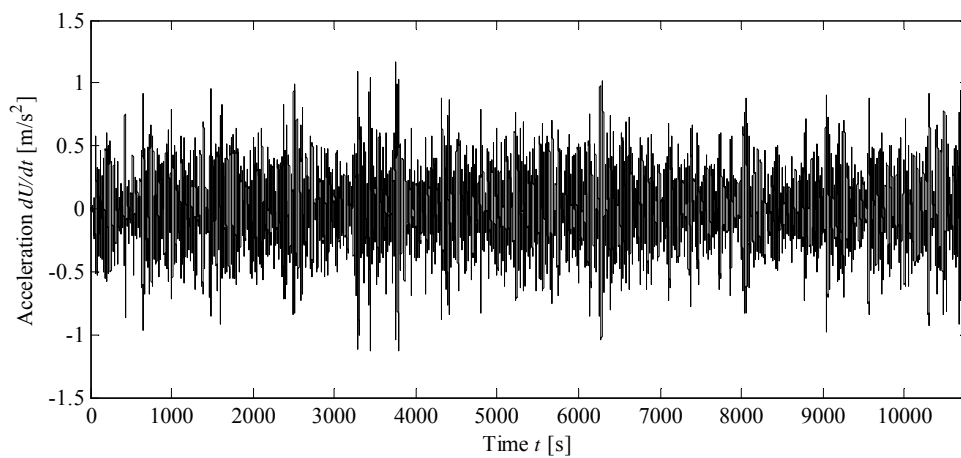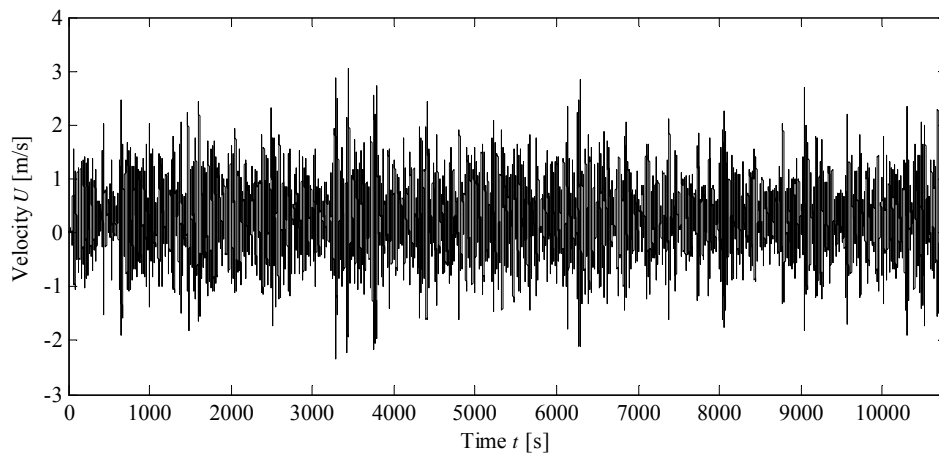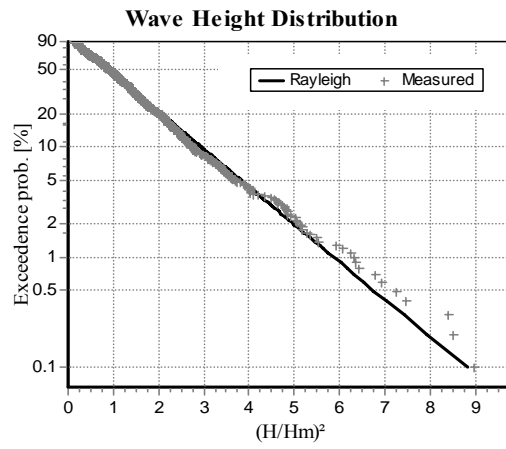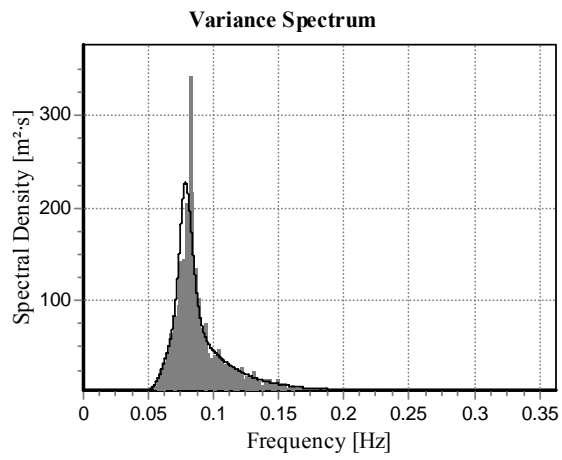
F EMPIRICAL PARAMETERS OF WAKE MODELS

Table 63: Empirical coefficients for forces and start-up effect of the Wake Models. All coefficients are dimensionless. They are defined in the project and may differ in appearance from the original references. Compiled upon literature study of the indicated references.

Force coefficients	Wake I Model	Wake II Model		Wake II Extended Model			
	Regular and	Regular waves		Regular waves		Irregular waves	
	irregular waves with and without current	Without Current	With current	Without Current	With current	Without Current	With current
C_A	0.25		-	0.20	0.48	0.20	0.45
C_M	2.5		-	5.0	2.9	4.0	2.92
C_{DS}	1.1				0.55	1.1	0.53
C_{LS}	0.8			0.26	3.72	0.26	3.58
α_D	0.38				0.57	0.38	0.55
β_D	1.0						
γ_D	-0.016						
δ_D	4.0						
α_L	9.8	8.5	9.8	4.4	6.6	5.3	6.6
β_L	0.65	0.95	0.65	0.15	0.95	1.15	0.05
γ_L	-1.0	-0.95	-1.0	-0.95	-0.75	-0.95	-0.75
δ_L	1.2	1.45	1.2	1.45	1.46	1.35	1.46
References	[Lambrakos et al. 1987, p128*]	[Soedigdo et al. 1998, p446, p456-458]	[Sabag et al. 2000, p1305]	[Aristodemo et al. 2006, p7] [Aristodemo et al. 2007, p6]			

Table 64: Empirical coefficients for forces and wake effect of the Wake Models. All coefficients are defined in the project and may differ in appearance from the original references. Compiled upon literature study of the indicated references.

	Wake I Model	Wake II Model		Wake II Extended Model			
	Irregular waves with and without current	Regular waves		Regular waves		Irregular waves	
		Without Current	With current	Without Current	With current	Without Current	With current
Wake coefficients	$K = 0.5$ $J = 0.5$	$n = 3$ $C_1 = 0.50$ $C_2 = 0.95$ $\phi = a_0 + a_1 KC + a_2 (KC)^2,$ $\begin{cases} a_0 = 188.6° \\ a_1 = -2.1° \\ a_2 = 0.03° \end{cases}$	$n = 1$ $C_{1,A} = 0.53$ $C_{1,B} = c_0 + c_1\, KC_{loc,B},$ $\begin{cases} c_0 = 0.64 \\ c_1 = -0.0032 \end{cases}$ $C_{2,A} = C_{2,B} = 0.95$ $\phi_A = a_0 + a_1 \frac{U_c}{U_m} + a_2 \left(\frac{U_c}{U_m}\right)^2,$ $\phi_B = a_0 - a_1 \frac{U_c}{U_m} + a_2 \left(\frac{U_c}{U_m}\right)^2,$ $\begin{cases} a_0 = 171° \\ a_1 = 241.25° \\ a_2 = 93.75° \end{cases}$	$\phi = a_0 + a_1 KC_{loc},$ (spanning)			
				$C_d = 0.8$ $\begin{cases} a_0 = 155° \\ a_1 = -2° \end{cases}$	$C_d = 1.1$ $\begin{cases} a_0 = 187.3° \\ a_1 = -2° \end{cases}$	$C_d = 0.6$ $\begin{cases} a_0 = 155° \\ a_1 = -2° \end{cases}$	$C_d = 1.1$ $\begin{cases} a_0 = 187° \\ a_1 = -2° \end{cases}$
References	[Lambrakos et al. 1987, p128]	[Soedigdo et al. 1998, p446, p456-458]	[Sabag et al. 2000, p1305]	[Aristodemo et al. 2006, p7] [Aristodemo et al. 2007, p6]			

REFERENCES

[Albertsen 1997]: *Stålkonstruktioner Elementer*

A. Albertsen, P. Ehlers, S. Kloch & I. Larsen, 1997
Aalborg University, Denmark
ISSN: 1395-8232 U9712

[Almar-Næss et al. 1985]: *Fatigue Handbook: Offshore Steel Structures*
Almar-Næss et al., 1985
Tapir

[Andersen 2006]: *Linear Elastodynamic Analysis*
Lars Andersen, 2006
Aalborg University, Denmark
DCE Lecture Notes
Volume 3
ISSN: 1901-7286

[Andersen 2006b]: *Lecture notes no. 8 from course in Material Modelling*
Lars Andersen, 2006
Aalborg University, Denmark

[Aristodemo et al. 2006]: *Modelling of periodic and random wave forces on submarine pipelines*
F. Aristodemo, G. R. Tomasicchio, P. Veltri, 2006
Proceedings of 25th International Conference on Mechanics and Arctic Engineering

[Aristodemo et al. 2007]: *Modelling of combined wave and current forces on smooth submarine pipelines*
F. Aristodemo, G. R. Tomasicchio, P. Veltri, 2007
Proceedings of 32th International Congress of IAHR - Coastal Structures

[Bonnerup 2005]: *Stålkonstruktioner efter DS412*
Bent Bonnerup & Bjarne Chr. Jensen, 2005
Nyt Teknisk Forlag
ISBN: 87-571-2514-7

[Braestrup et al. 2005]: *Marine Pipelines*
M.W. Braestrup et al., 2005
Blackwell Science
ISBN: 978-0632-05984-3

[Burckharth 2002]: *Støm- og bølgekræfter på stive legemer*
H.F. Burcharth, 2002
Aalborg University, Denmark
Udgave 2

[Byskov 2002]: *Elementary Continuum Mechanics for Everyone - and Some More*
Esben Byskov, 2002
Aalborg Tekniske Universitetsforlag
ISSN: 1395-8232 U0207

[Dassault Systèmes 2007]: *Abaqus Version 6.7 Documentation - Abaqus Analysis User's Manual*
Dassault Systèmes, 2007

[Dassault Systèmes 2007b]: *Abaqus Version 6.7 Documentation - Abaqus Theory Manual*
Dassault Systèmes, 2007

[Department of Mechanics and Materials 1999]: *CALFEM - A finite element toolbox to MATLAB, Version 3.3*
Department of Mechanics and Materials, 1999
JABE Offset
Lund University, Sweden
ISSN: 0281-6679

[Design Basis 2006]: *Design Basis for Pipelines, Risers, and Appurtenances*
Maersk Oil, 2006
Maersk Oil

[DNV No. 30.1 2004]: *Buckling Strength Analysis of Bars and Frames, and Sperical Shells*
Det Norske Veritas, 2004

[DNV-OS-F101 2000]: *Submarine Pipeline Systems*
Det Norske Veritas, 2000

[DNV-RP-C203 2005]: *Fatigue Design of Offshore Steel Structures*
Det Norske Veritas, 2005

[DNV-RP-E305 1988]: *On-Bottom Stability Design of Submarine Pipelines*
Det Norske Veritas, 1988

[DNV-RP-F105 2002]: *Free Spanning Pipelines*
Det Norske Veritas, 2002

[DNV-RP-F105 2006]: *Free Spanning Pipelines*
Det Norske Veritas, 2006

[DNV-Rules 1995]: *Rules for Classification of Fixed Offshore Installations*
Det Norske Veritas, 1995

[DS411 1999]: *Code of Practice for the structural use of concrete*
Dansk Standard, 1999
Volume 4

[DS412 1998]: *Code of Practice for the structural use of steel*
Dansk Standard, 1998
Volume 3.1

[Frigaard og Hald 2004]: *Bølgehydraulik*
Peter Frigaad og Tue Hald, 2004
Aalborg University, Denmark
Udgave 2

[Harremoës et al. 1980]: *Lærebog i geoteknik*
Harremoës, Krebs Ovesen, Moust Jacobsen, 1980
Polyteknisk Forlag
Udgave 4
ISBN: 87-502-0768-7

[Ibsen 1993]: *Poretryksopbygning i sand*
Lars Bo Ibsen, 1993
Aalborg University, Denmark

[Ibsen 1993b]: *Cyclic triaxial test on sand. Lund no 0. Bilag 2.*
Lars Bo Ibsen, 1993
Aalborg University, Denmark

[Justesen et al.1987]: *Forces On and Flow Around Near-bed Pipelines In Waves and Current*
P. Justesen, E.A. Hansen and J. Fredsøe, 1987
Tecnical University of Denmark

[Kramer 1996]: *Geotechnical earthquake engineering*
Steven Lawrence Kramer, 1996
Prentice-Hall
University of Washington, USA
ISBN: 0-13-374943-6

[Lambrakos et al. 1987]: *Wake Model of Hydrodynamic Forces On Pipelines*
K.F. Lambrakos, J.C. Chao, H. Beckmann, H.R. Brannon, 1987
Ocean Engineering
Volume 14.2

[Liu & Frigaard 2001]: *Generation and analysis of random waves*
Zhou Liu, Peter Frigaard, 2001
Aalborg University, Denmark
Udgave 3

[LICengineering 2005]: *Spanning Analysis*
Anders W Nielsen, Morten Christensen, 2005
LICengineering A/S

[Maersk 2008]: *Areas of Activity - Denmark*
  Maersk, 2008
  Maersk Oil
  http://www.maerskoil.com/da/AreasOfActivity/Denmark/
  Downloaded 22.03.2008

[Nielsen 2004]: *Vibration Theory, Vol. 1*
  Søren R.K. Nielsen, 2004
  Aalborg Tekniske Universitetsforlag
  ISSN: 1395-8232 U2004-1

[Nielsen 2005]: *Computational dynamics*
  Søren R.K. Nielsen, 2005
  Aalborg Tekniske Universitetsforlag
  Volume 9

[Nieslony 2003]: *Rain Flow Counting Method*
  Adam Nieslony, 2003
  Opole University of Technology, Poland
  http://www.mathworks.com
  Downloaded 24.01.2008

[Ovesen et al. 2007]: *Lærebog i geoteknik*
  Niels K. Ovesen, Leif D. Fuglsang, Gunnar Bagge et.al., 2007
  Polyteknisk Forlag
  ISBN: 87-502-0961-2

[Rice 1998]: *Elasticity of fluid-infiltrated porous solids (poroelasticity).*
  J. R. Rice, 1998
  Harvard University, USA
  http://esag.harvard.edu/rice/
  Downloaded 10.05.2008

[Sabag et al. 2000]: *Wake II Model for Hydrodynamic Forces on Marine Pipelines Including Waves and Currents*
  Said R. Sabag, Billy L. Edge and Iwan Soedigdo, 2000
  Ocean Engineering
  Volume 27.12

[Soedigdo et al. 1999]: *Prediction of Hydrodynamic Forces on Submarine Pipelines Using an Improved Wake II Model*
  Iwan R. Soedigdo, K. F. Lambrakos and Billy L. Edge, 1998
  Ocean Engineering
  Volume 26, 5

[Sumer & Fredsøe 1997]: *Hydrodynamics Around Cylindrical Structures*
   B. Mutlu Sumer and Jørgen Fredsøe, 1997
   World Scientific
   ISBN: 981-02-2898-8

[Wilcox 2002]: *Turbulence Modeling for CFD*
   David C. Wilcox, 2000
   DCW Industries
   Udgave 2
   ISBN: 0-9636051-5-1

[Zienkiewicz et al. 1999]: *Computational geomechanics with special reference to earthquake engineering*
   O. C. Zienkiewicz, A. H. C. Chan, M. Pastor, B.A. Schrefler, T. Shiomi, 1999
   John Wiley & Son Ltd.
   ISBN: 0-471-98285-7